

CHAPTER 6

Thermal-Hydraulic Design

Prepared by
Dr. Nikola K. Popov

Summary

This chapter covers the thermal-hydraulic design of nuclear power plants with a focus on the primary and secondary sides of the nuclear steam supply system. This chapter covers the following topics: evolution of the reactor thermal-hydraulic system; key design requirements for the heat transport system; thermal-hydraulic design principles and margins; design details of the primary and secondary heat transport systems; fundamentals of two-phase flow; fundamentals of heat transfer and fluid flow in the reactor heat transport system; other related topics.

Table of Contents

1	Introduction.....	10
1.1	Overview.....	10
1.2	Learning outcomes.....	12
1.3	Summary of relationship to other chapters.....	12
1.4	Thermal-hydraulic design.....	12
2	Reactor Types.....	14
2.1	CANDU reactor design.....	14
2.1.1	Reactor core and calandria vessel.....	17
2.1.2	Primary heat transport system design.....	19
2.1.3	Steam generators.....	20
2.1.4	Pressurizer.....	21
2.1.5	Primary pumps.....	22
2.1.6	Primary heat transport piping.....	22
2.1.7	Secondary heat transport system design.....	22
2.1.8	Turbine.....	23
2.1.9	Condenser.....	23
2.1.10	Heat exchangers and pumps.....	23
2.2	Problems.....	23
3	CANDU Thermal-Hydraulic Design Evolution.....	25
3.1	CANDU reactor evolution.....	25
3.1.2	Steam generators.....	27
3.1.3	Heat transport pumps.....	28
3.1.4	Reactor core.....	28
3.1.5	Reduction in radiation exposure.....	29
3.2	CANDU reactor types.....	30
3.2.1	Nuclear Power Demonstration station.....	30
3.2.2	Douglas Point.....	31
3.2.3	Pickering A and B.....	32
3.2.4	Bruce A and B.....	33
3.2.5	CANDU 6.....	34
3.2.6	Darlington.....	34
3.2.7	Advanced CANDU designs.....	35
3.3	Non-PHWR CANDU designs.....	37
3.3.1	CANDU-BLW.....	37
3.3.2	CANDU-OCR.....	38
3.4	Problems.....	39
4	Thermal-Hydraulic Design Requirements.....	40
4.1	Fuel requirements.....	40
4.1.1	Metallic fuels.....	42
4.1.2	Ceramic fuels.....	42
4.1.3	Dispersion fuels.....	43
4.2	General fuel sheath (cladding) requirements.....	44
4.2.2	Zirconium.....	45
4.3	Reactor coolant requirements.....	46
4.3.1	Ordinary water and heavy water coolants.....	46

4.3.2	Gaseous coolants.....	48
4.3.3	Liquid metal coolants.....	48
4.4	Moderator requirements.....	48
4.5	Control material requirements	50
4.5.1	Hafnium	50
4.5.2	Cadmium alloys	50
4.5.3	Rare-earth oxides	50
4.5.4	Gadolinium nitrate	51
4.5.5	Boron-containing materials.....	51
4.6	HTS design requirements and engineering considerations.....	52
4.7	Problems	54
5	Thermal-Hydraulic Design Limits and Margins.....	55
5.1	Heat generation parameter definitions	55
5.2	Thermal design limits	55
5.3	Thermal design margins.....	57
5.4	Problems	58
6	Thermal-Hydraulic Design Fundamentals.....	59
6.1	Two-phase flow fundamentals.....	59
6.1.1	Key parameters and definitions	59
6.1.2	Non-dimensional numbers.....	62
6.1.3	Flow patterns.....	65
6.1.4	The boiling process	70
6.1.5	Two-phase flow models.....	74
6.1.6	Two-phase flow in fuel bundles.....	75
6.1.7	Problems	77
6.2	Thermodynamics of nuclear energy conversion.....	78
6.2.1	Definitions.....	78
6.2.2	First law of thermodynamics	81
6.2.3	Reactor cycles	83
6.2.4	Second law of thermodynamics	86
6.2.5	Reactor power cycle.....	88
6.2.6	Improvements in reactor cycles	93
6.2.7	Entropy and the laws of thermodynamics.....	102
6.2.8	Problems	104
7	Heat Transfer and Fluid Flow Design.....	106
7.1	Heat transfer in the primary heat transfer system	106
7.2	Primary pumps.....	107
7.3	Steam generator heat balance.....	111
7.3.1	Steam generator without a pre-heater region	113
7.3.2	Approximate solution to steam generator without a pre-heater region.....	114
7.3.3	Calculation of main HTS parameters.....	116
7.3.4	Steam generator with pre-heater (simplified analytical solution).....	118
7.3.5	Steam generator with pre-heater (numerical solution).....	123
7.3.6	Problems	125
7.4	Heat transfer in the fuel elements	126
7.4.1	General heat conduction equation.....	126

7.4.2	Temperature distribution in the radial direction	127
7.4.3	Temperature distribution in the axial direction.....	132
7.4.4	Axial distribution of quality.....	136
7.4.5	Thermal conductivity and fuel element material properties	137
7.4.6	Problems	141
7.5	Fluid flow fundamentals	145
7.5.1	Introduction to pressure losses.....	145
7.5.2	Pressure drop conservation equations.....	147
7.5.3	Correlations for calculating pressure losses.....	149
7.5.4	Flow Instability	166
7.5.5	Problems	174
7.6	Heat transfer between the fuel elements and the coolant.....	176
7.6.1	Heat transfer regimes	176
7.6.2	Convective heat transfer in turbulent forced flow	177
7.6.3	Sub-cooled boiling heat transfer in forced flow	178
7.6.4	Critical heat flux (CHF).....	180
7.6.5	Transition and film boiling heat transfer	203
7.6.6	Single-phase heat transfer to vapour.....	217
7.6.7	Problems	218
7.7	Critical flow	221
7.8	Water hammer.....	221
7.8.1	Types of water hammer	222
7.8.2	Analytical models and computer codes for water hammer analysis.....	226
7.8.3	Diagnostics and assessment of water hammer.....	227
7.8.4	Prevention, mitigation, and accommodation of water hammer	228
7.8.5	Problems	230
7.9	Natural circulation	231
7.9.1	Natural circulation phenomenon.....	231
7.9.2	CANDU natural circulation	235
7.9.3	CANDU natural circulation experimental studies	240
7.9.4	Natural circulation calculations and predictions.....	241
7.9.5	Problems	243
8	References.....	244
9	Further Reading	247
10	Glossary	248
11	Nomenclature.....	249
12	Acknowledgements.....	250
13	APPENDIX A – Reactor Types.....	251
13.1	General evolution of reactor designs	251
13.2	Pressurized water reactors.....	252
13.2.1	General information	252
13.2.2	Reactor vessel	254
13.2.3	Steam generators.....	256
13.2.4	Primary pumps.....	256
13.2.5	Pressurizer.....	257
13.2.6	Reactor refuelling and reactivity control	257

13.2.7	Fuel assembly and fuel pin design	258
13.2.8	Reactor core design	262
13.2.9	WWER reactor design	262
13.3	Boiling water reactors	263
13.4	Gas-cooled reactors	267
13.4.1	Magnox reactors	267
13.4.2	AGR reactors	268
13.4.3	HTGCR Reactors	269
13.5	Channel-type reactors	269
13.5.1	SGHWR reactor	269
13.5.2	CANDU reactor	270
13.5.3	RBMK reactor	270
13.6	Fast breeder reactors	272

List of Figures

Figure 1	Heat engine concepts	13
Figure 2	Typical CANDU plant	15
Figure 3	CANDU 6 reactor cooling loops	16
Figure 4	CANDU reactor, fuel channel, and fuel bundle	18
Figure 5	CANDU calandria vessel and reactor vault	18
Figure 6	CANDU primary heat transport system	20
Figure 7	Typical steam generator design	21
Figure 8	Typical pressurizer design	21
Figure 9	Typical primary pump design	22
Figure 10	CANDU steam generator design evolution	28
Figure 11	Nuclear Power Demonstration (NPD) heat transport system	31
Figure 12	Douglas Point heat transport system	32
Figure 13	Pickering A heat transport system	32
Figure 14	Bruce heat transport system	33
Figure 15	Darlington heat transport system	34
Figure 16	ACR-1000 heat transport system	36
Figure 17	CANDU BLW heat transport system	37
Figure 18	CANDU OCR heat transport system	38
Figure 19	Fuel rod design types	41
Figure 20	Critical heat flux ratio	56
Figure 21	Thermal margins	58
Figure 22	Relationship between quality and void fraction [COL1972]	62
Figure 23	Flow patterns in vertical two-phase flow	66
Figure 24	Flow patterns in horizontal two-phase flow	66
Figure 25	Flow patterns and heat transfer regimes in horizontal heated tubes	67
Figure 26	Flow patterns and heat transfer regimes in vertical heated tubes	68
Figure 27	Flow pattern map in vertical flow [HET1982]	69
Figure 28	3-D representation of boiling surfaces	71

Figure 29 Boiling curve.....	71
Figure 30 Parametric trends of the boiling curve.....	72
Figure 31 Quality effects on the boiling curve.....	73
Figure 32 Heat transfer regimes in a boiling horizontal channel	73
Figure 33 Details of sub-cooled boiling phases in horizontal flow	74
Figure 34 Effect of tube diameter on quality and void fraction	76
Figure 35 Effect of bundle geometry on quality and void fraction	76
Figure 36 Change of thermodynamic states in a system.....	78
Figure 37 Concept of parameters of thermodynamic state in piston geometry	79
Figure 38 Ideal Carnot cycle.....	84
Figure 39 The concept of entropy in closed cycles.....	87
Figure 40 Carnot cycle for steam.....	89
Figure 41 Steam-water diagrams used in thermodynamic analyzes (a, b, c).....	90
Figure 42 Simplified Rankine cycle in a nuclear power plant.....	91
Figure 43 Typical impact of turbine outlet pressure on cycle thermodynamic efficiency.....	92
Figure 44 Typical impact of turbine inlet pressure on cycle thermodynamic efficiency.....	93
Figure 45 Rankine cycle with superheating	94
Figure 46 Rankine cycle with superheating and reheating.....	95
Figure 47 Rankine cycle with regeneration circuit	96
Figure 48 Rankine cycle with open feedwater reheating.....	97
Figure 49 Rankine cycle with multiple open reheaters	97
Figure 50 Rankine cycle with closed feedwater reheating.....	98
Figure 51 Rankine cycle with multiple closed reheaters	99
Figure 52 Rankine cycle with dryer.....	100
Figure 53 Real Rankine cycle with losses.....	101
Figure 54 Typical advanced PWR secondary cooling system	101
Figure 55 Typical CANDU 6 secondary cooling system.....	102
Figure 56 Reactor cooling systems	106
Figure 57 Primary pump flow diagram	107
Figure 58 Primary pump operating quadrants	109
Figure 59 Typical primary pump characteristics.....	110
Figure 60 Typical shutdown pump characteristics	111
Figure 61 Reactor steam generator loop.....	112
Figure 62 Steam generator simplified heat duty diagram.....	113
Figure 63 Steam generator heat duty diagram without pre-heating.....	113
Figure 64 Process for calculating primary loop parameters.....	116
Figure 65 Steam generator heat duty diagram with pre-heating	119
Figure 66 Reactor power versus heat-duty diagram of the SG	123
Figure 67 Steam generator numerical calculation concept.....	124
Figure 68 Nodalization concept for steam generator numerical calculation.....	124
Figure 69 Cross section of a cylindrical fuel pin.....	127
Figure 70 Radial temperature distribution in a fuel element.....	131
Figure 71 Radial temperature gradient per unit thickness in a fuel pin.....	132
Figure 72 Temperature distribution in the axial direction in a fuel element.....	135

Figure 73 Temperature distribution in the fuel cladding and the fuel element	136
Figure 74 Thermal conductivity in a fuel pin	138
Figure 75 Impact of oxygen-to-metal ratio on the heat conduction coefficient in fuel.....	138
Figure 76 Heat capacity of a fuel pin	139
Figure 77 Gap conductance in a fuel pin	139
Figure 78 Fuel aging effect on temperature in a fuel pin	140
Figure 79 Impact of gap thickness and linear power on heat conductance.....	140
Figure 80 Asymmetric temperature profiles in a fuel pin	141
Figure 81 Force-momentum balance in a control volume	147
Figure 82 Moody chart for friction factors	152
Figure 83 Martinelli-Nelson two-phase multiplier in separated flow	154
Figure 84 Single-phase pressure distribution over a square-edged orifice.....	156
Figure 85 Two-phase pressure distribution over a square-edged orifice	156
Figure 86 Bundle correction factor (37-element hexagonal bundle).....	157
Figure 87 Eccentricity effect	158
Figure 88 Eccentricity correction factor	158
Figure 89 Bundle junction misalignment effect.....	160
Figure 90 Typical single-phase pressure distribution over misaligned bundles.....	160
Figure 91 Typical pressure drop in misaligned fuel bundles	161
Figure 92 Typical misaligned junction pressure drop signatures	161
Figure 93 Typical two-phase pressure distribution over misaligned bundles.....	162
Figure 94 Pressure gradient along a flow channel in boiling.....	163
Figure 95 Example of abrupt area changes and orifice	164
Figure 96 Pressure drop behaviour with abrupt area changes and orifice	164
Figure 97 Pressure drop components.....	165
Figure 98 Concept of channel flow instability	168
Figure 99 Channel flow instability under low heat flux	169
Figure 100 Impact of different pump curves on channel flow instability	170
Figure 101 Definition of channel flow excursion instability in a single channel	171
Figure 102 Principles of flow excursion instability in two parallel channels.....	173
Figure 103 Results of flow excursion instability in two parallel channels.....	174
Figure 104 Concepts of CHF, dryout, and burnout.....	181
Figure 105 Transitions among CHF mechanisms.....	182
Figure 106 Pool boiling CHF mechanisms.....	183
Figure 107 Flow boiling CHF mechanisms	183
Figure 108 Effect of inlet temperature and mass flux.....	186
Figure 109 Effect of outlet pressure in pool boiling	186
Figure 110 Effect of outlet pressure on flow boiling	187
Figure 111 Effect of heated length on local CHF	187
Figure 112 Effect of quality on local CHF.....	188
Figure 113 Effect of tube diameter on local CHF.....	188
Figure 114 Concept of operating margins	194
Figure 115 Critical channel power	195
Figure 116 CHF margin definitions.....	196

Figure 117 CHF margin evaluation methods (a, b, c).....	198
Figure 118 CANDU bundle experimental simulator	200
Figure 119 Axial flux distribution in full-scale bundle test	200
Figure 120 CHF variation along a heated surface	200
Figure 121 Different types of spacer devices for CHF robustness.....	201
Figure 122 CHF behaviour around fuel bundle spacer devices	201
Figure 123 Types of transition boiling and film	204
Figure 124 Concept of transition boiling in pool boiling	205
Figure 125 Minimum film pool boiling – Taylor instability.....	206
Figure 126 Film boiling types	207
Figure 127 Pool film boiling mechanisms with horizontal heated wall.....	208
Figure 128 Pool film boiling patterns.....	208
Figure 129 Forced convection film boiling patterns	209
Figure 130 Film boiling heat transfer temperature and velocity profiles	210
Figure 131 Film boiling heat transfer mechanisms.....	211
Figure 132 Bundle dry patches in the dryout plane	215
Figure 133 Bundle circumferential temperature profiles.....	216
Figure 134 Rapid valve operation	222
Figure 135 Flow of sub-cooled water with steam condensing in vertical pipe (water cannon)	223
Figure 136 Counter-current flow of steam and water in a horizontal pipe	223
Figure 137 Pressurized water flowing in a vertical pipe filled with steam.....	224
Figure 138 Hot water entering a lower-pressure line	225
Figure 139 Steam-driven water slug in piping system.....	225
Figure 140 Filling of voided piping system.....	226
Figure 141 Principles of natural circulation	231
Figure 142 Various types of natural circulation.....	232
Figure 143 Natural circulation in CANDU	236
Figure 144 Onset of bi-directional flow in CANDU	238
Figure 145 Criteria for flow reversal in a CANDU core	238
Figure 146 Intermittent buoyancy-induced flow in CANDU.....	239
Figure 147 Typical temperature histories in a CANDU channel in natural circulation.....	240
Figure 148 Reactor generations.....	251
Figure 149 PWR primary reactor cooling system	254
Figure 150 Typical PWR reactor vessel	255
Figure 151 Typical PWR square fuel assembly design	258
Figure 152 Typical PWR fuel design	259
Figure 153 Typical PWR fuel assembly support spacer plates	260
Figure 154 Typical PWR reactor control sites.....	260
Figure 155 Typical PWR control assembly (cluster) design	261
Figure 156 Typical PWR control-rod design.....	261
Figure 157 Russian WWWR reactor design	263
Figure 158 BWR reactor design	264
Figure 159 Typical BWR reactor vessel coolant circulation.....	265
Figure 160 BWR reactor fuel assemblies in the core.....	265

Figure 161 BWR fuel and control assemblies	266
Figure 162 Typical Magnox reactor design	267
Figure 163 Typical AGR reactor design	268
Figure 164 Typical HTGCR reactor design	269
Figure 165 SGHWR reactor	270
Figure 166 RBMK reactor design	271
Figure 167 Fast reactor design.....	273

List of Tables

Table 1 Typical fuel characteristics for key reactor types	26
Table 2 CANDU main process parameters and features	27
Table 3 Evolution of D ₂ O content in the core and of power in the fuel channel	29
Table 4 Summary of uranium fuel characteristics [POP2014]	41
Table 5 Summary of fuel cladding characteristics [POP2014]	44
Table 6 Summary of coolant characteristics [POP2014]	47
Table 7 Summary of moderator characteristics [POP2014]	49
Table 8 Factors affecting pressure drop	146
Table 9 CANDU distribution of pressure drop in the primary loop	146
Table 10 Separate CHF effects in fuel bundles	185
Table 11 Sample of CHF look-up table.....	191
Table 12 Sample of PDO look-up table [IAEA2001]	214
Table 13 Typical PWR reactor parameters	253

1 Introduction

Section 1 provides an introduction to thermal-hydraulic design. It defines the expectations and learning outcomes for this chapter and indicates the relationship of this chapter to other chapters in this textbook.

The objective of this chapter is to describe the generic thermal-hydraulic design of nuclear reactors under normal operating conditions, with a specific focus on design details of CANDU reactors.

This chapter covers the thermal-hydraulic design of a CANDU nuclear power reactor, with general comparisons to other reactor types and designs. Thermal-hydraulic design covers the reactor primary and secondary heat transport systems. In fact, the primary heat transfer design defines the maximum power levels (globally and locally) that can be safely generated in the reactor core and thus defines the design characteristics of many systems and components, such as the reactor core physics and the fuel design.

1.1 Overview

This section describes the objectives, principles, and methodologies of reactor thermal-hydraulic design. The thermal-hydraulic design of the reactor process systems that are required to transport heat energy away from the nuclear reactor source and transform this heat energy into useful work (generally electrical energy) are the focus of nuclear engineering and of this chapter.

Section 2 presents the principles of reactor design, with a focus on CANDU reactor design. Designs of other reactor types are described in Appendix A, in which the focus is on providing a historical perspective on reactor thermal-hydraulic and systems design and on pressurized water reactors (PWRs) and boiling water reactors (BWRs).

Section 3 covers the design evolution of the CANDU reactor, including a general description of the overall design of the CANDU heat transport system and the design and evolution of the main components such as primary pumps, steam generators, and the reactor core.

Section 4 defines the thermal-hydraulic design requirements, including fuel cladding (fuel sheath), coolant, fuel, moderator materials, and control materials. Reactor core component materials are discussed and component requirements assessed. This section also discusses various fuel-coolant-moderator arrangements, their optimization, and their performance within the reactor design. Advantages and disadvantages of all the variations are discussed and possible solutions suggested. Finally, the section provides general requirements for the thermal-hydraulic design process.

Section 5 discusses reactor thermal-hydraulic design limits from the perspective of various reactor designs. It explains the concepts of reactor thermal margins and their application to reactor design assessment. Reactor thermal margins are an important parameter in reactor thermal-hydraulic design because they provide assurance that the heat generated by the fuel is removed from the reactor core under all possible operating conditions.

Section 6 covers thermal-hydraulic design fundamentals. The first part of this section presents

the fundamentals of single- and two-phase flow and heat transfer. Two-phase flow and heat transfer present a number of thermal-hydraulic design challenges, which are explained and discussed in this section. In addition, this section covers the thermodynamics of the reactor primary and secondary heat transport systems. The concepts of thermodynamic laws and their application to reactor design are presented. The concept of reactor thermodynamic efficiency is defined and its application to reactor performance assessment explained. Various secondary system designs are discussed, and a description of the secondary side components, such as steam turbines, steam condensers, feedwater systems and pre-heaters, and feedwater pumps, is provided.

Section 7 is the key section in this chapter because it describes the design of reactor heat transfer and fluid flow. This section outlines primary heat transport system behaviour, describes the various mathematical models, and discusses the most important characteristics of the primary heat transport system. The design and operation of the primary pumps is described. The design and operation of the steam generators is covered in detail because this component connects the primary and secondary heat transport systems, and therefore understanding its behaviour is essential for understanding overall reactor thermal-hydraulic behaviour. Flow stability in single-channel and parallel-channel instability situations is explained and its relevance to reactor and pump operation presented.

Also presented in Section 7 are heat transfer in the fuel elements and their heat transfer behaviour and operation in the reactor. Various topics are covered, such as fuel pellet cladding gap heat conduction, variability of heat conductivity in the fuel with temperature, and the influence of other important parameters. Fluid flow fundamentals are also covered, including calculation of pressure drop in the primary heat transport system under single- and two-phase operating conditions, calculation of flow resistance and its impact, and other important aspects.

Heat transfer between fuel and coolant is also discussed in Section 7, including heat transfer regimes in single-phase and two-phase operation, with a particular focus on boiling heat transfer in a CANDU fuel channel. The concept of critical heat flux is defined and discussed, along with various critical heat flux approaches, experimental data, and prediction methods. The impact of critical heat flux on reactor thermal margins is discussed and methods for improvement identified. An important part of the critical heat flux prediction model is the look-up table, which is explained and its application described. Part of this section is devoted to post-critical heat flux heat transfer, i.e., transition boiling and film boiling. Various heat transfer modes are discussed, with particular attention to CANDU fuel bundles. Most of the important heat transfer correlations are listed and explained and their application discussed.

Finally, the last few sub-sections of Section 7 are devoted to special topics in reactor thermal-hydraulic design. One section explains the critical flow phenomenon and its relevance to safety analysis, as well as the water hammer phenomenon. It provides insights on the risk from the water hammer hazard and provides high-level information on preventing this phenomenon in reactor design.

The last part of Section 7 covers natural circulation, which is an important phenomenon because it provides assurance that reactor decay heat will be removed from the core if forced-

flow cooling is lost. This section describes the natural circulation phenomenon and focusses on its application in CANDU reactors. The CANDU-specific phenomena of core cooling in the absence of forced flow and of intermittent buoyancy-induced flow in a CANDU fuel channel are covered.

1.2 Learning outcomes

The goal of this chapter is to help the reader to develop:

- An understanding of the principles and concepts of thermal-hydraulic design of nuclear reactors.
- An understanding of the evolution of the CANDU thermal-hydraulic design.
- Knowledge of general design principles, with a focus on the main parameters, design limits, and thermal-hydraulic margins by which the thermal-hydraulic design is characterized.
- An understanding of the design concepts and key features of the primary and secondary heat transport systems.
- Knowledge of the details of heat transfer and fluid flow and the heat transfer methodology used in the thermal hydraulics of the reactor heat transport system.
- A basic knowledge of unique CANDU thermal-hydraulic features and behaviour.

The reader needs to be generally familiar with other topics and disciplines related to thermal hydraulics. In addition, it is assumed that the reader has a basic understanding of fluid flow and heat transfer phenomena.

1.3 Summary of relationship to other chapters

Thermal-hydraulic design is fundamental to reactor design and behaviour. Therefore, a good understanding of thermal-hydraulic topics is required to understand the other chapters in this textbook.

This chapter is tightly connected to the chapters covering core physics, fuel design, and safety design and analysis. Furthermore, this chapter provides the knowledge base for understanding Chapter 7 on thermal-hydraulic analysis.

1.4 Thermal-hydraulic design

Nuclear reactor thermal-hydraulic design is concerned with designing the process systems required to transport heat (energy) from the nuclear reactor core (i.e., fuel) and to transform this heat energy into useful work (i.e., electrical energy) in the turbine-generator unit.

Thermal-hydraulic design is associated with a number of interrelated systems, including the reactor core, the heat transport system, steam generators, turbines, the pressure control system, the coolant inventory control system, and the power control systems. In addition, a number of components are important, including valves, pumps, pipes, vessels, and heat exchangers, and a number of engineering and scientific disciplines, including reactor physics, heat transfer, fluid mechanics, thermodynamics, chemistry, metallurgy, control, and stress analysis.

The most important role of reactor design from a safety perspective is to ensure that:

- the fission reaction can be achieved and controlled (addressed by the physical core design and fuel design);
- heat can be removed from the core to the ultimate heat sink (addressed by the thermal-hydraulic design);
- the reactor operation can be monitored (addressed by the instrumentation and control design), and
- the radioactive material can be contained within the reactor facility (addressed by the radiation protection and civil engineering design). Among the most important aspects of reactor engineering with respect to safe operation is the heat transfer and fluid flow (i.e., the thermal-hydraulic design).

The basic concept of a nuclear power plant is presented in **Figure 1**; it is similar to that of any other thermal power plant. The overall objective is to produce useful shaft work using a thermodynamic heat engine (a turbine) with a heat source (a reactor) and a heat sink (a lake, the sea, or the atmosphere). Following this basic concept, a number of variations of the nuclear power plant have been designed.

A number of inter-related systems and components are integrated into nuclear power plant design and interact with each other. Understanding their limitations and characteristics is an essential part of reactor design. Consequently, the process designer must appreciate the characteristics and limitations of all the major components and systems to carry out the detailed design of a particular system, i.e., to make intelligent choices. Design is, after all, the process of constraining the possible alternatives (in reaching a design objective) down to one choice. The overall goal is to provide an effective process within the context of the whole operation. This means that the system must perform its process function safely and efficiently at a reasonable cost. The interplay of these key concepts and systems constitutes “the design process”.

The final arbitrators in resolving the conflicting demands of each subsystem are: adequate level of safety, low overall cost, material limits (temperature, mechanical stress, erosion, corrosion, etc.), regulations, past experience, standardized design requirements, and quality assurance (QA).

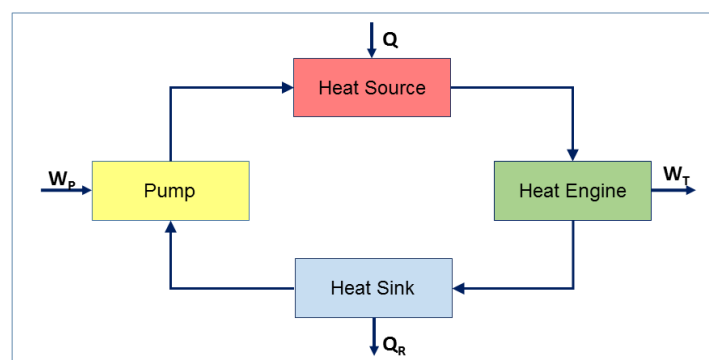


Figure 1 Heat engine concepts

2 Reactor Types

A number of reactor types are operating around the world, and many more have been designed in the past 50+ years of nuclear energy utilization, but never built. Many of these reactor types use very different physical and thermal-hydraulic concepts; however, only a handful have been able to ensure commercial viability over the past 50 years.

A number of these reactor types have proven to be commercially and economically competitive, the most successful of which include [ELW1990]:

- Pressurized water reactors (PWRs)
- Boiling water reactors (BWRs)
- Gas cooled reactors
- Channel type reactors.

Although a detailed discussion of these reactor types is beyond the scope of this text, the general evolution of reactor design and several of these designs are discussed in Appendix A.

The CANDU reactor design is a channel-type reactor, and a general overview, as relevant to the topic of thermal hydraulics, is presented in Section 2.1.

2.1 CANDU reactor design

The CANDU reactor has been designed and built by the Canadian nuclear industry [AECL1978, AECL1997], based on research and development undertaken by AECL, and has been successfully operating for 50 years in Canada and internationally. This is an important reactor type because, unlike other power reactors, it uses natural rather than enriched uranium and therefore offers much flexibility for countries wanting to enter into nuclear programs and fuel fabrication without requiring expensive uranium enrichment services. This section provides a brief description of the thermal hydraulics of CANDU reactors. Other sections in this chapter provide more detailed information about the thermal-hydraulic design of the CANDU reactor and its other systems and components.

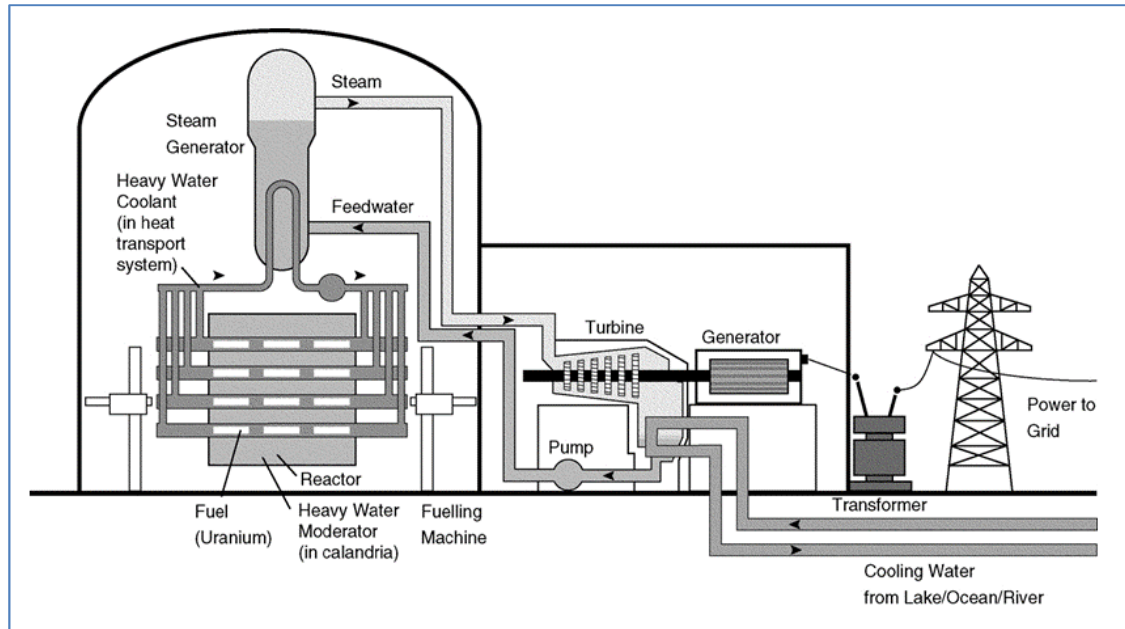
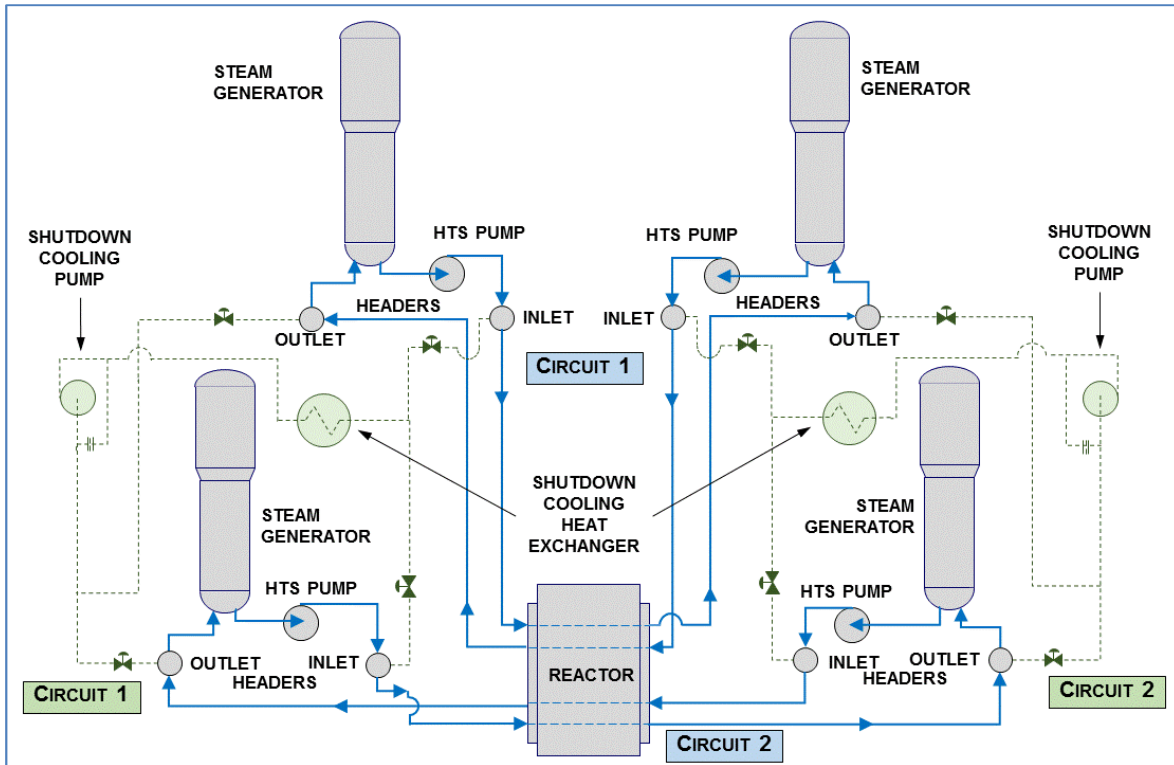


Figure 2 Typical CANDU plant

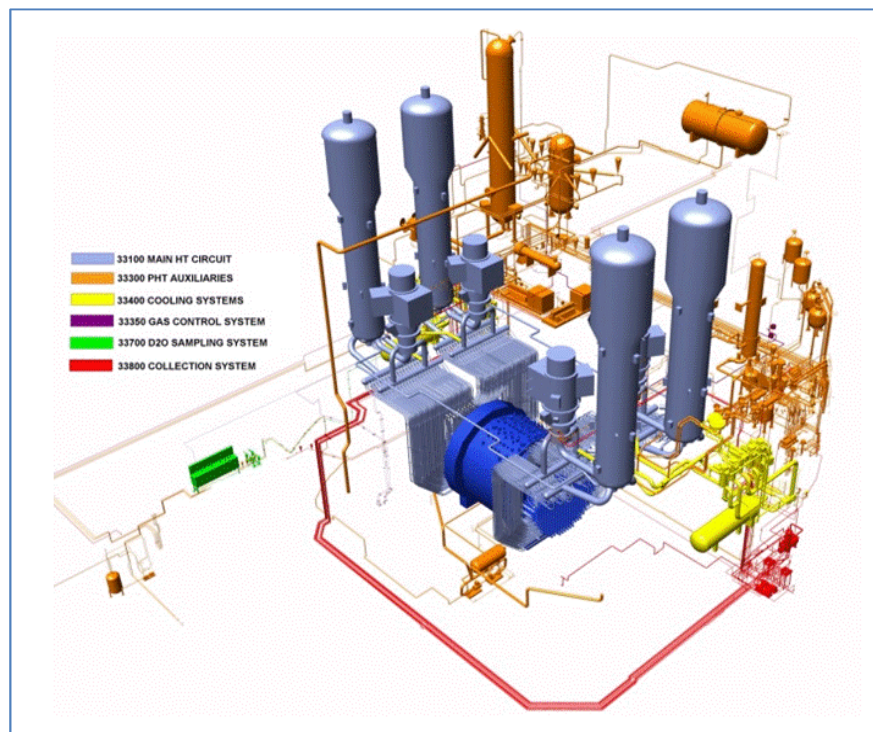
Figure 2 provides a schematic diagram of a typical CANDU heat transport system.

Figure 3a provides a detailed diagram of the CANDU 6 primary heat transport system (blue solid lines) and the shutdown system (green dashed lines) [AECL1981]. Figure 3b provides a 3D view of the CANDU 6 cooling system layout in the reactor building (the nuclear island) [AECL2005].

A CANDU nuclear steam supply system's power production process starts like that of any other nuclear steam supply system, with controlled fission in the reactor core.



a) CANDU 6 primary and shutdown cooling loops



b) CANDU 6 cooling loops in containment – 3D view

Figure 3 CANDU 6 reactor cooling loops

2.1.1 Reactor core and calandria vessel

The core in a CANDU reactor is horizontal (Figure 4), with reactor channels in the core containing the reactor fuel and heavy water coolant, whereas the heavy water moderator is in the calandria vessel surrounding the reactor core [AECL2009a, AECL2010]. The reactor is made up of a stainless-steel horizontal cylinder, the calandria, closed at each end by end shields that support the horizontal fuel channels spanning the calandria and provide personnel shielding. In the CANDU 6 design, the calandria is housed in and supported by a light water-filled, steel-lined concrete structure, the reactor vault, which provides thermal shielding (Figure 5). In the Darlington/Bruce CANDU reactor design, the calandria vessel is housed in a steel shield tank assembly, which performs a similar function to the CANDU 6 calandria vault. The calandria contains heavy water (D₂O) moderator at low temperature and pressure, reactivity control mechanisms, and several hundred fuel channels.

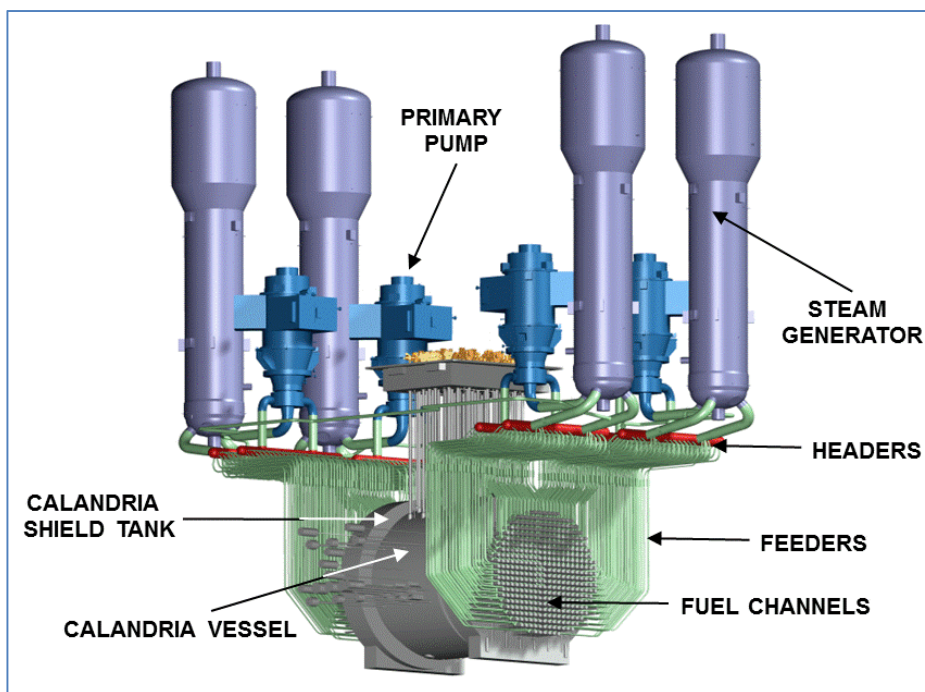


Figure 4a) Typical CANDU reactor and heat transport system

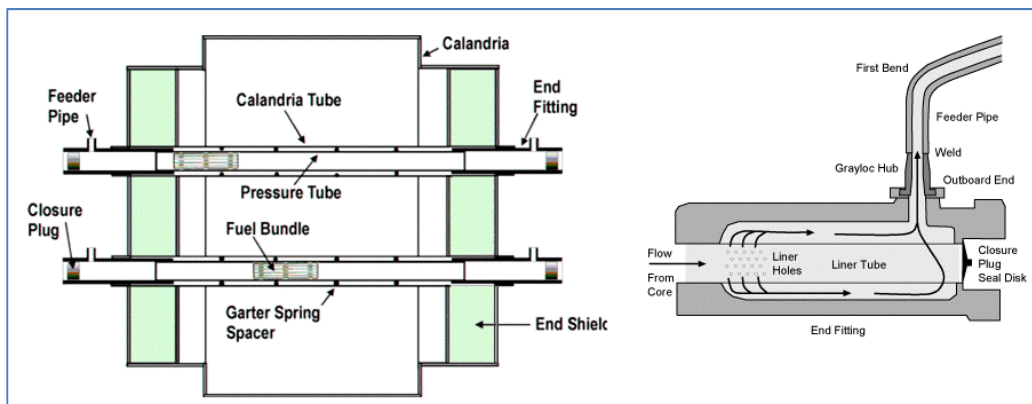


Figure 4b) Typical CANDU fuel channel

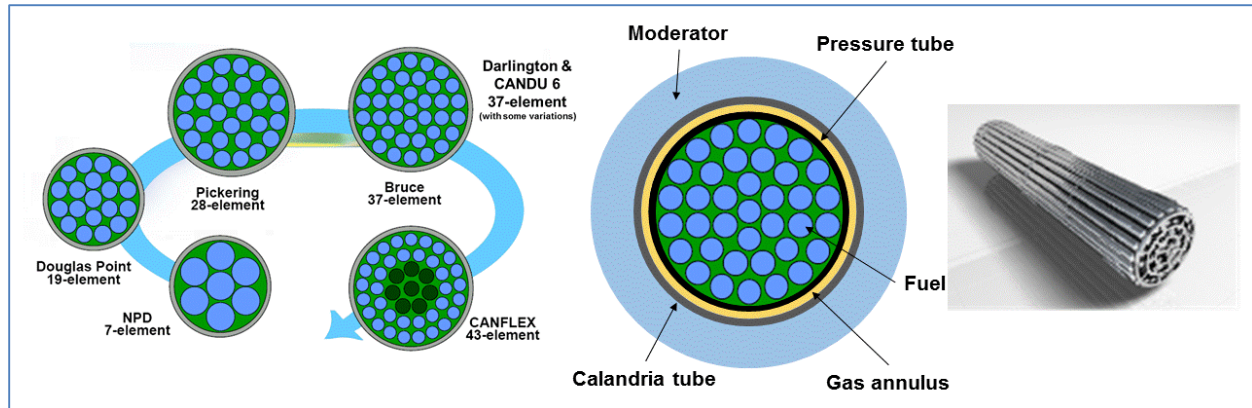


Figure 4c) Typical CANDU fuel bundle

Figure 4 CANDU reactor, fuel channel, and fuel bundle

Neutrons produced by nuclear fission are moderated (slowed) by the D_2O in the calandria. The moderator D_2O is circulated through systems that cool and purify it and control the concentrations of the soluble neutron absorbers used to adjust reactivity.

The fuel channels are also shown in Figure 4c. Each fuel channel supports 12 fuel bundles in the reactor core (13 in the Darlington/Bruce CANDU design). The fuel channel assembly includes a zirconium alloy pressure tube, a zirconium calandria tube, stainless steel end-fittings at each end, and four spacers that maintain separation of the pressure and calandria tubes. Each pressure tube is thermally insulated from the cool, low-pressure moderator by the CO_2 -filled gas annulus between the pressure tube and the concentric calandria tube.

The CANDU fuel bundle typically consists of 37 elements (although advanced 43-element designs have been qualified, and 28-element designs are still in service at Pickering station) arranged in circular rings, as shown in Figure 4c.

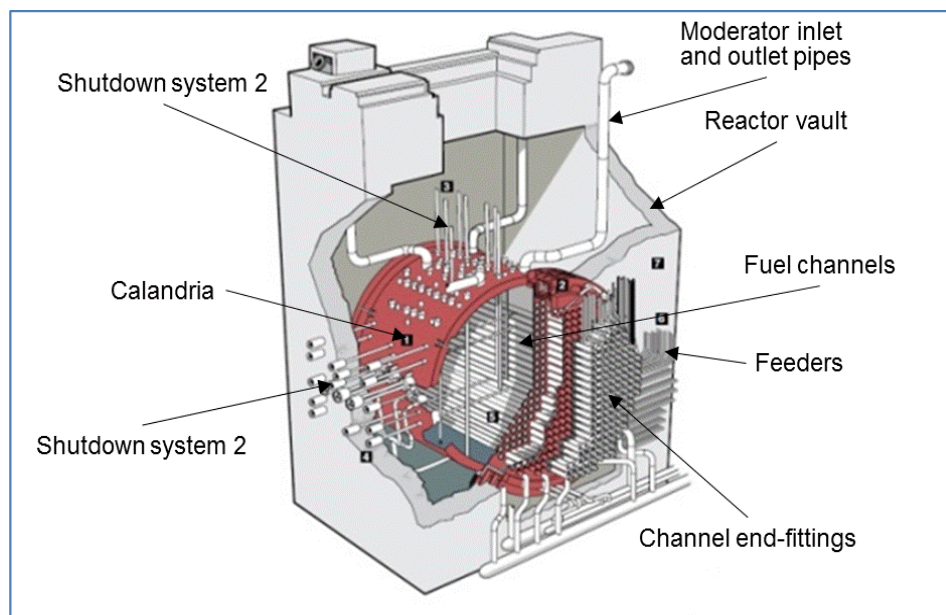


Figure 5 CANDU calandria vessel and reactor vault

Each fuel element consists of natural uranium in the form of cylindrical pellets of sintered uranium dioxide contained in a zircaloy-4 sheath closed at each end by an end cap. The fuel elements are held together by end plates at each end to form the fuel bundle. The required fuel element separation is maintained by spacers brazed to the fuel elements at the transverse mid-plane. The outer fuel elements have bearing pads brazed to the outer surface to support the fuel bundle in the pressure tube.

The CANDU reactor assembly, shown in Figure 5, includes the fuel channels contained in and supported by the calandria. Each end shield consists of an inner and an outer tube sheet joined by lattice tubes at each fuel channel location and a peripheral shell. The inner spaces of the end shields are filled with steel balls and are light water-cooled. The fuel channels, supported by the end shields, are located on a square lattice pitch. The calandria is filled with heavy water moderator at low temperature and pressure.

2.1.2 Primary heat transport system design

The CANDU primary heat transport system consists of primary, secondary, and tertiary loops, as shown in Figure 2 [AECL2009a]. There are several variations of the CANDU heat transport system design, the latest being the Pickering, Bruce/Darlington, and CANDU 6 designs. The CANDU 6 heat transport system design is described in the following sections.

The heat transport system (HTS) circulates pressurized D₂O coolant through the fuel channels to remove the heat produced by fission in the nuclear fuel. The coolant transports the heat to steam generators, where it is transferred to light water to produce steam to drive the turbine. Two HTS coolant loops (one in the Bruce design) are provided in CANDU reactors (Figure 6). Each loop has one inlet and one outlet header, as well as one primary pump and one steam generator at each end of the reactor core. D₂O is fed to each fuel channel through individual inlet feeder pipes from the inlet headers and is returned from each channel through individual outlet feeder pipes to the outlet headers. Each heat transport system loop is arranged in a “figure-of-eight”, with the coolant making two passes in opposite directions through the core during each complete circuit and the pumps in each loop operating in series. The coolant flow in adjacent fuel channels is in opposite directions.

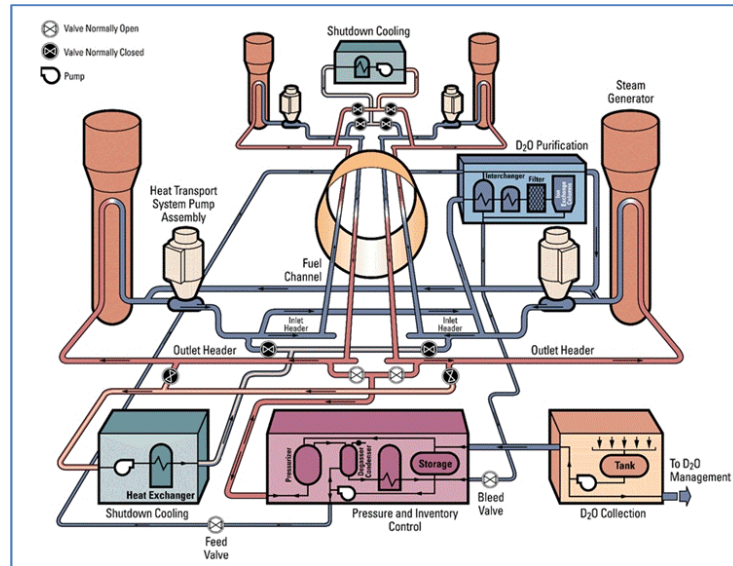


Figure 6 CANDU primary heat transport system

In most CANDU reactors, the pressure in the heat transport system is controlled by a pressurizer connected to the outlet headers at one end of the reactor. Valves provide isolation between the two loops and the pressurizer in the event of a loss-of-coolant accident.

Figure 6 provides a view of the “figure-of-eight” design of the CANDU heat transport system. On the right side, this figure shows the CANDU heat transport system to scale, with all feeders connected to the reactor core. Coolant is transported from the outlet headers to the steam generator by a large steam generator inlet pipe. Primary coolant from the steam generator outlet is transferred to the primary pump by means of a large pump suction pipe and from the pump to the inlet header by means of large pump discharge pipes.

The main components of the reactor primary heat transport system, in addition to the reactor, are the steam generators, primary pumps, connecting piping to each channel, distribution headers, large piping connecting these to the pumps and the steam generators, and the pressurizer. These components are described in the next few sections.

2.1.3 Steam generators

The CANDU steam generators consist of an inverted U-tube bundle within a cylindrical shell. Heavy water coolant passes through the U-tubes [AECL2009a, AECL2010]. The steam generators include an integral pre-heater on the secondary side of the U-tube outlet section and integral steam-separating equipment in the steam drum above the U-tube bundle. A typical steam generator structure is shown in Figure 7.

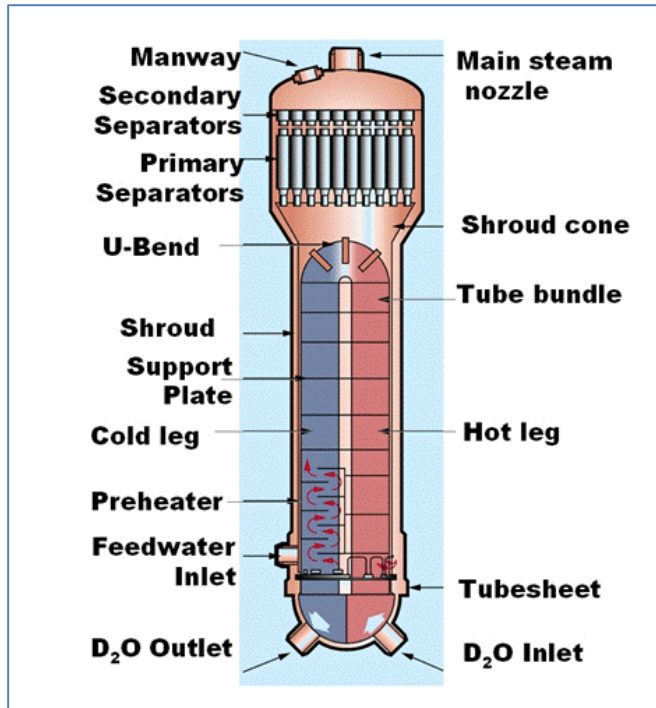


Figure 7 Typical steam generator design

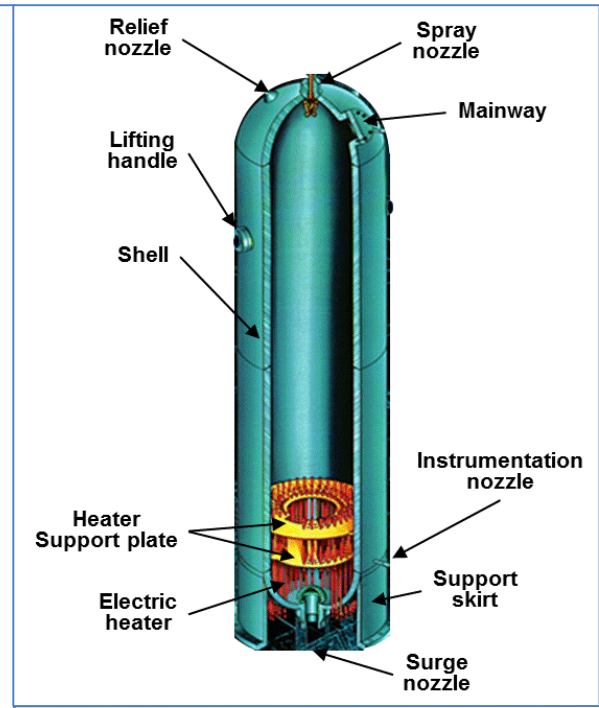


Figure 8 Typical pressurizer design

Operation and design details and calculations for the steam generator are provided in Section 7.3. The steam generator plays an important role in reactor heat transport system operation because it connects the reactor operation with the turbine-generator operation.

2.1.4 Pressurizer

The pressure in the reactor primary coolant system is maintained at a controlled level by a pressurizer. Figure 8 shows a view of a typical pressurizer [AECL2009a, AECL2010]. The pressurizer contains steam in the upper section of its cylinder and water in the lower section. The pressurizer is connected to the primary loop through a surge nozzle at the bottom. Heaters are provided at the bottom of the pressurizer internals, and a spray nozzle, relief nozzle, and safety nozzle are installed at the top of the pressurizer head.

A “positive surge” of water from the primary loop because of increasing loop pressure is compensated for by injecting cold water from the top of the pressurizer, which condenses the steam in the upper portion and thus reduces system pressure.

A “negative surge” of water empties the pressurizer, reducing steam pressure at the top of the pressurizer and thus loop pressure. In this situation, the electrical heaters at the bottom of the pressurizer are automatically activated, converting a portion of the water into steam and resulting in a loop pressure increase. By performing these sequences (i.e., creating steam when the loop pressure is too low or decreasing steam when the loop pressure is too high), the pressurizer maintains loop pressure within a certain design range and also ensures smooth pressure changes in the primary loop.

2.1.5 Primary pumps

The primary pumps used in the CANDU heat transport system are vertical, centrifugal motor-driven pumps with a single suction and a double discharge [AECL2009a, AECL2010]. As shown in Figure 9, the pump impeller is at the bottom of the pump, and the pump shaft extends upward to the pump motor, passing through a number of pump seals and holding the pump flywheel.

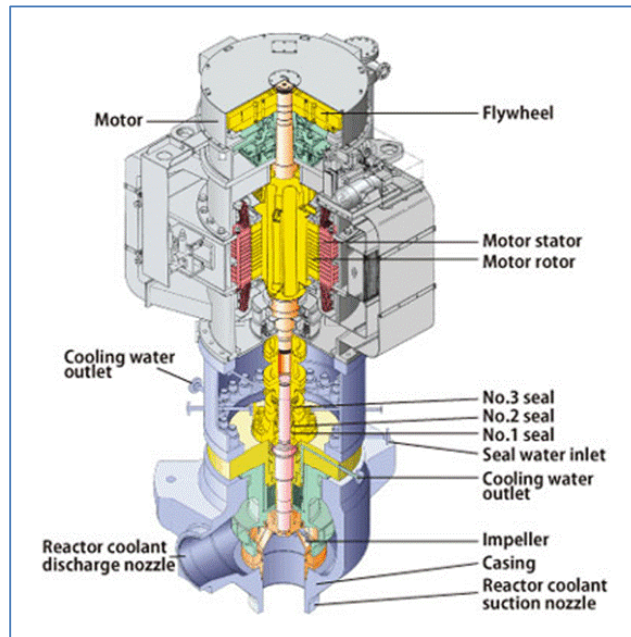


Figure 9 Typical primary pump design

Cooling of the reactor fuel in the event of electrical power supply interruption is maintained by the rotational momentum of the heat transport pumps during reactor power rundown and by natural convection flow after the pumps have stopped. More information on pump function, design, and operation is provided in later sections of this chapter.

2.1.6 Primary heat transport piping

The CANDU reactor contains a relatively large number of pipes, called feeders, and manifolds, called headers, in the primary heat transport system, which are used to distribute coolant to the fuel channels in the core. Although these components have important functions and are mentioned in this chapter, a detailed discussion is beyond the scope of this textbook. Note that feeders are unique to reactor designs with fuel channels and provide a number of design advantages, but are also vulnerable to certain types of accidents and aging effects, as mentioned in other chapters.

2.1.7 Secondary heat transport system design

The NPP secondary heat transport system transfers the generated energy from the primary closed circuit to the secondary, where the heat energy is transferred into mechanical energy of rotation in the turbine and then into electrical energy by the electric generator. The main

components of the secondary heat transport system are the steam turbine, condenser, heat exchangers, feedwater pumps, valves, and piping; these are covered in the next few sections.

2.1.8 Turbine

The CANDU steam turbine is typically a tandem compound unit, directly coupled to an electrical generator by a single shaft. It consists of one double-flow high-pressure cylinder followed by external moisture separators, five steam reheaters, and three double-flow low-pressure cylinders. The turbine is designed to operate with saturated inlet steam. The turbine system includes main steam stop valves, governor valves, reheat intercept valves, and emergency stop valves. All these valves close automatically in the event of a turbine protection system trip.

In the following sections, more details are provided about turbine operation, efficiency, and other relevant parameters.

2.1.9 Condenser

The turbine condenser consists of three separate shells. Each shell is connected to one of the three low-pressure turbine exhausts. Steam from the turbine flows into the shell, where it is condensed by flowing over a tube bundle assembly through which cooling water is pumped. The condenser cooling water typically consists of a once-through circuit that uses water from an ocean, lake, or river or is connected to cooling towers. The condensed steam collects in a tank at the bottom of the condenser called the “hot well”. A vacuum system is provided to remove air and other non-condensable gases from the condenser shell. The condenser is designed to accept turbine bypass steam to permit reduction of reactor power from 100% to 70% if the turbine is unavailable.

2.1.10 Heat exchangers and pumps

On its return to the steam generators, condensate from the turbine condenser is pumped through the feedwater heating system. Typically, it first passes through three low-pressure feedwater heater units, each of which contains two heaters fed by independent regenerative lines. (This arrangement permits maintenance work to be carried out on the heaters with only a small effect on turbine generator output.) Two of the heater units incorporate drain cooling sections and the third a separate drain cooling stage. Next, the feedwater enters a deaerator, where dissolved oxygen is removed. From the deaerator, the feedwater is pumped to the steam generators through two high-pressure feedwater heaters, each incorporating drain cooling sections (see Figure 55).

Several stages of feedwater pumps are installed to raise the pressure from the condenser pressure (vacuum) of 4–6 kPa to the steam generator pressure of 4.7 MPa. More information on heat exchanger design and calculations is provided in later sections of this chapter.

2.2 Problems

1. Name and describe the function of the main components of the CANDU primary heat transport system.

2. Describe the main components of the pressurizer in a CANDU reactor, with a detailed explanation of the method it uses to control the primary heat transport system pressure.
3. Provide a detailed description of the steam generator function, with specific reference to its role in the relationship between the primary and secondary heat transport systems. Comment on the relationship of these systems with the overall size of the steam generators.

3 CANDU Thermal-Hydraulic Design Evolution

To obtain a better understanding of CANDU design concepts, one needs to understand how the design has evolved over the past 50 years [AECL1978, AECL1997]. This section provides information focussing on the reasons why certain evolutionary steps were taken and why certain design solutions were abandoned, based on operating experience and on evolving regulatory requirements. The design evolution is covered from two perspectives: general evolution resulting from nuclear operating and regulatory experience around the world, and CANDU-specific operating and regulatory experience in Canada.

3.1 CANDU reactor evolution

The evolution of the heat transport system is of primary importance in understanding the evolution of power reactor technology. The primary heat transfer system contains the reactor core and the fuel and is therefore an important link between the reactor thermal-hydraulics, physics, and fuel.

The evolution of the heat transport system, which is described in this section, captures the design evolution of the reactor core, the fuel and fuel channels in the CANDU reactor, the type and number of primary heat transfer loops, and the primary pumps and steam generators. Also covered are the evolution of the systems and components on the secondary side of the heat transfer.

The CANDU design had its beginnings in the early 1950s, with preliminary engineering studies on a 20 MWe and a 200 MWe plant [AECL1997]. The design concepts were based on experimental confirmation at the ZEEP, NRX, and NRU experimental reactors at the AECL Chalk River Laboratory facilities. These studies eventually culminated in commitments to the construction of NPD and Douglas Point. NPD began operating in 1962 and Douglas Point in 1966. At the same time, commitments were made to construct Pickering in 1964 and Bruce in 1969. The 1970s witnessed the excellent operating performance of Pickering and Bruce and further commitments to construct the Gentilly-2 (Quebec), Embalse (Cordoba, Argentina), Point Lepreau (New Brunswick), Wolsong (Korea), Pickering B (Ontario), Bruce B (Ontario), and Darlington (Ontario) plants.

In most cases, successive plants have meant an increase in reactor power output. Evolutionary developments have been undertaken to fit the requirements of stricter safety goals, higher ratings and sizes, new regulations, better reliability and maintainability, and lower costs. These evolutionary changes have been introduced in the course of engineering parallel reactor projects with overlapping construction schedules—circumstances which provide close contact with the practical realities of economics, manufacturing, construction activities, and performance in plant commissioning. Features for one project furnished alternative concepts for other plants on the drawing board at that time, and the experience gained in first application yielded a sound basis for re-use in succeeding projects. Thus, the experience gained in NPD, Douglas Point, Gentilly-1, and KANUPP contributed to Pickering and Bruce. In turn, all these plants contributed to the CANDU 6 design (i.e., Gentilly-2, Point Lepreau, Wolsong, Cernavoda, Embalse, and Qinshan). The evolutionary changes that have taken place are discussed in the following sections.

Table 1 provides a general comparison of key design features of other reactor types with those of CANDU [GAR1999, POP2014, POP2015]. Table 2 provides information on the evolution of various key components in CANDU heat transport systems.

Table 1 Typical fuel characteristics for key reactor types

Characteristic	BWR	PWR	AGR	LMFBR	CANDU
Moderator	H ₂ O	H ₂ O	Graphite	-	D ₂ O
Coolant	H ₂ O	H ₂ O	CO ₂	Molten Salt	D ₂ O
Neutron Energy	Thermal	Thermal	Thermal	Fast	Thermal
Fuel	Enriched UO ₂	Enriched UO ₂	Enriched UO ₂	PuO ₂ /UO ₂	Natural UO ₂
Fuel Geometry	Cylindrical pellet in clad tube	Cylindrical pellet in clad tube			
Fuel Assembly	Up to 10 x 10 rod array	Up to 17 x 17 rod array	Concentric circles	Hexagonal rod array	37-element fuel bundles (typ.)

3.1.1 Primary heat transport system

The evolution of the CANDU design has involved a continuing quest for higher reliability, better equipment maintainability, and reduced radiation doses to operating staff. This has been manifested in a dramatic reduction in the number of components, as shown in Table 2. For example, NPD had approximately 100 valves per MW in the nuclear steam supply system. This was reduced to less than 1 valve per MW in the Bruce, Gentilly-2, and Darlington designs. In addition, there are no valves in the large HTS main piping (past the Pickering design). The number of steam generators has gone from 12 in Pickering, to 8 in Bruce, to 4 in the CANDU 6 and Darlington designs. Other evolutionary changes have included improvements in sub-cooling margins, increased gross and channel flowrates, and increases in system pressure and temperature. All materials in the heat transport circuit are now specified for very low levels of cobalt to minimize radiation fields, thus improving CANDU radiation protection robustness.

Table 2 CANDU main process parameters and features

Parameter	Douglas Point	Pickering	Bruce/Darlington	CANDU 6
Power Output MW _e	210	515	750 / 850	700
Number of Channels	306	390	480	380
Number of Pumps	10	16	4	4
Pump Type	Vertical Centrifugal Single Stage			
Power per Pump kW	600	1170	> 8250	> 5250
Pump Code	BPVC Sect. VIII	BPVC Sect. VIII	BPVC Sect. III Class 1	BPVC Sect. III Class 1
Pump Seismic Classification	None	None	DBE Category 'A'	DBE Category 'A'
Number of Steam Generators	80	12	4 or 8	4
SG Power MW/boiler	2.5	~ 45	~ 95	150
SG Material	M-400	M-400	I-600	I-800
Number of SG Tubes	196	2600	> 4200	3550

3.1.2 Steam generators

Steam generator size has been generally limited by the industrial capability to produce the generators. Figure 10 [GAR1999] shows the evolution of the steam generator in terms of its size and power. The power of the Darlington steam generators is close to 800 MW. Current CANDU 6 plant designs typically have four steam generators.

Monel was used as the tubing material for Douglas Point, RAPP, KANUPP, and Pickering. This material has proven quite satisfactory for the non-boiling coolant conditions of those plants. Inconel 600 was used in NPD and in Bruce. This is a more costly material than Monel; however, its corrosion resistance in a boiling environment (as in Bruce) is much superior. Currently, Incoloy 800 is used in all 600-MW class CANDU 6 operating reactors. This material is more or less equal in most respects to Inconel 600, has greater resistance to intergranular attack, and is somewhat lower in cost.

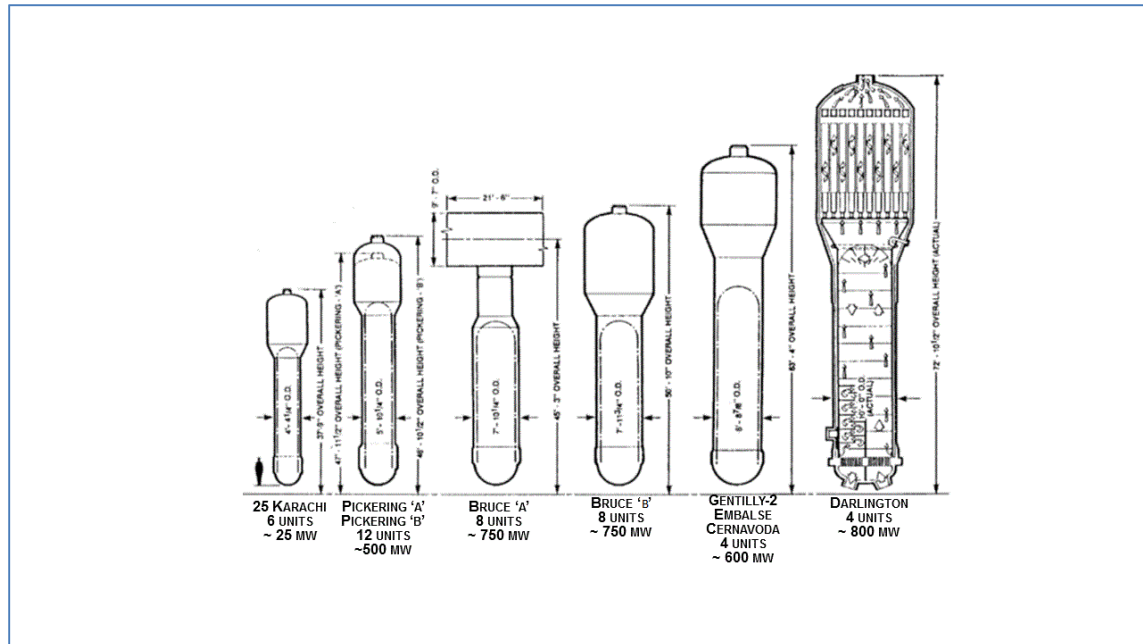


Figure 10 CANDU steam generator design evolution

3.1.3 Heat transport pumps

Pump-motor sets have retained essentially the same configuration in all CANDU stations, i.e., vertical electric motor-driven, centrifugal, volute-type casing, one radial guide bearing in the pump with pumped fluid as lubricant, a tilting pad-type guide and double-acting thrust bearing in the motor, and mechanical shaft seals. Table 2 provides information on the evolution of the primary pump [GAR1999].

Maintainability has been improved by providing interchangeable sub-assemblies. Appropriate shielding placement has made it possible to change a pump motor on Bruce while the reactor continues to operate at 60%–70% power.

There has been a trend away from solid rotor flywheels (Douglas Point to Gentilly-2) to additional packages of rotor laminations located just outboard of the main rotor (Point Lepreau, Bruce 'B'). This manner of fabrication eliminates the requirement for in-service inspection because it is highly unlikely that a defect could grow from one lamination to another.

Regulatory requirements for pumps have grown from minimal at the beginning to the present time, at which the pump pressure boundary is considered in the same way as for nuclear pressure vessels (ASME Section III, Class I). Consequently, non-destructive examination (NDE) and quality assurance requirements have increased considerably.

3.1.4 Reactor core

In 1955, a detailed design of a demonstration natural uranium reactor was carried out. It was called the Nuclear Power Demonstration (NPD) and was based on a vertical pressure vessel concept [AECL1997]. In 1957, this was changed to a horizontal pressure tube configuration—a

configuration which has remained in subsequent heavy water-cooled reactors. The horizontal configuration aided the on-line fuelling scheme by making double-ended fuelling feasible. It also permitted the use of vertical safety control rods, which did not interfere with the pressure tubes and feeders.

Reactor core evolutionary changes have been intended to achieve:

- a) large increases in core rating with the minimum increase in reactor size (higher power density enabling reduction in capital cost);
- b) reduction in shop fabrication costs through simplification and standardization;
- c) reduction in field assembly and shortened construction schedules through more shop fabrication and modularization.

Table 3 Evolution of D₂O content in the core and of power in the fuel channel

Reactor Design	D ₂ O in Core per MW Thermal [m ³ /MWth]	MW Thermal per Metre Length of Fuel Channel [MWth/m]
NPD	0.410	0.163
Douglas Point	0.169	0.453
KANUPP	0.182	0.443
Pickering A	0.157	0.752
Bruce A & B	0.112	0.881
Gentilly-2	0.105	0.931

The major impact of higher power densities on capital costs is to reduce the heavy water inventory. The amount of heavy water in the reactor core per MW produced in the reactor is listed in Table 3. Higher power densities required more MWs of power produced per metre length of fuel channel.

3.1.5 Reduction in radiation exposure

Canada has accepted the recommendations made by the International Commission on Radiological Protection (ICRP) on maximum permitted doses for occupationally exposed persons.

Note that severe accident doses are different from these normal operating doses and that discussion is ongoing about these doses, especially under the influence of the accident in Fukushima, Japan in 2011.

The major factors affecting the radiation dose accumulated by a worker are:

- a) Amount of equipment.
- b) Frequency of failure.
- c) Time required for repair, service, and inspection.
- d) Radiation conditions (fields and airborne concentrations).

Because radiation dose is proportional to the product of these four factors, a reduction in any factor will reduce the dose received. The following general classification of some solutions in the design stage has emerged:

- 1) Avoid adding equipment.
- 2) Eliminate equipment and remove unnecessary redundancy.
- 3) Simplify equipment.
- 4) Provide necessary equipment of high reliability.
- 5) Relocate equipment to lower radiation fields.
- 6) Eliminate materials such as cobalt, which could become highly radioactive.
- 7) Provide better chemical control and purification.
- 8) Arrange for quick removal for shop maintenance.
- 9) Extend interval between maintenance periods.
- 10) Reduce *in-situ* maintenance times.
- 11) Provide adequate space around equipment.
- 12) Provide adequate shielding so that maintenance can take place in low fields.

3.2 CANDU reactor types

Over the past 60 years, AECL in Canada has designed many types of CANDU reactors, some of which were built and operated, and some of which were never built or were abandoned. This section provides a brief overview of these past CANDU designs, with a view to understanding the evolution of the CANDU heat transport system and its thermal-hydraulic design [AECL1997].

3.2.1 Nuclear Power Demonstration station

Figure 11 shows the simplified HTS schematic for the Nuclear Power Demonstration (NPD) CANDU design [GAR1999, POP2014]. This was the first reactor design prepared by AECL. The HTS circuit contained in-line isolating valves for maintenance purposes. Pump reliability was enhanced by using three 50%-capacity pumps with check valves to prevent reverse flow through the non-operating pump. The check valves were placed at the pump discharge, of course, rather than at the suction to meet net positive suction head (NPSH) requirements. The 66 inlet and 66 outlet feeders at each end of the core terminated in a reactor inlet and a reactor outlet header respectively. Hence, bidirectional channel flow was used to limit spatial reactivity feedback. Channel flow was trimmed to match the radial power distribution by inserting an orifice plate into the inlet end fittings. All feeders were of the same diameter. Pump flywheels were used to match the power rundown during a Class IV power failure to ensure adequate fuel cooling, as in all CANDU stations. Boilers were placed above the core to enhance thermo-siphoning. Feed and bleed provided pressure and inventory control.

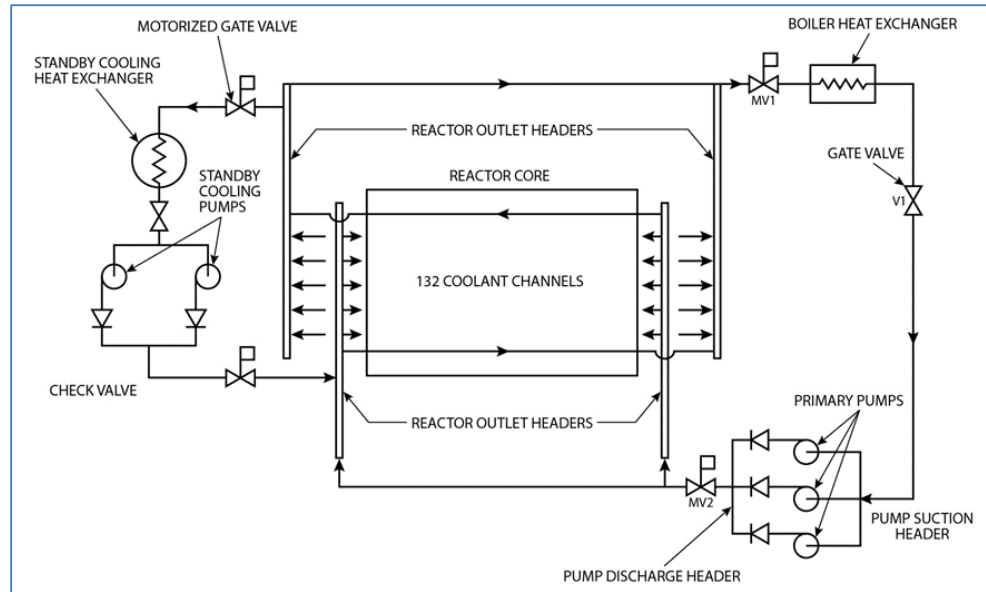


Figure 11 Nuclear Power Demonstration (NPD) heat transport system

The NPD nuclear station had some significant design features that were quite different from other CANDU stations. There was only one set of inlet and outlet headers, with relatively long connecting pipes running from one side to the other of the reactor vessel. The end fittings of the reactor fuel channels did not have shield plugs, leading to a large holdup of heavy water in this region. The core itself consisted of two fuel bundle types. The central region had 19-element bundles, and the outer region had 7-element bundles.

Another difference from later CANDU reactors is that the steam generator was a horizontal U-tube vessel with the steam drum situated above and connected to the steam generator by a series of four-inch risers and downcomers.

3.2.2 Douglas Point

The Douglas Point power plant was the first station to incorporate features typical of later CANDU designs [GAR1999, POP2014]. Figure 12 shows a simplified HTS schematic for the Douglas Point design. This station used the “figure-of-eight” loop layout. This configuration had the advantage of reducing D_2O holdup and pressure drop by eliminating the long piping runs to the far end of the core, which were inherent in the NPD design. This introduced the possibility of east-west (loop end-to-end) imbalances. Redundancy in pumps was required to achieve adequate reliability. As in NPD, bidirectional channel flow, check valves at pump discharges, and isolation valves were used. Channel flow was trimmed to match the radial power distribution using different feeder sizes or orifice plates in inlet feeders and shield plugs.

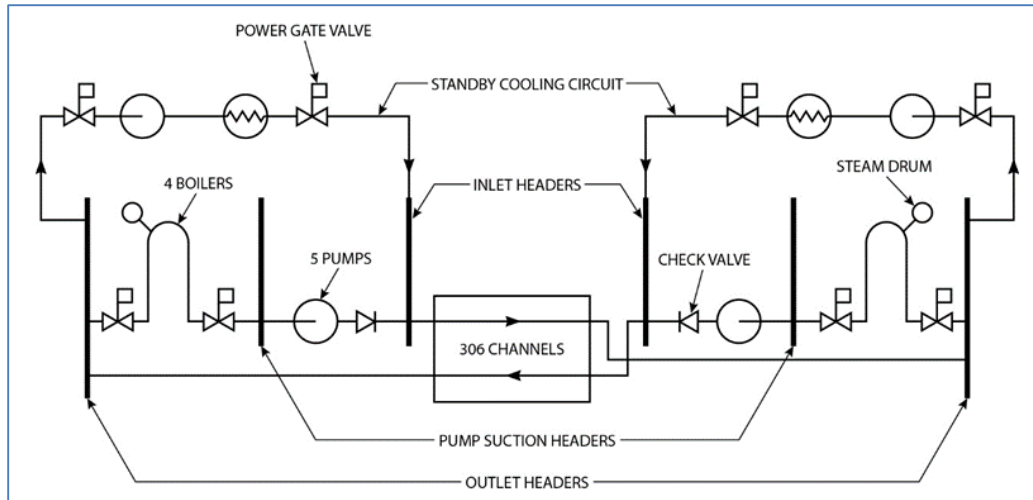


Figure 12 Douglas Point heat transport system

3.2.3 Pickering A and B

The Pickering stations have a similar thermal-hydraulic design to Douglas Point. The Pickering heat transport system is shown in Figure 13 [OPG2000]. Power output was increased to 540 MWe, and two loops were used to reduce the rate of blowdown in the event of a loss-of-coolant accident (LOCA).

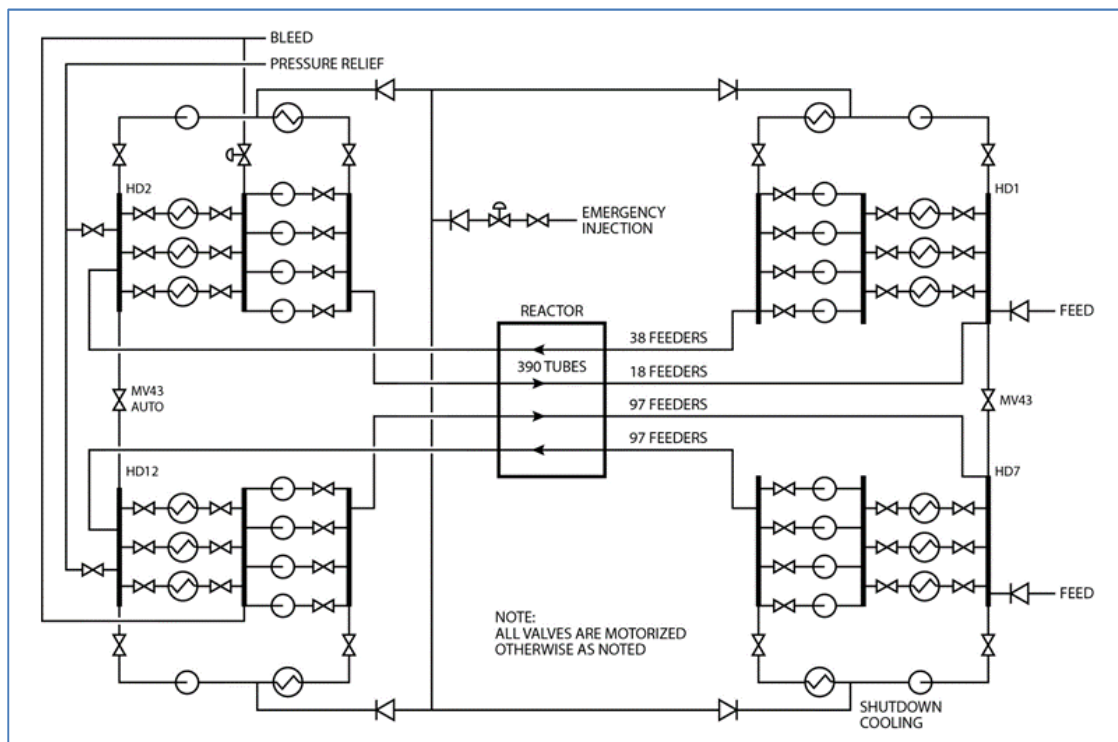


Figure 13 Pickering A heat transport system

A loop interconnect was provided to reduce loop-to-loop imbalance. Manufacturing limits on steam generators and pumps led to the use of 12 operating steam generators and 12 operating

pumps with four reserve pumps. Component isolation was still possible, but check valves were eliminated because of the leakage and poor reliability experienced at the Douglas Point plant. Trimmed channel flow was achieved by varying feeder sizes and inlet feeder orifice plates. The Pickering fuel bundle has 28 fuel elements and is the only CANDU design currently operating with 28-element fuel.

3.2.4 Bruce A and B

Figure 14 shows the simplified schematic of the Bruce HTS system [BPR2000]. It shows a significant difference in layout compared to the Pickering station. For Bruce (and later stations, such as CANDU 6 and Darlington), the reliability experience gained from previous plants justified the elimination of stand-by pumps. For radiation protection and maintenance reasons, valves were eliminated. Manufacturing now permitted larger components, and therefore eight steam generators and four pumps were included. Channel flow was not trimmed to meet power distribution capability as in all other CANDUs. A constant radial flow distribution was maintained by changing feeder sizes to account for geometry and feeder length differences. As in all CANDU designs, fuel channel flow velocity was limited to 10 m/s due to concerns about fretting of the fuel bundle and pressure tubes. The Bruce channel design had thirteen 37-element fuel bundles located in the fuel channel, but the core length was kept the same. Therefore, at each end of the core, half a fuel bundle protruded out of the reactor core region.

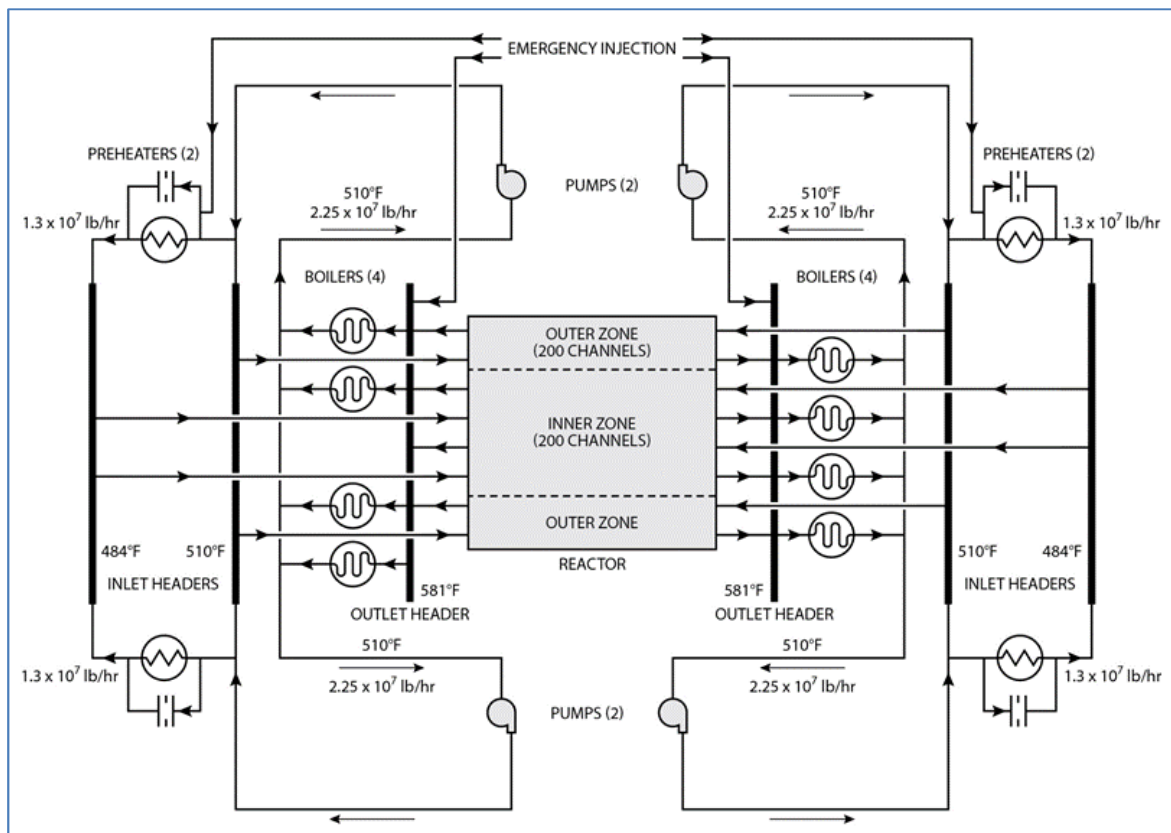


Figure 14 Bruce heat transport system

3.2.5 CANDU 6

The CANDU 6 has been discussed in previous and following sections. The figure-of-eight loop HTS design was adopted as of the Pickering design [AECL2009a, AECL2010]. However, also as in the Bruce design, fewer components were used. Increased confidence in knowledge of two-phase flow led to the use of boiling under normal conditions in the HTS. Erosion and corrosion concerns at the steam generator inlet limited the quality to 4.5% at this position or nominally 4% at the reactor outlet header (ROH). Erosion/corrosion concerns also limited single- and two-phase coolant flow velocities to a maximum value of 15.25 m/s to 16.75 m/s. The presence of boiling required a surge tank or pressurizer to accommodate the larger shrink and swell during transients. The pressurizer was used for pressure control (using heaters and steam bleed valves), whereas inventory control remained as feed and bleed. This is the same approach as in the Bruce design because the Bruce design is nominally single-phase. A heat transport system schematic of the CANDU 6 design is shown in Figure 3.

3.2.6 Darlington

The HTS schematic for the Darlington design, shown in Figure 15, is similar to the CANDU 6 design. The Darlington reactor core design is similar to the Bruce reactor core design (480 fuel channels with 13 bundles per channel) [OPG2002]. The Darlington HTS process conditions were chosen to be very close to those of the CANDU 6 because that was the state of the art at that time. An optimization program showed that higher tube pressures, higher qualities, and higher velocities were economical. However, state-of-the-art engineering limits on pressure tubes, qualities, and velocities forced the optimization to stop at these limits, which were the same as for the CANDU 6 design.

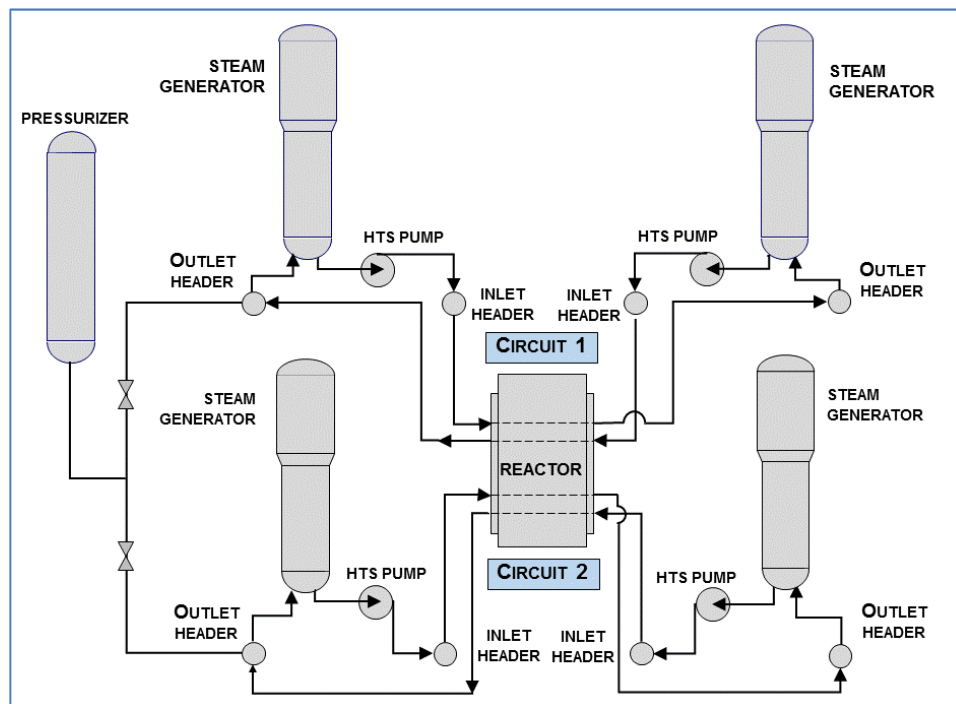


Figure 15 Darlington heat transport system

The HTS for Darlington was designed by Ontario Hydro with design support from AECL. AECL retained responsibility for the primary HTS between the headers (RIH, feeders, end-fittings, fuel channels, and ROH), whereas Ontario Hydro assumed design responsibility for the rest of the system.

The Darlington HTS design has four inlet headers, two on each side of the calandria vessel, and two outlet headers, one on each side of the calandria vessel. This configuration enables mixing in the outlet headers between the two loops, a feature that is useful for balancing the coolant parameters in both loops. However, it also exhibits some weaknesses in achieving isolation of the intact loop when the other loop is exposed to a break and a large LOCA situation.

3.2.7 Advanced CANDU designs

The advanced CANDU designs responded to continuing emphasis on safety, reliability, and maintainability (R&M), quality assurance (QA), reduction in radiation doses, standardization, modularization, and capital cost reduction. The excellent performance record of Pickering and Bruce was maintained through a vigorous R&D program and a common-sense approach to QA. Along with maintaining the above features, some of the high-level design directions were:

- a) Reduction of capital cost;
- b) Minimization of all areas of cost, from engineering to fabrication, construction, and commissioning; and
- c) Shortening of the overall construction schedule.

Heat transport system and process designs also reflected the evolution in the state of the art, notably in the following areas:

- 1) Critical heat flux;
- 2) Erosion/corrosion velocity limits;
- 3) Single- and two-phase pressure drop and heat transfer correlations;
- 4) Thermo-siphoning;
- 5) Safety guidelines and requirements;
- 6) Stability aspects of two-phase flows;
- 7) Two-phase pump performance requirements;
- 8) Pump seals;
- 9) Process modelling (e.g., pressurizer, headers, boilers);
- 10) Creep of fuel channels;
- 11) Fuel design (fretting, hydraulic characteristics);
- 12) Power output and other constraints as required by clients;
- 13) Feeder sizing criteria.

3.2.7.1 CANDU 3, CANDU 9, and ACR-700

The CANDU 3, CANDU 9, and ACR-700 conceptual and preliminary designs were completed in the 1990s and 2000s to meet a market need for small low-cost power reactors, large natural uranium-fuelled reactors, and customer-specific needs respectively. Each of these reactor types had different heat transport designs; however, no stations were built using these reactor designs, and they were abandoned by AECL.

3.2.7.2 ACR-1000

The ACR-1000 conceptual and preliminary design was completed at the end of the 2000s; however, no station was built using this reactor design. Figure 16 shows the key features of the primary ACR-1000 heat transport system [AECL2009b]. The ACR-1000 reactor uses light water as coolant with a low level of fuel enrichment (around 2.1%). This combination, along with certain fuel design changes, resulted in negative void reactivity. The fuel design consisted of a 43-element bundle (CANFLEX) with low-enriched uranium fuel and with the central and intermediate rings of larger diameter than the outer two rings. The central element did not have fuel in it, and the outer two rings had pins with a certain percentage of neutron absorber to achieve negative void reactivity. The fuel had target burn-up as high as 20,000 MWd/t. Reactor power was about 3200 MWt with 520 fuel channels in the core.

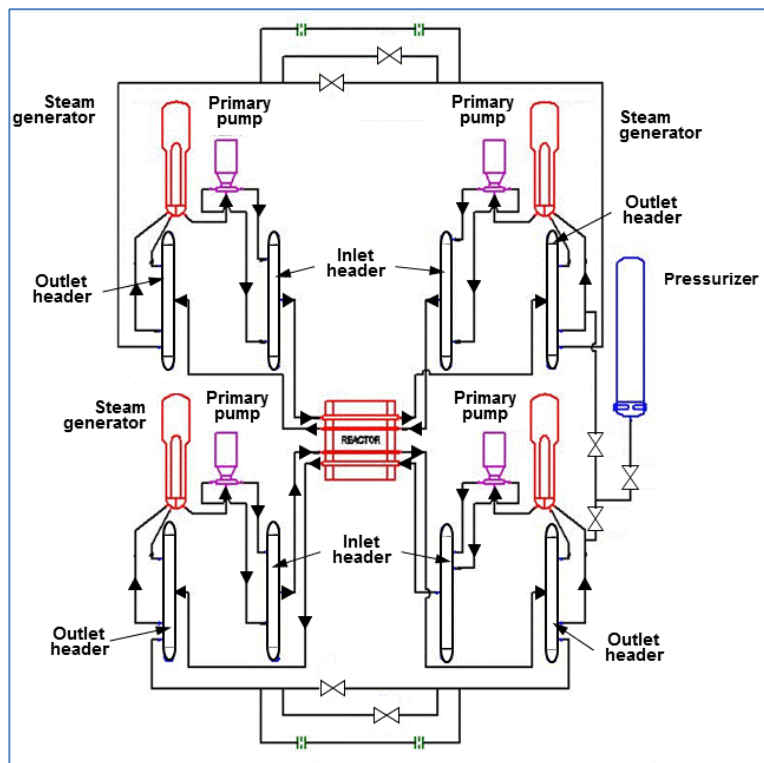


Figure 16 ACR-1000 heat transport system

The heat transport system has two figure-of-eight loops with four steam generators, with four pumps, two pumps, and two steam generators on each side of the loop. Although this reactor design has a negative void reactivity and from this perspective does not need to have two primary loops to reduce the power pulse in a large LOCA, it had two loops for a different reason. Because the reactor power was high, in addition to other reasons, having one loop (as in ACR-700) would require very large steam generators and primary pumps. Hence, splitting the core into two loops brought the scale of the steam generators and primary pumps closer to those readily available on the market.

The reactor pressure was high (about 13 MPa), along with high inlet and outlet temperatures, resulting in better thermal efficiency than earlier models.

3.2.7.3 Enhanced CANDU 6

The Enhanced CANDU 6 (EC6) design followed the CANDU 6 design, but included a number of design changes to enhance safety, operability, maintainability, constructability, and economics [AECL2009a, AECL2010]. Most of these changes were made in the reactor safety systems, with few in the thermal-hydraulic design. The EC6 heat transport system basically followed the CANDU 6 design, which has been covered in previous sections.

3.3 Non-PHWR CANDU designs

A number of CANDU-generic reactor designs were completed that either did not use heavy water coolant or were horizontal. These designs were never used in any CANDU stations, but they present a particular set of design directions that were considered in the past. These designs were later abandoned for various reasons, eventually focussing AECL's design effort on the horizontal heavy water reactor, known as CANDU, which was fuelled, moderated, and cooled in a horizontal direction. Some of these early designs are covered in the following sections.

3.3.1 CANDU-BLW

This was the second version of the basic CANDU concept to reach the prototype reactor stage (the 250 MWe Gentilly-1 plant) [AECL1997]. Its major difference from the others lay in the choice of coolant: boiling light (ordinary) water, hence its name, BLW. Its reactor coolant and turbine systems were fundamentally the same as those of the BWR described earlier, i.e., a direct cycle was used.

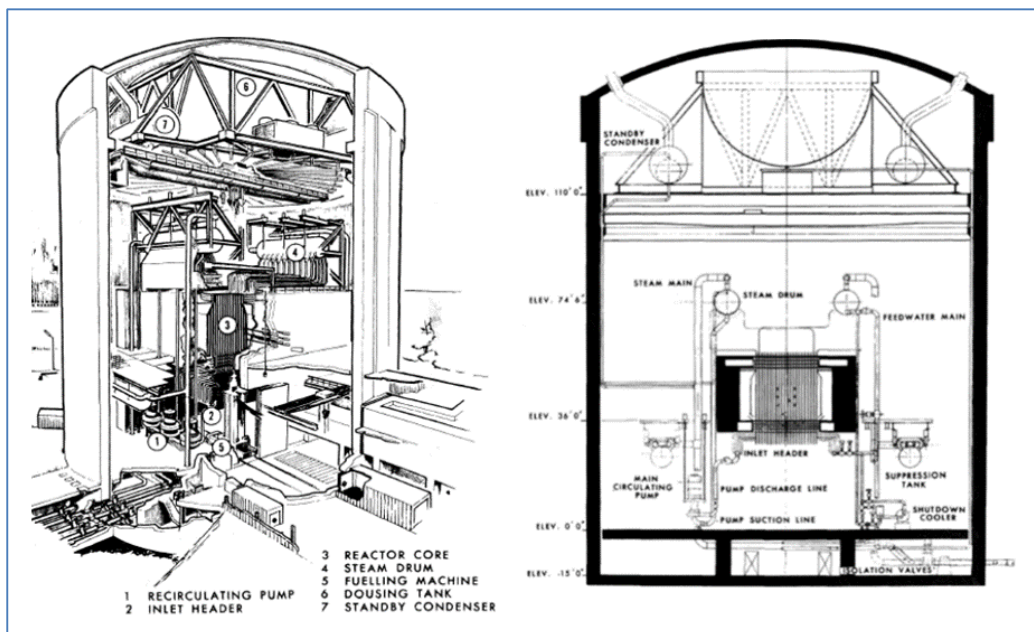


Figure 17 CANDU BLW heat transport system

For this version, a vertical orientation was chosen. A number of detailed considerations relating to the boiling coolant led to this choice.

Figure 17 provides a schematic illustration of the design. Ordinary water is pumped to the bottom of each fuel channel through an individual feeder pipe. As the water passes upwards and absorbs heat from the fuel, a fraction ($\sim 18\%$) is evaporated to steam. The resulting steam/water mixture then flows to a conventional steam drum where the steam and water are separated. The steam then flows to the turbine, and the water, mixed with incoming feedwater in the drum, flows down to the circulating pumps, completing the cycle.

The British developed a similar version, called the SGHWR (steam-generating heavy water reactor). A 100 MWe prototype was built. It differed from the Gentilly-1 design in that it used slightly enriched fuel. This enabled lower-purity heavy water moderator to be used, reducing capital costs. The fuelling costs were, however, somewhat higher.

In Japan, another similar version, called the FUGEN reactor, was developed and operated for about 20 years. The moderator cooling system was similar to the conventional CANDU version.

3.3.2 CANDU-OCR

A third version of the basic CANDU concept used an organic fluid as the coolant [AECL1997]. It would have been similar to the PHWR concept, except that the boilers would likely be of the “once-through” type, with some steam superheating provided. This was made possible because the coolant temperature at the reactor outlet could be $\sim 100^\circ\text{C}$ higher than with heavy water cooling.

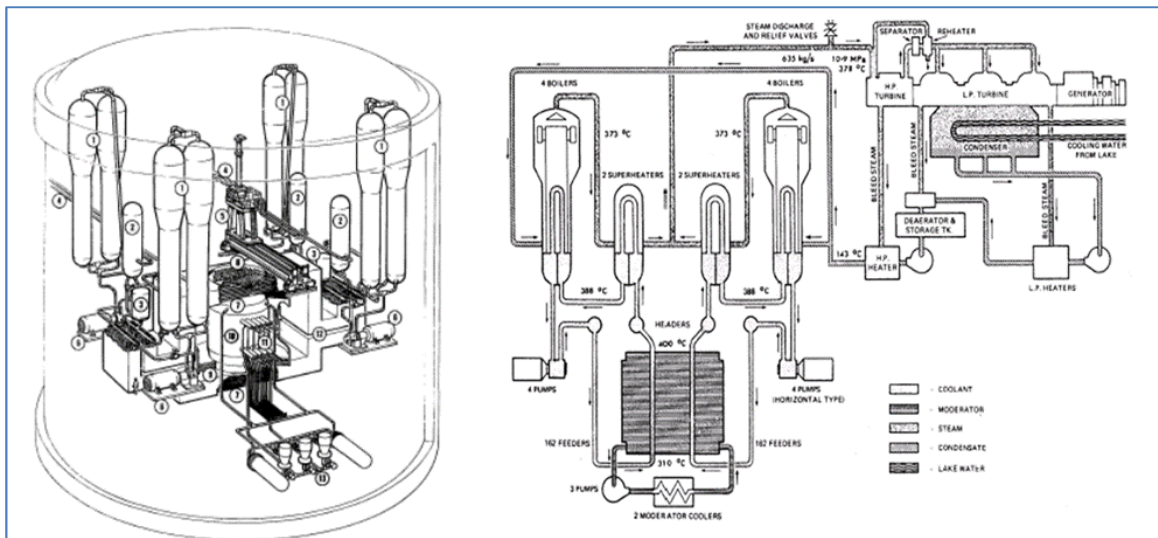


Figure 18 CANDU OCR heat transport system

The Whiteshell Reactor-1 (WR-1) experimental reactor at the AECL Whiteshell establishment used this concept, except that the heat was used only for building heating, i.e., no turbine was provided. The reactor operated under coolant conditions which were the same as those used in a commercial power plant.

Figure 18 shows a design drawing of the CANDU-OCR reactor with the key features explained above. This reactor was never built because this concept was abandoned due to certain weaknesses that were encountered, such as fire protection with coolant that is naturally

flammable, aging of the coolant (which required constant replacement and hence had a negative impact on reactor availability (associated outage frequency)), and radiation protection of the removed aged coolant.

One of the benefits of using organic coolant is that it is a mixture of several components and therefore does not boil completely at a certain temperature. This helps to avoid going through a two-phase region at one pressure and temperature, thus avoiding problems with critical heat flux. Organic coolant also helps to achieve much higher coolant temperatures in the core without the need to elevate the core pressure (as would be necessary for water). This improves thermal efficiency significantly and makes the mechanical design easier and “lighter” because of lower core pressures.

3.4 Problems

1. Describe and contrast the main similarities and differences between a CANDU primary heat transport system and a PWR primary heat transport system design.
2. List three different CANDU reactor designs and explain the differences between each of their heat transport system designs.
3. Identify four impacts of radiation doses on workers and list the general solutions that have emerged at the design stage to mitigate their impacts.
4. Explain the benefits of using organic coolant in the CANDU-OCR design.

4 Thermal-Hydraulic Design Requirements

This section covers power reactor design requirements with a focus on the thermal-hydraulic design of the reactor core [GAR1999, POP2014]. However, it should be kept in mind that the thermal-hydraulic design is tightly linked to and interfaces with other aspects of reactor design, particularly core physics and fuel design. Therefore, in various sections throughout this chapter, these interfaces are mentioned and covered to the extent necessary to obtain a better understanding of thermal-hydraulic design.

Relevant core configurations for various reactor types are covered, with a specific focus on the CANDU design. Requirements for coolant, fuel, moderator, and key materials used for reactor control and construction are covered, typical materials used for these components discussed, options considered, and analysis provided.

When discussing fuel, coolant, and moderator requirements, note that neutron economy is repeatedly mentioned as an important parameter [GLA1967]. This is true even for enriched uranium reactors because the amount of fissile isotope enrichment, and hence the cost of the fuel, is very sensitive to the neutron economy of the reactor. This is particularly so because uranium enrichment is very costly because it involves an isotope separation rather than a chemical separation process. In addition to cost, the fuel enrichment process involves a number of safeguards, regulations, and rules, which make this process politically sensitive.

4.1 Fuel requirements

In all commercial power reactors, fuel is used in solid form and in various geometries such as solid rods (cylindrical), plates, spheres, or annular configurations (see Figure 19). The key parameter governing fuel design, with respect to thermal hydraulics, is the external surface area-to-volume ratio. Good heat transfer to the coolant medium is promoted by high values of this ratio, whereas low fuel manufacturing costs and good neutron economy generally are promoted by low values of this ratio. This presents a “classical” optimization problem during reactor design. Therefore, from this perspective, the annular fuel geometry best meets this requirement; plate fuel is next, and cylindrical fuel is the worst. However, in most power reactors in operation today, cylindrical fuel rods are used, primarily due to lower manufacturing costs.

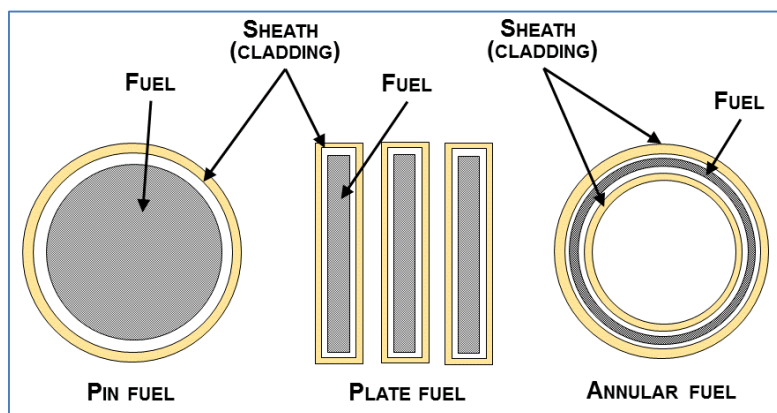


Figure 19 Fuel rod design types

Fuel requirements include (but are not limited to):

- a) Low cost – both material and fabrication.
- b) Good neutron economy.
- c) Good corrosion resistance to coolant.
- d) Physical stability under effects of radiation, temperature, and pressure.

Typical uranium-based fuel materials that have been considered or used include:

- 1) Uranium metal.
- 2) Uranium / other material alloy.
- 3) Ceramic uranium dioxide.
- 4) Uranium carbide.
- 5) Uranium silicide.

A summary of uranium fuel characteristics is presented in Table 4 [POP2014].

Table 4 Summary of uranium fuel characteristics [POP2014]

U Fuel Form	Cost	Neutron Economy	Corrosion	Physical Stability
U Metal	Lowest	OK	Poor	Poor (swelling)
U Alloy	Higher	Lower	OK	OK
UO₂	Higher	Lower	Excellent	Excellent. High T.
UC	Lower than UO ₂	UO ₂ <UC<U Metal	Good, except against water	Good. High T.
US	~UC	~UC	Good even with water	~UC

Among uranium-based fuels, uranium metal is generally lowest in manufacturing cost and highest in neutron economy, the latter because of its high density and the absence of other neutron-absorbing elements. However, it has poor corrosion resistance to most coolants, which is important in the event of fuel cladding failure. Its geometric stability in reactor use is poor, primarily because of the swelling effects of fission products with specific volume greater than that of the parent uranium.

Large quantities of alloying agents, such as zirconium, can be used, which effectively solve the geometric stability and coolant corrosion problems. Unfortunately, both cost and neutron

economy suffer.

Uranium dioxide is the form in which uranium fuel is used in the vast majority of today's power reactors. It is somewhat more expensive to manufacture and less neutron-economical than uranium metal because of its lower density, but possesses excellent corrosion resistance to most coolants and a high degree of geometric stability. Being a ceramic, it can withstand high operating temperatures, which has been the deciding factor.

Uranium carbide may be attractive as a fuel for future reactor designs. It is relatively inexpensive to manufacture (comparable to UO_2) and has somewhat better neutron economy than UO_2 (because of its higher density), but not as good as that of uranium metal. It has good corrosion resistance against many coolants, but unfortunately not to water. Its dimensional stability is good, and it can operate at high temperatures.

Uranium silicide is a more recent development with most of the advantages of uranium carbide and in addition adequate resistance to corrosion by water coolants.

4.1.1 Metallic fuels

Unalloyed uranium metal is a very poor reactor fuel because it exhibits substantial growth under irradiation. Highly irradiated specimens have been known to show axial growth equal to more than 60% of the original sample length.

Uranium metal is highly chemically reactive and can be used at high temperatures with only a few coolants, e.g., carbon dioxide and helium. Low-alloy uranium fuel (with a small amount of alloying material) has been demonstrated to increase corrosion resistance to high-temperature water and to improve irradiation stability. Good results have been obtained with U_3Si (U-3.8 wt.% Si). Irradiation stability is somewhat improved, and corrosion resistance is about 500 times greater than that of unalloyed uranium. More satisfactory fuels can be obtained by addition of alloying materials, for example, 10–20 wt.% Mo or Nb alloys containing 10%–13.5% molybdenum; this option has appeared most promising.

Fuels that are highly satisfactory from both the irradiation-damage and water-corrosion standpoints can be obtained with large additions of alloying material. The only high-alloy uranium fuels in current power-reactor application are alloys of uranium and zirconium because of the good neutron economy features of zirconium.

4.1.2 Ceramic fuels

Uranium dioxide is the most widely used of all reactor materials [POP2014]. It has an irradiation stability far superior to that of metallic fuels and can withstand the high burn-up required for economical power-reactor application. When properly prepared, it exhibits excellent resistance to high-temperature water or sodium.

Uranium dioxide is obtained from the gaseous UF_6 product of the diffusion plant. Hydrolysis of UF_6 produces UO_2F_2 , which is reacted in a dilute ammonia solution to form a precipitate of ammonium diuranate. This precipitate is calcined to UO_3 , which is then reduced to UO_2 by hydrogen at about 800°C. The oxide is produced as a fine powder, which needs to be pressed

into a high-density compact form followed by sintering at high temperature into cylindrical pellets.

The thermal conductivity of uranium dioxide is quite low. At the high power output required in power-reactor service, this leads to very high temperature gradients across the fuel element. The resulting thermal stresses generally lead to radial cracking of the pellets during operation. However, this cracking does not appear to cause any deterioration in fuel performance, provided that the pellets are suitably restrained by cladding. Fuel element centreline melting does remain a concern and imposes an important safety margin criterion.

The chief limitation on UO_2 fuel performance is the swelling caused by gaseous fission products. At low and moderate burn-up, the swelling is slight and roughly linear with burn-up. Above a critical burn-up, the swelling increases markedly, and continued exposure of the fuel leads to unacceptable dimensional changes. The critical burn-up is primarily a function of fuel density, a value of about 17×10^3 MWd/tHE (heavy elements) being obtained with fuel of 97% oxide density and a value on the order of 42×10^3 MWd/tHE with 93% density fuel.

Thorium dioxide (ThO_2) behaves similarly to UO_2 under irradiation. Thermal stress-induced cracking is also observed in ThO_2 fuels.

Carbide fuels are intended primarily for use in fast-breeder reactors (where they provide better breeding ratios). Because these reactors operate on the U-Pu cycle, the fuel consists of mixed uranium and plutonium oxides. Thermal conductivity of UC is substantially better than that of UO_2 . Hence, considerably higher specific powers are possible without risk of centreline melting. However, at higher temperatures, the swelling rate becomes excessive. The higher thermal conductivity of carbide fuel leads to a much lower Doppler coefficient than that obtained with an oxide core (the Doppler effect is the change in frequency of a wave for an observer moving relative to its source). Because the Doppler coefficient in the fuel is the main component of negative reactivity feedback in most accident situations, designing a safe carbide-fuelled core may be more difficult than designing an oxide core.

Nitride fuels have also been considered for use in fast reactor fuel.

4.1.3 Dispersion fuels

In a dispersion-type fuel, particles of fissile material are embedded in a metallic ceramic matrix [POP2014]. Such fuels can generally withstand significantly higher burn-up than alloy fuels. If the fuel particles are separated sufficiently, the areas damaged by fission fragments will not overlap, and a continuous metal phase will remain.

UO_2 and PuO_2 can be dispersed in aluminum, stainless steel, and zirconium alloys. The low-temperature limitation on the use of aluminum eliminates these dispersions from consideration for use in power reactors. Although stainless steel suffers from no such limitation, poor neutron economy eliminates it from consideration in commercial reactors. Dispersion of UO_2 in zirconium alloys forms highly satisfactory fuels if highly enriched uranium is used. Fuel performance is still limited by fuel swelling.

The most important dispersion fuel in use today is the dispersion of mixed uranium-thorium carbides or oxides in graphite. These dispersions are used in high-temperature gas-cooled

reactors. Dispersion is achieved by multiple layers of pyrolytic carbon.

4.2 General fuel sheath (cladding) requirements

During fission, new isotopes of a wide variety of elements are produced. Many of these remain radioactive for a significant time after they are generated and hence constitute a potential radiation hazard to plant operators and the public at large. It is therefore clearly desirable to keep these fission products “bottled up” within the fuel where they are generated. This is the primary function of the fuel sheath (or cladding in light water reactor technology).

The fuel cladding takes the form of an impervious “skin” or “shell” which encloses the fuel material. The most important requirements that cladding material should meet are [GAR1999, POP2014]:

- a) Corrosion resistance to coolant.
- b) Mechanical durability.
- c) High operating temperature capability (high melting temperature).
- d) Good neutron economy.
- e) Low cost, both material and fabrication.
- f) Impermeability to fission products.

The following cladding materials have been considered or are currently used in operating reactors:

1. Aluminum.
2. Magnesium (Magnox).
3. Stainless steel.
4. Ceramics.
5. Zirconium (used in CANDU reactors).

A summary of fuel cladding characteristics is presented in Table 5.

Table 5 Summary of fuel cladding characteristics [POP2014]

Cladding Type	Corrosion Resistance	Mechanical Durability	High T Capability	Neutron Economy	Cost	FP Containment
Al	Good, except at high T	Low	Low	Good	Low	Good
	~Al, Ok for CO ₂	~ Al	> Al	~ Al	> Al	~ Al
Stainless Steel	Good	Good	Good	Poor	Good	Good
	OK	OK	OK	Excellent	High	Good
Ceramic	Good	Brittle	Excellent	OK	OK	OK

4.2.1 Aluminum, magnesium, stainless steel, and ceramic

Aluminum and its alloys possess many attractive properties such as low cost, easy fabrication, high ductility (important in preventing cladding failures), good neutron economy, and

impermeability to fission products. Their major disadvantages for power reactor use are poor mechanical properties at high temperatures and poor high-temperature corrosion resistance with most coolants. Because the latter are temperature-dependent, aluminum alloys are widely used in research reactor fuels where cladding operating temperatures are low, but are not currently used in power reactors.

Magnesium alloys are similar to aluminum alloys in most regards. An alloy called “Magnox” has, however, better high-temperature properties and adequate corrosion resistance to permit its use in some CO₂-cooled power reactors (i.e., Magnox reactors, used in the past and described in Appendix A).

Stainless steel is a very attractive material in all major regards except for its poor neutron economy. It has been and still is used in a number of reactors where its poor neutron economy is somewhat less important because enriched uranium fuel is used. Stainless steels are used as cladding in reactors where high-temperature service is needed. This type of cladding was used in the British high-temperature, CO₂-cooled reactors. Both gas-cooled and sodium-cooled fast-reactor designs use stainless-steel cladding.

Most cladding materials in current use are metals, although ceramic-type materials have seen limited use in certain applications.

4.2.2 Zirconium

Zirconium, in its various low-alloy forms, is by far the most common cladding material in current use. It is the primary material type used for CANDU reactor fuel cladding. Despite its relatively high base material cost, it combines to a large degree all the desirable cladding properties for use with most coolants.

The primary advantage of zirconium as a cladding material is its very low cross section for thermal neutrons, which greatly improves neutron economy. Zirconium has very good water corrosion resistance at high temperatures. Adding tin, iron, and chromium to zirconium greatly improves its mechanical properties. The best-known zirconium alloys are Zircaloy 2, 3, and 4, which have found wide application as cladding for power reactor fuel elements.

Zirconium alloys are unsuitable for use at very high temperatures, even though the melting point of zirconium is 1852°C. At 862°C, zirconium transforms from a close-packed hexagonal structure to one that is body-centred cubic, and it is necessary to stay below this phase change. At these temperatures, a reaction with UO₂ can occur at the cladding inner interface of the zirconium.

Zirconium alloys exhibit significant creep at the temperatures and stresses typical of PWR reactor design. Creep rates increase markedly with temperature and are accelerated by reactor irradiation.

At high temperatures (beginning at above 800°C), zirconium chemically reacts with steam to release hydrogen in an exothermic reaction. This reaction must be considered in evaluating any LOCA event that could expose the fuel elements to steam. Reaction of an appreciable fraction of the cladding could add significantly to the severity of the accident. Moreover, the mechanical properties of ZrO₂ are not as favourable as those of zirconium.

The last point to be made about zirconium cladding is its cost. Zirconium tubes are more expensive than stainless-steel tubes. Fabrication costs are also higher because all welding must be done in an inert atmosphere. However, the decrease in fuel costs more than offsets the increased material and fabrication costs.

Most power reactors in operation today use zirconium alloy as cladding material.

4.3 Reactor coolant requirements

The purpose of reactor coolant is to transport the heat generated in the reactor fuel either to the turbine (direct-cycle reactor) or to intermediate heat exchangers (indirect-cycle reactor). The coolants may be liquids, two-phase liquid/vapour mixtures, or gases.

Reactor coolant must meet the following general requirements [POP2014]:

- a) High heat capacity
- b) Good heat transfer properties
- c) Low neutron absorption
- d) Low neutron activation
- e) Low operating pressure at high operating temperature
- f) Non-corrosive to fuel cladding and coolant system
- g) Low cost.

The following coolant materials have been considered or are currently used in operating reactors:

1. CO₂ gas
2. Helium
3. Ordinary water
4. Heavy water
5. Organic fluid
6. Molten salt
7. Liquid metal.

The main commercial power reactor coolant types are described briefly in the following sections.

The CANDU reactor design is the only reactor design that uses heavy water as both a moderator and a coolant and is fuelled by natural uranium fuel.

A summary of coolant characteristics is presented in Table 6.

4.3.1 Ordinary water and heavy water coolants

Of the candidate HTS liquid coolants, ordinary (light) water is by far the most commonly used. It is inexpensive, has excellent heat transfer properties, and is adequately non-corrosive to the zirconium alloys used for fuel cladding and reactor structural components and to ferritic or austenitic steel coolant system materials. Its disadvantages include only moderate neutron economy and relatively high vapour pressure under coolant temperatures at power reactor HTS conditions. It is activated by neutrons in the reactor core, but this activity dies away rapidly,

permitting reasonable access to the coolant system for shutdown maintenance. A further disadvantage is that water transports system corrosion products, permitting them to be activated in the reactor core. These activated corrosion products then create shutdown radiation fields in the coolant system. The water coolant may be used as a liquid in an indirect-cycle system or may be permitted to boil, producing steam in a direct-cycle system.

Table 6 Summary of coolant characteristics [POP2014]

Coolant Type	Cost	Neutron Economy	Corrosive	Heat Capacity	HT Coeff.	HT Coeff.	Activation
CO ₂ Gas	< He	Good	OK, except high T	Low	Low	Low	Low
	Higher	Good	Good, if pure	Low	Low	Low	Low
H ₂ O	Very Low	Moderate	OK	High	Excellent	Excellent	Yes, short T _{1/2}
D ₂ O	High	Excellent	OK	High	Excellent	Excellent	Yes, short T _{1/2}
Organic	Moderate	H ₂ O < organic < D ₂ O	Excellent	High	Excellent	Excellent	None
	High	Moderate	Select Materials	High	Excellent	Excellent	Yes, long T _{1/2}

Heavy water is used as both coolant and moderator in CANDU-type reactors. Its outstanding advantage is much better neutron economy than ordinary water. Its primary disadvantage is its high cost, plus a somewhat higher tendency to activate into tritium. Otherwise, its properties are similar to those of ordinary water.

The relatively ionizing irradiation (including γ 's released because of neutron-radiative capture) causes decomposition (radiolysis) of water. Decomposition occurs in both H₂O and D₂O by the same mechanism. The rate of gas evolution (radiolysis) is proportional to radiation flux and decreases with increasing temperature.

Radiolysis of water is an important phenomenon that must be considered in analysis of accident events (as well as in normal operation) in a power reactor. Hydrogen is produced by radiolysis of water discharged from any break and can accumulate in the reactor building. Radiolysis of discharged water can occur because of γ -radiation from the sources within the discharged water (high contribution) or from the reactor fuel (low contribution). Above a certain concentration, hydrogen will burn at an explosive rate, creating a high risk to reactor components and building structures (e.g., in the Fukushima accident). The accumulation of hydrogen produced by radiolysis of discharged water in a LOCA event can be controlled by passive autocatalytic recombiners.

Water circulated through a reactor core exhibits appreciable induced radioactivity. The γ activity induced is primarily due to the 7.4 s half-life ¹⁶N produced by fast-neutron interaction with ¹⁶O. Additional activity may be introduced by activation of dissolved impurities and dissolved or suspended corrosion products. Hence, water purification is an important process that is continuously performed by dedicated systems.

4.3.2 Gaseous coolants

Two common gaseous coolants are in use: CO₂ and helium. CO₂ has the advantages of low cost, low neutron activation (important in minimizing radiation fields from the coolant system), high allowable operating temperatures, good neutron economy, and for gases, relatively good heat transfer properties at moderate coolant pressures. At very high temperatures, CO₂ tends to corrode neutron-economical fuel cladding materials and the graphite moderator used in most gas-cooled reactors. Its chief drawback, as for all gases, is its poor heat transfer properties relative to liquids. As a result, coolant pumping power requirements tend to be very high, particularly if high reactor power densities are to be achieved (which is desirable to minimize reactor capital costs).

A good gaseous coolant should have a low neutron-absorption cross section, high heat capacity, and high thermal conductivity.

All gaseous coolants have the disadvantage that a significant fraction of the plant energy output must be used to circulate the coolant. Furthermore, the low heat transfer coefficient requires a large heat transfer area. This may require a larger core or the use of extended surfaces (fins).

4.3.3 Liquid metal coolants

Certain liquid metals can be used as coolants. Of these, only sodium and a sodium-potassium eutectic called NaK have achieved significant use. Their advantages include excellent heat transfer properties and very low vapour pressures at high temperatures. Fuel cladding and coolant system materials require careful selection to avoid “corrosion”. Their chief disadvantages include incompatibility with water (the turbine working fluid), relatively high neutron absorption, a relatively high melting point (leading to coolant system trace heating requirements), and high coolant activation with sustained radiation fields after reactor shutdown.

Liquid metal coolants are important only for fast reactors because these metals are poor neutron moderators. Sodium is one of the most suitable liquid-metal coolants.

Sodium becomes radioactive when ²⁴Na is formed by neutron capture. This radioisotope has a 15-h half-life and emits gamma rays of 1.37 and 2.75 MeV [GAR1999]. Hence, shielding of the cooling system is necessary. Care must be taken to ensure a leak-tight system. Sodium is chemically reactive and will burn on exposure to air, evolving the oxide as dense smoke. Furthermore, it reacts violently with water, producing NaOH and hydrogen gas.

4.4 Moderator requirements

Most currently operating power reactors are of the thermal type, i.e., the energy of the neutrons causing fission is in the thermal range. Because the neutrons produced by fission have very high energies, they must be slowed down, or “thermalized”. The medium used for this is called the moderator. It is deployed as a continuous medium surrounding the fuel “cells”. The fuel cells form a geometric pattern, called the reactor “lattice”. The optimum spacing between these fuel cells is a function of several variables, including the mass of fuel per

cell, the mean free path of the neutrons being thermalized, the degree to which the moderator wastefully absorbs neutrons, and the cost of the moderating medium. A summary of moderator characteristics is presented in Table 7 [POP2014].

The best moderator is something that is the same size as a neutron, i.e., the hydrogen atom, ${}^1\text{H}_1$. However, hydrogen does absorb neutrons as well. The deuterium atom, ${}^2\text{H}_1$, at twice the mass of hydrogen, is almost as good a slowing-down agent, but because it already has an extra neutron in the nucleus, it has a very low absorption cross section. Therefore, deuterium is a far better moderator overall than hydrogen. By using deuterium in the form of heavy water, natural uranium can be used as a fuel. If ordinary water is used, the fuel must be enriched in ${}^{235}\text{U}$.

A good moderator has a high scattering cross section, a low absorption cross section, and slows down the neutron in the least number of collisions (high lethargy, ξ).

The desirable properties of moderators are:

- a) High moderating efficiency
- b) Low neutron absorption
- c) Resistance to irradiation and corrosion
- d) Low cost, including material, manufacture, and installation.

The following materials have been considered or are currently used as moderators in operating reactors:

1. Graphite
2. Ordinary water
3. Heavy water.

Graphite has been widely used as a moderator for power reactors. The carbon atom is relatively “light”, graphite is relatively inexpensive, and carbon is a relatively weak absorber of neutrons. Nevertheless, the carbon atom is sufficiently large, leading to relatively long neutron mean free paths for thermalization, that graphite-moderated reactors tend to be large. Furthermore, the relatively large amount of graphite required leads to significant neutron wastage through absorption.

Table 7 Summary of moderator characteristics [POP2014]

Moderator Type	Cost	Neutron Economy	Moderator Efficiency	Irradiation Stability	Activation	Mean Free Path
Graphite	OK	$\text{H}_2\text{O} <$ $\text{Graphite} <$ D_2O	Medium	Excellent	Irrelevant	Long
${}_2$	Very Low	Moderate	Low	Excellent	Good	Small
D_2O	High	Excellent	Highest	Excellent	Good	Medium

Ordinary water is a much more efficient moderator in terms of the neutron mean free path for thermalization because of its hydrogen atoms. It is also very inexpensive. Unfortunately, however, hydrogen also has a significant “appetite” for absorbing thermal neutrons, which hurts neutron economy. Most of the reactors operating in the world use ordinary water as coolant and moderator.

Heavy water is almost as good as ordinary water in terms of neutron mean free path because the deuterium atoms (which replace the hydrogen atoms in ordinary water) are relatively “light”. Its outstanding advantage relative to ordinary water is that it has a very small “appetite” for absorbing neutrons. Hence, it promotes a high level of neutron economy. Its major disadvantages are its high cost and the possibility of its activation into tritium.

4.5 Control material requirements

Reactor control is most commonly accomplished by moving control rods or control mechanisms in the reactor core or by injecting liquid containing material (poisons) with high neutron-absorption cross section in the thermal and near-thermal range [POP2014] into the coolant and/or moderator.

4.5.1 Hafnium

Hafnium is one of the best control-rod materials for water-cooled reactors. It is found together with zirconium and is created as a by-product of the separation process for zirconium. Hafnium is chemically similar to zirconium and shows the same high resistance to corrosion by high-temperature water.

Hafnium consists of four isotopes, each of which has an appreciable neutron absorption cross section. Note that the capture of neutrons in one isotope leads to the production of the next higher isotope, which is also an effective absorber. Therefore, hafnium remains an effective poison for a significant time.

4.5.2 Cadmium alloys

By alloying cadmium, which has a high thermal-absorption cross section, with silver and indium, which have high resonance absorption, a highly effective absorber is produced. The alloy is typically composed of 80% Ag, 15% In, and 5% Cd, can be readily fabricated, and has adequate strength at water-reactor temperatures.

These alloys have exhibited moderate resistance to corrosion by hot water after plating with nickel. Bonding of the base to the nickel was ensured by heating the control rod to an elevated temperature before reactor exposure. Corrosion under reactor conditions was good, but in subsequent use of the alloy, it was encapsulated in stainless-steel tubes so that direct contact with the coolant was eliminated.

Cadmium is typically used in several types of CANDU reactivity mechanism designs. For example, the shut-off rods in CANDU reactors are composed of a thin layer of tubular cadmium sandwiched between stainless steel layers.

4.5.3 Rare-earth oxides

Several of the rare earths (e.g., samarium, europium, and gadolinium) have both high thermal-neutron-absorption cross sections and significant resonances in the epithermal region. The oxides, the only chemical form in which the rare earths have been considered, can be formed into refractory ceramic pellets. Because the oxides hydrate rapidly in hot water with attendant

swelling, their use in water-cooled reactors could lead to difficulties. They may, however, be suitable for use in gas-cooled reactors. Dispersions of rare-earth oxides in metals such as stainless steel have been prepared. Such dispersions, when suitably clad, can be used as water-cooled reactor-control rods because in the event of a cladding fracture, only the oxide particles on the dispersion surface would become hydrated.

4.5.4 Gadolinium nitrate

The CANDU reactor uses a gadolinium nitrate (GdNO_3) solution in water as a reactor control (shutdown) poison. Tanks full of concentrated GdNO_3 solution are maintained under pressure by helium gas. The solution can be injected into the moderator system at a reactor shutdown trip signal, which provides a fast and effective reactor shutdown mechanism. To restart the reactor, the gadolinium nitrate is removed from the moderator by a purification system. Because the poison is introduced into a low-temperature, low-pressure moderator, there are no corrosion-related concerns.

4.5.5 Boron-containing materials

The very high neutron absorption cross section of ^{10}B and the low cost of boron have led to wide use of boron-containing materials in thermal-reactor control rods and burnable poisons. Unalloyed metallic boron is not suitable for control-rod use.

Boron alloyed or dispersed in stainless steel forms inter-metallic compounds with iron, nickel, and chromium in the metal matrix. The result is a major decrease in ductility. Acceptable materials can be obtained by limiting the boron concentration to 2–3 wt.% B. The boron-stainless steel materials have adequate corrosion resistance in water-cooled reactors.

The performance of boron-stainless steel materials is limited because of the $^{10}\text{B}(n, \alpha)$ reaction, which leads to severe swelling localized at the surface of the element (due to the short travel distance of the alpha particles).

Boron carbide (B_4C) is of much greater interest than elemental boron. Boron carbide can be formed into pellets and effective control elements produced by placing these within stainless-steel tubes. In high-temperature gas-cooled reactor designs, control elements can also be produced by dispersing B_4C in graphite.

In addition to its use in control elements, boron has been used (in PWRs) to control reactivity changes with fuel burn-up by dissolving boric acid in the coolant. Immediately after refuelling, enough boric acid is added to the coolant so that the reactor is just critical with all control rods nearly completely withdrawn. As burn-up proceeds, the boric acid concentration in the coolant is reduced to maintain criticality exactly (“chemical shim control”). However, one significant disadvantage of boric acid in coolant is that it is corrosive to heat transport system and reactor components (i.e., Davis-Besse pressure vessel head corrosion) and must be carefully monitored and mitigated.

Boron may also be used to compensate for the change in reactivity with fuel lifetime through “burnable poison”. In this scheme, a small amount of boron is incorporated in the fuel or into special burnable poison rods to reduce the beginning-of-life reactivity. Boron burn-up causes a

reactivity increase that partially compensates for the reactivity decrease due to fuel burn-up and accumulation of fission products. Stainless-steel-boron alloys and dispersions can be used successfully for this purpose because the boron burn-up in such rods can be kept low. Alternatively, pellets of boron-silicate glass encapsulated in hollow stainless-steel tubes may be used.

4.6 HTS design requirements and engineering considerations

This section provides a discussion of design requirements and engineering considerations for the heat transport system and associated systems, which transfer fission heat to the reactor coolant to produce steam in the steam generators.

This sub-section will discuss some of the thermal-hydraulic features that characterize the CANDU system.

The main objectives of the heat transport system are to provide heat transfer at high thermal efficiency and to enable the maximum amount of energy to be extracted from the fuel without surpassing safe operating limits.

The requirements for such a system can be summarized as follows:

- a) Due to the decay heat produced by the fuel even when the reactor is shut down, continuous coolant flow must be provided. This leads to requirements for pumps, pump flywheels, stand-by cooling, thermo-siphoning, and various other system functions.
- b) Costs should be minimized with due regard for other requirements. This usually leads to trade-offs between, for example, heavy water (D_2O) costs, pumping power costs, equipment and piping size and costs, and layout and engineering constraints.
- c) Layout should minimize radiation exposure and maximize maintainability and accessibility within other constraints.
- d) Provision must be made for pressure and inventory control of the heat transfer system. Excessively high pressure could damage fluid boundaries (pipes, etc.). Low pressure could lead to high coolant voiding and possible fuel damage as well as pump damage from cavitation. Low inventory jeopardizes coolant circulation and pressure control.
- e) The system must be sufficiently reliable because downtime leads to high replacement energy costs, high person-rem exposure, and high repair costs.
- f) The design should provide high process efficiency.
- g) The system should exhibit ease of constructability to reduce the initial cost and time of construction and to enhance maintainability.
- h) The system should meet, and preferably surpass, all safety and licensing requirements.

Various coolants can be used in the CANDU design to achieve these objectives and requirements.

Any nuclear station design involves trade-offs in design features to achieve the lowest-cost power within safety limits.

Another nuclear consideration is that the coolant should have a low induced radioactivity. Both H₂O and D₂O produce ¹⁶N and ¹⁹O, which emit γ's in the 6–7 MeV range. This leads to reduced accessibility and maintainability while on power. The short half-life (<1 minute) allows shutdown accessibility. Tritium, abbreviated as ³H or T, has a 12-year half-life and represents a major dose challenge for the CANDU station. Because tritium is a β-emitter, the problem is one of leakage, leading to possible absorption or ingestion by humans. Organic coolant has very little induced reactivity and aids in ease of operation and accessibility.

Coolants should also be stable in a radiation environment. At the high system pressure of the heat transport systems of H₂O and D₂O, radiolysis is not a problem.

The choice of coolant also depends on other factors such as pumping power, heat capacity, heat transfer coefficients, flow rates, pressure drop, boiling point, freezing point, corrosion, flammability, thermal stability, and cost.

Water (both D₂O and H₂O) is an attractive heat transport fluid because it offers a good balance of the considerations described above. In addition, water requires less pumping power for a given amount of heat removal.

For the Bruce reactors (which generate about 750 MWe), approximately 24 MWs of pumping power are required for each reactor. This represents over 2% of the electrical power generated [GAR1999]. Because a MW saved here by reducing pumping power is gained as electrical output, considerable emphasis is placed on lowering pumping power.

Limiting flow rates for coolant water, in addition to ensuring adequate heat transfer rates from the fuel and to the steam generator tubes, depend on many factors such as temperature, the presence of boiling, water chemistry, geometry, and flow regime. Fretting considerations have led to a 10 m/sec limit on fuel channel velocity in single-phase water. Erosion/corrosion considerations have led to limits of 4.3 to 6.1 m/s in the steam generator tubes and 16.8 m/s in heat transport piping.

The fuel distribution in the coolant is designed to maximize the fuel surface-to-volume ratio so that the largest heat transfer surface can be exposed to the coolant for maximum heat transfer without drying out the fuel surface. However, if this approach is carried to extremes, the fuel volume in the core will be less than the optimum, and parasitic neutron absorption by the sheath will increase. Present designs use 37 or 28 elements in a fuel bundle.

Use of boiling in the coolant permits higher heat transfer due to the high heat transfer coefficient of nucleate boiling, but introduces challenges to the attempt to minimize pressure drop and pump size, as well as other two-phase flow effects.

Ideally, the coolant temperature should be as high as possible for maximum overall thermal efficiency. Therefore, a high-boiling-point, low-vapour-pressure liquid is desirable so that the heat transport system can operate at the lowest possible pressure. This reduces the thickness of the pressure boundary and hence is important for reducing parasitic burn-up in the core. Organic coolant is far superior to water from this point of view.

In the case of organic coolant, the secondary-side H₂O pressure is higher than the primary-side pressure. Hence, boiler tube leaks will cause a water leak into the primary coolant system.

Corrosion of heat transport system materials must be minimized because of possible deterioration, flow restrictions, and contamination with active isotopes.

The CANDU-PHW heat transport system has water coolant, low-cobalt carbon steel piping, stainless-steel end fittings, Zircaloy pressure tubes, and Monel or Incoloy steam generator tubes. A pH of 10.2 to 10.8 is maintained by lithium hydroxide and hydrogen gas added to keep the dissolved oxygen content low to help minimize corrosion. The intent is to produce and maintain a continuous and adherent film of magnetite on all carbon steel surfaces. Corrosion with organic coolant is a lesser problem and can be controlled by degassing, using N₂ cover gas, and using a dechlorinator system.

No flammability or thermal stability problems exist with water (except for the possible Zr-water reaction producing H₂ during a LOCA).

The cost of D₂O is high, making it the more expensive coolant. This contributes to a high capital cost for the CANDU-PHW, but a low operating cost due to the efficient use of natural U.

4.7 Problems

1. Identify and explain the primary reasons that natural uranium ceramic is used as the traditional fuel in the CANDU reactor design.
2. Identify and explain the primary reasons that zirconium and zirconium alloys are used as the fuel cladding material in the CANDU reactor design.
3. Identify and explain several advantages and drawbacks of using heavy water as a moderator and coolant in the CANDU reactor design.
4. Summarize and explain the main heat transport system design requirements for the CANDU reactor design, as related to the main objectives of the system.

5 Thermal-Hydraulic Design Limits and Margins

This section covers the basic design principles of power reactor design, including reactor thermal-hydraulic characteristics, along with an overview of these for different reactor types, but with an emphasis on the CANDU design. It also covers the energy production and transfer parameters, the thermal design limits, and the thermal design margins, with a discussion on the reactor thermal-hydraulic figure of merit.

5.1 Heat generation parameter definitions

This section covers the reactor power production parameters generally used in reactor engineering. Energy production in a nuclear reactor is expressed in a variety of terms that are used by various disciplines.

The volumetric energy (heat) generation rate, q''' (kW/m³), is mostly used by reactor physicists because they deal with the fission reaction rate that results in a volumetric energy generation rate in the fuel. This term does not provide any information about heat transfer in the core, nor does it indicate any level of core margin.

The surface heat flux, q'' (kW/m²), is most important to the core thermal-hydraulic designer and is directly related to reactor thermal margins. The thermal-hydraulic engineer deals with heat transfer from the fuel element surface to the coolant.

The linear heat generation rate or power rating, q' (kW/m), is important to both the thermal/fuel designer and the metallurgical designer because it expresses fuel performance characteristics in terms of linear power rating. Fuel design, testing, and qualification are usually described using this parameter.

The rate of energy generation per fuel element, q (kW), is useful in expressing heat generated separately in each fuel element, which is used in modelling heat transfer phenomena in the core.

The core power, Q (kW), is used in overall calculations of core energy output. Usually, for marketing purposes, this core power is expressed in terms of electrical power delivered by the plant to the grid, or occasionally in terms of net electric power accounting for plant internal energy consumption. However, for thermal-hydraulic design purposes, reactor power is expressed in terms of reactor thermal power. Roughly speaking, reactor electric power is equal to reactor thermal power divided by reactor thermal efficiency.

The core power density, Q''' (kW/m³), is used as a figure of merit for core thermal performance. This power level accounts for various materials in the core and thus provides information on reactor core compactness and effectiveness.

The core specific power, $Q/(\text{mass of fissionable atoms})$ (i.e., kW/kg), is used as a figure of merit for core thermal performance from the nuclear physics perspective.

5.2 Thermal design limits

Core thermal design limits are expressed in terms of several parameters, including heat flux

from the fuel elements to the coolant, fuel centreline maximum temperature in the core, fuel cladding maximum temperature in the core, bundle maximum power, and channel maximum power.

Figure 20 presents the important concept of reactor thermal limits with respect to the critical heat flux (CHF). The definition, assessment, and calculation of the CHF are covered in the following sections. Reactor thermal-hydraulic design must ensure that the CHF is not reached in any fuel element or bundle in the reactor core. The CHF is the heat flux at the surface of the fuel element that results in a sudden change in heat transfer regime from liquid in good contact with the heated surfaces, to loss of local liquid contact with surfaces because of vapour blanketing the fuel-element surface. This phenomenon leads to severe reduction of the heat transfer coefficient, and for heat flux-controlled surfaces (like fuel rods in a reactor), in a significant increase in fuel temperature as well as damage to or failure of fuel sheaths.

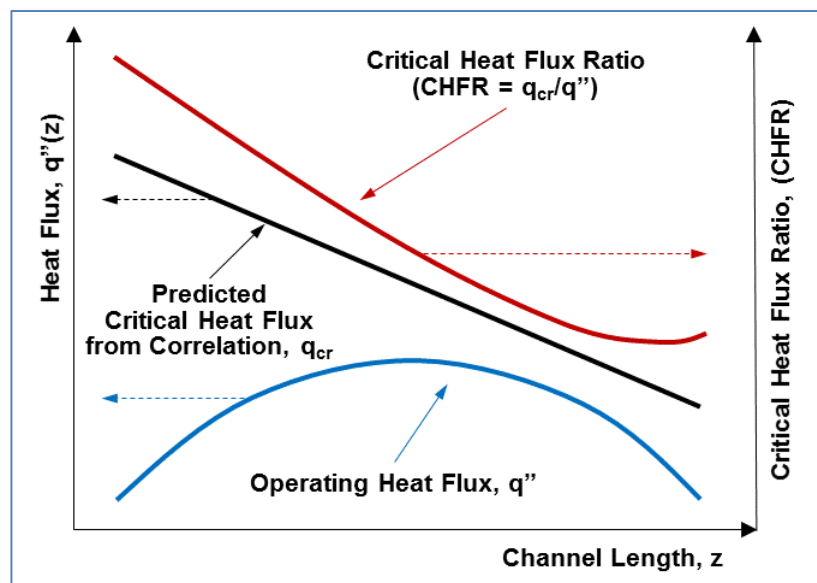


Figure 20 Critical heat flux ratio

Figure 20 shows a typical variation of the heat flux and the critical heat flux along a fuel element. For simplicity, the reactor heat flux in the core is assumed to be represented by a cosine function that peaks at the centre of the core. As will be seen later, the CHF follows a decreasing curve from the fuel channel inlet to the fuel channel outlet. In Figure 20, the ratio of CHF and local heat flux is also illustrated, which is one way to assess how close the reactor is to the occurrence of CHF anywhere in the core.

The key objective of thermal-hydraulic reactor core design, for a desired core power, is to ensure that the heat flux in all fuel elements in the core will remain below the CHF. The CHF is among the important parameters in core thermal-hydraulic design. Note that local power in the core will vary with position along the fuel channel, including the end flux peaking at bundle ends, and from channel to channel in the radial direction of the calandria.

Fuel melting and cladding melting are other important factors and are dealt with in later sections of this chapter.

CANDU reactor design-related CHF phenomena are further described in Section 7.6.4.

5.3 Thermal design margins

This section defines thermal design margins in terms of heat generation rate and the resulting heat flux from the fuel to the coolant. Variation of the reactor parameters in the reactor core is taken into account to define the core average quantities, maximum hot channel quantities, and maximum fuel element quantities that are used in the design space to optimize reactor design options. The heat generation rate during normal operation and the postulated design basis events define the key design limit for which power reactors need to be designed with a certain margin.

Design margins are applied to parameters of primary importance to ensure that the reactor can be safely operated without exceeding important limits. These important operating parameters are assumed to be inside a so-called *safe operating envelope*, which defines the range of values that a particular parameter can take on during reactor operation. The left side of Figure 21 shows a general definition of the safe operating envelope, identifying the optimal operating range, the lower and upper alarm range, the lower and upper buffer zone, and the range where reaching the failure point will be immanent for any of the important thermal margin parameters.

Some of the key operating parameters that are usually considered by thermal-hydraulic designers are:

- Coolant temperature
- Coolant pressure
- Critical heat flux
- Fuel maximum temperature (centreline)
- Fuel cladding maximum temperature
- Bundle maximum power
- Channel maximum power
- Reactor total thermal power.

The thermal design margins function as the most important parameter for demonstrating the robustness, operability, and flexibility of a given reactor design and serve as the main standard of comparison for the safety level of various reactor types. One of the key thermal design margin parameters is the ratio of the critical heat flux to the operating surface heat flux, which must satisfy a reference allowable value that meets economic as well as regulatory requirements.

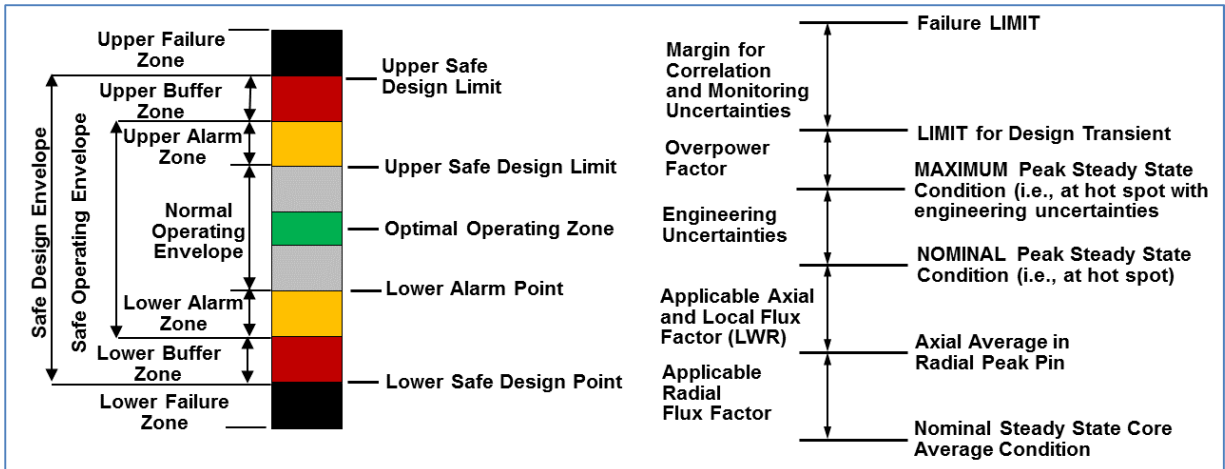


Figure 21 Thermal margins

The required core thermal margins are shown on the right side of Figure 21. Variations in neutron flux and the resulting power generation rate in the core in the radial and axial directions are represented by the corresponding peaking factors. These must be added to the nominal value (the core average value) to obtain the nominal peak steady-state value of the margin parameter. Then uncertainties in the calculated parameters and other engineering uncertainties are “stacked” on top of the peaking factors to arrive at the maximum peak steady-state condition.

During transients, the appropriate overpower factor must be stacked on top of the maximum peak steady-state power to obtain the limit value for design transients. On top of this limit, there should be a margin for all uncertainties in calculating the margin parameter values and the uncertainties in monitoring global and local reactor parameters. This brings the margin parameter to the failure limit.

The left side of Figure 21 indicates that if reactor operation drifts to the lower or upper alarm point, the reactor control systems will provide corrections to certain reactor parameters to bring the reactor operation back within the safe operating envelope. Beyond the safe operating envelope is the safe design envelope. If any of the reactor key safety parameters drifts into this buffer zone, a reactor trip may occur and shut down the reactor. The reactor trip parameters have their own margins, which are required to manage reactor shutdown adequately and to ensure safe reactor shutdown while preventing spurious trips.

5.4 Problems

1. Explain the relationship among the reactor core thermal parameters: reactor core power, core volumetric generation rate, heat flux, critical heat flux, and linear power.
2. Draw a diagram of core thermal margins to explain the relationship among the various elements that must be considered to ensure that appropriate margins are available.

6 Thermal-Hydraulic Design Fundamentals

This section covers the fundamental aspects of thermal-hydraulic design, heat transfer, and fluid flow in the reactor primary and secondary cooling system. It also provides the fundamentals of two-phase flow and the thermodynamics of the nuclear energy conversion process.

6.1 Two-phase flow fundamentals

Heat transfer and fluid flow with boiling water play an important role in nuclear reactor thermal hydraulics. This section discusses two-phase flow definitions and basic theory. It covers flow regimes, experimental observations and data, and application to reactor thermal hydraulics. It also provides a brief description of various two-phase flow models.

6.1.1 Key parameters and definitions

Two-phase flow is encountered in many engineering systems in the chemical, process, power generation, and petroleum industries, including oil-gas pipelines, boilers, heat exchangers, refrigeration equipment, and evaporators, as well as in nuclear reactor applications. Fully understanding the implications and models of two-phase flow is important for proper design of reactor cooling systems and for modelling fluid flow and heat transfer in the reactor under different conditions. Two-phase flow has a profound impact on the ability to remove heat from the nuclear reactor, which is the primary objective of thermal-hydraulic design.

As a simple approximation, two-phase flow can be treated as an extension of single-phase flow. However, in reality, two-phase flow can be very complex due to uncertainty in various interfacial parameters. To simplify the situation, often experimentally obtained correlations are used in design calculations.

Two-phase flow is simultaneous flow of any two phases (liquid-gas/vapour, solid-gas, or liquid-solid) of a single substance. Examples include reactor fuel channels and steam generators. This phenomenon is also referred to as “single-component two-phase flow”. However, two-phase flow can consist of two components, and in this case, it is referred to as simultaneous flow of the liquid and gas phases of two substances, for example in oil-gas pipelines. This is also referred to as “two-component two-phase flow” [HET1982].

The primary parameters used in two-phase flow modelling are:

- Thermal: thermal power, temperature, heat flux, etc.
- Hydraulic: pressure, mass flow rate, fluid temperature, pressure drop, etc.
- Geometric: flow and heated areas, hydraulic and heated equivalent diameters, etc.

Along with these primary parameters, in two-phase flow analysis, the following calculated parameters are commonly used:

- Mass flux, heat flux
- Mass quality, equilibrium quality, thermodynamic quality
- Void fraction.

In addition, two-phase flow calculations require fluid property information such as density, viscosity, enthalpy, thermal conductivity, and heat capacity, which are functions of the primary fluid parameters listed above.

Void fraction is the ratio of the cross-sectional area occupied by vapour and gaseous phases to the total flow area of a pipe [WAL1969]. The opposite of void fraction is the liquid fraction, as given by Eq. (1):

$$\alpha = \frac{A_g}{A}; \quad (1-\alpha) = \frac{A_f}{A}. \quad (1)$$

Equation (2) defines mass quality as the ratio of vapour mass flow to total mass flow. The opposite is the liquid quality:

$$x = \frac{W_g}{W} = \frac{W_g}{W_f + W_g}; \quad (1-x) = \frac{W_f}{W} = \frac{W_f}{W_f + W_g}. \quad (2)$$

Mass flux is the mass flow rate per unit flow area and is given by Eq. (3):

$$G = \frac{W}{A} = \rho v = \frac{v}{\nu}. \quad (3)$$

Gas and liquid mass fluxes are defined using the steam quality, as in Eq. (4):

$$G_g = G x; \quad G_f = G(1-x). \quad (4)$$

Volumetric flux (usually referred to as superficial velocity) is the volumetric flow rate over total flow area, as in Eq. (5) [WAL1969]:

$$j = \frac{Q}{A}. \quad (5)$$

The corresponding vapour and liquid volumetric fluxes are given by relationships similar to the void fraction, as in Eq. (6):

$$j_g = \frac{Q_g}{A}; \quad j_f = \frac{Q_f}{A}. \quad (6)$$

Using the relationships defined in the previous equations, the vapour and liquid phase velocities can be expressed as in Eqs. (7) and (8):

$$v_g = \frac{W_g}{\rho_g A_g} = \frac{Q_g}{A_g} = \frac{G x}{\rho_g \alpha}, \quad (7)$$

$$v_f = \frac{W_f}{\rho_f A_f} = \frac{Q_f}{A_f} = \frac{G(1-x)}{\rho_f (1-\alpha)}. \quad (8)$$

These equations assume that no relative motion exists between the two phases. However, if a two-phase mixture is moving, the vapour, because of its buoyancy, density, and different resistance characteristics, tends to move at a higher velocity than the liquid. In a homogeneous

system, a slip ratio S is defined as equal to one in the absence of flow or in homogeneous flow and greater than one in non-homogeneous two-phase systems. S is defined as the ratio of the average velocity of the vapour to that of the liquid. Hence, the slip ratio is defined as the ratio between the vapour velocity and the liquid velocity, as in Eq. (9) [WAL1969]:

$$S = \frac{v_g}{v_f} = \frac{W_g \rho_f A_f}{W_f \rho_g A_g} = \left(\frac{x}{1-x} \right) \left(\frac{\rho_f}{\rho_g} \right) \left(\frac{1-\alpha}{\alpha} \right). \quad (9)$$

Experimental data or theoretical correlations for S covering all possible operating and design variables do not exist. In boiling-water reactor studies, values for S may be estimated from data that closely approach those of interest. To do this, a certain amount of individual judgment is necessary. Otherwise, experimental values of S under conditions similar to a particular design must be obtained. This procedure is usually expensive and time-consuming, but may be necessary in some cases.

The importance of obtaining accurate values of S may best be emphasized by the following discussion. One step in the core channel design procedure is to set a maximum value of alpha at the channel exit. This is usually determined from nuclear (moderation) considerations. A corresponding value of x at the selected S is then determined from the above equations. The latter determines the heat generated in the fuel channel. In design, the usual procedure is to assume a constant value of S along the length of the fuel channel. This simplification may introduce error into the results. However, S has been observed to be fairly constant over most of the channel length, indicating this assumption to be a good one.

The quality of the flowing liquid-vapour mixture can be expressed using Eq. (2) in terms of liquid and vapour mass flow rates. There is an equivalent quality of a stationary liquid-vapour mixture, which can be expressed by a similar relationship involving liquid and vapour mass. The mass flow quality varies between 0% and 100%, i.e., no vapour to 100% vapour in the flow. Note that mass quality does not carry information about the thermal state of the fluid. However, where appropriate in experimental or theoretical work, if the two phases are in thermal equilibrium (at the same enthalpy or temperature), mass quality can be called equilibrium mass quality.

Often in thermal-hydraulic experiments or calculations, thermodynamic quality is used. It is expressed in terms of a ratio of enthalpies, as in Eq. (10), where h_m is the mixture enthalpy and h_g and h_f are vapour and liquid saturation enthalpies. Thermodynamic enthalpy can be negative when the liquid is below saturation condition (sub-cooled) or greater than one when steam is superheated. From Eq. (10), thermodynamic quality does not carry information about the flows (velocities) of the two phases. Usually, thermodynamic quality is expressed for a mixture at hydrodynamic equilibrium (i.e., both phases travelling at the same velocity) and is sometimes referred to simply as equilibrium quality [COL1972, DEL1981]:

$$x_{th} = \frac{h_m - h_f}{h_g - h_f}. \quad (10)$$

It is very important to understand the relationship between mass flow quality and void fraction. There is no meaningful relationship between thermodynamic quality and void fraction because

void fraction refers to flow geometry, whereas thermodynamic quality refers to the thermal properties of the phases. The relationship between mass flow quality and void fraction is obtained by manipulating the above equations and can be expressed as in Eq. (11) [WAL1969]:

$$\alpha = \frac{x \cdot v_g}{(1-x)v_f + x \cdot v_g} = \frac{1}{1 + \left(\frac{1-x}{x}\right)\left(\frac{v_f}{v_g}\right)}. \quad (11)$$

Figure 22 shows the relationship between void fraction and mass flow quality. As expected, at or above the critical pressure of 22.12 MPa, the void fraction and quality are identical because the liquid and vapour phases no longer exist for water regardless of pressure and temperature.

Further examination of Figure 22 shows the following:

1. For constant quality, void fraction decreases with pressure.
2. For any pressure, $d\alpha/dx$ decreases with quality.
3. At low quality values, $d\alpha/dx$ increases as pressure decreases and becomes very large at low pressure.
4. At atmospheric pressure, a low quality (about 2%) generates almost 100% void fraction because of the low vapour density.

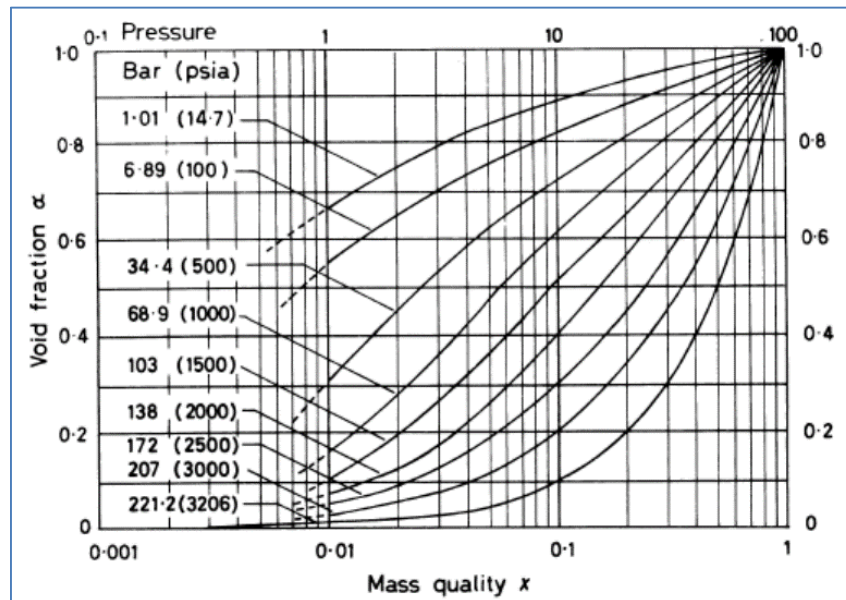


Figure 22 Relationship between quality and void fraction [COL1972]

For CANDU fuel channel exit conditions, because the pressure is approximately 10 MPa and the quality is typically 2%–4%, the void fraction can be as high as 30%.

6.1.2 Non-dimensional numbers

Dimensionless numbers in fluid mechanics are an important tool to capture various parameters and phenomena into a relationship that is applicable to a wide range of parameter values. This section covers the most important dimensionless numbers that are used throughout this

chapter and are important in analyzing mass, momentum, and heat transfer. The most important dimensionless numbers are listed in the following sections.

6.1.2.1 Reynolds number

The Reynolds number (Re) is a dimensionless number that measures the ratio of inertial to viscous forces and consequently quantifies the relative importance of these two types of forces under a given flow condition. The Reynolds number can be defined for a number of different situations where a fluid is in motion relative to a surface. These definitions generally include the fluid properties of density and viscosity, plus a velocity and a characteristic length or characteristic dimension. This dimension is a matter of convention; for example, a radius or a diameter is equally valid for spheres or circles, but one is chosen by convention. For flow in a pipe or a sphere moving in a fluid, the internal diameter is generally used today. Other shapes such as rectangular pipes or non-spherical objects have an *equivalent diameter* defined. The velocity may also be a matter of convention in some circumstances, notably stirred vessels. With these conventions, the Reynolds number is defined by Eq. (12) [HET1982, ELW1978]:

$$Re = \frac{\rho \cdot v^2 L^2}{\mu \cdot v \cdot L} = \frac{\rho \cdot v \cdot L}{\mu} = \frac{v \cdot L}{\nu}, \quad (12)$$

where:

- v is the mean velocity of the object relative to the fluid (m/s)
- L is a characteristic linear dimension (the length travelled by the fluid; the hydraulic diameter when dealing with river systems) (m)
- μ is the fluid dynamic viscosity (Pa·s or N·s/m² or kg/(m·s))
- ν is the kinematic viscosity ($\nu = \mu/\rho$) (m²/s)
- ρ is the fluid density (kg/m³).

For flow in a pipe, the Reynolds number is given by Eq. (13) [WAL1969]:

$$Re = \frac{\rho \cdot v \cdot D_H}{\mu} = \frac{v \cdot D_H}{\nu} = \frac{Q \cdot D_H}{\nu \cdot A}, \quad (13)$$

where:

- D_H is the hydraulic diameter of the pipe, i.e., its characteristic length travelled (m)
- Q is the volumetric flow rate (m³/s)
- A is the pipe cross-sectional area (m²).

For shapes such as square, rectangular, or annular ducts where the height and width are comparable, the characteristic dimension for internal flow situations is taken to be the hydraulic diameter D_H as defined by Eq. (14):

$$D_H = \frac{4A}{P}, \quad (14)$$

where A is the cross-sectional area and P is the wetted perimeter. The wetted perimeter for a channel is the total perimeter of all channel walls that are in contact with the flow. This means that the length of the channel exposed to air or steam is *not* included in the wetted perimeter.

6.1.2.2 Nusselt number

In heat transfer at a boundary (surface) within a fluid, the Nusselt number (Nu) is the ratio of convective to conductive heat transfer across (normal to) the boundary, as in Eq. (15) [HET1982, ELW1978]. In this context, convection includes both advection and conduction. Named after Wilhelm Nusselt, it is a dimensionless number. The conductive component is measured under the same conditions as the heat convection, but with a (hypothetically) stagnant (or motionless) fluid.

A Nusselt number close to one, meaning that convection and conduction are of similar magnitude, is characteristic of “slug flow” or laminar flow. A larger Nusselt number corresponds to more active convection, with turbulent flow typically in the 100–1000 range.

The convection and conduction heat flows are parallel to each other and to the surface normal of the boundary surface and are all perpendicular to the mean fluid flow in the simple case:

$$Nu_L = \frac{\text{Convective heat transfer}}{\text{Conductive heat transfer}} = \frac{h \cdot L}{k_f}, \quad (15)$$

where:

- L is the characteristic length (m)
- k_f is the thermal conductivity of the fluid (kW/m °K)
- h is the convective heat transfer coefficient (kW/m² °K).

The characteristic length should be selected in the direction of growth (or thickness) of the boundary layer. Some examples of characteristic length are the outer diameter of a cylinder in (external) cross flow (perpendicular to the cylinder axis), the length of a vertical plate undergoing natural convection, or the diameter of a sphere. For complex shapes, the length may be defined as the volume of the fluid body divided by the surface area. The thermal conductivity of the fluid is typically (but not always) evaluated at the film temperature, which for engineering purposes may be calculated as the mean (average) of the bulk fluid temperature and the wall surface temperature.

For relations defined as a local Nusselt number, the characteristic length should be taken as the distance from the surface boundary to the local point of interest. However, to obtain an average Nusselt number, this relation must be integrated over the entire characteristic length.

Typically, for free convection, the average Nusselt number is expressed as a function of the Rayleigh number and the Prandtl number as: $Nu=f(Ra, Pr)$ [HET1982]. For forced convection, the Nusselt number is generally a function of the Reynolds number and the Prandtl number, or $Nu=f(Re, Pr)$. Empirical correlations are available for a wide variety of geometries that express the Nusselt number in the forms described above.

6.1.2.3 Prandtl number

The Prandtl number (Pr) is a dimensionless number that represents the ratio of momentum diffusivity (kinematic viscosity) to thermal diffusivity [HET1982, ELW1978]. It is named after the German physicist Ludwig Prandtl and is defined by Eq. (16):

$$Pr = \frac{\nu}{\alpha} = \frac{\text{viscous diffusion rate}}{\text{thermal diffusion rate}} = \frac{c_p \mu}{k}, \quad (16)$$

where:

- ν is the kinematic viscosity, $\nu = \mu/\rho$ (m^2/s)
- α is the thermal diffusivity, $\alpha = k/(\rho c_p)$ (m^2/s)
- μ is the dynamic viscosity ($\text{Pa s} = \text{N s}/\text{m}^2$)
- k is the thermal conductivity ($\text{W}/(\text{m K})$)
- c_p is the specific heat ($\text{J}/(\text{kg K})$)
- ρ is the density (kg/m^3).

Note that whereas the Reynolds number is subscripted with a length scale variable, the Prandtl number contains no such length scale in its definition and is dependent only on the fluid and the fluid state. As such, the Prandtl number is often found in property tables alongside other properties such as viscosity and thermal conductivity.

6.1.2.4 Weber number

The Weber number (We) is a dimensionless number in fluid mechanics that is often useful in analyzing fluid flows with an interface between two different fluids, especially for multiphase flows with strongly curved surfaces. It can be thought of as a measure of the relative importance of the fluid's inertia compared to its surface tension [HET1982, ELW1978]. The quantity is useful in analyzing thin film flows and the formation of droplets and bubbles. It is named after Moritz Weber and can be expressed by Eq. (17) [HET1982, ELW1978]:

$$We = \frac{\text{fluid inertia}}{\text{surface tension}} = \frac{\rho \cdot v^2 \cdot l}{\sigma}, \quad (17)$$

where

- ρ is the density (kg/m^3)
- v is the mean velocity of the object relative to the fluid (m/s)
- l is the characteristic length, typically the droplet diameter (m)
- σ is the surface tension (N/m).

6.1.3 Flow patterns

When a liquid is vaporized in a heated tube or a heated channel, the liquid and vapour generated take on a variety of configurations known as flow patterns. The particular flow pattern depends on pressure, flow, heat flux, entrance conditions (i.e., local phase distribution at the inlet), and channel geometry; however, the strongest influences on the flow pattern are the phase mass flow rates or velocities. Because the name given to a flow pattern is largely subjective, many terms exist in the literature which purport to describe the various possible phase distributions. The sequence of flow patterns generally encountered in vertical upwards concurrent flow for increasing levels of thermodynamic quality is shown below. As steam mass flow increases (i.e., velocity increases) and steam temperature increases, the fluid flow

patterns change from single-phase sub-cooled liquid to single-phase steam flow, passing through the flow regimes as indicated from left to right on the diagram below. Indications are provided in this diagram of the values of thermodynamic quality x for various flow regimes.

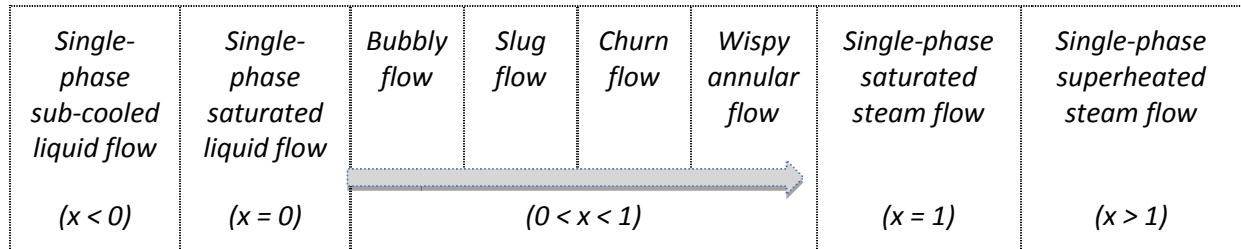


Figure 23 shows the flow patterns for vertical flow. These flow patterns are generally symmetrical across the pipe cross section.

In horizontal flow, the flow patterns are similar. However, in horizontal flow, gravity has a different effect, and depending on the mass flow rate in the tube or channel, stratified flow may occur with bubbly flow, slug flow, and wispy annular flow patterns. The flow patterns typical of horizontal two-phase flow are shown in Figure 24. A cross-sectional view of various flow patterns in horizontal flow is shown in Figure 25, in which gravity plays a significant role, so that the combination of gravity and drag force at the liquid-vapour interface can result in various cross-sectional flow patterns.

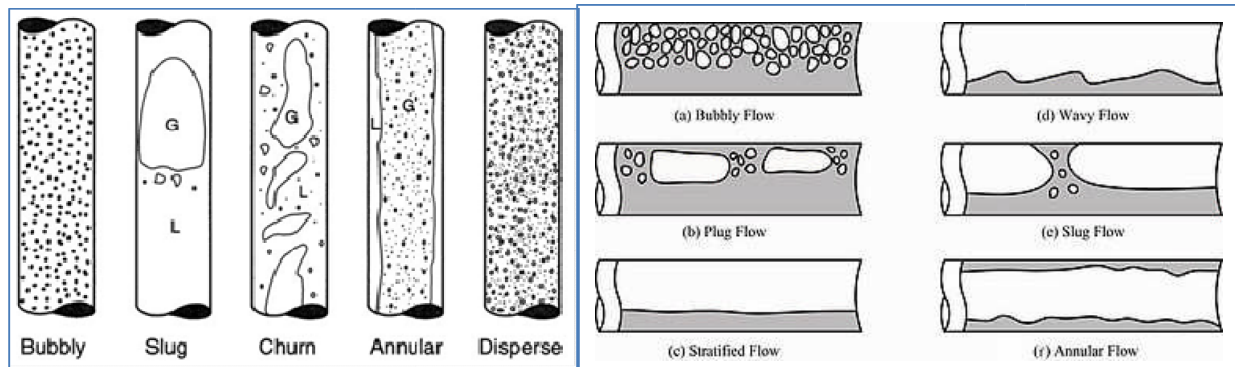
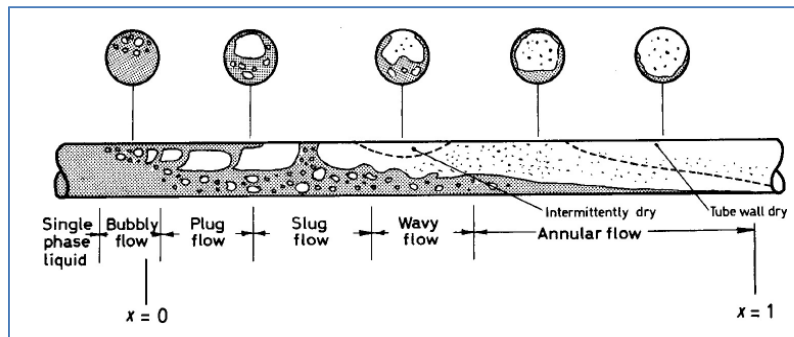
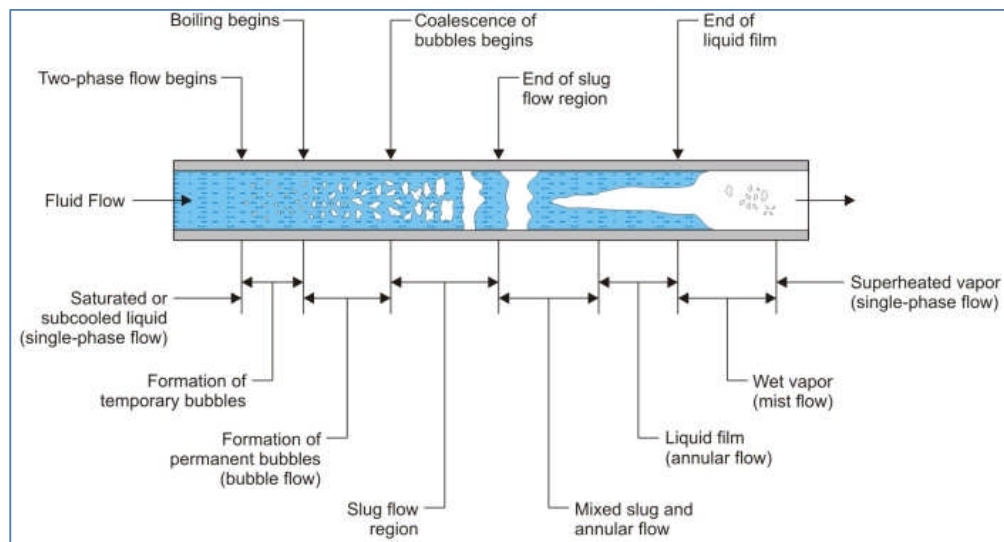


Figure 23 Flow patterns in vertical two-phase flow

Figure 24 Flow patterns in horizontal two-phase flow



a) Flow regimes in a horizontal heated channel



b) Evolution of flow regimes in a horizontal tube

Figure 25 Flow patterns and heat transfer regimes in horizontal heated tubes

The distribution of phases inside a confined area strongly depends on:

- Liquid and vapour velocities.
- Fuel channel geometry and fuel bundle geometry, particularly in reactors where fuel channels are interconnected in the radial direction, like PWRs and BWRs.
- Surface (wall) heating, which influences near-wall flow patterns, resulting in an internal void gradient.
- Appendages, which homogenize flow patterns at downstream locations; the patterns transition back to a basic pattern at locations farther away.

Figure 26 shows the flow patterns and heat transfer regimes for two different situations in vertical flow [DEL1981]. On the left side, a reactor channel is shown with the following parameters: high liquid mass flow rate, high heat flux from the walls, and high water sub-cooling, which is typical of PWRs. To the left of the reactor channels on the first vertical line, corresponding flow patterns are shown for this situation, whereas the leftmost line shows the heat transfer regimes for these flow patterns. Starting from bottom to top, the following pairs of flow pattern and heat transfer regime (note that “film” on this figure refers to steam film next to the heated walls) are typically observed:

- a) Single-phase liquid – single-phase forced convection to liquid;
- b) Bubbly flow – nucleate boiling;
- c) Inverted annular flow – inverted annular flow film boiling;
- d) Dispersed droplet flow – dispersed flow film boiling; and
- e) Single-phase vapour – single-phase forced convection to vapour.

Note that in Figure 26, the point where the wall loses contact with the liquid is shown at the transition between bubbly flow and inverted annular flow.

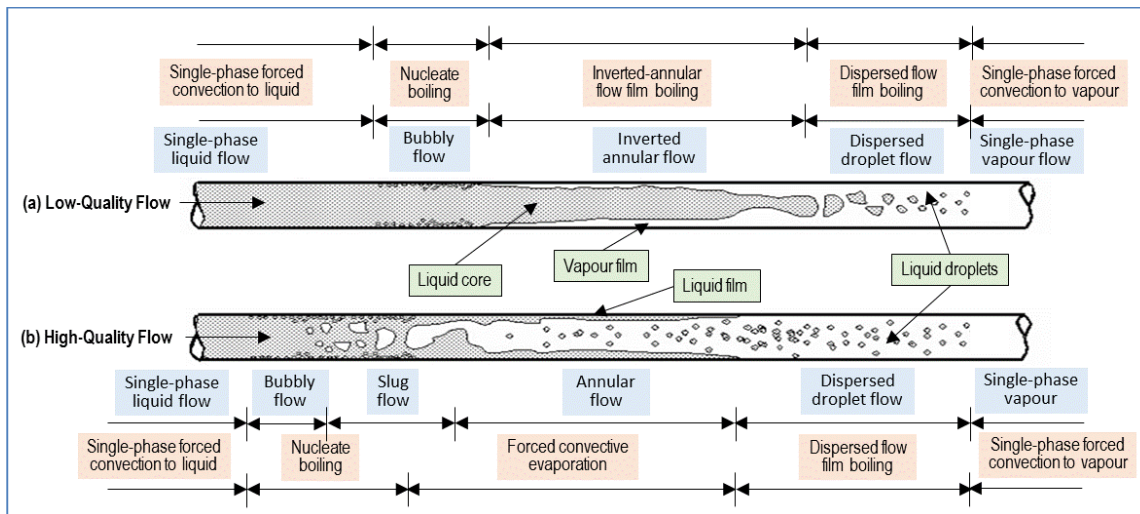


Figure 26 Flow patterns and heat transfer regimes in vertical heated tubes

On the right side of Figure 26, a reactor channel is shown with the following parameters: low liquid mass flow rate, medium heat flux from the walls, and saturated water; this is typical of BWRs. To the right of the reactor channel on the first vertical line, corresponding flow patterns are shown for this situation, whereas the rightmost line shows the heat transfer regimes for these flow patterns. Starting from bottom to top, the following pairs of flow pattern and heat transfer regime (note that “film” in this figure refers to steam film next to the heated walls) can be observed:

- a) Single-phase liquid – single-phase forced convection to liquid;
- b) Bubbly flow and slug flow – nucleate boiling;
- c) Annular flow – forced convective evaporation;
- d) Dispersed droplet flow – dispersed flow film boiling;
- e) Single-phase vapour – single-phase forced convection to vapour.

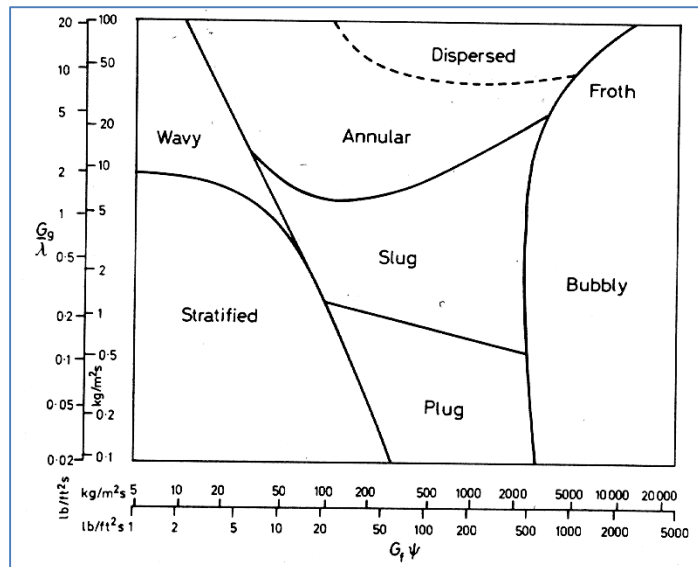


Figure 27 Flow pattern map in vertical flow [HET1982]

Note that in Figure 26, the point where the wall loses contact with the liquid is shown at the transition between annular flow and dispersed droplet flow. Figure 26 indicates that the flow patterns at the entry and exit of the fuel channel are similar for the two cases. The difference is how and where the wall and the liquid lose contact. In addition, the amount of water or the void fraction percentage in the channel does not necessarily determine the contact of liquid with the heated walls. Therefore, as long as the walls are in contact with liquid water, heat transfer is good, and the amount of water in the channel is not important.

Two-phase flow parameters change significantly from one flow pattern to another, in particular the interfacial area between the two phases, and this has a significant impact on the exchange of mass, momentum, and heat between phases. In principle, the degree of thermal and hydraulic disequilibrium between phases has a significant impact on the sustainability of certain flow patterns. Therefore, certain flow patterns, like churn flow, exhibit instability and fast transitions. Various two-phase flow parameters are affected differently by flow patterns, and hence various correlations and models are needed to capture phenomena for each flow pattern. This implies the need for well-defined and predictable flow patterns in two-phase flow modelling.

Many scientists and researchers in recent decades have tried to correlate flow patterns using selected parameters.

Figure 27 shows such an attempt for a vertical flow regime. In this figure, the flow patterns are defined as a function of gas and liquid momentum fluxes. In this example, the flow patterns are correlated by several dimensionless number groups.

6.1.4 The boiling process

Because water as the working fluid in LWRs and CANDUs undergoes a change of phase during heat transfer from the nuclear reactor primary to the secondary cooling system, it is important to understand the boiling process, its phenomena, and its parametric trends.

As liquid is being heated to saturation, with additional heating, boiling starts. Hence, boiling initiation is strongly dependent on pressure, i.e., the saturation temperature. There are two distinctive types of boiling: one is referred to as pool boiling, and the other is forced convective boiling. Vapour formation can take the following forms:

- at the liquid surface to the open environment, when the liquid is superheated;
- homogeneous (internal heating within the fluid at the molecular level); and
- heterogeneous (requires nucleation sites in the fluid or at the heated surface).

Heterogeneous boiling from nucleation sites is a complex boiling mechanism that depends on a number of forces acting on a vapour bubble, including dynamic forces, buoyancy, and surface tension forces. Much research has been devoted to bubble formation at nucleation sites and is presented in a number of two-phase flow textbooks [TON1965, TON1975]. Further discussion of bubble dynamics and formation at nucleation sites is beyond the scope of this textbook.

Figure 28 shows a three-dimensional representation of the two-phase boiling water region as a function of heat flux, temperature, and thermodynamic quality. This figure indicates different flow and heat transfer regimes along the path of changing thermodynamic quality. At high water sub-cooling, the critical heat flux is high, but it diminishes as quality increases. The definition of critical heat flux and its impact on heat transfer in the two-phase region are discussed in Section 7.7.

The boiling process can be analyzed in two distinct situations: pool boiling and forced convective boiling. Pool boiling refers to conditions typical of vessels with unlimited volume and under near-atmospheric pressure. Forced convective boiling refers to boiling in enclosed piping and vessels in which pressure may reach very high values, and in which flow is ensured by an operating pump.

Figure 29 shows a pool boiling process in a diagram relating heat flux to the degree of wall temperature superheating (i.e., the temperature difference between the wall temperature and the saturation temperature). This figure shows a cross section of the 3-D curve in Figure 28 at low quality. Three heat transfer regimes can be seen: nucleate (or sub-cooled) boiling, transition boiling, and film boiling. These three regimes are separated by two important points: the critical heat flux, and the minimum film boiling temperature. The minimum film boiling temperature, sometimes called the Leidenfrost temperature, represents the maximum temperature at which wetting of the heated surface is possible.

Figure 29 also indicates in which direction the process evolves from left to right and vice versa. If heat flux is increasing, then after the CHF point is reached, the surface becomes detached from liquid contact. Beyond this point, heat transfer by liquid evaporation (latent heat of vaporization) is severely reduced. Therefore, because heat transfer to liquid is severely reduced, but heat flux continues to be delivered from internal regions of the wall to the wall

surface, the wall surface temperature significantly increases, as represented by the horizontal dashed line on the diagram from CHF to the film boiling curve (sometimes referred to as the heat flux-controlled region). This significant increase in wall surface temperature can lead to surface damage and melting, which is very troubling in a nuclear reactor where the fuel rod cladding is a major barrier to fission product release.

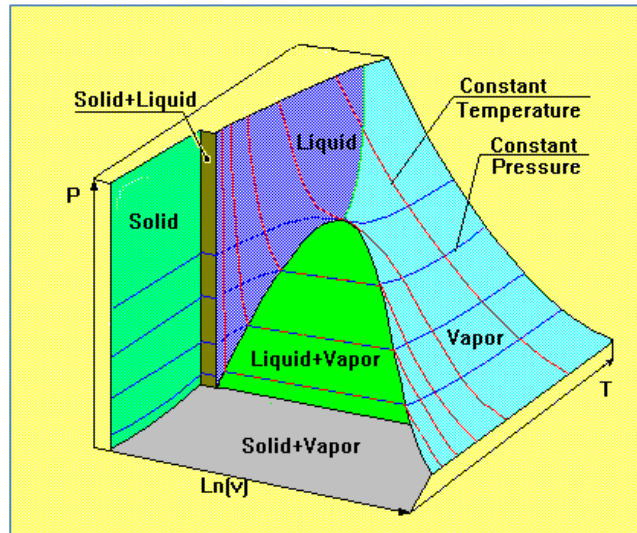


Figure 28 3-D representation of boiling surfaces

On the other hand, as the heat flux is reduced from the region of film boiling back to the CHF point, moving along the bottom part of the curve, it reaches the minimum film boiling temperature. From this point, the heat flux starts to increase in the transition boiling region, during which the heated surface becomes intermittently wetted and dried while the wall temperature is reduced. Once the CHF point is reached by moving from right to left in the diagram, the wall surface is in continued and sustainable contact with the liquid coolant, and heat flux is reduced below the CHF value. This path is sometimes referred to as the temperature control part of the boiling curve.

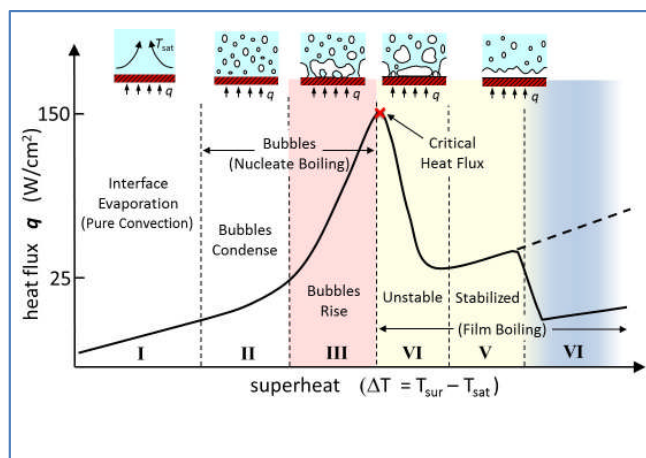


Figure 29 Boiling curve

Figure 29 shows a boiling curve with heat transfer regimes clearly marked. This figure represents one cross section of Figure 28. It shows the heat flux below saturation (in the sub-cooled region), where forced convection to liquid occurs. The transition point between forced convection to liquid and nucleate boiling is called the onset of nucleate boiling and designates the conditions under which the first bubbles start to grow on the wall surface.

Figure 30 shows the parametric trends on the boiling curve [LEU2004, POP2014]. As the mass flux increases in an annular flow regime, the minimum wetting temperature increases, and the boiling curve flattens out. As the mass flux increases in forced convective sub-cooled or low-quality boiling, the CHF and the minimum wetting temperature increase, but the boiling curve retains its shape.

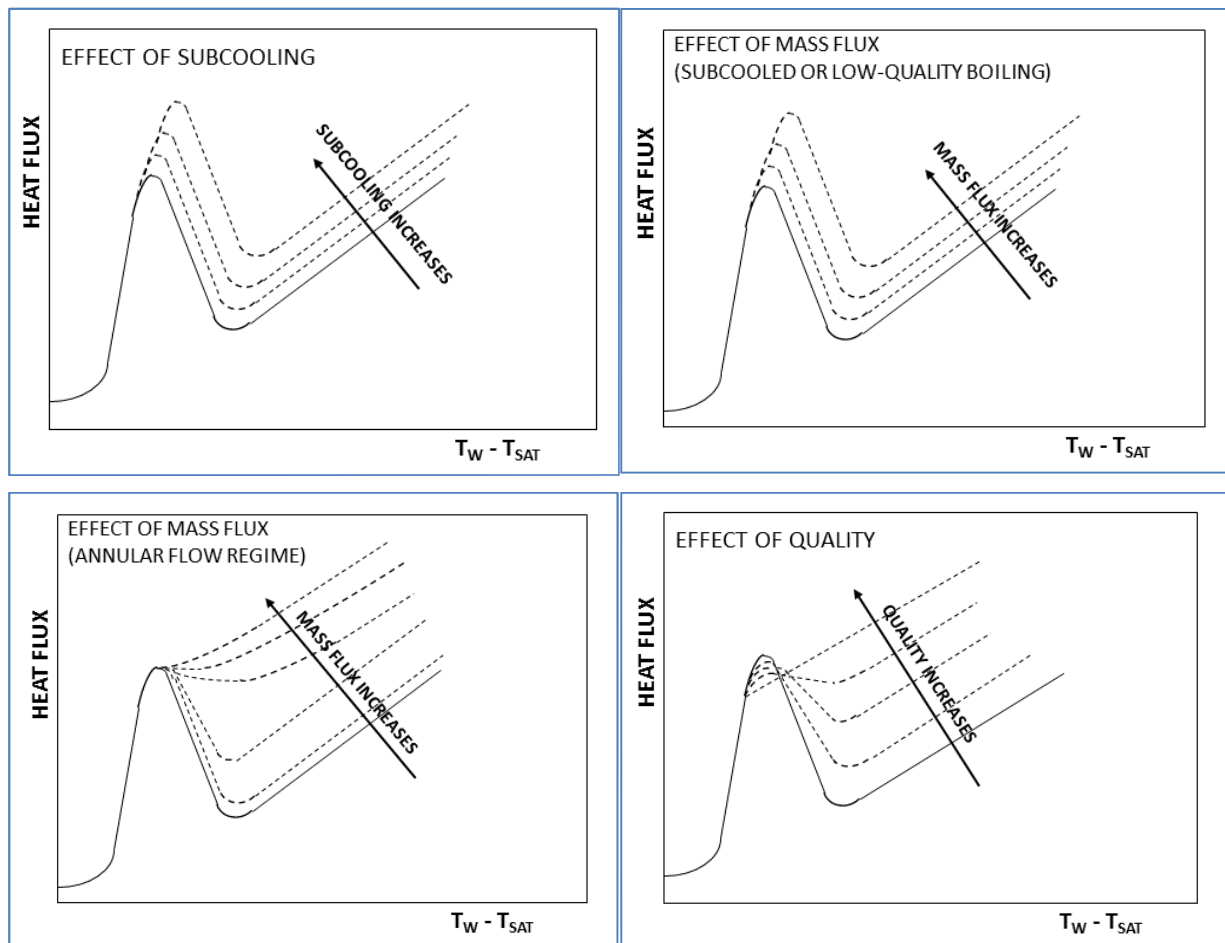


Figure 30 Parametric trends of the boiling curve

A similar effect is seen when increasing the degree of liquid sub-cooling; the CHF point and the minimum wetting temperature increase, but the boiling curve retains its shape. The effect of quality is more complex and is shown in Figure 31.

Figure 31 [LEU2004, POP2013] shows the impact of thermodynamic quality on the boiling curve. For quality equal to or greater than one, the boiling curve is transformed into a straight line, and therefore the CHF concept is not relevant, but the wall temperature increases as the quality increases above one. For saturated boiling ($x = 0$), the boiling curve has the usual S-

shape. As quality increases above zero, the CHF significantly decreases. Moreover, if the quality drops further below zero (i.e., the liquid becomes more sub-cooled), the CHF also increases, and the boiling curve becomes steeper in the nucleate boiling region.

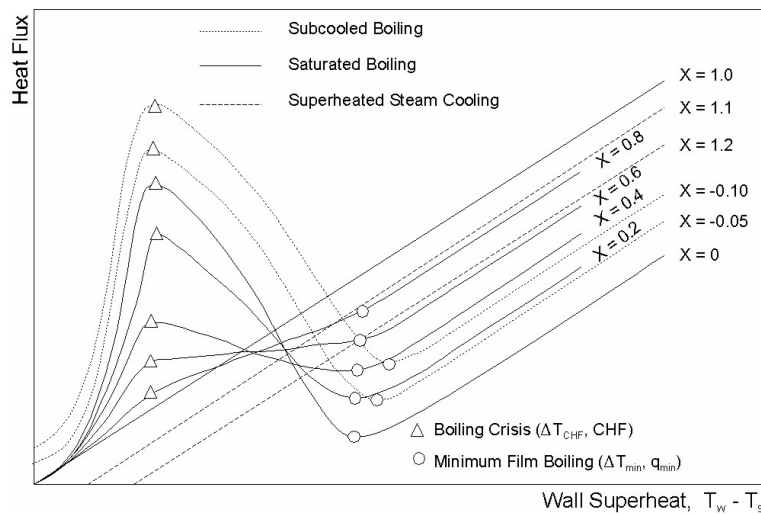


Figure 31 Quality effects on the boiling curve

Figure 32 shows the flow patterns and heat transfer regimes in a boiling channel. In the top part of the figure, the temperature distributions along the heated channel in the coolant and at the wall surface are shown. It is possible to recognize the flow patterns that are most likely to occur given the temperature difference between the coolant and the wall. Note that nucleate boiling starts after the wall surface temperature has risen above the water saturation temperature by a certain amount. Nucleate boiling continues in areas C through F, and then at the point of dryout, when the CHF has been reached, the wall surface temperature exhibits a rapid increase as wall cooling decreases due to loss of contact between the wall and the liquid.

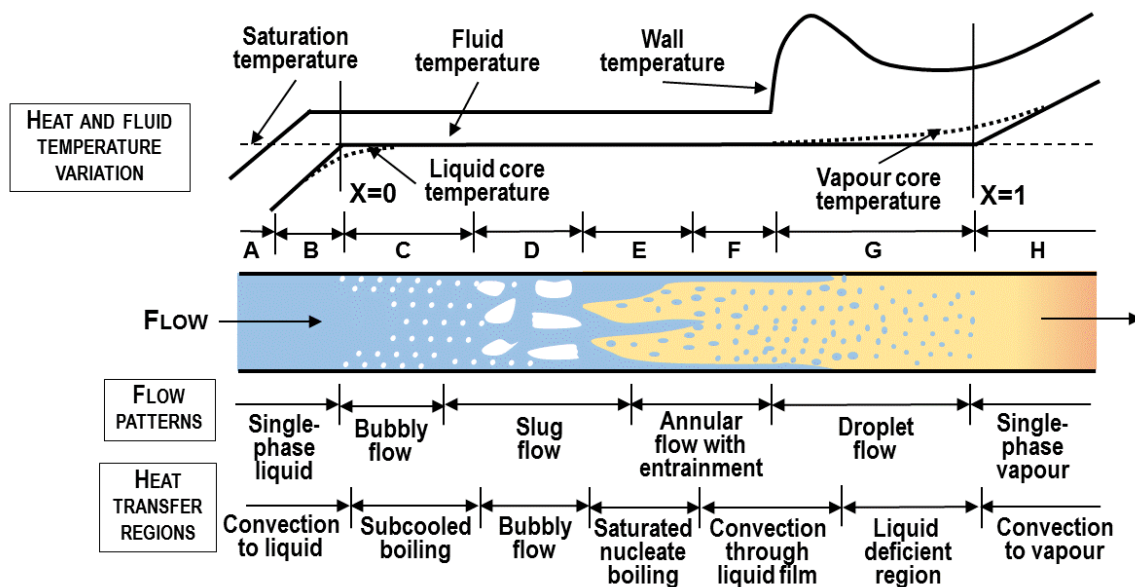


Figure 32 Heat transfer regimes in a boiling horizontal channel

Figure 33 provides model details on the transition from forced convection to liquid and nucleate boiling. It also shows the point of initiation of nucleate boiling, when the first bubbles appear on the wall surface. At the point of net vapour generation, the bubbles can detach from the walls and move to the bulk liquid. A further increase in heat flux at the wall surface happens when the liquid temperature reaches saturation, which creates an opportunity for bubbles to become detached from the wall in great numbers and move with the liquid flow, leading to significant phase separation and disequilibrium.

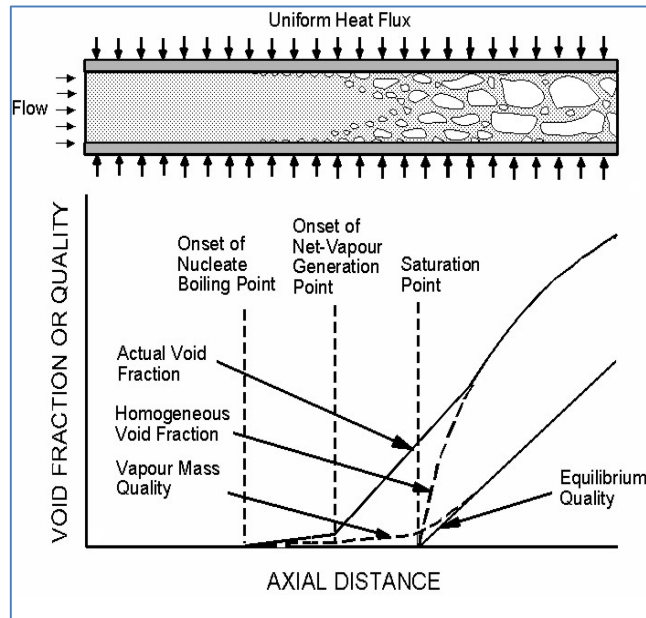


Figure 33 Details of sub-cooled boiling phases in horizontal flow

Three main types of models are used to analyze two-phase flow:

- “homogeneous” flow models,
- “separated” flow models, and
- “flow pattern” or “drift flux” models.

The basic equations are solved within the framework of each of these idealized representations. To apply these models, it is necessary to know when each should be used and to be able to predict the transition from one pattern to another.

6.1.5 Two-phase flow models

The homogeneous model and the separated flow model are the two most widely used and tested models of two-phase flow that are presently available. The homogeneous model considers two-phase flow as a homogenized mixture (pseudo-fluid) possessing average fluid properties. It neglects any local effect that flow patterns may have on two-phase flow and ignores interaction between phases. In other words, the homogenous model considers the phases to be in hydrodynamic and thermodynamic equilibrium.

The homogeneous model is applicable only if the flow parameters do not vary rapidly and thermal disequilibrium has little influence. Although the homogeneous model predicts the

dependence of the two-phase friction multiplier on pressure and quality reasonably well, it has two unsatisfactory features: (a) the friction multiplier is a function of pressure and quality only and is independent of mass flux; and (b) it generally under-predicts low-quality data. Many early software codes used in CANDU design, such as SOPHT [SOP1980], used this type of modelling.

The separated flow model considers the two phases to be segregated into two streams: one of liquid, and one of vapour. Conservation equations are written separately for each phase, and interaction between phases is taken into account by constitutive relationships. The basic equations for the separated flow model are not dependent on the particular flow configuration adopted. The basic assumptions of the separated flow model in analyzing two-phase pressure drop are:

- a) The velocities of each phase are constant, but not necessarily equal in any given cross section within the zone occupied by the phase.
- b) Thermodynamic equilibrium exists between the two phases.
- c) Empirical correlations can be used to relate the two-phase friction multiplier and the void fraction to the dependent flow variables.

Among the various flow patterns, this model would be expected to be most valid for the annular flow pattern. Newer versions of the separate flow model can accommodate both thermodynamic and hydrodynamic disequilibrium between the flow phases.

The drift flux approach satisfactorily accounts for the influence of mass velocity on the void fraction as seen in the separated flow model, and an empirical expression may be used to provide the required relationship between the void fraction and the independent flow pattern.

With the separate flow model and the drift flux model, appropriate void fraction calculations must be performed to ensure model fidelity. Many correlations have been proposed and used in various models; a listing of these correlations is beyond the scope of this handbook (further details can be found in [WAL1969]). Very often used as a void fraction correlation is the homogeneous equation given by Eq. (18):

$$\alpha = \frac{x_a v_g}{(1-x_a) v_f + x_a v_g}. \quad (18)$$

Another often-used void fraction correlation is the Armand-Massina correlation [LEU2004], which is given by the following equation:

$$\alpha = \frac{(0.833 + 0.167 x_a) x_a v_g}{(1-x_a) v_f + x_a v_g}. \quad (19)$$

6.1.6 Two-phase flow in fuel bundles

Two-phase flow in fuel bundles is very complex and requires significant experimental support to understand important phenomena and develop adequate models and correlations. Further information about fuel bundle effects will be given in later sections of this chapter.

The CANDU fuel bundle experimental void fraction database includes data for bundles with 3 to

37 fuel pins, in addition to tube and annulus data. The experimental database includes a wide range of flow conditions with uniformly heated fuel elements or fuel elements with certain radial and axial heating profiles. Figure 34 illustrates that bundle geometries with 6 and 37 fuel elements do not significantly affect the relationship between void fraction and quality [LEU2004, POP2013].

Figure 35 also shows that the impact of the hydraulic diameter of a 7-element bundle does not have a significant impact on the relationship between void fraction and thermodynamic quality, except for very low quality values (representing highly sub-cooled conditions) [LEU2004, POP2013].

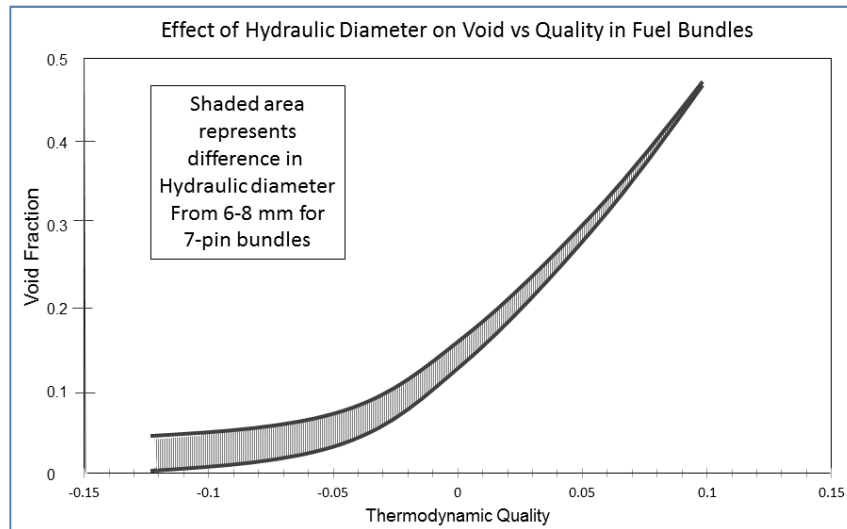


Figure 34 Effect of tube diameter on quality and void fraction

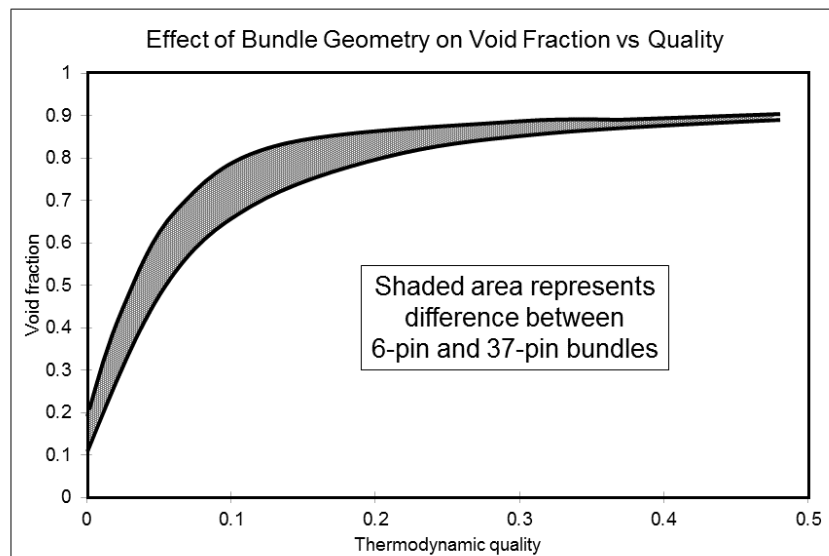


Figure 35 Effect of bundle geometry on quality and void fraction

6.1.7 Problems

1. Explain the relationship between the mass quality and the void fraction in two-phase flow.
2. Explain the difference between the mass quality and the thermodynamic quality in two-phase flow.
3. Explain the main characteristics of the boiling curve, the main parameters that are important for two-phase flow calculations, and the main parameters that influence its shape.
4. Explain the key flow patterns that can occur in vertical and horizontal two-phase flow in heated channels. Explain how the flow regime maps are developed and used in reactor thermal-hydraulic design.
5. Explain the possible models used in two-phase flow calculations, their range of applicability and key features.
6. A BWR reactor operates at a thermal power of 1400 MWt. Water enters the bottom of the reactor core at 275 °C, and passes through the core at a flow rate of 6050 kg/s. the reactor operates at pressure of 7 MPa. Calculate the steam flow rate produced in the reactor.

6.2 Thermodynamics of nuclear energy conversion

This section discusses the thermodynamics of energy conversion in nuclear reactor systems, including a description of the laws of thermodynamics. It provides definitions of basic thermodynamic laws, followed by a description of reactor power cycles, starting with the Carnot cycle, and followed by the Rankine cycle. The definition and analysis of cycle thermal efficiency is discussed, and methods for improving efficiency are described.

6.2.1 Definitions

This section describes the most important concepts and parameters in reactor thermodynamic analysis. Consider a system undergoing a change from state 1 to state 2, as shown in Figure 36. Initially, the system is at energy level E_1 . Then, after a certain amount of energy, Q , is added to the system and a certain amount of work, W , is performed by the system, the system is brought to energy level E_2 . It would be interesting to discover by what parameters this change is driven and how effective is the energy exchange between the system and its surroundings.

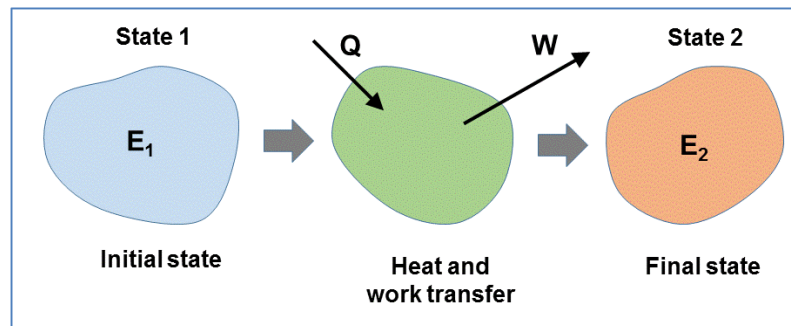


Figure 36 Change of thermodynamic states in a system

6.2.1.1 Work

Figure 37 shows a practical example of the general concept shown in Figure 36. In Figure 37, a piston is moved from a position 1 to a position 2 by sequentially moving small amounts of weight applied at the piston stem. Initially, the piston is under pressure p_1 , with volume V_1 and temperature T_1 . After moving a certain amount of weight, the piston ends up at pressure p_2 , volume V_2 , and temperature T_2 . The system volume changed by $dV=A \cdot dx$ each time a weight was removed.

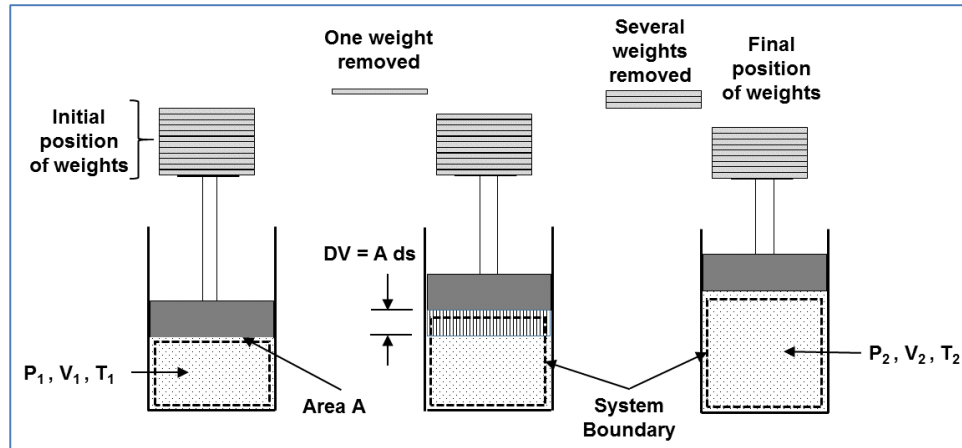


Figure 37 Concept of parameters of thermodynamic state in piston geometry

The infinitesimal amount of work done by the system (shown in Figure 37) is given by Eq. (20) [SAA1966]:

$$dW = f dx = p A dx = p dV . \quad (20)$$

Assuming that the fluid is an ideal gas and that the above process has been performed at a constant temperature (i.e., is an isothermal process), then the total work performed by weight removal is given by Eq. (21):

$$W_{1-2} = \int_1^2 p dV = \int_1^2 mRT \frac{dV}{V} = mRT \ln \left(\frac{V_2}{V_1} \right) . \quad (21)$$

For a constant-pressure process (i.e., an isobaric process), the total work is given by Eq. (22):

$$W_{1-2} = p \int_1^2 dV = p(V_2 - V_1) . \quad (22)$$

For a constant-volume process, because the piston does not move, no work is performed, as stated by Eq. (23):

$$W_{1-2} = \int_1^2 p dV = 0 . \quad (23)$$

One can use the ideal gas law from thermodynamics of gases, as given by Eq. (24):

$$p \cdot V = m \cdot R \cdot T , \quad (24)$$

where P is pressure [MPa or N/m²]; V is volume [m³]; m is mass [kg]; T is temperature [°K]; and R is the gas constant [N·m/(kg °K) or J/(kg °K)].

6.2.1.2 Heat

Heat as a form of energy exists in all bodies and is essential for energy transfer. The nature of heat is associated with the movements or vibration of molecules or atoms at the microscopic level in any body, solid, liquid, or gas. Each energy transfer process eventually ends up being a heat transfer process, i.e., it involves transfer of molecular movement or vibration from one body to another. Even the energy exchanged by radiation eventually ends up being transferred

into molecular movement. Transfer of energy as heat is a microscopic process because it represents the microscopic motion and interactions of microscopic constituents such as molecules and photons.

The level of molecular movement in a certain body or system is measured in terms of its temperature. The higher the level of excitement of the microscopic constituents of a system, the higher will be its temperature. Hence, a temperature difference between two bodies or two systems is essential to the heat transfer process because it sets up the potential for energy transfer.

Often assumptions and simplifications are made in heat transfer processes to analyze and understand certain aspects more effectively [BIR1960, ROH1985]. One of these is the assumption of an adiabatic process, which means that during the process, no heat transfer to and from a given system undergoing adiabatic change is made with any surrounding systems. Another important assumption is to treat a system as isolated from the surrounding systems. This means that in addition to no heat transfer with the surrounding systems, there is also no work exchanged with the surrounding systems.

6.2.1.3 Energy

Energy is a conserved property of a physical system, which cannot be observed directly, but can be calculated from the system's state. The energy of a system can present itself in various forms and is therefore difficult to describe by a comprehensive definition. Often, the best description of energy is as "the capacity to perform work".

For the thermal-hydraulic design engineer, three energy components are of most importance [LEU2004, POP2013]:

- Internal energy, E_U [kJ], or specific internal energy e_u [kJ/kg] (internal energy is usually simply expressed in U , or u);
- Kinetic energy, E_K [kJ], or specific kinetic energy, e_k [kJ/kg]; and
- Potential energy, E_p [kJ], or specific potential energy, e_p [kJ/kg].

Internal energy describes the thermodynamic energy of system molecules or atoms (referred to as heat). Kinetic energy is the energy of motion, which is carried by a body or system with a certain mass. Potential energy is energy possessed by a system when moving from one place to another in a force field, such as a gravitational field, an electro-magnetic field, or the nuclear force field in the atom. Most often for a thermal-hydraulic engineer, potential energy denotes the gravitational potential.

The total energy of a system in thermal-hydraulic terms can be expressed as the sum of the above components by Eq. (25) or Eq. (26):

$$E = E_U + E_K + E_p = U + E_K + E_p, \quad (25)$$

$$e = e_u + e_k + e_p = u + e_k + e_p. \quad (26)$$

The energy of a system depends on the temperature, pressure, velocity, and elevation of the system with respect to its surroundings.

6.2.1.4 Enthalpy

Enthalpy is a measure of the total energy of a thermodynamic system. It includes the internal energy, U (or thermodynamic potential) and the volume and pressure (the energy required to make room for a system change). Enthalpy is useful in describing system thermodynamic changes because it simplifies the description of energy transfers and system changes. Enthalpy is a thermodynamic property of a substance.

Consider a system undergoing a change because of addition of heat (energy) to the system at constant temperature; its total energy change can be described in terms of the system's internal energy and the product of the system's pressure and volume, as in Eq. (27):

$$\int_1^2 dQ = \int_1^2 dU + \int_1^2 P \cdot dV . \quad (27)$$

The sum of the system's internal energy and the product of its pressure and volume defines its enthalpy level, as shown by Eq. (28):

$$H = U + P V . \quad (28)$$

On a unit mass basis, the specific enthalpy is shown by Eq. (29), where specific heat is $q = Q/M$, specific internal energy is $u = U/M$, specific volume is $v = V/M$, M is mass, and P is pressure:

$$h = u + P v . \quad (29)$$

Enthalpy is a state parameter and can be expressed in terms of other parameters. For sub-cooled or super-heated conditions, $h = f(P, T)$, and for saturated conditions, $h = f(P)$ or $h = f(T)$, it is expressed in terms of pressure or temperature. In the two-phase region, the following equation can be used to calculate mixture enthalpy (under homogeneous conditions):

$$h_m = x \cdot h_g + (1-x) \cdot h_f = h_f + x \cdot h_{fg} , \quad (30)$$

where h_g is the enthalpy of the saturated gas, h_f is the enthalpy of the saturated liquid, and h_{fg} is the latent heat of vaporization.

6.2.2 First law of thermodynamics

The first law of thermodynamics is one of the most fundamental laws of nature; it simply states that the total energy change in a system is equal to the total energy supplied to the system from surrounding systems minus the energy transferred to the surrounding systems [SAA1966]:

Energy supplied – Energy removed = Change of energy level.

Hence, for a system with a particular mass that remains constant during the process, the first law of thermodynamics can be expressed as in Eq. (31):

$$Q - W = \Delta E = E_2 - E_1 . \quad (31)$$

The above equation written per unit mass becomes Eq. (32):

$$q - w = \Delta e = e_2 - e_1 . \quad (32)$$

With these definitions, it is now possible to define the work performed by a system that goes through an isobaric process as in Eq. (33):

$$W = \int_1^2 P dV = P(V_2 - V_1). \quad (33)$$

Using the first law of thermodynamics, as in Eq. (31), and substituting this equation into Eq. (33), one obtains the following equation:

$$Q - P(V_2 - V_1) = U_2 - U_1. \quad (34)$$

Rearranging the terms in Eq. (34) yields Eq. (35), which clearly shows the advantage of using enthalpy because it can provide a better expression of the first law of thermodynamics:

$$\begin{aligned} Q &= U_2 - U_1 + P(V_2 - V_1) \\ &= (U_2 + PV_2) - (U_1 + PV_1) = H_2 - H_1 = \Delta H. \end{aligned} \quad (35)$$

In the case of a system with multiple energy and work inputs and outputs, the first law of thermodynamics must be applied to the sum of these inputs and outputs, as in Eq. (36). Thus, Eq. (37) is obtained as an energy balance equation:

$$\Delta E = 0 = \sum \text{energy inflow} - \sum \text{energy outflow} \quad (36)$$

$$\begin{aligned} &= \frac{1}{2}mV_1^2 + mu_1 + Q + P_1V_1 + mgZ_1 \\ &= -\frac{1}{2}mV_2^2 - mu_2 + W - P_2V_2 - mgZ_2. \end{aligned} \quad (37)$$

Converting Eq. (37) in terms of specific parameters yields the following equations in terms of internal energy (Eq. (38)) and enthalpy (Eq. (39)):

$$q - w = \left[u_2 + Pv_2 + \frac{1}{2}V_2^2 + gZ_2 \right] - \left[u_1 + Pv_1 + \frac{1}{2}V_1^2 + gZ_1 \right], \quad (38)$$

$$q - w = \left[h_2 + \frac{1}{2}V_2^2 + gZ_2 \right] - \left[h_1 + \frac{1}{2}V_1^2 + gZ_1 \right]. \quad (39)$$

In the case of a turbine, there is no heat addition ($q = 0$) and no change in elevation for a horizontal turbine ($Z_1 = Z_2$), and therefore:

$$w = [h_1 - h_2] - \frac{1}{2}[V_1^2 - V_2^2]. \quad (40)$$

For a flow through a horizontal nozzle, there is neither heat addition nor work delivered ($q = w = 0$) and no change in elevation ($Z_1 = Z_2$), and therefore:

$$V_1^2 = V_2^2 + 2[h_1 - h_2]. \quad (41)$$

Finally, there is a special form of the energy balance equation that is very useful to thermal-

hydraulic engineers for calculating fluid parameters in a pipe flow—the Bernoulli equation—in which neither heat addition nor work is delivered ($q = w = 0$):

$$\left[h_1 + \frac{1}{2}V_1^2 + gZ_1 \right] = \left[h_2 + \frac{1}{2}V_2^2 + gZ_2 \right] = const, \tag{42}$$

$$\left[u + Pv + \frac{1}{2}V^2 + gZ \right] = const. \tag{43}$$

Equation (43) clearly shows that the key fluid parameters for a flow are connected, so that to add up to a constant, an increase in one parameter must result in a reduction in the other parameters. For example, considering horizontal flow, an increase in fluid velocity results in a decrease in fluid pressure, and vice versa.

6.2.3 Reactor cycles

Nuclear reactors directly or indirectly produce steam that performs a thermodynamic cycle, which is used to convert nuclear energy using the energy conversion chain shown in the diagram below.

<i>Nuclear fission</i>	<i>Nuclear fuel internal energy</i>	<i>Cooling Fluid</i>	<i>Steam production</i>	<i>Turbine rotational energy</i>	<i>Generator magnetic field</i>	<i>Electrical energy</i>
<i>Converts mass into kinetic energy of nuclear particles</i>	<i>Converts kinetic energy of nuclear particles into molecular motion of the fuel mass</i>	<i>Converts fuel internal energy into internal energy of the coolant</i>	<i>Converts internal energy of the coolant into steam production</i>	<i>Converts steam energy into kinetic energy (rotation) of the turbine shaft</i>	<i>Converts the kinetic energy of the turbine shaft into rotation of generator magnetic poles</i>	<i>Converts generator magnetic energy into electrical energy</i>

The shaded area of the diagram represents the thermodynamic cycle that is implemented with the objective of delivering work to the electric generator.

This process leads to rejection of a certain part of the thermal energy into the environment (lake, river, sea, or the atmosphere) to be able to close the cycle; this will be explained in later sections.

With regard to energy generation, the cycle thermodynamic efficiency, η_t is defined to provide a measure of cycle performance:

$$\eta_t = \frac{W}{Q_{in}}. \tag{44}$$

6.2.3.1 Carnot cycle

The Carnot cycle is a theoretical thermodynamic cycle that represents the most efficient way of converting a given amount of thermal energy between two thermal reservoirs into work (turbine work), or conversely the most efficient way of converting a given amount of work into creating a temperature difference between two reservoirs (refrigeration).

Figure 38 shows an ideal Carnot cycle in pressure versus volume and temperature versus entropy diagrams. The Carnot cycle consists of the following processes [SAA1966]:

- delivering heat to the cycle by a reversible isothermal expansion process (process from points 1 to 2 in Figure 38);
- delivering work output by isentropic expansion of gas (process from points 2 to 3 in Figure 38);
- rejecting waste heat from the cycle by reversible isothermal compression of gas (process from points 3 to 4 in Figure 38); and
- inputting work into the cycle by isentropic compression of gas (process from points 4 to 1 in Figure 38).

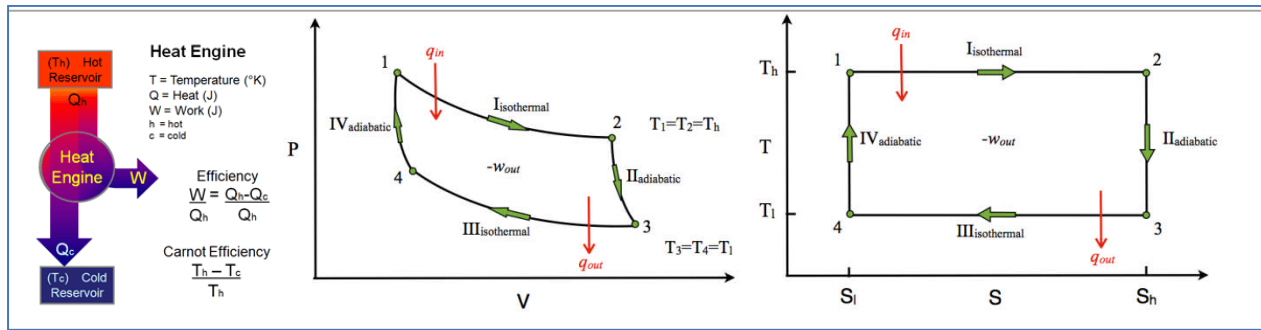


Figure 38 Ideal Carnot cycle

To calculate the thermal efficiency of the Carnot cycle, it is necessary to calculate the total heat delivered and the total work performed and to use these results in Eq. (44).

For the process from points 1 to 2 (at constant temperature, $\Delta U_{1-2} = \int_1^2 m c_v dT = 0$):

$$W_{1-2} = \int_1^2 p dV = m R T_1 \int_1^2 \frac{dV}{V} = m R T_1 \ln \frac{V_2}{V_1}. \quad (45)$$

Using the first law of thermodynamics, from Eq. (31), the heat addition can be expressed as:

$$Q_{1-2} - W_{1-2} = \Delta U_{1-2} = 0, \quad (46)$$

$$Q_{1-2} = W_{1-2} = m R T_1 \ln \frac{V_2}{V_1}. \quad (47)$$

For the process from points 2 to 3 (with no heat addition, $Q_{2-3} = 0$):

$$W_{2-3} = \int_2^3 p dV = \int_2^3 C V^{-\gamma} dV = \frac{p_3 V_3 - p_2 V_2}{-\gamma + 1}, \quad (48)$$

$$\Delta U_{2-3} = \int_2^3 m c_v dT = m c_v (T_3 - T_2). \quad (49)$$

Using the first law of thermodynamics, from Eq. (31), the link between internal energy change and delivered work is:

$$Q_{2-3} = \Delta U_{2-3} + W_{2-3} = 0. \quad (50)$$

For the process from points 3 to 4 (at constant temperature, $\Delta U_{3-4} = 0$):

$$W_{3-4} = m R T_3 \ln \frac{V_4}{V_3} = Q_{3-4}. \quad (51)$$

For the process from points 4 to 1 (with no heat addition, $Q_{4-1} = 0$):

$$W_{4-1} = \frac{p_1 V_1 - p_4 V_4}{-\gamma + 1}, \quad (52)$$

$$\Delta U_{4-1} = m c_v (T_1 - T_4) = -W_{4-1}. \quad (53)$$

These equations have used the following thermodynamic relationships to calculate the thermal efficiency:

- For a quasi-static adiabatic process:

$$T_2 V_2^{\gamma-1} = T_3 V_3^{\gamma-1} \quad \text{and} \quad T_4 V_4^{\gamma-1} = T_1 V_1^{\gamma-1}. \quad (54)$$

- For an isothermal process

$$T_1 = T_2 \quad \text{and} \quad T_3 = T_4, \quad (55)$$

$$p_1 V_1 = p_2 V_2 \quad \text{and} \quad p_3 V_3 = p_4 V_4. \quad (56)$$

- Volume relation

$$\frac{V_2}{V_1} = \frac{V_3}{V_4}. \quad (57)$$

Hence, the net work done can be obtained by summing up the work in the separate processes described by Eqs. (45), (48), (51), and (52) and using the relationships provided by Eqs. (54), (55), (56), and (57):

$$W_{\text{cycle}} = W_{1-2} + W_{2-3} + W_{3-4} + W_{4-1} \quad (58)$$

$$= m R T_1 \ln \frac{V_2}{V_1} + \frac{p_3 V_3 - p_2 V_2}{-\gamma + 1} + m R T_3 \ln \frac{V_4}{V_3} + \frac{p_1 V_1 - p_4 V_4}{-\gamma + 1},$$

$$W_{\text{cycle}} = m R (T_1 - T_3) \ln \frac{V_2}{V_1}. \quad (59)$$

Now the cycle thermal efficiency can be obtained from Eq. (44):

$$\eta_t = \frac{\text{net work done}}{\text{heat input}} = \frac{W_{\text{cycle}}}{Q_{\text{in}}} = \frac{W_{\text{cycle}}}{Q_{1-2}} = \frac{m R (T_1 - T_3) \ln (V_2 / V_1)}{m R T_1 \ln (V_2 / V_1)} = \frac{T_1 - T_3}{T_1} = 1 - \frac{T_3}{T_1}. \quad (60)$$

One important observation can be made from Eq. (60): the thermal efficiency of the cycle depends on the temperatures of the upper and lower thermal reservoirs. Hence, the higher the temperature at which heat is added to the cycle and the lower the temperature at which heat is extracted from the cycle, the higher will be the thermal efficiency. Therefore, design efforts to improve cycle thermal efficiency are usually directed towards increasing the temperature at which heat is delivered to the cycle. However, it is also evident that this cycle will operate more efficiently if the lower temperature is reduced.

6.2.4 Second law of thermodynamics

The second law of thermodynamics is a very important law of nature and primarily applies to thermodynamics. This law indicates that over time, differences in temperature, pressure, and chemical potential decrease in an isolated physical system, leading eventually, with a time constant that depends on the system thermodynamic inertia, to a state of thermodynamic equilibrium.

There are other definitions of this law, depending on the discipline. The above definition is given in the context of thermodynamics, but this law can also be considered from the perspectives of quantum mechanics or astrophysics, and in such cases, its definition is adjusted to the objectives of the corresponding discipline.

The second law of thermodynamics has many implications, of which a few are stated below:

- Carnot's principle [CAR2015]: The historical origin of the second law of thermodynamics was in Carnot's principle. It refers to the Carnot engine, fictively operating in a very slow mode (quasi-static) so that heat is transferred between two thermal reservoirs that maintain their internal equilibrium. The Carnot principle, which originated at the beginning of the 19th Century, is still valid today. It states that, *"The efficiency of a quasi-static or reversible Carnot cycle depends only on the temperature of the two heat reservoirs, and is independent of the working substance. A Carnot engine operated in this way is the most efficient possible heat engine using these two temperatures"*.
- Clausius' statement [CLA2015]: *"It is impossible to construct a device that executes a thermodynamic cycle so that the sole effect is to produce a transfer of heat energy from a body at a low temperature to a body at a high temperature"*.
- Kelvin's statement [KEV2015]: *"It is impossible, by means of inanimate material agency, to derive mechanical effect from any portion of matter by cooling it below the temperature of the coldest of the surrounding objects"*.
- Kelvin-Planck statement [KPL2015]: *"It is impossible to construct a device that executes a thermodynamic cycle, exchanges heat energy with a single reservoir, and produces an equivalent amount of work"*.
- Planck's principle [PLA2015]: *"The internal energy of a closed system is increased by an isochoric adiabatic process"*.

Whichever definition is used for the second law of thermodynamics leads to the basic conclusion that any time an energy transfer is performed, from thermal to mechanical to

electrical or vice versa, a penalty is paid in terms of increasing the disorder of the isolated system. In other words, thermal energy cannot be converted into work by a cyclic process with 100% efficiency.

The mathematical formulation of the second law of thermodynamics is best visualized using Figure 39. In this figure, on the left side, a generalized thermodynamic cycle is shown taking place between a hot reservoir at temperature T_H and a cold reservoir at temperature T_C . On the right side, the Carnot cycle diagram is shown between the same boundaries. Therefore, the area in red, labelled as Q_C , is the amount of energy exchanged between the system and the cold reservoir. The area in white, labelled as W , is the amount of work exchanged by the system and its surroundings. The amount of heat exchanged with the hot reservoir, labelled as Q_H , is the sum of the two, Q_C and W . If the system is behaving like an engine, the process moves clockwise around the loop, and if it behaves as a refrigerator, it moves counter-clockwise.

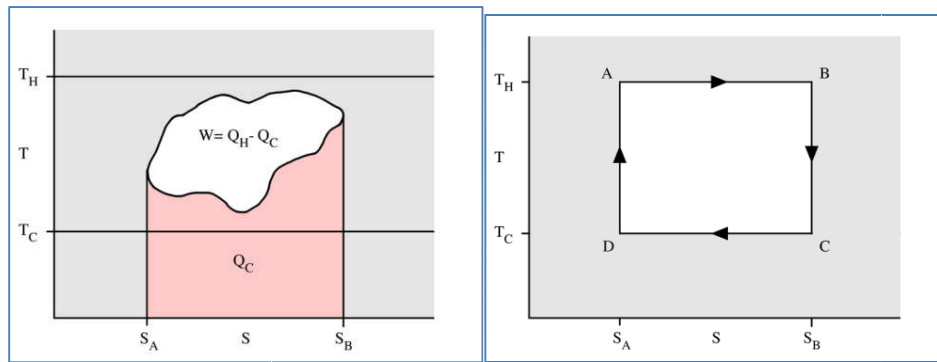


Figure 39 The concept of entropy in closed cycles

From the above, and because the energy addition to the cycle and the energy extraction from it have opposite signs, it follows that:

$$\frac{T_H}{T_C} = -\frac{Q_H}{Q_C} \Rightarrow \frac{Q_C}{T_C} + \frac{Q_H}{T_H} = 0. \tag{61}$$

This can be generalized by splitting the general reversible cycle shown in **Figure 39** into a number of infinitesimally small Carnot cycles. For each small cycle, noting that common boundaries cancel, the following relation can be obtained:

$$\frac{\Delta Q_C}{T_C} + \frac{\Delta Q_H}{T_H} = 0. \tag{62}$$

Summing all cycles and performing a circular integration:

$$\sum \frac{\Delta Q}{T} = 0 \Rightarrow \oint \frac{\Delta Q}{T} = 0. \tag{63}$$

The above equation also indicates that the line integral $\int_L \delta Q/T$ is path-independent [SAA1966]. Because the closed integral is equal to zero, dQ/T must be an exact differential and

must be a state variable, i.e., a property of the state of the material, like internal energy, pressure, temperature, density (u, P, T, ρ), etc. This differential is defined to be the entropy, S .

Because S is a system property, it is possible to express any equilibrium state in terms of S plus one other state variable (T, P , or something else):

- In a reversible process (Figure 40), the quantity, $\delta Q/T$, from point A to point B is the same regardless of the path;
- Hence, the entropy, S , can be defined as

$$S_B - S_A = \int_A^B \frac{\delta Q}{T} \Big|_{\text{reversible}} ; \quad (64)$$

- Specific entropy, s (J/kg K).

For a reversible process, heat addition and heat extraction from the cycle are defined as:

$$Q_H = T_H(S_B - S_A), \quad (65)$$

$$Q_C = T_C(S_A - S_B) = -T_C(S_B - S_A). \quad (66)$$

Using Eqs. (65) and (66), the net work done by the cycle is defined as:

$$W_{\text{cycle}} = Q_H - Q_C = T_H(S_B - S_A) - T_C(S_B - S_A) = (T_H - T_C)(S_B - S_A). \quad (67)$$

Therefore, the thermal efficiency is defined using Eq. (44) as:

$$\eta_t = \frac{W_{\text{cycle}}}{Q_H} = \frac{(T_H - T_C)(S_B - S_A)}{T_H(S_B - S_A)} = \frac{T_H - T_C}{T_H} = 1 - \frac{T_C}{T_H}. \quad (68)$$

The following relation represents the generalization of the entropy definition for reversible and irreversible processes:

$$\oint \frac{\Delta Q}{T} \leq 0 \quad \text{or} \quad \Delta S \geq \int \frac{\delta Q}{T}. \quad (69)$$

Hence, for reversible processes, the equality sign applies, whereas for irreversible processes, i.e., realistic processes, the < sign applies. All real processes are considered irreversible. This indicates that for closed systems, any process, regardless of the path, results in an increase in entropy.

6.2.5 Reactor power cycle

Figure 40 shows how an ideal Carnot cycle is applied with water as the working fluid. On the right side, isothermal addition of energy (heat) to the cycle is achieved between the saturated water and saturated steam states. Extraction of waste heat from the cycle is carried out isothermally in the two-phase region.

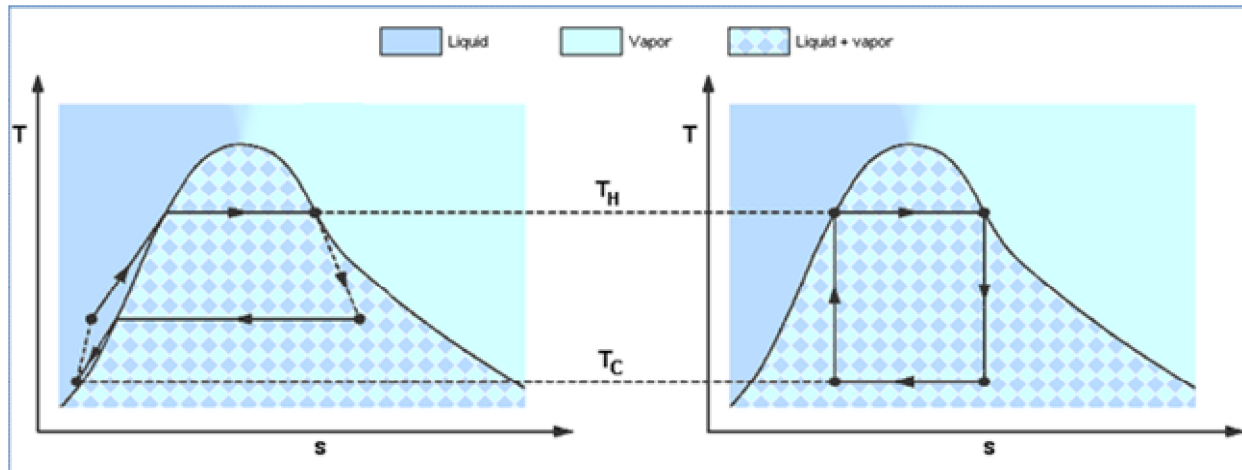


Figure 40 Carnot cycle for steam

The ideal Carnot cycle is impossible to achieve with real turbo machinery. Therefore, a variation of the Carnot cycle, called the Rankine cycle, is shown on the left side of Figure 40 [SAA1966]. This cycle performs complete condensation of the steam at the lower thermal reservoir temperature. Hence, water enters the adiabatic compression in the pump as liquid water. With this modification, more heat rejection is needed to bring the feedwater to saturation, avoiding a liquid-vapour mixture in the pump. This reduces thermal efficiency.

Figure 41 shows the steam-water diagrams used by thermal engineers and designers [WIK2015a]. The first part, Figure 41a, shows the P - v diagram, followed by Figure 41b, the T - s diagram, and Figure 41c, the h - s diagram. The P - v diagram is useful for representing changes in volume between different points in the cycle. Note that pressure and temperature are linked parameters at saturation conditions, and hence in the two-phase area, both join in the same straight line. The T - s diagram shows temperature changes in the cycle for given entropies. This diagram is useful for the Carnot and Rankine cycles because heat addition and heat extraction are performed as isothermal processes, which are straight horizontal lines in this diagram.

According to the ideal Carnot cycle and the ideal Rankine cycle, isentropic expansion and isentropic compression (no losses) are represented by vertical straight lines, which make the diagram a very easy way to observe heat changes as square areas. On the other hand, the h - s diagram is very useful to the turbo machinery designer because each energy change during any of the processes is shown as a vertical increment on the y-axis, whereas reversibility or irreversibility of the cycle is easily observable on the x-axis.

Figure 42 shows an ideal Rankine cycle for a nuclear power plant (ideal because irreversibility is not taken into account). The left side shows the NPP secondary side with the steam generator and other equipment. Certain points in the diagram are labelled on the reactor sketch with numbers.

The separate processes of the cycle as labelled on the left side with their position are:

- Heat supplied: area 6-1-2-2A-3-4-5-6
- Heat removed: area 6-1-4-5-6

- Net work done: area 1-2-2A-3-4-1.

The assumptions of this idealized Rankine cycle are:

- Negligible changes in kinetic energy and potential energy;
- All processes are reversible; and
- Negligible pressure and heat losses.

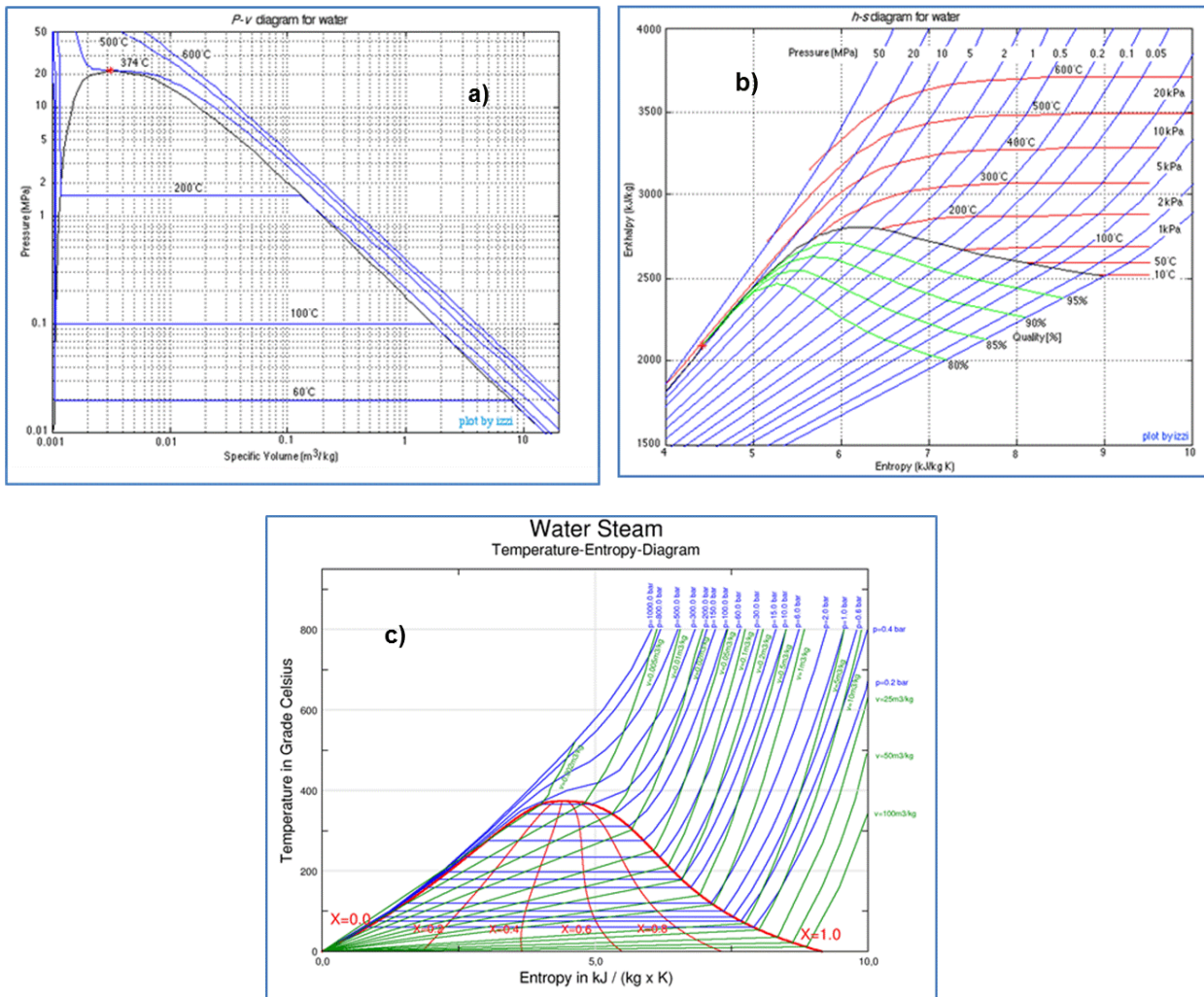


Figure 41 Steam-water diagrams used in thermodynamic analyzes (a, b, c)

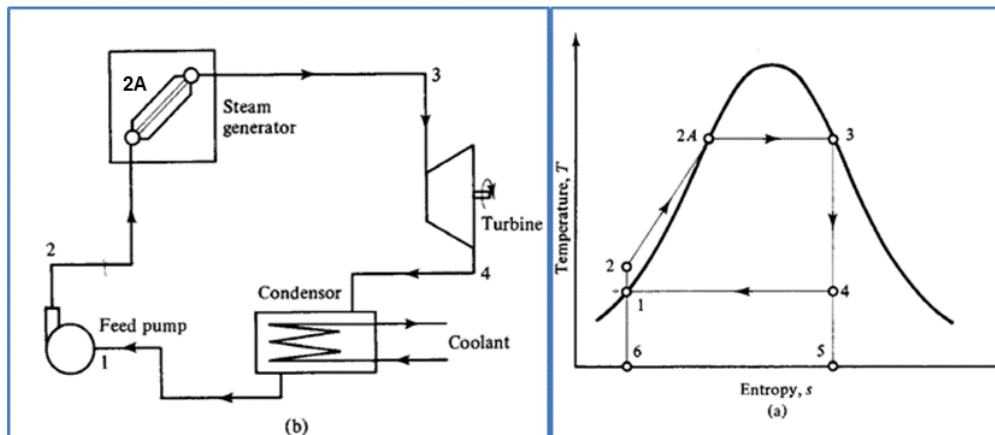


Figure 42 Simplified Rankine cycle in a nuclear power plant

The thermodynamic power cycle in reactor systems is similar to the Rankine cycle. As sketched in Figure 42, the steam generator boils the working fluid (water) isothermally (at saturation temperature), the turbine expands the fluid and performs shaft work, the condenser extracts the reject heat and condenses the fluid, and the feedwater pump returns the fluid to the steam generator at pressure. Of course, the realistic reactor cycle is not reversible, but the principles of the cycle are the same. The typical cycle used in power plants is called the Rankine cycle. The T - s and h - s diagrams for an ideal simple Rankine cycle are given in Figure 41 and Figure 42.

In the ideal Rankine cycle in Figure 42, saturated steam (point 3) enters the turbine and expands isentropically to position 4. At point 4, the wet steam enters the condenser, where heat is removed until the fluid is condensed to a saturated liquid at point 1. After leaving the condenser at saturation pressure P_2 , the fluid is compressed isentropically from pressure P_2 to the boiler pressure P_1 . The high-pressure liquid enters the boiler at point 2, where the fluid is first brought to saturation at pressure P_2 (point 2A) and then vaporized to saturated steam at point 3.

In process 1-2 (isentropic compression in the feedwater pump), no heat is exchanged with the surroundings, i.e., $q_{1-2} = 0$. Hence, the work input to achieve isentropic compression is given by Eq. (70):

$$-w_{1-2} = -(h_2 - h_1) = -\int_1^2 v dp \sim -v_1(p_2 - p_1). \quad (70)$$

In process 2-2A-3 (heating at constant pressure in the boiler), no work is exchanged with the surroundings, i.e., $w_{2-3} = 0$. Hence, using the h - s diagram, the heat addition to the system is obtained as a difference of enthalpies, as given by Eq. (71):

$$q_{2-3} = q_{in} = h_3 - h_2. \quad (71)$$

In process 3-4 (isentropic expansion in the turbine), no heat is exchanged with the surroundings, i.e., $q_{3-4} = 0$. Hence, the work delivered by the turbine is given by Eq. (72):

$$w_{3-4} = h_3 - h_4. \quad (72)$$

In process 4-1 (heat removal at constant pressure in the condenser), no work is exchanged with the surroundings, i.e., $w_{4-1} = 0$. Hence, the heat extraction from the system is obtained as a difference of enthalpies, as given in Eq. (73):

$$-q_{4-1} = h_4 - h_1. \quad (73)$$

The net work performed by this cycle can be obtained as:

$$w_{cycle} = w_{3-4} + w_{1-2} = (h_3 - h_4) - (h_2 - h_1). \quad (74)$$

The thermal efficiency of the ideal Rankine cycle is obtained by Eq. (75):

$$\eta_{Rankine} = \frac{w_{cycle}}{q_{in}} = \frac{(h_3 - h_4) - (h_2 - h_1)}{h_3 - h_2} = \frac{q_{2-3} - q_{4-1}}{q_{2-3}}. \quad (75)$$

As noted earlier, the thermal efficiency of the ideal simplified Rankine cycle is much less than that of the Carnot cycle because more heat is wasted to the environment. The performance of the Rankine cycle can be improved in practice by:

- (1) raising the boiler pressure
- (2) lowering the exhaust pressure
- (3) using superheat
- (4) using reheat.

Options (1), (3), and (4) effectively raise the inlet temperature, whereas (2) effectively lowers the outlet temperature, with a corresponding effect on cycle efficiency.

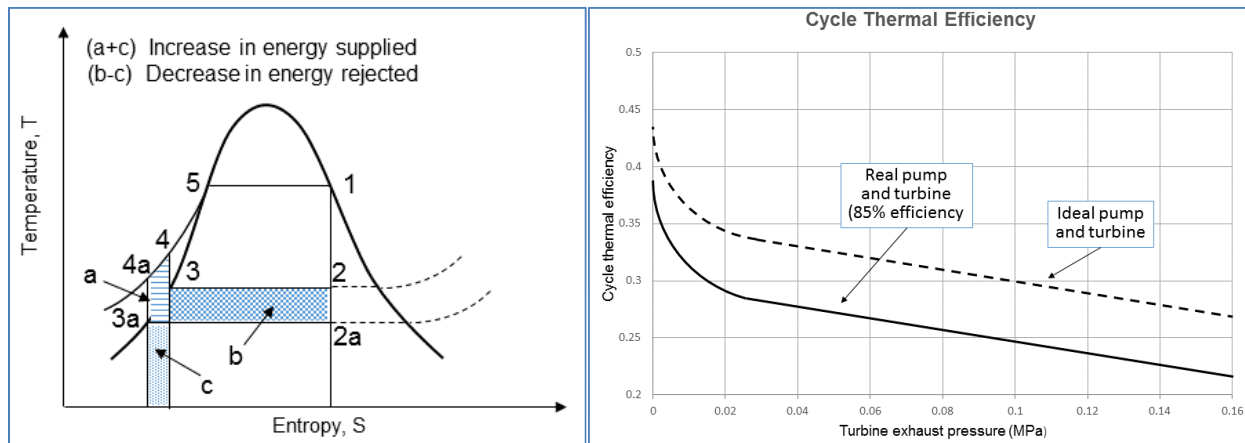


Figure 43 Typical impact of turbine outlet pressure on cycle thermodynamic efficiency

The condenser pressure is limited by the temperature of the available cooling water, the size and cost of the condenser, and the size of the vacuum pumps required to deaerate the condenser. Figure 43 shows the impact of a condenser pressure decrease in a typical PWR nuclear plant. The practical lower limit on condenser pressure is 3–6 kPa(a). Consequently, options (1), (3), and (4) are used to achieve increased efficiency [TOD2011].

The increase in boiler pressure results in an increase in the net work performed by the cycle, with a corresponding decrease in heat rejected. Figure 44 shows the impact of an inlet pressure increase in a typical PWR nuclear plant [TOD2011]. However, for the indirect power cycle, the downside of raising the boiler pressure (and the temperature because the steam is saturated) is that it forces the primary-side temperature to increase to provide sufficient ΔT to transfer the heat from the primary to the secondary side. This higher primary-side temperature requires higher primary-side pressure, which in turn requires thicker pressure vessel walls. In a pressure vessel-type reactor, this can be costly or can lead to reduced plant reliability or life. In pressure tube reactors, the main drawback is the increased parasitic neutron absorption in the pressure tube walls, which need to be thicker, resulting in lower fuel burn-up.

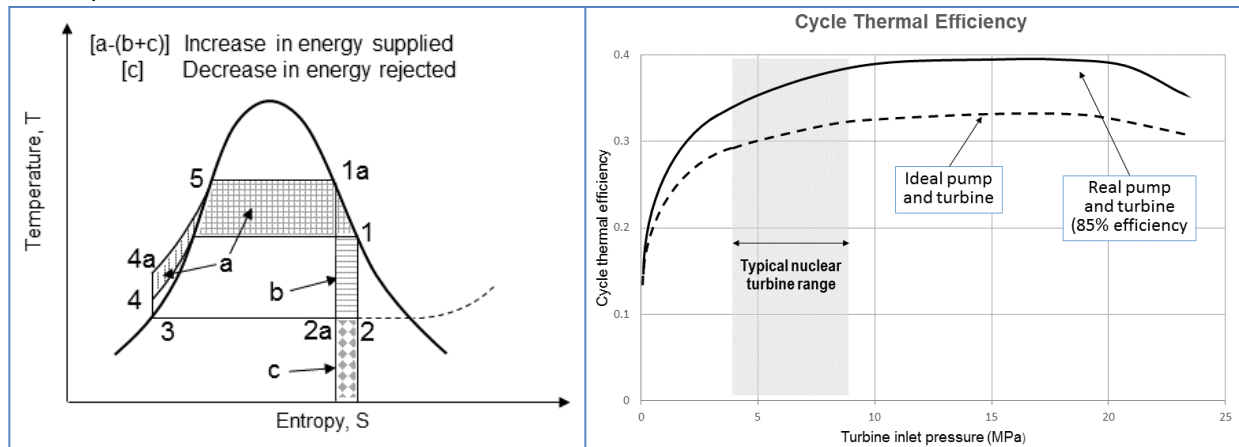


Figure 44 Typical impact of turbine inlet pressure on cycle thermodynamic efficiency

6.2.6 Improvements in reactor cycles

In the following sections, improvements to the Rankine cycle used in power reactors are described, their usefulness discussed, and their consequences analyzed. The improvements described in the following sections are used in power reactors with certain variations and design specifics by various reactor types and vendors. However, they all contribute to higher NPP thermal efficiency, which is considered as an important marketing parameter.

6.2.6.1 Rankine cycle with superheat

Figure 45 illustrates the Rankine cycle with superheat [LEU2004, POP2013]. Superheat causes a net increase in the temperature at which heat is received, with a resulting improvement in cycle efficiency. Another important factor is that the amount of moisture in the fluid leaving the turbine is reduced, which increases turbine efficiency and reduces turbine blade erosion. However, when using superheat, one must have a high-temperature heat source or else reduce boiler pressure. Some recent approaches and ideas include use of traditional gas-fired superheaters in combination with nuclear power reactors.

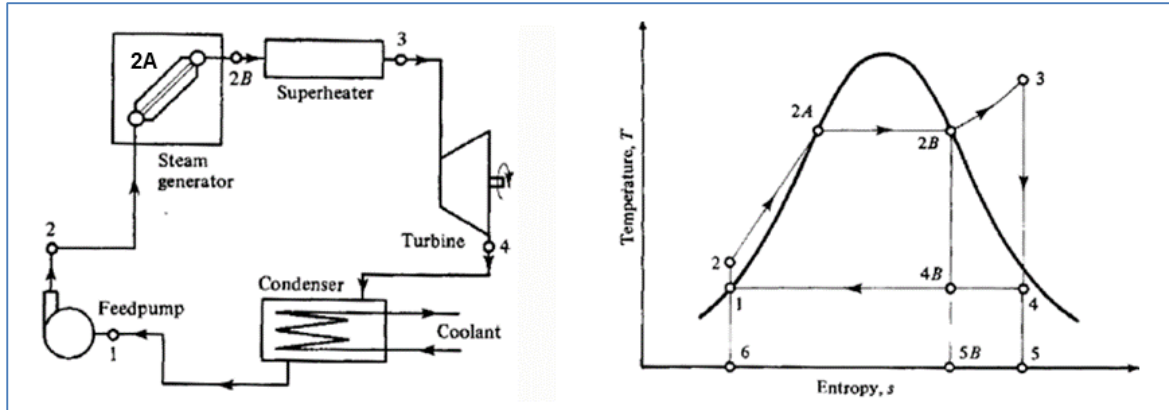


Figure 45 Rankine cycle with superheating

The differences between the cycle with superheat and the simple Rankine cycle are:

- Increased net work output (area 2B-3-4-4B-2B)
- Increased heat supply (area 2B-3-4-5B-2B)
- Increased exhaust steam quality from x_{4B} to x_4 .

The thermal efficiency of the cycle with superheat is given by Eq. (76) and is higher than for the simple Rankine cycle:

$$\eta_{\text{Superheat}} = \frac{w_{\text{cycle}}}{q_{\text{in}}} = \frac{q_{2-3} - q_{4-1}}{q_{2-3}} = \frac{(h_3 - h_4) - (h_2 - h_1)}{h_3 - h_2} \quad (76)$$

6.2.6.2 Reheat cycle

The effective temperature of heat addition is increased and the moisture content further reduced by using reheat in the Rankine cycle. A schematic diagram of the power plant and an appropriate temperature-entropy diagram are shown in Figure 46 [LEU2004, POP2013]. High-pressure, superheated steam is expanded in a high-pressure turbine to an intermediate pressure 4 and the fluid then returned to a second-stage boiler and superheater and reheated to state 3A. The reheated steam is then expanded in a low-pressure turbine to the final exhaust pressure 4A. The moisture content of the working fluid is drastically reduced by use of reheat, and this approach is used in all fossil-fuelled and many nuclear power plants (without the superheating part).

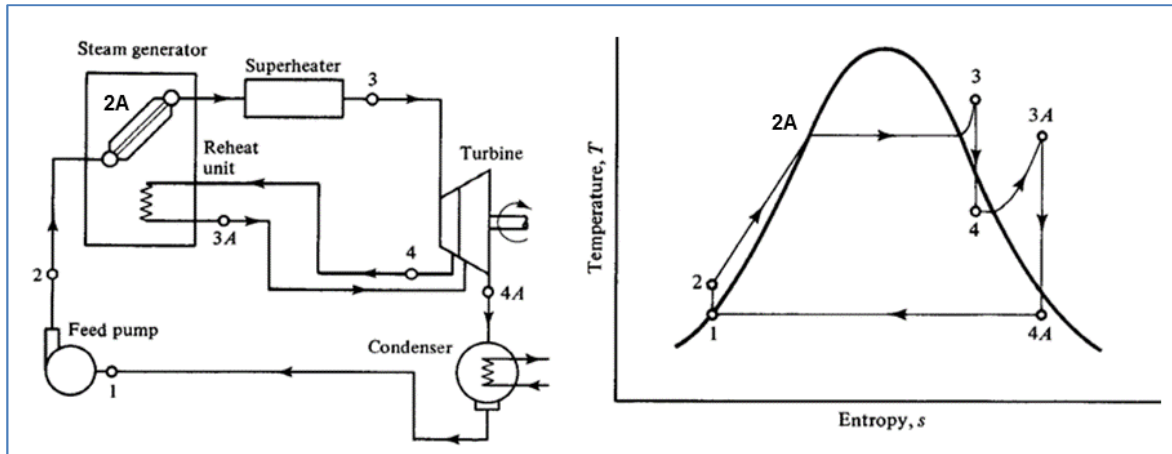


Figure 46 Rankine cycle with superheating and reheat

The approach used to compute the work and the efficiency of reheat cycles is the same as that used in the example problem for the simple Rankine cycle. One calculates the work produced in each turbine separately and the required pumping work. Heat is added to the fluid at two different stages of the cycle and is given by the difference in enthalpy between states 3 and 2 and states 4 and 3A. Wet steam at point 4 is removed after the high-pressure turbine stage, reheated at constant pressure to a superheated state, and admitted to the low-pressure turbine stage. Superheated steam at point 3A is expanded to the design exhaust pressure at point 4A.

The net work performed by this cycle is given by Eq. (77):

$$w_{\text{cycle}} = w_{1-2} + w_{3-4} + w_{3A-4A} = (h_1 - h_2) + (h_3 - h_4) + (h_{3A} - h_{4A}). \quad (77)$$

The heat supplied to this system is given by Eq. (78):

$$q_{\text{in}} = (h_3 - h_2) + (h_{3A} - h_4). \quad (78)$$

The thermal efficiency of this cycle is given by Eq. (79):

$$\eta_{\text{Reheat}} = \frac{(h_1 - h_2) + (h_3 - h_4) + (h_{3A} - h_{4A})}{(h_3 - h_2) + (h_{3A} - h_4)}. \quad (79)$$

6.2.6.3 Regeneration cycle

In theory, modifications to the cycle can be made to reduce cycle irreversibility. One of the principal sources is the sensible heat addition required to bring the boiler feedwater up to saturation temperature. This is accomplished by using some of the flow through the turbine to heat the feedwater. To achieve reversibility, a possible setup is shown in Figure 47, where internal heat from the turbine is used to heat the feedwater in process 2-2A [LEU2004, POP2013]. This cycle could provide the same thermal efficiency as the Carnot cycle. However, this is not a practical modification because it is impossible to design a turbine to serve as both a power-production device and a heat exchanger. Modifications have, however, been designed to make this design change more practical, one of which is presented in the next section.

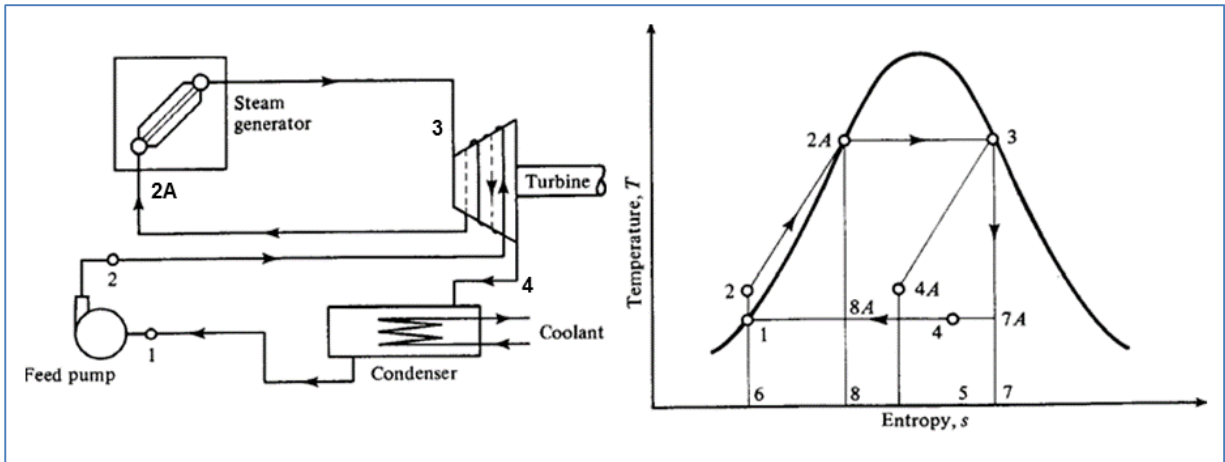


Figure 47 Rankine cycle with regeneration circuit

6.2.6.4 Rankine cycle with feedwater heaters

This improvement is based on the regeneration principle, which was briefly covered in the previous section. This improvement is based on extracting a small amount of steam at an intermediate pressure from the turbine and using it to heat feedwater.

Two types of feedwater heaters exist in practice:

- Open type, in which direct contact between extracted steam and feedwater is achieved, resulting in good heat transfer; and
- Closed type, in which only thermal contact between extracted steam and feedwater is achieved.

For both types, the reheating is usually designed in several stages. The following sections cover both these types in detail.

6.2.6.5 Rankine cycle with open feedwater heater

Figure 48 shows the Rankine cycle with one open feedwater heater (the left side shows the loop and the right side the T - s diagram of the cycle) [LEU2004, POP2013].

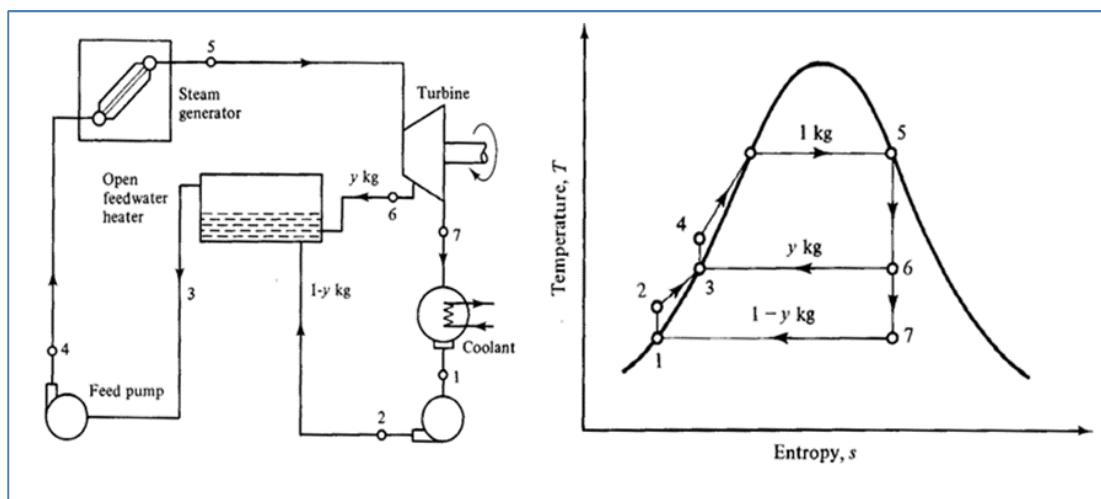


Figure 48 Rankine cycle with open feedwater reheating

The extraction fraction of steam is calculated from an energy balance on the feedwater heater using Eq. (80):

$$\dot{m}(1-y)h_2 + \dot{m} y h_6 = \dot{m} [y + (1-y)]h_3,$$

$$(1-y)h_2 + y h_6 = h_3. \tag{80}$$

The pump work is obtained by summing the work from both pumps, as given by Eq. (81):

$$w_{pump} = w_{1-2}(1-y) + w_{3-4}. \tag{81}$$

The turbine work is obtained by summing up the two parts of the turbine expansion, one with the full steam flow, and one with the $(1-y)$ portion of the steam flow, as in Eq. (82):

$$w_{turbine} = w_{5-6} + (1-y)w_{6-7}. \tag{82}$$

The heat supplied to the cycle is not affected by the heater and is given by Eq. (83):

$$q_{4-5} = h_5 - h_4. \tag{83}$$

Usually, operating NPPs have multiple stages of feedwater heating; an example of a plant with two open feedwater heaters is shown in Figure 49.

Using the heat balance at both heaters, one can obtain the enthalpies downstream from the mixing points Z and Y, as shown in Eqs. (84) and (85):

$$h_4 = \frac{\dot{m}_{1''}h_{1''} + \dot{m}_4h_4}{\dot{m}_{1''} + \dot{m}_4} = \frac{\dot{m}_{1''}h_{1''} + \dot{m}_4h_4}{\dot{m}_1 - \dot{m}_1}, \tag{84}$$

$$h_5 = \frac{\dot{m}_1h_1 + (\dot{m}_1 - \dot{m}_1)h_5}{\dot{m}_1}. \tag{85}$$

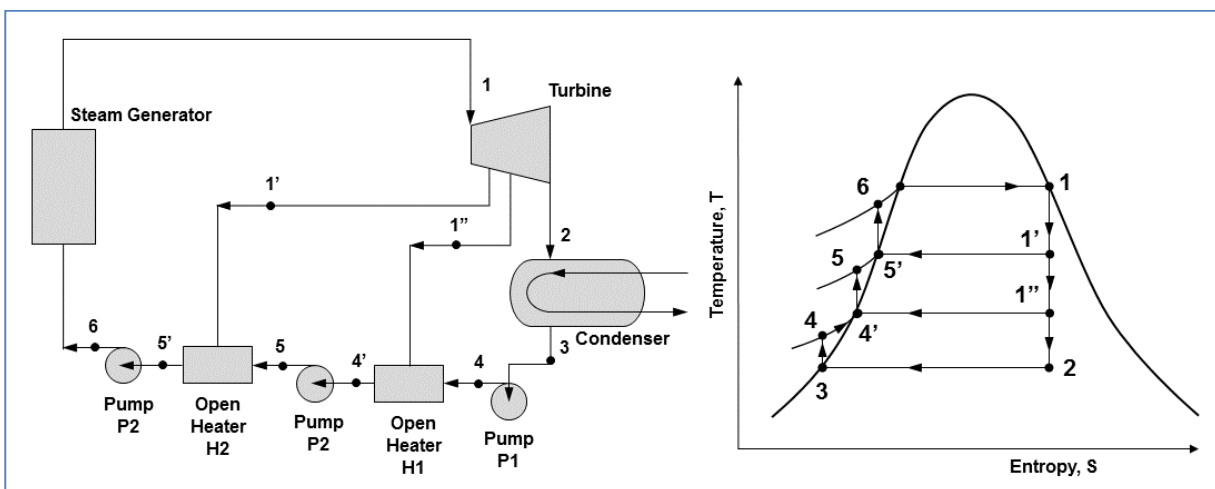


Figure 49 Rankine cycle with multiple open reheaters

The turbine work in this case is obtained by summing up the work at the three parts before and after the steam extractions, as shown in Eq. (86):

$$w_T = \dot{m}_1 (h_1 - h_{1'}) + (\dot{m}_1 - \dot{m}_{1'}) (h_{1'} - h_{1''}) + \dot{m}_2 (h_{1''} - h_2). \quad (86)$$

6.2.6.6 Rankine cycle with closed feedwater heater

Figure 50 shows the Rankine cycle with one closed feedwater heater (the left side shows the loop and the right side the T - s diagram of the cycle) [LEU2004, POP2013].

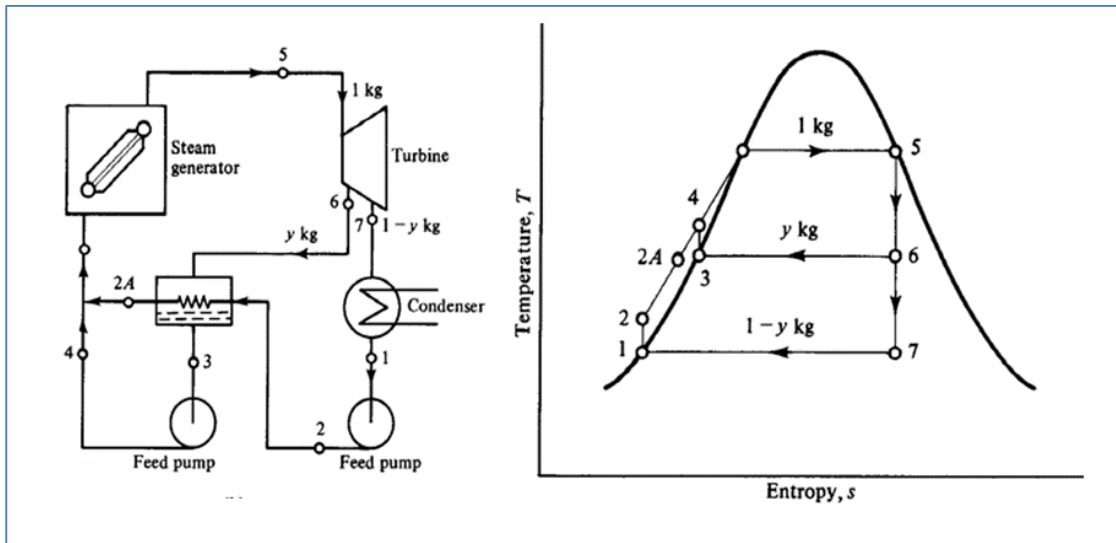


Figure 50 Rankine cycle with closed feedwater reheat

The extraction fraction of steam is calculated from an energy balance on the feedwater heater using Eq. (87):

$$(1-y)h_2 + y h_6 = (1-y) h_{2A} + y h_3. \quad (87)$$

The pump work is obtained by summing the work from both pumps, as given by Eq. (88):

$$w_{pump} = w_{1-2} (1-y) + w_{3-4}. \quad (88)$$

The turbine work is obtained by summing up the two parts of the turbine expansion, one with the full steam flow, and one with the $(1-y)$ portion of the steam flow, as in Eq. (89):

$$w_{turbine} = w_{5-6} + (1-y) w_{6-7}. \quad (89)$$

The heat supplied to the cycle is not affected by the heater and is given by Eq. (90):

$$q_{in} = (h_5 - h_{2A}) (1-y) + (h_5 - h_4) y. \quad (90)$$

Usually, operating NPPs have multiple stages of feedwater heating; an example of a plant with two closed feedwater heaters is shown in Figure 51 [POP2013].

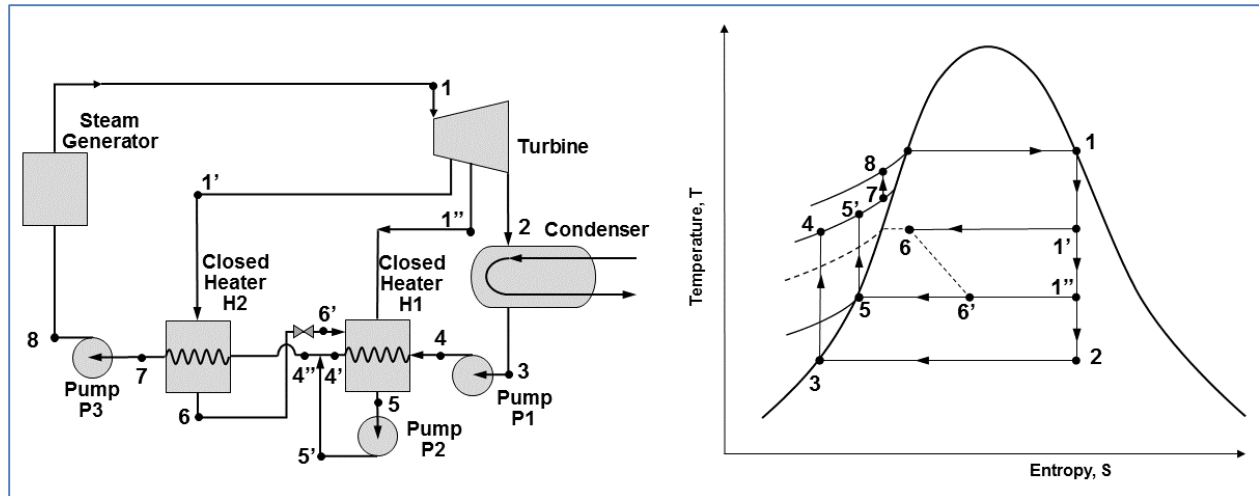


Figure 51 Rankine cycle with multiple closed reheaters

Using the heat balance at both heaters, one can obtain the enthalpies downstream from the exit points 1 and 2, as shown in Eqs. (91), (92), and (93):

$$h_4 = \frac{\dot{m}_1 h_1 + \dot{m}_4 h_4 + \dot{m}_1 h_6 - (\dot{m}_1 - \dot{m}_1) h_5}{\dot{m}_1}, \tag{91}$$

$$h_{4''} = \frac{\dot{m}_4 h_4 + (\dot{m}_1 + \dot{m}_1) h_5}{\dot{m}_1}, \tag{92}$$

$$h_7 = \frac{\dot{m}_1 (h_1 - h_6) + \dot{m}_1 h_4}{\dot{m}_1}. \tag{93}$$

6.2.6.7 Thermal efficiency moisture separation

The role of the moisture separator between the high-pressure and low-pressure turbines in the cycle is two-fold:

- to provide feedwater heating, thus improving cycle thermal efficiency; and
- to remove moisture from the steam, enabling dry steam to enter the low-pressure turbine (thus reducing water droplet erosion of the turbine blades).

Figure 52 shows an example of a moisture separator where, using the principle of the open heater, the extracted moisture from the separator is mixed with the feedwater, thus transferring the latent heat of condensation to the feedwater [POP2013].

By defining the parameters at certain points in the T - s diagram, $h_{1''} = h_f$ (at p_1) and $(1-x_1)\dot{m}_1$ and $h_{1''} = h_g$ (at p_1) and $x_1\dot{m}_1$, and by performing an energy balance at the separator, one can obtain the enthalpy after the mixing point using Eq. (94):

$$h_5 = \frac{h_{1''} x_1 \dot{m}_1 + h_4 x_1 (\dot{m}_1 - \dot{m}_1)}{\dot{m}_1}. \tag{94}$$

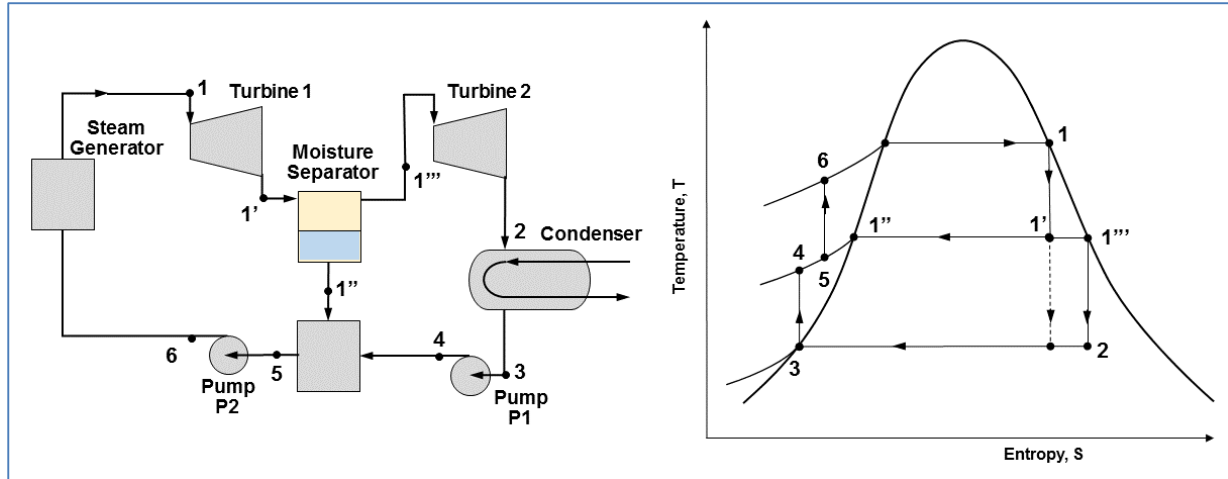


Figure 52 Rankine cycle with dryer

6.2.6.8 Actual Rankine cycle

The real Rankine cycle is not reversible because of various losses that occur in nature and that must be accounted for. Figure 53 shows the real Rankine cycle and the impact of various losses [TOD2011]. The left figure shows the pump losses, the middle figure shows the losses in the steam lines to the turbine, and the right figure shows the losses in the turbine. Some of these losses are listed below:

- Irreversible frictional losses at various places in the turbo machinery;
- Irreversible heat losses from various piping, vessels, etc.;
- Pump losses, in particular:
 - Heat loss to the surroundings;
 - Fluid friction with the pump blades;
 - Mechanical losses due to friction (bearings, gears, etc.);
- Turbine losses, in particular:
 - Pressure drop between the superheater and turbine, which reduces entrance pressure from P_1 to P_2 ;
 - Heat loss to the surroundings, which reduces the temperature change from point b to point c;
 - Steam expansion inside the turbine, which is irreversibly adiabatic (non-isentropic) and hence reduces efficiency and increases steam quality;
 - Mechanical friction; and
 - Steam bypass outside the turbine blade passages.

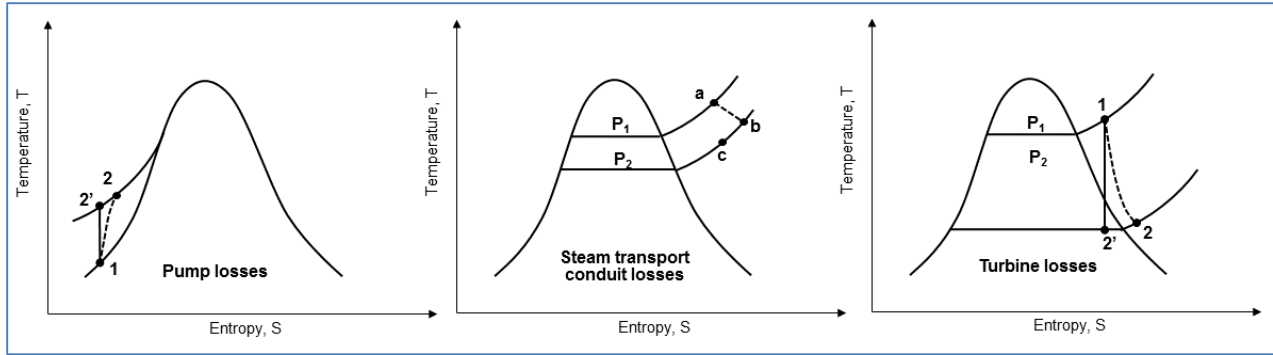


Figure 53 Real Rankine cycle with losses

6.2.6.9 Sample PWR and CANDU 6 cycle diagrams

Figure 54 shows a typical secondary side of an advanced PWR reactor [APR2011]. It is clear that multiple feedwater heaters, one moisture separator, and double reheaters have been designed into the system. The secondary system operates with two feedwater pumps at two different pressures.

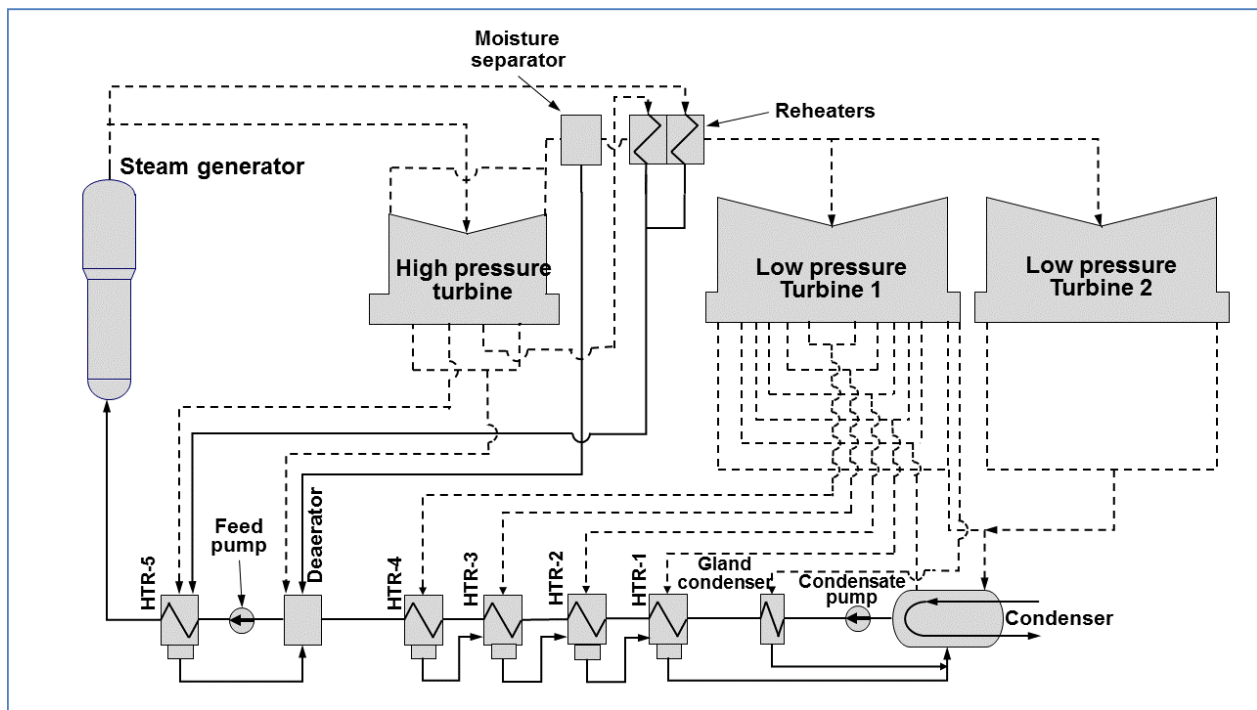


Figure 54 Typical advanced PWR secondary cooling system

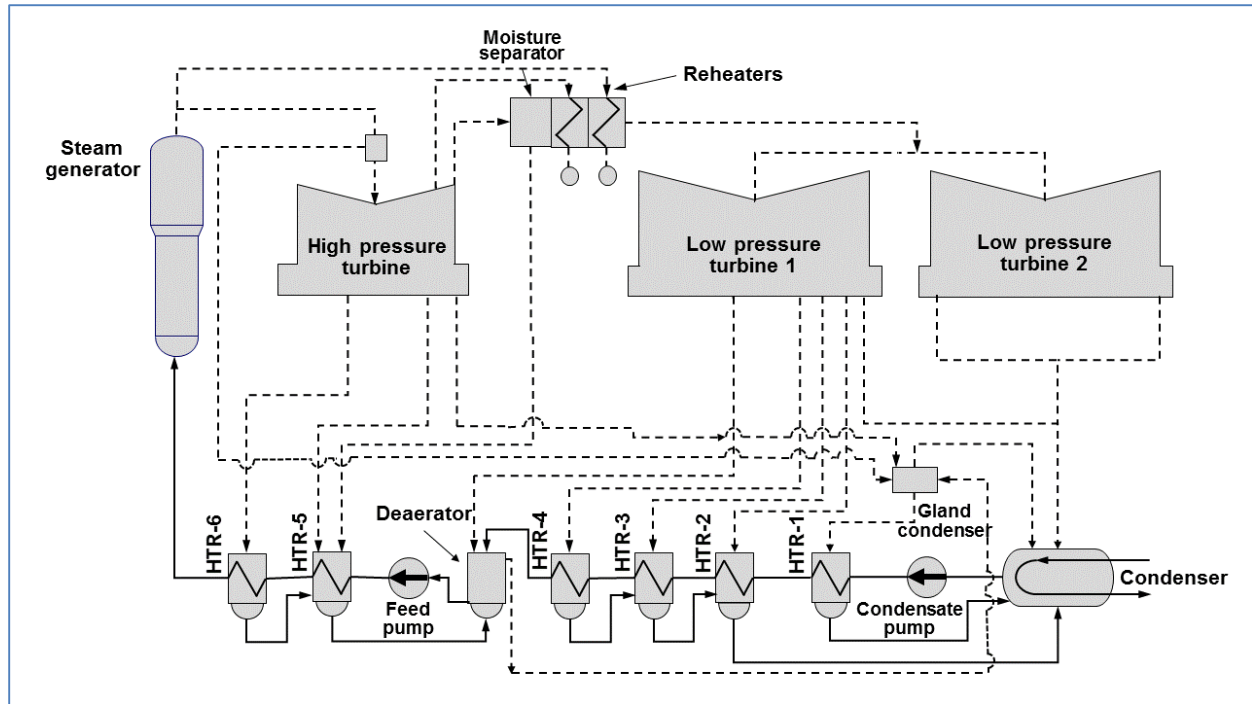


Figure 55 Typical CANDU 6 secondary cooling system

Figure 55 shows a typical CANDU 6 Rankine cycle [AECL2010]. This plant has one double-sided high-pressure turbine and two double-sided low-pressure turbines. On the low-pressure turbine, there is one open feedwater heater and three consecutive closed feedwater heaters. On the high-pressure turbine, there are two closed feedwater heaters. Between the high-pressure and low-pressure turbines, several stages of moisture separators deliver heating to the feedwater heaters. The thermal efficiency of such an arrangement is around 35%.

6.2.7 Entropy and the laws of thermodynamics

Entropy is a state parameter and can be expressed in terms of other parameters. For sub-cooled or superheated conditions, $s=f(P,T)$, and for saturated conditions, $s=f(P)$ or $s=f(T)$, it is expressed in terms of pressure or temperature. In the two-phase region, the following equation can be used to calculate mixture entropy (under homogeneous conditions):

$$s_m = x \cdot s_g + (1-x) \cdot s_f = s_f + x \cdot s_{fg}, \quad (95)$$

where s_g is the entropy of the saturated gas, s_f is the entropy of the saturated liquid, and s_{fg} is the entropy change during vaporization.

Entropy is a quantitative measure of the microscopic (molecular) disorder of a system. Entropy generated through any process in an isolated system cannot be negative. Moreover, entropy is a non-conserved property (it always increases in isolated systems). In engineering processes, entropy increase is a measure of irreversibility in these processes (a measure of engineering system inefficiency or of system losses).

Entropy change is closely associated with heat transfer. In heat transfer from a hotter to a

colder subsystem, the hotter subsystem exhibits a decrease in entropy, whereas the cold system shows an increase. However, the increase in the cold subsystem is greater, thus making the entropy change of the combined system positive.

Probably the most important outcome of the entropy changes in certain processes is the fact that every process ends up with a certain penalty for moving energy in any direction. In other words, any energy exchange between different systems results in an entropy increase, i.e., there is always a certain cost when moving energy from one place to another, or transferring energy from one form to another. Any conversion of energy in a system from one form to another or any exchange of work with its surroundings must be accompanied by some irreversible dissipation of energy to the surroundings.

Entropy can be seen as the ability to expend energy to carry out a task. For example, a fully charged battery has low entropy, which increases as the battery is used; or a clockwork toy has low entropy when wound up, which increases as it unwinds.

Processes in nature change in the direction of reaching equilibrium. Entropy reaches a maximum value when equilibrium is reached. Entropy is statistical in nature because it explains how phenomena in the micro world affect phenomena in the macro world, capturing the probability of a number of micro events to cause a macro effect.

In modern thermodynamics, the laws of thermodynamics are known as:

- First law – characterizes the energy balance;
- Second law – characterizes cycle/system efficiency;
- Third law – characterizes entropy at near-zero temperatures; and
- Zeroth law – characterizes thermodynamic equilibrium.

The zeroth law of thermodynamics states that if two bodies are in thermodynamic equilibrium (at the same temperature) with a third body, then they are in thermodynamic equilibrium with each other. This is a fundamental law that defines the relationship between different systems (bodies) operating and interacting with each other. This law should have been labelled as the first law, but because it was defined later, it was called the zeroth law to avoid confusion.

The first law of thermodynamics states that the change of internal energy in a system is equal to the amount of heat supplied, minus the amount of work performed by the system on its surroundings. In other words, it states that energy can be converted from one form to another, but cannot be created or destroyed, i.e., everything requires energy to do anything. Different forms of energy must be fed into a system before it can perform any useful work or create any impact on its surroundings.

The second law of thermodynamics states that the entropy of an isolated system never decreases because isolated systems spontaneously evolve toward thermodynamic equilibrium, i.e., the state of maximum entropy. Moreover, it states that a certain cost must always be paid when moving energy from one place to another or transferring energy from one form to another. When it appears that a system's entropy decreases, this generally means that the system is not isolated from its surroundings and that by scaling up to a larger system, it will be

found that the system is a part of a larger system with lower entropy.

The third law of thermodynamics states that the entropy of a perfect crystal drops to zero when the temperature of the crystal is at absolute zero. However, according to quantum theory, because nothing can be considered to be truly at rest, every molecule, atom, or subatomic particle will always have a minimum amount of energy even when cooled to absolute zero (the zero point energy). Hence, one may take the third law as stating the minimum entropy level at a temperature of absolute zero.

6.2.8 Problems

1. Calculate the Rankine cycle thermal efficiency which operates at saturated steam at pressure of 7 MPa, and temperature in the condenser is 30°C. Calculate the steam quality at the exit of an ideal turbine following an adiabatic expansion to condenser pressure for the above conditions, and for the conditions if the turbine has 85% efficiency. Compare the results with the Carnot cycle.
2. A steam generator in a PWR nuclear power plant produces 3200 t/h saturated steam at pressure of 5 MPa. The temperature in the condenser is 35°C. Calculate the ideal turbine power assuming that it operates in Rankine cycle, and the steam quality at the turbine exit.
3. In a Rankine cycle the working fluid enters the turbine at 4.5 MPa with condenser temperature of 35°C. Calculate the thermal efficiency of this cycle assuming that:
 - a. no preheaters are used;
 - b. one preheater is used to preheat the feed water to 60°C below the saturation temperature; and
 - c. the feed water is preheated in 3 preheaters to the same temperature as above.

Given:

- a. Turbine inlet pressure, $P_i=4.5$ MPa
- b. Condenser temperature $T_c=35$ °C or 308 °K
- c. Feedwater heater outlet temperature, $T_F=T_{sat}-60$ °C

Assumptions

- a. The Rankine cycle described in the problem statement is for a CANDU 6 reactor
- b. Steam entering the turbine is saturated
- c. Losses in the turbine and pumping losses are the same in all cases, since it is the difference in efficiency that is important here assume these losses are negligible.
4. Consider an emergency water tank that is supposed to deliver water to a reactor following a loss of coolant event. The tank is pressurized by the presence of nitrogen at 1.0 MPa. The water is discharged through a 0.2 m ID pipe. The reservoir has a diameter of 5 m, and the water level is 15 m above the reactor. Calculate the maximum flow rate delivered to the reactor if the water is inviscid and reactor pressure is (a) 0.8 MPa, and (b) 0.2 MPa.
5. Two alternative steam cycles are proposed for a nuclear power plant, as variation of the Rankine ideal cycle, all three operating between the steam temperature of 293°C and condensing temperature of 33°C. The first one operates with condensate in saturated conditions, while the feedwater downstream of the condensate pumps is subcooled.

The steam is saturated at the inlet of the expander. (a) Assuming ideal machinery, calculate the cycle thermal efficiency and steam rate for each cycle.

6. Water at 100 kPa and 20 °C flows through a smooth, circular pipe of 2 cm ID, and length of 3 m. If the flow velocity is 3 m/s, calculate the pressure drop along the pipe and the pumping power necessary to maintain the flow in the pipe.
7. Explain the 1st and 2nd law of thermodynamics and the relationship between these laws. Provide examples of their application in reactor thermal-hydraulics design. Explain the role of entropy in reactor thermal-hydraulics.
8. Develop an expression for thermal efficiency for a secondary heat transport system shown in Figure 55 (CANDU-typical). Show the thermal efficiency in a generic expression by using generic values of key parameters and by making appropriate assumptions.

7 Heat Transfer and Fluid Flow Design

7.1 Heat transfer in the primary heat transfer system

The heat balance in the primary heat transport system is covered in this section, including heat balance in the reactor core and heat balance in a steam generator. An interpretation of the relationship between the primary and secondary loop parameters is provided, and the role of the steam generator as a connection between the primary and secondary loops is explained. Approximations in the steam generator heat transfer model are used to derive trends for various parameters that affect the steam generator design. Analytical and numerical models are developed and used to calculate the distribution of key parameters along the primary and secondary sides of the generator, and the steam generator heat duty diagram is developed and explained.

Figure 56 shows a simplified diagram of the reactor primary heat transport system. The reactor is the heat source, because it is in the reactor that heat is generated. The steam generator is the heat sink, which takes the heat out of the primary heat transport system and transfers it to the secondary heat transport system. The primary pump serves as the driver of the flow in the primary heat transport system by removing heat from the heat source (the reactor) and dumping it into the heat sink (the steam generator).

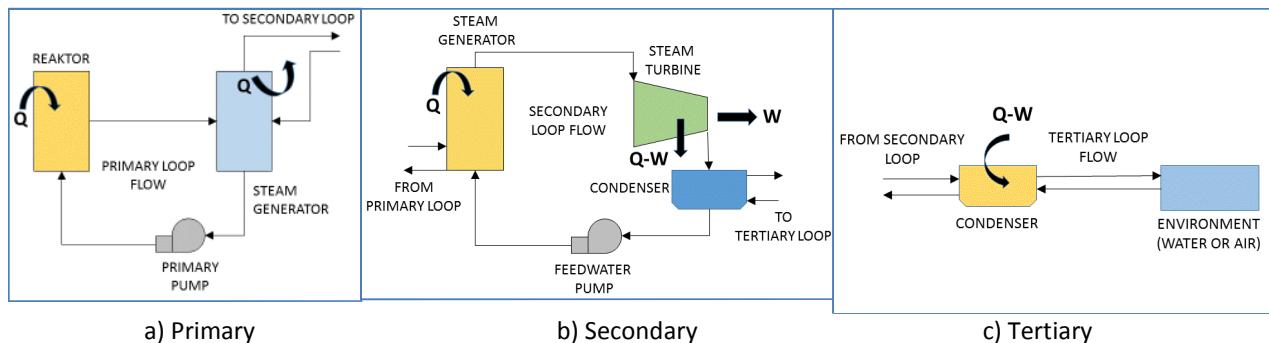


Figure 56 Reactor cooling systems

The heat balance in the reactor can be described by a simple algebraic equation, Eq. (96), from which the reactor heat production can be expressed by Eq. (97):

$$W_p h_{p,hot} = W_p h_{p,cold} + Q, \quad (96)$$

$$Q = W_p (h_{p,hot} - h_{p,cold}), \quad (97)$$

where: W_p = primary coolant mass flow rate (kg/s)
 $h_{p,hot}$ = core exit enthalpy (hot leg), (kJ/kg)
 $h_{p,cold}$ = core inlet enthalpy (cold leg) (kJ/kg)
 Q = reactor power transferred to the coolant (kJ/s or kW).

7.2 Primary pumps

The primary pumps are the vital component in the reactor heat transport system (HTS). The primary function of the reactor HTS is to provide continuous heat removal from the reactor core in normal operation, during transients, and during reactor shutdown, and the primary pumps are the essential components that support this function. HTS pump start-up and shut-down are routine operations of the reactor HTS. Pump failures due to loss of power or inadvertent operator action are relatively common events in all nuclear power plants and are considered in the safety case for each reactor type.

The primary side flow is determined by a balance between the head generated by the primary heat transport system pumps (HTS pumps) and the circuit pressure losses due to friction, losses, and other effects.

Figure 57 shows the pressure drop in the loop as a function of mass flow rate in the loop. The pump operating point is indicated at the intersection between the pump head curve and the system flow resistance curve. The system pressure drop curve follows a quadratic law because it depends on the square of the flow velocity, i.e., the square of the mass flow rate (or mass flux), as in Eq. (43). The pump head curve may have various shapes depending on the pump type and design. For “short periods” of time, in transition to the stable operating point, the pump and the system can temporarily operate outside the stable operating point. In this respect, a “short period” of time should be considered in relation to the pump and system hydraulic inertia.

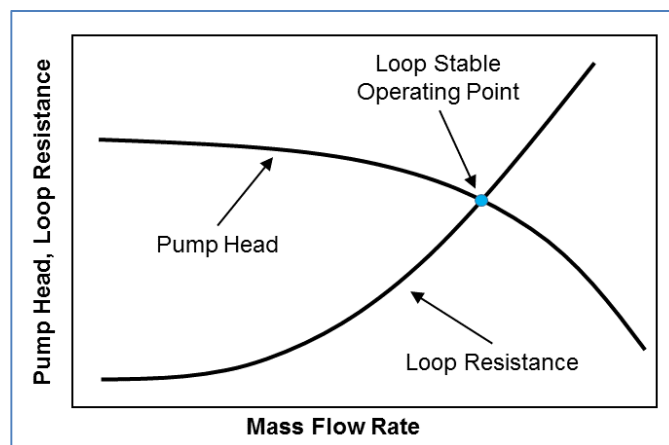


Figure 57 Primary pump flow diagram

Accurate prediction of pump performance includes specification of its head (H), torque (τ), discharge or volumetric flow rate (Q), and rotor speed (ω). The pump motor, by exerting a torque on the rotating shaft, provides energy to the impeller, which creates the flow associated with a head increase from the pump suction to the pump discharge side.

The pump motor provides torque for:

- overcoming frictional resistance and any local losses in the loop (piping, valves, core, etc.);

- overcoming frictional losses in the pump rotating parts;
- acceleration of fluid in the loop; and
- acceleration of pump rotating parts (including the flywheels).

For a pump, only two parameters can be considered independent among H , Q , τ , and ω . The other two are determined from the pump characteristics. It is commonly assumed that the pump steady-state characteristics also hold for transient conditions. The pump characteristics are described by specific relationships, called homologous relationships) [TOD1990]:

$$\frac{H_1}{\omega_1^2} = \frac{H_2}{\omega_2^2}, \quad \frac{Q_1}{\omega_1} = \frac{Q_2}{\omega_2}, \quad \frac{H_1}{Q_1^2} = \frac{H_2}{Q_2^2}. \quad (98)$$

Pump manufacturers produce realistic relationships from pump tests, for example, relating the head to both volumetric flow and pump angular velocity, as given by Eq. (99):

$$\frac{H_1}{\omega^2} = a_1 + a_2 \left(\frac{Q}{\omega} \right) + a_3 \left(\frac{Q}{\omega} \right)^2. \quad (99)$$

The common approach is to use non-dimensional parameters with respect to the rated pump performance conditions (rated conditions refer to the rated quantities, which represent the point of pump best performance as defined by the manufacturer), as given by Eq. (100):

$$v = \frac{Q}{Q_R}, \quad h = \frac{H}{H_R}, \quad \alpha = \frac{\omega}{\omega_R}, \quad \beta = \frac{\tau}{\tau_R}. \quad (100)$$

These non-dimensional parameters are used to express homologous pump relationships in a form similar to Eq. (98), in which the actual parameters are expressed in their non-dimensional forms. Homologous relationships of these forms are used in computer programs describing pump behaviour.

Figure 58 shows the four possible types, i.e., quadrants, of pump operation. Computer models must be able to simulate pump performance in any of the four quadrants, and therefore pump manufacturers must provide information about pump operation in all quadrants [TOD1990]. During a coast-down transient, the pump may pass from the normal pumping region, quadrant I, through the reverse flow but positive rotation region, quadrant II, to reverse flow and rotation, quadrant III, unless the rotor is equipped with an anti-reverse ratchet to avoid this quadrant (such as in most reactor HTS pumps).

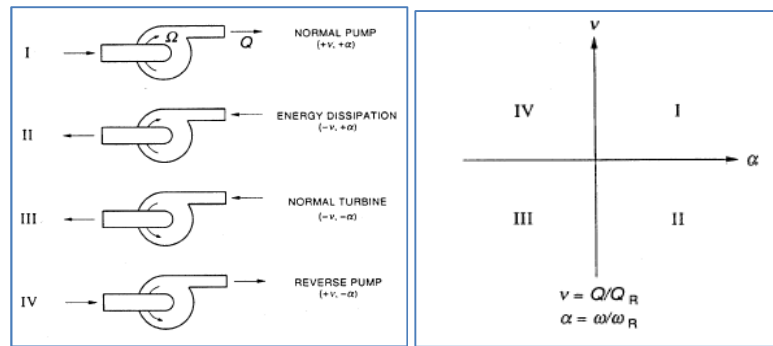


Figure 58 Primary pump operating quadrants

In postulated events with breaks at the pump suction or discharge side and different pump operation control logic, a pump can operate in any of the first three quadrants. Therefore, pump tests are performed to develop pump homologous relationships for all four possible operating quadrants.

Pump characteristics under transient flow conditions have been investigated and tested. One of the most important conditions that must be avoided in operation of reactor HTS pumps is two-phase flow in the bubbly flow regime. Pump characteristics deteriorate significantly following initiation of bubble formation in the pump suction. Moreover, prolonged operation in two-phase flow (the bubbly flow regime) can damage the pump impeller blades.

One of the most important objectives of HTS flow design is to make sure that the pump suction pressure does not fall below the net positive suction head required (NPSHR) [POP2014]. For a pump to deliver its rated output, the absolute pressure (including the velocity head $V^2/2g$) of the fluid at the pump inlet must exceed the vapour pressure by an amount sufficient to overcome any entrance or frictional losses between the point of entry into the pump and the impeller. The NPSH is defined as the absolute pressure at the pump inlet expressed in metres of liquid, plus the velocity head, minus the vapour pressure of the fluid at pumping temperature, and corrected to the elevation of the pump centreline in the case of horizontal pumps, or to the entrance of the first-stage impeller for vertical pumps.

NPSHR (required) is determined by the pump manufacturer and is defined as a function of pump speed and pump capacity. NPSHA (available) represents the energy level of the fluid over the vapour pressure at the pump inlet and is determined entirely by the system preceding the pump. Unless $NPSHA \geq NPSHR$ under any operating condition, some of the fluid will vaporize in the pump inlet, and vapour bubbles will be carried onto the impeller. These bubbles will collapse violently at some point downstream of the pump inlet (usually at some point on the pump impeller blade surface) as the pressure is increased in the pump, producing very sharp, crackling noises accompanied by physical damage to the pump impeller surface. This phenomenon is known as *cavitation* and is highly undesirable (in fact, it represents a micro water hammer effect on the impeller surface). The net mechanical effect of cavitation is pump vibration and impeller damage, whereas the net effect on pump performance is loss of pump efficiency and pump head.

The primary side flow is determined by a balance between the head generated by the primary

pumps and the circuit head losses due to friction:

$$\Delta P_{pump} = \Delta P_{circuit} \quad (101)$$

Normally, the pump head curve is provided in the form of a polynomial such as Eq. (102):

$$\Delta P_{pump} = A_0 + A_1 \cdot W + A_2 \cdot W^2 + \dots \quad (102)$$

The hydraulic network losses are proportional to the square of the velocity, i.e., the mass flow rate, along with a loss coefficient, as shown by Eq. (103):

$$\Delta P_{circuit} = K \cdot W^2 \quad (103)$$

Figure 59 and Figure 60 show the pump curves of two pumps in the CANDU HTS; the first is the primary HTS pump, and the second is the shutdown cooling pump.

These pumps have very different functions. The HTS primary pump operates almost continuously during the operating lifetime of the plant, and therefore the requirements on this pump are very demanding. The shutdown pump operates normally when the reactor is shut down to help remove decay heat from the reactor core. Both diagrams show pump volumetric flow rate on the x-axis, pump head on the left y-axis, and pump efficiency, pump power, and NPSHR on the right y-axis.

Figure 59 and Figure 60 show that pump head declines with increasing volumetric flow, whereas pump power increases [POP2014]. This means that because of momentum balance considerations, if a pump is required to produce higher volumetric flow, its head will be lower. Note that for a pump delivering higher volumetric flow, the pump power must increase. Dotted lines in Figure 59, labelled S1, S2, and S3, show three possible system configurations that impose different flow resistance.

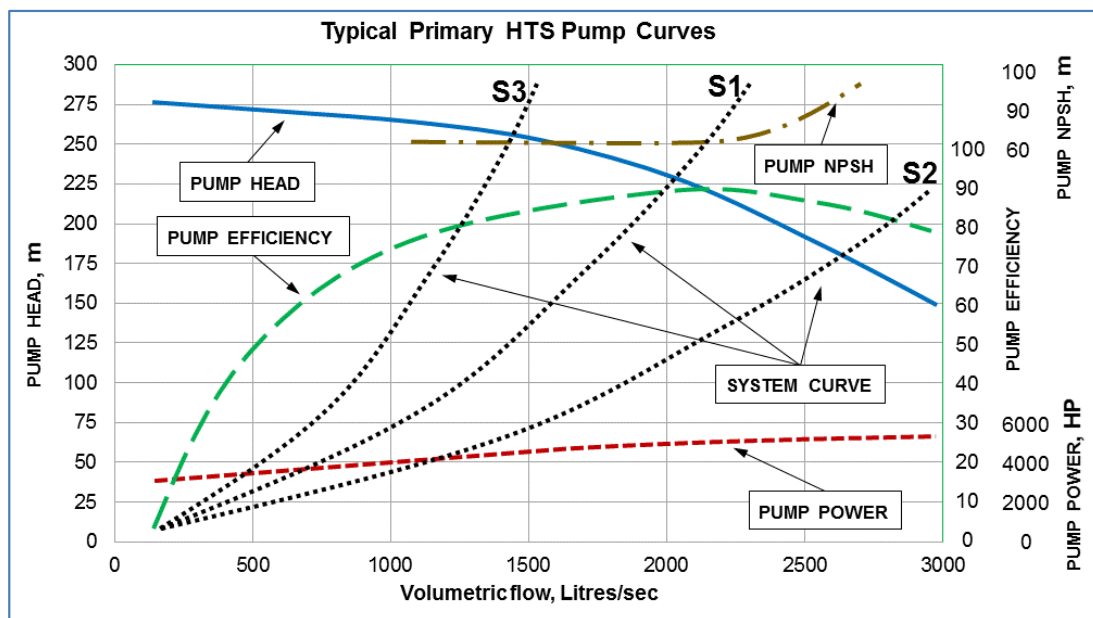


Figure 59 Typical primary pump characteristics

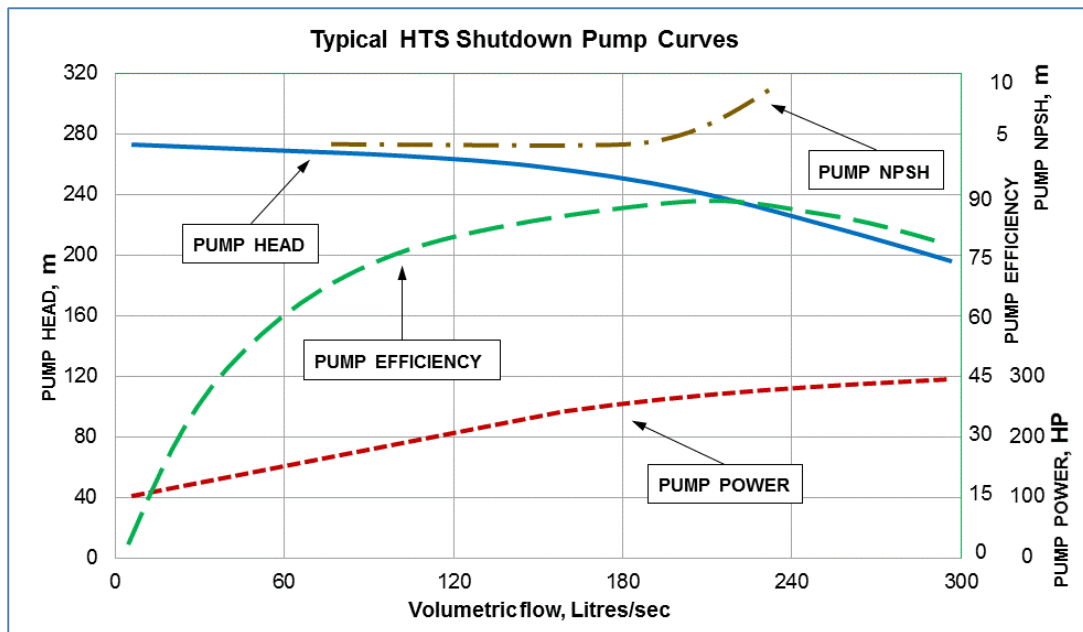


Figure 60 Typical shutdown pump characteristics

The efficiency curve is usually bell-shaped, and it shows that the highest efficiency is achieved in a relatively narrow range of volumetric flow rate. Pump efficiency is very important for the HTS pump because it operates continually over 60 years of plant life, and therefore a small loss of efficiency can result in a relatively large loss of plant earned value. Efficiency drops very sharply if the pump volumetric flow rate moves outside a narrow range.

The NPSHR curve is relatively flat over a wide range of volumetric flow rates. In fact, well-designed pumps should have NPSHR curves as flat as can possibly be obtained. However, when the volumetric flow rate exceeds a certain value, the NPSHR curve starts to increase fast, creating an area of pump cavitation risk.

7.3 Steam generator heat balance

The steam generator has a very important role in energy transport from the reactor core to the turbine and the electrical generator because it connects the primary and secondary loops. Hence, understanding steam generator behaviour is important in understanding plant behaviour.

A simplified steam generator heat balance is shown in Figure 61. The feedwater flow W_{FW} enters the steam generator with enthalpy h_{FW} and exits with enthalpy h_{SAT} . The primary mass flow rate in the reactor is W_p .

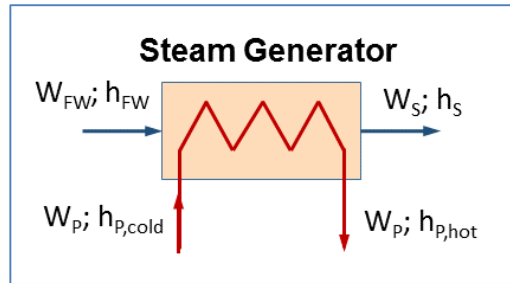


Figure 61 Reactor steam generator loop

The heat transfer from the primary to the secondary steam generator side is expressed by Eq. (104):

$$dQ = U_{SG} \cdot (T_p - T_s) \cdot dA, \quad (104)$$

where U_{SG} is the overall (global) heat transfer coefficient ($\text{kJ/m}^2\text{-}^\circ\text{C}$),

A is the heat transfer area in the steam generator (m^2),

T_p is the primary-side temperature ($^\circ\text{C}$), and

T_s is the secondary-side temperature ($^\circ\text{C}$).

The total heat transfer in the steam generator can be obtained by integrating the above equation over the length of the steam generator tubes and is given by Eq. (105):

$$Q = \int_Q dQ = \int U_{SG} \cdot (T_p - T_s) \cdot dA. \quad (105)$$

Figure 62 shows a general heat-duty diagram for a steam generator with a pre-heater and with saturated primary coolant entering the steam generator U-tubes (i.e., with a certain percentage of quality). The y-axis indicates fluid temperatures, and the x-axis provides a conceptual representation of space in the steam generator. In this diagram, no heat losses or pressure losses are shown (i.e., an ideal steam generator is assumed).

The primary coolant moves through the U-tubes from right to left in the diagram, starting as saturated with a certain percentage of quality and becoming sub-cooled as it transfers the heat to the secondary side. The secondary coolant (feedwater) enters sub-cooled (zero mass quality, i.e., negative thermodynamic quality) and, as it receives heat from the primary side, heats up to saturation. Thereafter, the secondary coolant boils off as it receives more heat through the steam generator. Note that the point at the primary coolant temperature where the secondary coolant temperature reaches saturation is called the “pinch point” [GAR1999, POP2014].

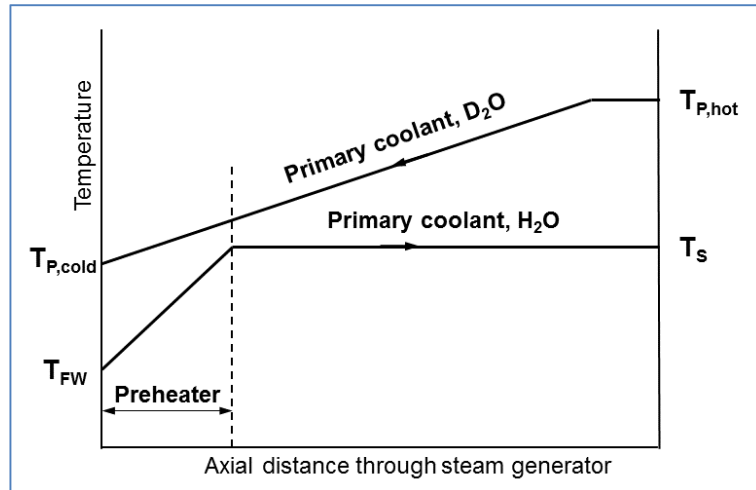


Figure 62 Steam generator simplified heat duty diagram

From the above discussion, it is clear that sufficiently good heat transfer is required to achieve acceptable steam pressure. The steam generator calculation of U-tube length, diameter, and number (i.e., the area used in heat transfer) is carefully performed so that heat transfer from the primary to the secondary side is achieved efficiently with as little heat loss as possible, and so that the economic constraints of manufacturing the steam generator and the system can be satisfied.

7.3.1 Steam generator without a pre-heater region

To achieve a better understanding of the behaviour and design of the steam generator and the impact of its various parameters, it is useful to analyze first a simplified version of the steam generator with no pre-heater, with saturated feedwater entering the steam generator, and with sub-cooled primary coolant entering the steam generator. This simplified steam generator is shown in Figure 63 [GAR1999].

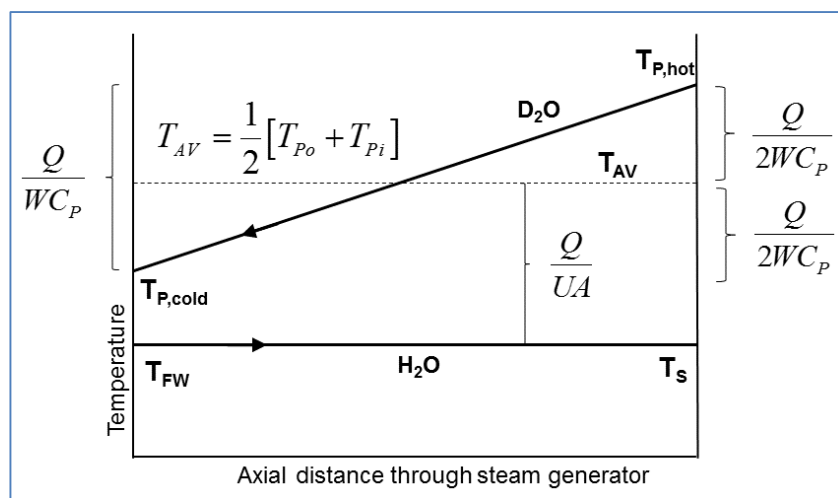


Figure 63 Steam generator heat duty diagram without pre-heating

The primary-side heat balance in the steam generator can be obtained by integrating Eq. (105).

Assuming that the global heat transfer coefficient U_{SG} is constant along the steam generator, the primary coolant temperature variation is linear along the U-tube, and by separating primary and secondary side terms, one obtains Eq.(106):

$$Q = U_{SG} A_{SG} \frac{(T_{p,hot} + T_{p,cold})}{2} - U_{SG} A_{SG} T_s. \quad (106)$$

Equation (106) can be further simplified into Eq. (107):

$$Q = U_{SG} A_{SG} \left[\frac{T_{p,hot} + T_{p,cold}}{2} - T_s \right]. \quad (107)$$

The temperatures can be replaced by enthalpies using Eq. (108):

$$h \approx C_p \cdot T + constant. \quad (108)$$

Using Eqs. (108) and (107), the heat transferred in the steam generator can be given by Eq. (109):

$$Q = \frac{U_{SG} A_{SG}}{C_p} \left[\frac{h_{p,hot} + h_{p,cold}}{2} - h_s \right]. \quad (109)$$

Using Eq. (96) we find:

$$Q = \frac{U_{SG} A_{SG}}{C_p} \left[\frac{h_{p,hot} + h_{p,cold}}{2} - h_s \right] = W_p \cdot (h_{p,hot} - h_{p,cold}). \quad (110)$$

The secondary side steam flow can be calculated by an energy balance on the secondary side of the steam generator, as given by Eq. (110); using this equation, one can calculate the mass flow rate at the secondary side, as given by Eq. (111):

$$Q = W_s (h_s - h_{FW}), \quad (111)$$

$$W_s = \frac{Q}{(h_s - h_{FW})}. \quad (112)$$

7.3.2 Approximate solution to steam generator without a pre-heater region

Combining Eqs. (97), (101), (110), and (112) yields the set of four equations describing the heat transfer in the primary and secondary loops, as shown by Eq. (113) [GAR1999, POP2014]:

$$\begin{aligned} Q &= W_p (h_{p,hot} - h_{p,cold}) \\ Q &= \frac{U_{SG} A_{SG}}{C_p} \left[\frac{h_{p,hot} + h_{p,cold}}{2} - h_s \right] = U_{SG} A_{SG} \left[\frac{T_{p,hot} - T_{p,cold}}{2} - T_s \right]. \\ \Delta P_{pump} &= \Delta P_{circuit} \\ Q &= W_s (h_s - h_{FW}) \end{aligned} \quad (113)$$

From the first equation in Eq. (113), one can obtain the reactor outlet (hot) enthalpy:

$$h_{p,hot} = \frac{Q}{W_p} + h_{p,cold} \quad (114)$$

The second equation in Eq. (113) can be transformed into the following equation by dividing it by the primary mass flow rate and using Eq. (114), while also neglecting heat losses between the reactor and the steam generator:

$$\frac{Q}{W_p} = \frac{U_{SG} A_{SG}}{C_p W_p} \left[\frac{Q}{2W_p} + h_{p,cold} - h_s \right] = \frac{U_{SG} A_{SG}}{W_p} \left[\frac{Q}{2C_p W_p} + T_{p,cold} - T_s \right] \quad (115)$$

Rearranging Eq. (115) in terms of outlet enthalpy at the steam generator and outlet temperature, one can obtain Eq. (116) and Eq. (117):

$$h_{p,cold} = \frac{Q}{W_p} \left[\frac{C_p W_p}{U_{SG} A_{SG}} - \frac{1}{2} \right] + h_s = \frac{QC_p}{U_{SG} A_{SG}} - \frac{Q}{2W_p} + h_s \quad (116)$$

$$T_{p,cold} = \frac{Q}{W_p} \left[\frac{W_p}{U_{SG} A_{SG}} - \frac{1}{2C_p} \right] + T_s \quad (117)$$

From Eqs. (116) and (117), all the parameters Q , W_p , C_p , A_{SG} , U_{SG} , etc., are positive quantities. Therefore, the reactor inlet enthalpy (and temperature) will rise as the primary flow rate increases, will rise as the secondary-side temperature (saturation temperature) and enthalpy increase, and may go up or down as power changes.

Substituting Eq. (116) into Eq. (117),

$$Q = \frac{U_{SG} A_{SG}}{C_p} \left[\frac{h_{p,hot} + h_{p,cold}}{2} - h_s \right] = U_{SG} A_{SG} \left[\frac{T_{p,hot} - T_{p,cold}}{2} - T_s \right] \quad (118)$$

The enthalpy (and temperature) at the steam generator primary side inlet can be obtained as follows:

$$h_{p,hot} = \frac{Q}{W_p} \left[\frac{C_p W_p}{U_{SG} A_{SG}} + \frac{1}{2} \right] + h_s = \frac{QC_p}{U_{SG} A_{SG}} + \frac{Q}{2W_p} + h_s \quad (119)$$

$$T_{p,hot} = \frac{Q}{W_p} \left[\frac{W_p}{U_{SG} A_{SG}} + \frac{1}{2C_p} \right] + T_s \quad (120)$$

Using Eqs. (116), (117), (119), and (120), one can obtain the following useful relationships [GAR1999, POP2014]:

$$h_{p,aver} = \frac{h_{p,hot} + h_{p,cold}}{2} = \frac{Q}{W_p} \left(\frac{C_p W_p}{U_{SG} A_{SG}} \right) + h_s = \left(\frac{QC_p}{U_{SG} A_{SG}} \right) + h_s \quad (121)$$

$$T_{p,hot} - T_{p,aver} = \frac{Q}{W_p} \left(\frac{W_p}{U_{SG} A_{SG}} + \frac{1}{2C_p} \right) + T_s - \frac{Q}{W_p} \frac{W_p}{U_{SG} A_{SG}} - T_s = \frac{Q}{2W_p C_p} \quad (122)$$

$$T_{p,aver} = \frac{T_{p,hot} + T_{p,cold}}{2} \quad T_{p,aver} - T_{p,cold} = \frac{Q}{2C_p W_p} \quad T_{p,aver} - T_s = \frac{Q}{U_{SG} A_{SG}}, \quad (123)$$

$$T_{p,hot} - T_{p,cold} = \frac{Q}{W_p C_p} \quad T_{p,hot} - T_s = \frac{Q}{U_{SG} A_{SG}} + \frac{Q}{2W_p C_p} \quad T_{p,cold} - T_s = \frac{Q}{U_{SG} A_{SG}} - \frac{Q}{2W_p C_p}. \quad (124)$$

7.3.3 Calculation of main HTS parameters

From an HTS designer perspective, the key question is how to design the primary heat transport system. As long as the primary flow rate, or the reactor inlet and outlet enthalpies, have not yet been defined, it is necessary to make an assumption about one of these to be able to calculate the other parameters when the desired reactor power is given.

Given a rough estimate of flow for calculating U_{SG} (which is not a strong function of flow because W_p is large and flow is turbulent), T_{aver} can be calculated, as well as an estimate of the spread of $T_{p,aver}$ ($\pm Q/2W_p C_p$). This gives a good first estimate of temperatures and enthalpies. With the above enthalpy, temperature, and density estimates, the circuit losses can be calculated and compared with available pump head and flow. The flow estimate can be updated and the whole procedure repeated until convergence is reached.

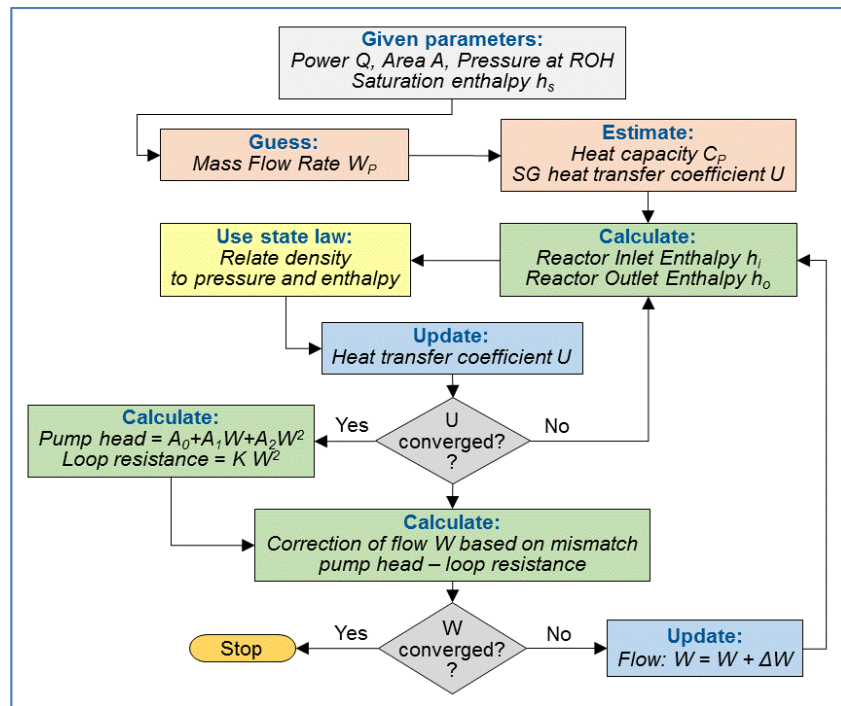


Figure 64 Process for calculating primary loop parameters

Figure 64 illustrates the process used to calculate the primary heat transport system parameters [GAR1999, POP2014]. Note that first the reactor power, the steam generator, and the outlet header pressure and saturation enthalpy are defined. Then the primary flow rate is assumed. This makes it possible to define the steam generator global heat transfer coefficient and the primary fluid heat capacity. Then using Eqs. (116) and (119), the reactor inlet and

outlet enthalpies can be calculated. Once these are defined, the next step is to define other primary fluid state parameters from the state laws, such as the fluid density for the inlet and outlet reactor enthalpy. After these parameters are defined, it is necessary to check whether the assumed U_{SG} has converged. If not, U_{SG} is updated, and another round of these calculations is performed.

After convergence on U_{SG} is reached, the pump head and primary loop resistance can be calculated because the primary flow rate has been defined. The last step is to check whether the pump head and the loop resistance match. If not, then the whole process shown in Figure 64 must be repeated.

Problem 7.3.3.1

To illustrate that this process leads to convergence, a sample calculation will be performed using typical CANDU 6 parameters as given by Eq. (125) [GAR1999, POP2014].

$$\begin{aligned}
 Q &\approx 2000 [MW_{th}] \\
 W &\approx 8000 [kg / s] \\
 T_s &\approx 265 [^{\circ}C] \Rightarrow h_s \approx 1150 [kJ / kg] \\
 C_p &\approx 5 [kJ / kg - ^{\circ}C] \\
 U_{SG} &\approx 5 [kJ / s - ^{\circ}C - m^2] \Rightarrow (C_p W_p / U_{SG} A_{SG}) \approx 0.625 \\
 A_{SG} &\approx 3200 [m^2]
 \end{aligned} \tag{125}$$

Equation (116) can be expressed in terms of primary flow rate, as shown by Eq. (123):

$$W_p = \frac{Q}{2 \left[\frac{C_p Q}{U_{SG} A_{SG}} + h_s - h_{p,cold} \right]} \tag{126}$$

From the above equation, one can define the infinitesimal change in the primary flow rate with the reactor inlet enthalpy as follows:

$$\frac{\delta W_p}{\delta h_{p,cold}} = \frac{Q}{2 \left[\frac{C_p Q}{U_{SG} A_{SG}} + h_s - h_{p,cold} \right]^2} = \frac{Q}{2 \left[\frac{Q}{2W_p} \right]^2} = \frac{2W_p^2}{Q} \tag{127}$$

Substituting the parameters for CANDU 6 from Eq. (125) into Eq. (127),

$$\frac{\delta W_p}{\delta h_{p,cold}} = \frac{2 \left(8000 \left[\frac{kg}{s} \right] \right)^2}{2 \cdot 10^6 \left[kW \equiv \frac{kJ}{s} \right]} = 64 \left[\frac{kg^2}{kJ \cdot s} \right] \tag{128}$$

If Eq. (128) is expressed in terms of the initial values of primary flow rate and reactor inlet enthalpy, the result gives the change in the primary flow rate as a function of reactor inlet

enthalpy with respect to the initial value (a guessed value):

$$\frac{\delta \left(\frac{W_p}{W_{p,o}} \right)}{\delta \left(\frac{h_{p,cold}}{h_{p,cold,o}} \right)} = \frac{\delta W_p}{\delta h_{p,cold}} \cdot \frac{h_{p,cold,o}}{W_{p,o}} = 64 \cdot \frac{1181 \cdot 25}{8000} \cong 9.0. \quad (129)$$

Therefore, the change in primary flow rate will be nine times the change in reactor inlet enthalpy:

$$\delta \left(\frac{W_p}{W_{p,o}} \right) = 9.0 \cdot \delta \left(\frac{h_{p,cold}}{h_{p,cold,o}} \right). \quad (130)$$

Hence, if we were to guess the reactor inlet enthalpy, and our guess were only 25% wrong, the primary flow rate would be in error by about 225%. This indicates that the process involving assuming reactor inlet enthalpy first is inherently divergent. However, if we were to guess the primary flow rate, and if we were in error by about 25%, the calculated reactor inlet enthalpy would be in error by only 2.8%. Therefore, this process is inherently convergent. This confirms that the process for primary heat transport system design shown in Figure 64 is appropriate.

End of Problem 7.3.3.1.

7.3.4 Steam generator with pre-heater (simplified analytical solution)

Figure 65 shows a simplified heat-duty diagram for a steam generator with a pre-heater for a fully sub-cooled primary side [GAR1999, POP2014]. This figure shows that the secondary-side temperature changes from T_{FW} to T_s (i.e., from feedwater to saturation temperature). The steam generator design may include a section that is targeted to perform feedwater pre-heating, or it may not have a specific section. Whatever the design, steam generator pre-heating will always be relevant because the feedwater enters the steam generator in a sub-cooled state and needs to be heated up to saturation before the steam generator can boil it and generate steam.

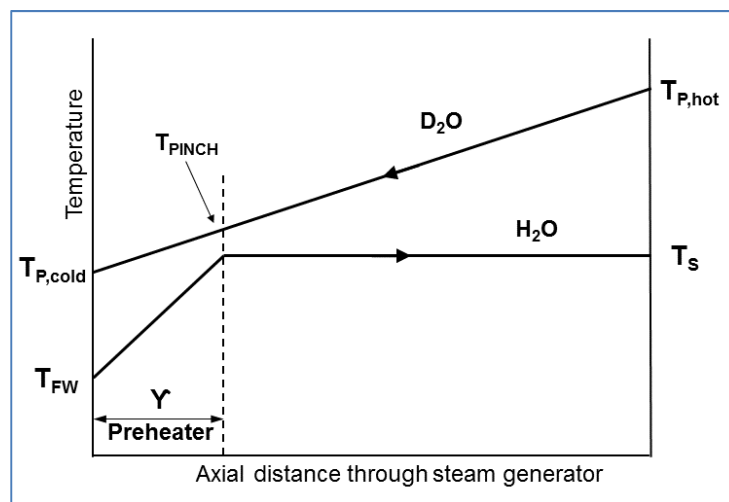


Figure 65 Steam generator heat duty diagram with pre-heating

The reactor heat balance equation is given by:

$$Q = W_p C_p (T_{p,hot} - T_{p,cold}), \quad (131)$$

where Q is reactor power (or steam generator power), C_p is D₂O heat capacity (assumed constant), $T_{p,hot}$ is ROH temperature, and $T_{p,cold}$ is RIH temperature.

The elementary amount of heat transferred from the primary to the secondary side of the steam generator can be captured using the Fourier law:

$$dQ = U_{SG} (T_p - T_s) dA_{SG}, \quad (132)$$

where U_{SG} is the overall heat transfer coefficient through the SG piping, dA_{SG} is the incremental heat transfer area from the primary to the secondary side, T_p is the D₂O temperature in the SG tubes, and T_s is the H₂O temperature in the SG shell.

As shown in Figure 65, the secondary side of the steam generator can be split into two parts, the pre-heater part and the boiler part. Therefore, the heat transferred from the primary to the secondary side can also be divided into two parts, as shown in Eq. (133):

$$Q = Q_{PREHEATER} + Q_{BOILER}. \quad (133)$$

The fraction of the steam generator area involved in pre-heating is indicated by γ . The pre-heater part of the steam generator brings the feedwater to saturation. The primary-side temperature at which the secondary side is brought to saturation is denoted as T_{PINCH} .

Using Eq. (113), the total heat exchanged between the primary and secondary sides in the steam generator can be shown by means of the following relation [GAR1999, POP2014]:

$$Q = \gamma U_{SG} A_{SG} \left[\frac{T_{p,cold} + T_{PINCH}}{2} - \frac{T_s + T_{FW}}{2} \right] + (1 - \gamma) U_{SG} A_{SG} \left[\frac{T_{p,hot} + T_{PINCH}}{2} - T_s \right], \quad (134)$$

where T_s is the saturation temperature at the secondary side and T_{FW} is the feedwater temperature at the inlet of the steam generator secondary side.

The pinch temperature can be expressed in terms of steam generator parameters using Eq. (124):

$$T_{PINCH} = T_{p,cold} + \gamma (T_{p,hot} - T_{p,cold}) = T_{p,cold} + \gamma \frac{Q}{C_p W_p}. \quad (135)$$

By substituting Eq. (135) into Eq. (134), one can obtain the heat transfer in the steam generator as expressed by the following equation:

$$Q = U_{SG} A_{SG} \left[\left(\frac{T_{p,hot} + T_{p,cold}}{2} \right) - T_s + \frac{\gamma}{2} (T_s - T_{FW}) \right]. \quad (136)$$

Recall the relationship between the reactor inlet and outlet temperature from Eq. (124):

$$T_{p,hot} = \frac{Q}{W_p C_p} + T_{p,cold} \quad (137)$$

The reactor inlet and outlet temperatures can be expressed by the following relationship:

$$T_{p,cold} = \frac{Q}{W_p C_p} \left[\frac{W_p C_p}{U_{SG} A_{SG}} - \frac{1}{2} \right] - \frac{\gamma}{2} (T_s - T_{FW}) + T_s, \quad (138)$$

$$T_{p,hot} = \frac{Q}{W_p C_p} \left[\frac{W_p C_p}{U_{SG} A_{SG}} + \frac{1}{2} \right] - \frac{\gamma}{2} (T_s - T_{FW}) + T_s. \quad (139)$$

By examining Eq. (138), one can evaluate the impact of reactor power on the variation of reactor inlet temperature. The saturation temperature T_s at the secondary side does not depend on reactor power if the pressure on the secondary side is kept constant. The variation in feedwater temperature, T_{FW} , can be assumed to be linearly dependent on reactor power. The primary flow rate W_p , the heat capacity C_p , the area of the steam generator A_{SG} , and the steam generator global heat transfer coefficient U_{SG} exhibit second-order variation with reactor power Q .

To define the dependence of reactor inlet temperature on reactor power, it is necessary to evaluate the impact of the remaining parameter, i.e., the steam generator pre-heater area γ , on reactor power.

The heat addition to the secondary side of the steam generator in the pre-heater area can be calculated as:

$$Q_{PREHEATER} = W_s C_{p,s} (T_s - T_{FW}). \quad (140)$$

The heat extraction from the primary side of the steam generator can be calculated from Eq. (134) as follows:

$$Q_{PREHEATER} = \gamma U_{SG} A_{SG} \left[\left(\frac{T_{p,cold} + T_{PINCH}}{2} \right) - \left(\frac{T_s - T_{FW}}{2} \right) \right]. \quad (141)$$

Combining Eqs. (140) and (141) leads to the following expression for the steam generator pinch area [GAR1999, POP2014]:

$$\gamma = \frac{W_s C_{p,s} (T_s - T_{FW})}{U_{SG} A_{SG} \left[\frac{(T_{p,cold} + T_{PINCH})}{2} - \frac{(T_s - T_{FW})}{2} \right]}. \quad (142)$$

The most strongly variable parameter in Eq. (142) is the feedwater flow W_{FW} . The heat balance on the secondary side given by Eq. (140) can be rearranged in terms of enthalpies as follows:

$$Q = W_s h_s - W_{FW} h_{FW}. \quad (143)$$

Because $W_s \approx W_{FW}$, it is appropriate to assume that $h_s \approx \text{constant}$ and $h_{FW} \approx \text{constant}$.

Therefore, feedwater flow and steam generator pre-heater area are proportional to reactor power, i.e., $W_{FW} \propto Q$ and $\gamma \propto Q$.

It is normally desirable to describe the pre-heater area in terms of a ratio between the pre-heater area at 100% power and at current power, as follows:

$$\gamma = \frac{\gamma_{100} Q}{Q_{100}}, \quad (144)$$

where γ_{100} is the pre-heating fraction at 100% full power and $Q_{100} = Q$ at 100% full power.

By substituting Eq. (144) into Eqs. (138) and (139), the reactor inlet and outlet temperatures can be obtained as follows:

$$\begin{aligned} T_{p,cold} &= \frac{Q}{W_p C_p} \left[\frac{W_p C_p}{U_{SG} A_{SG}} - \frac{1}{2} \right] - \frac{\gamma_{100} Q}{2Q_{100}} [T_s - T_{FW}] + T_s \\ &= \frac{Q}{Q_{100}} \left[\frac{Q_{100}}{W_p C_p} \left(\frac{W_p C_p}{U_{SG} A_{SG}} - \frac{1}{2} \right) - \frac{\gamma_{100}}{2} (T_s - T_{FW}) \right] + T_s, \end{aligned} \quad (145)$$

$$T_{p,hot} = \frac{Q}{Q_{100}} \left[\frac{Q_{100}}{W_p C_p} \left(\frac{W_p C_p}{U_{SG} A_{SG}} + \frac{1}{2} \right) - \frac{\gamma_{100}}{2} (T_s - T_{FW}) \right] + T_s. \quad (146)$$

It is clear that the reactor inlet and outlet temperatures are equal to the steam saturation temperature with corrections to capture the primary-side and secondary-side effects. Both these effects are roughly proportional to reactor power. Hence, at 0% full reactor power, $T_{p,cold} = T_s$ and $T_{p,hot} = T_s$.

Problem 7.3.4.1

To illustrate the above analysis and the magnitude of the correction terms, a sample CANDU 6 assessment can be performed with the following given parameters:

- Reactor power $Q_{100} = 2.064 \times 10^6$ [kJ/s]
- Steam generator global heat transfer coefficient: $U_{SG} = 4.5$ [kJ/sec °C m²]
- Steam generator area: $A_{SG} = 3200$ [m²] per steam generator (12,800 [m²] total for a four-loop reactor)
- Primary flow rate: $W_p = 8250$ [kg/s]
- Heat capacity of primary loop: $C_p = 4.25$ [kJ/kg °C]
- Steam generator pre-heating portion: $\gamma_{100} = 0.15$ at 100% full power
- Feedwater temperature: $T_{FW} = 177$ [°C] at 100% full power
- Secondary-side temperature (at saturation): $T_s = 260$ [°C]

Using the above parameters, the reactor inlet temperature can be calculated using Eq. (145):

$$T_{p,cold} = \frac{Q}{Q_{100}} [58.86(0.60 - 0.50) - 6.22] + 260 = \frac{Q}{Q_{100}} [6.32 - 6.22] + 260. \quad (147)$$

Hence, even at 100% full power, the net correction to the reactor inlet temperature $T_{p,cold}$ is less than 0.1°C. Even allowing for large variations in U_{SG} and other parameters, the effect on $T_{p,cold}$ is expected to be small over the full power range. This has been confirmed by detailed calculations. The reactor outlet temperature can be calculated using Eq. (146):

$$T_{p,hot} = \frac{Q}{Q_{100}} [64.75 - 6.22] + 260 = \frac{Q}{Q_{100}} (58.53) + 260. \quad (148)$$

At 100% full power, the reactor outlet temperature T_o is 318.5 [°C], which is greater than the saturation temperature of 310 [°C] at 10 [MPa]. Hence, the assumption of no boiling at the reactor outlet header is not correct. Therefore, the calculation must be repeated with an estimate of the amount of boiling using the following expression:

$$Q = Q_{subcool} + Q_{boil} = W_p C_p \left[(T_{p,sat} - T_{p,cold}) + \frac{x h_{fg}}{C_p} \right] = W_p C_p (T_{p,sat} - T_{p,cold}) + W_p x h_{fg}. \quad (149)$$

The power level at which boiling starts is given by Eq. (146), into which the CANDU 6 parameters from Eq. (148) are introduced to obtain the following expression:

$$\frac{T_{p,hot} - 260}{58.53} = \frac{310 - 260}{53.53} = \frac{Q}{Q_{100}} = \frac{50}{53.53} = 0.854. \quad (150)$$

This means that boiling starts in a CANDU 6 core when the reactor power is at 85.4% of full power. In other words, it means that out of 100% reactor power, 85.4% is used to heat the primary fluid to saturation and 14.6% is used to boil some of the primary fluid.

If this information is used in Eq. (149), the following expression can be obtained for the reactor power split in the primary heat transport system:

$$\frac{Q}{Q_{100}} = \frac{Q_{subcool}}{Q_{100}} + \frac{Q_{boil}}{Q_{100}} = \frac{W_p C_p}{Q_{100}} [T_{p,sat} - T_{p,cold}] + \frac{W_p x h_{fg}}{Q_{100}} = 0.854 + 0.146. \quad (151)$$

Hence, using just the boiling part of Eq. (151), the steam quality at the reactor outlet header can be calculated as follows:

$$x = \frac{0.146 Q_{100}}{W_p h_{fg}} = \frac{0.146 \cdot 2.064 \cdot 10^6 [kJ / s]}{8250 [kg / s] \cdot 800 [kJ / kg]} = 0.045. \quad (152)$$

In the above calculation of the steam quality in the reactor outlet header as 4.5%, it was assumed that the value of 85.4% of the total reactor power to onset of boiling as calculated by Eq. (152) remains valid as the power goes up beyond the onset of boiling. Hence, it follows that the parameters that determine the onset of boiling, W_p , C_p , U_{SG} , A_{SG} , T_s , and T_{FW} , have been assumed not to change significantly when boiling starts in the primary heat transport system. This is only approximately true: W_p and U_{SG} are affected by the presence of two-phase flow. However, the approximation used in the above calculation is good enough to illustrate the point.

End of Problem 7.3.4.1

Enough information is now available to sketch out the heat duty diagram as a function of power. Figure 66 presents the impact of reactor power on the heat-duty diagram of the steam generator [GAR1999, POP2014].

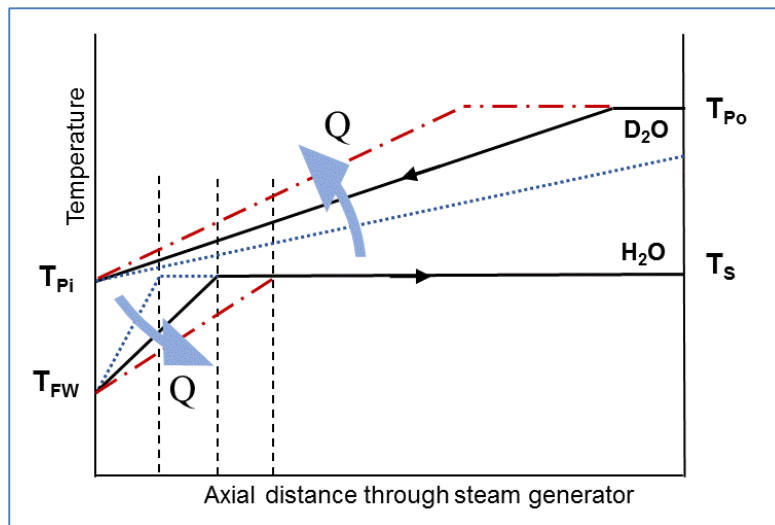


Figure 66 Reactor power versus heat-duty diagram of the SG

It is clear from the figure that the increase of reactor power impacts the primary side in such a way that the primary fluid temperature curve becomes steeper, eventually reaching saturation and starting to boil. The higher the reactor power, the greater will be the quantity of the primary fluid that will be converted to steam, and the higher will be the quality of the primary coolant in the reactor outlet header.

The reactor power also affects the secondary side. The lower the reactor power, the larger will be the pre-heater part of the steam generator, i.e., more of the steam generator heat transfer area will be engaged in pre-heating feedwater, and less will be available to boil the secondary fluid.

7.3.5 Steam generator with pre-heater (numerical solution)

Consider the steam generator to be a counter-current heat exchanger, with the simplified heat-duty diagram shown in Figure 67. For any small segment dz of the heat exchanger, according to the figure, the heat transferred from the primary to the secondary side can be calculated using the Fourier law:

$$dQ = U_{SG} (T_p - T_s) dA_{SG}. \quad (153)$$

The primary and secondary temperatures will vary with position in the steam generator. Energy balance on the primary and secondary sides gives the following expressions:

$$dQ = -W_p dh_p, \quad (154)$$

$$dQ = W_s dh_s. \quad (155)$$

The minus sign indicates a heat flow from the primary to the secondary side, i.e., the enthalpy of the primary fluid decreases, and the enthalpy of the secondary fluid increases.

For a single phase on either side, one can relate enthalpy with temperature as follows: $dh=C_p \cdot dT$.

Therefore, the change in fluid temperatures along the steam generator primary and secondary sides can be expressed as:

$$dT_p = -\frac{U_{SG} dA_{SG} (T_p - T_s)}{C_{p,p} W_p}, \quad (156)$$

$$dT_s = \frac{U_{SG} dA_{SG} (T_p - T_s)}{C_{p,s} W_s}. \quad (157)$$

The steam generator area can be conveniently divided into N segments, each described as $\Delta A_{SG}=A_{SG}/N$. The numerical algorithm for calculating the fluid temperatures simply starts at one end of the heat exchanger with known or assumed temperatures and flows at that boundary and repeatedly applies Eqs. (156) and (157) as it moves forward to the other end of the heat exchanger. The principle of the calculation is shown in Figure 68. If the calculations start at the cold end (where feedwater enters and primary fluid exits), single-phase flow on both sides can be ensured.

At each successive nodal point, the fluid temperatures can be calculated by the following expressions [GAR1999, POP2014]:

$$T_{p,i+1} = T_{p,i} + \frac{U_{SG} A_{SG}}{C_{p,p} N W_p} (T_{p,i} - T_{s,i}), \quad (158)$$

$$T_{s,i+1} = T_{s,i} + \frac{U_{SG} A_{SG}}{C_{p,s} N W_s} (T_{p,i} - T_{s,i}). \quad (159)$$

At each nodal point i , the calculated temperature should be compared to the saturation point. Once the saturation temperature is reached, the secondary-side temperature remains at the saturation temperature.

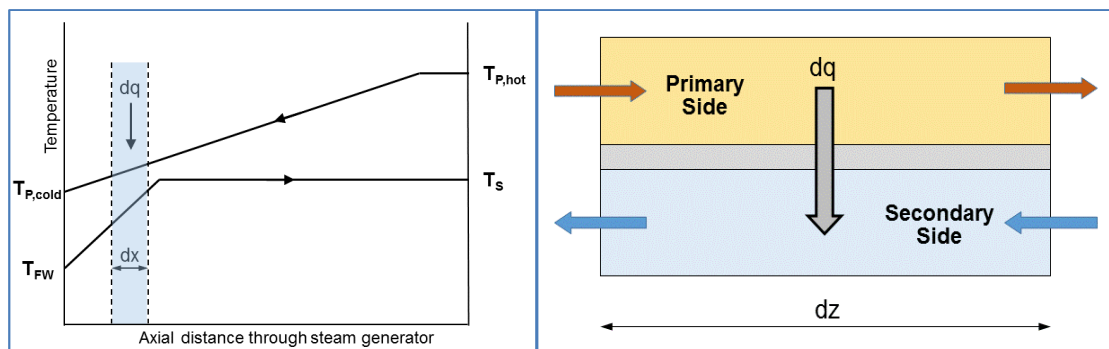


Figure 67 Steam generator numerical calculation concept

Figure 68 Nodalization concept for steam generator numerical calculation

The result is the temperature profiles for both the primary and secondary sides for the given flow rates, area, heat transfer coefficient, and cold side temperatures. Equation (153) is used to accumulate the total heat transferred by the heat exchanger. If the heat transferred is above or below the desired heat transfer, then iteration is required. Typically, it is desirable to know the primary-side temperature profile for a given set of secondary-side conditions, given the primary-side flow and a given steam generator geometry and heat transfer coefficient. In this case, the primary side inlet temperature is varied until the target Q is met; once again, the primary side “floats” on the secondary side.

The effect of power is seen through W_s , which is proportional to Q . For low Q , T_s will rise rapidly to the saturation temperature. This decreases the effective temperature difference between the primary and secondary sides. Hence, T_p will not rise as quickly as in the high-power case.

7.3.6 Problems

1. Explain the difference in the design of steam generators that have an area designed for preheating of feed water and these that do not. Explain how feed water heating is achieved in both types of design. Explain the role of the pinch point in both types of design.
2. Using the values provided in Problem 7.3.4.1, draw a heat duty diagram of a corresponding steam generator following the format provided in Figure 66.
3. Explain the process for calculating main parameters of the primary heat transport system.
4. Using the values provided in Problem 7.3.4.1, and using the steam generator heat balance template equations, calculate analytically the steam generator parameters. Determine the effect of steam generator fouling on the steam generator performance. Determine the effect of power level on the steam generator performance.
5. Using the values provided in Problem 7.3.4.1, and using the steam generator heat balance equations use numerical technique to calculate steam generator parameters. Determine the effect of steam generator fouling on the steam generator performance. Determine the effect of power level on the steam generator performance. Determine the impact of the numerical calculation increments on the precision of the calculations.

7.4 Heat transfer in the fuel elements

Heat transfer in the fuel, cladding, and coolant is very important from the perspective of adequate thermal design of the reactor core. The most important objective of the thermal designer is to ensure that the heat generated in the reactor at any reactor state is continuously removed from the core within adequate thermal margins.

This section describes the calculation of temperature profiles in the radial and axial directions in the fuel, cladding, and coolant. It also discusses the key parameters and their influence on primary heat transport system design. Note that coolant mixing within the bundle geometry is beyond the scope of this text.

7.4.1 General heat conduction equation

The interface between the fuel and the coolant is centrally important to reactor design because it limits the heat flux that can be removed from the fuel to the coolant, thus limiting the reactor power output.

For a solid body, the general thermal energy balance equation can be written as follows [BIR1960, TOD2011]:

$$\iiint_V \frac{\partial(\rho \cdot e)}{\partial t} dV = \iiint_V q'''(\vec{r}, t) dV - \iint_S \vec{q}''(\vec{r}, t) \hat{n} dS, \quad (160)$$

where ρ is the material density, e is the internal energy, V is the volume, S is the surface area, q''' is the volumetric heat generation, q'' is the heat flux, and \hat{n} is the unit vector on the surface. The term on the left-hand side is the heat storage term, which represents the net change in energy level. The first term on the right-hand side of the equation is the heat generation term, which describes the heat generated at any time and any volume in the solid body. The second term on the right-hand side shows the net energy exchange from the body to the surroundings. The right-hand side shows the net energy exchange from the body to the surroundings. Gauss' Law connects the surface integral to a volume integral of a body that is enclosed by a given surface [BIR1960]:

$$\iint_S \vec{q}''(\vec{r}, t) \hat{n} dS = \iiint_V \nabla q''(\vec{r}, t) dV. \quad (161)$$

Using Gauss' Law and Eq. (161), the surface integral in the energy balance equation, Eq. (160), can be converted to a volume integral, following which the volume integral can be dropped for all terms in the equation, and the internal energy e can be replaced by the temperature T times the heat capacity c :

$$\frac{\partial(\rho c T)}{\partial t} = q'''(\vec{r}, t) - \nabla q''(\vec{r}, t). \quad (162)$$

In addition, a relation is needed to specify the heat flux in terms of temperature. In a solid body, Fourier's law of thermal conduction is applicable and can be expressed as follows [ELW1978]:

$$q''(\vec{r}, t) = -k \cdot \nabla T(\vec{r}, t). \quad (163)$$

Hence, substituting Eq. (163) into Eq. (162) leads to an equation describing the temperature distribution in a solid body in which heat generation and conduction take place:

$$\frac{\partial(\rho c T)}{\partial t} = q'''(\vec{r}, t) - \nabla \left[k \nabla T(\vec{r}, t) \right], \quad (164)$$

where the solid body density ρ is in $[kg/m^3]$; the specific heat capacity c is in $[J/(kg \text{ } ^\circ K)]$; the heat conductivity k is in $[J/(m \text{ } ^\circ K \text{ } sec)]$; the heat flux q'' is in $[J/(m^2 \text{ } sec) = W/m^2]$; the heat generation rate q''' is in $[J/(m^3 \text{ } sec) = W/m^3]$; the temperature T is in $[^\circ K]$; and α is defined as $(k/\rho c)$ $[m^2/sec]$.

7.4.2 Temperature distribution in the radial direction

Consider a typical cylindrical fuel pin composed of a fuel element surrounded by metal cladding, as shown in Figure 69. The fuel pellets are in the fuel element and are surrounded by a small gap between the fuel and the cladding, which offers substantial resistance to heat transfer. The flowing coolant surrounds the pin. This discussion will consider the fuel, gap, cladding, and coolant separately to develop the temperature profile in each material. Then the resulting equations will be combined to yield the full fuel-to-coolant temperature profile. It is sufficient for the present purposes to focus on the steady state to provide an illustration of a fuel temperature distribution and the separate contributions of thermal resistance through various materials. The steady-state version of Eq. (164) will not have the term on the left-hand side, meaning that the heat generated in the fuel is equal to the heat removed by the coolant:

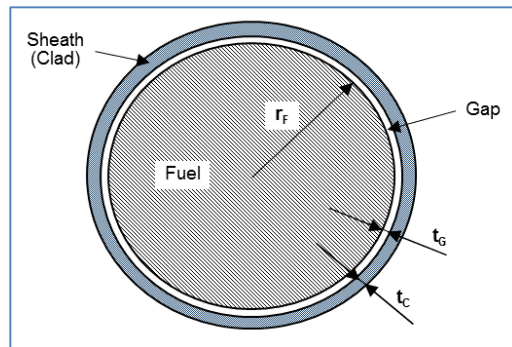


Figure 69 Cross section of a cylindrical fuel pin

$$\nabla \left[k_f \nabla T(\vec{r}, t) \right] = q'''(\vec{r}, t). \quad (165)$$

For a cylindrical fuel pellet, Eq. (165) must be expanded into cylindrical coordinates:

$$\frac{1}{r} \frac{d}{dr} \left(k_f r \frac{dT}{dr} \right) = q'''(r). \quad (166)$$

Equation (166) must be integrated twice; after the first integration, it is transformed into the following equation:

$$k_f r \frac{dT}{dr} = -\frac{r^2}{2} q'''(r). \quad (167)$$

The constant of integration is zero because the temperature gradient at $r=0$ is zero. The thermal conductivity, k , is a strong function of T in fuel, and therefore its variation needs to be taken into account in the integration process. However, in the first step, its average value \bar{k}_f can be assumed to be within the range of fuel temperature variation. Hence, the second subsequent integration results in the following relation:

$$\int_{T_o}^{T_F} k_f(T) dT \equiv \bar{k}_f (T_F - T_o) = -\frac{r_F^2}{4} q'''(r), \quad (168)$$

where the subscript 0 indicates the centre point and the subscript F indicates the fuel pellet radius. Because $T=T_o$ at $r=0$, the constant of integration is again zero. Finally, with the assumption of average fuel conductivity in the fuel pellet, the temperature difference across the fuel pellet has the following form:

$$\Delta T_{fuel} \equiv T_o - T_F = \frac{r_F^2}{4k_f} q''' = \frac{q'}{4\pi k_f}, \quad (169)$$

where $q' = \pi r_F^2 q'''$ is the linear power density. Note that by using linear power density, the same ΔT is obtained for a given q' regardless of the fuel radius.

Problem 7.4.2.1

Calculate for UO_2 ceramic fuel the radial temperature difference in the fuel. For UO_2 ceramic fuel, k_f is typically $0.02-0.03$ [W/cm²K]. At $q'=500$ [W/cm], ΔT_{fuel} in the fuel pellet is about 1400°C .

End of Problem 7.4.2.1

In the gap between the fuel pellet and the cladding, no heat is generated. Therefore, for steady-state conditions, Eq. (164) transforms into the following equation:

$$\frac{1}{r} \frac{d}{dr} \left(k_g r \frac{dT}{dr} \right) = 0. \quad (170)$$

This equation can be readily integrated once to yield the following equation:

$$k_g r \frac{dT}{dr} = \text{const}. \quad (171)$$

The constant of integration is determined by considering the heat flux q'' at the fuel-gap interface:

$$-k_g \left[\frac{dT}{dr} \right]_{r=r_F} = q'' = \frac{q'}{2\pi r_F}. \quad (172)$$

Substituting Eq. (172) into Eq. (171) yields the following equation:

$$k_g r \frac{dT}{dr} = -\frac{q'}{2\pi} \Rightarrow k_g \frac{dT}{dr} = -\frac{q'}{2\pi r}. \quad (173)$$

Assuming that the gap conductivity does not change significantly with temperature and performing integration, the temperature difference in the gap can be obtained as:

$$k_g \Delta T_{GAP} = k_g (T_F - T_C) = \frac{q'}{2\pi} \ln \left(\frac{r_F + t_G}{r_F} \right). \quad (174)$$

The subscript C indicates the gap-cladding interface. The boundary condition $T=T_C$ at $r=r_F+t_G$ is incorporated into this solution. Finally, the gap temperature difference is obtained as:

$$\Delta T_{GAP} = \frac{q'}{2\pi k_G} \ln \left(\frac{r_F + t_G}{r_F} \right). \quad (175)$$

Because the natural logarithm of a small number can be approximated by the number itself, i.e., $\ln(1+x) \approx x$ [GAR1999, POP2014], the gap temperature difference is:

$$\Delta T_{GAP} = \frac{q'}{2\pi r_F} \left(\frac{t_G}{k_G} \right). \quad (176)$$

Problem 7.4.2.2

Calculate for UO_2 fuel the radial temperature difference in the fuel-cladding gap. The gap conductivity k_G is about $0.002 \text{ W/cm}^2\text{K}$, but it varies considerably with the amount of fission product gases. For a gap thickness of 0.005 cm , ΔT_{GAP} is about 300°C for q' of 500 W/cm .

End of Problem 7.4.2.2

Because with irradiation the fuel will swell to touch the cladding at certain points (because the surfaces have a certain degree of roughness), an effective heat transfer coefficient, h_G , is used:

$$h_G (\Delta T_{GAP}) = q''. \quad (177)$$

Therefore, taking into account the relationship between heat flux and the linear power $q' = \pi r_F^2 q''$, the temperature difference in the gap can be obtained as follows:

$$\Delta T_{GAP} = \frac{q'}{2\pi r_F h_G}. \quad (178)$$

Problem 7.4.2.3

Calculate for UO_2 fuel the radial temperature difference in the fuel-cladding gap. A heat transfer coefficient of $0.5\text{--}1.1 \text{ W/cm}^2\text{K}$ gives a ΔT_{GAP} less than 300°C .

End of Problem 7.4.2.3

For the gap region described above, the steady-state equation for the cladding region, in which there is no heat generation, is similar:

$$\frac{1}{r} \frac{d}{dr} \left(k_c r \frac{dT}{dr} \right) = 0. \quad (179)$$

This equation is solved in the same manner as for the gap to yield:

$$k_c \Delta T_{CLAD} = k_c (T_C - T_S) = \frac{q'}{2\pi} \ln \left(\frac{r_F + t_G + t_C}{r_F + t_G} \right) \Rightarrow \Delta T_{CLAD} = \frac{q'}{2\pi k_c} \ln \left(\frac{r_F + t_G + t_C}{r_F + t_G} \right). \quad (180)$$

The subscript S indicates the cladding-coolant surface interface. The boundary condition $T=T_S$ at $r=r_F+t_G+t_C$ is incorporated into this solution.

Because the natural logarithm of a small number can be approximated by the number itself, i.e., $\ln(1+x) \approx x$ [GAR1999, POP2014], the gap temperature difference is:

$$\Delta T_{CLAD} = \frac{q'}{2\pi (r_F + t_G)} \left(\frac{t_C}{k_C} \right). \quad (181)$$

Problem 7.4.2.4

Calculate for UO_2 fuel the radial temperature difference in the fuel cladding. The cladding conductivity k_C is about $0.11 \text{ W/cm}^\circ\text{K}$, giving a ΔT_{CLAD} of about 80°C for a q' of 500 W/cm .

End of Problem 7.4.2.4

The heat flux from the cladding to the coolant is determined as:

$$q'' = h_S (T_S - T_{FL}), \quad (182)$$

where T_{FL} is the bulk temperature of the coolant fluid. Hence, the temperature drop from the cladding surface to the bulk fluid temperature is:

$$\Delta T_{COOL} = \frac{q'}{2\pi h_S (r_F + t_C + t_G)}. \quad (183)$$

Problem 7.4.2.5

Calculate for UO_2 fuel the radial temperature difference in the cladding-to-coolant interface. A heat transfer coefficient of $\sim 4.5 \text{ W/cm}^2\text{K}$ gives a ΔT_{COOL} of about 10°C – 20°C .

End of Problem 7.4.2.5

By summing up Eqs. (169), (178), (181), and (183), the overall temperature difference between the fuel centreline and the bulk coolant can be obtained according to the following equation:

$$T_o - T_{FL} = \frac{q'}{2\pi} \left(\frac{1}{2k_f} + \frac{1}{h_G r_F} + \frac{t_G + t_C}{k_C (r_F + t_G)} + \frac{1}{h_S (r_F + t_G + t_C)} \right). \quad (184)$$

The expression in brackets in Eq. (184) is the thermal resistance across the fuel element:

$$R_{th} = \left(\frac{1}{2k_f} + \frac{1}{h_G r_F} + \frac{t_G + t_C}{k_C (r_F + t_G)} + \frac{1}{h_S (r_F + t_G + t_C)} \right). \quad (185)$$

Hence, the centreline fuel temperature is greater than the coolant temperature by an amount that depends on the amount of heat generated and on various resistances to heat flow. For a given fuel design, most of the parameters are fixed under normal operation. The one exception is the heat transfer coefficient to the coolant, h_S , which is covered in Section 7.6.

Figure 70 shows a radial temperature distribution across the fuel element for two linear power rates [POP2014]. Linear power level 45 [kW/m] represents full-power operation of the fuel element in the middle of the core. Linear power level 15 [kW/m] represents operation at full power at the core ends, or at a certain decay power level shortly after reactor shutdown. This figure shows that the highest temperature difference occurs in the fuel pellet (above 1400°C at full power) because UO_2 is a poor heat conductor, but its melting temperature is approximately 2800°C–2900°C. The temperature difference in the gap is significant considering that the gap is very thin. The cladding and the water are very good heat conductors, and therefore the temperature difference is relatively small.

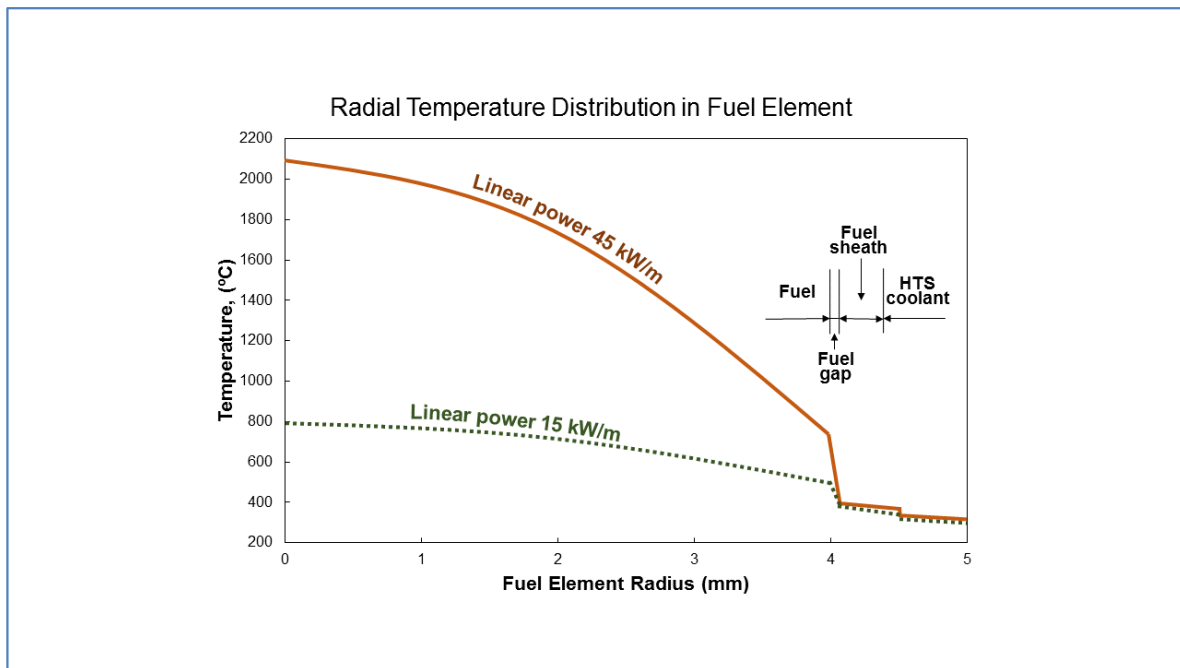


Figure 70 Radial temperature distribution in a fuel element

The fuel element design must ensure that given the coolant pressure and saturation temperature, the fuel pellet centreline temperature avoids exceeding the melting temperature by a good margin. This objective also applies to the temperature transients in design basis events.

Figure 71 shows the temperature gradient for various fuel element materials in absolute terms and per unit thickness [POP2014]. This figure clearly indicates that the highest relative

contribution is from the fuel-cladding gap and the second highest from the fuel pellet.

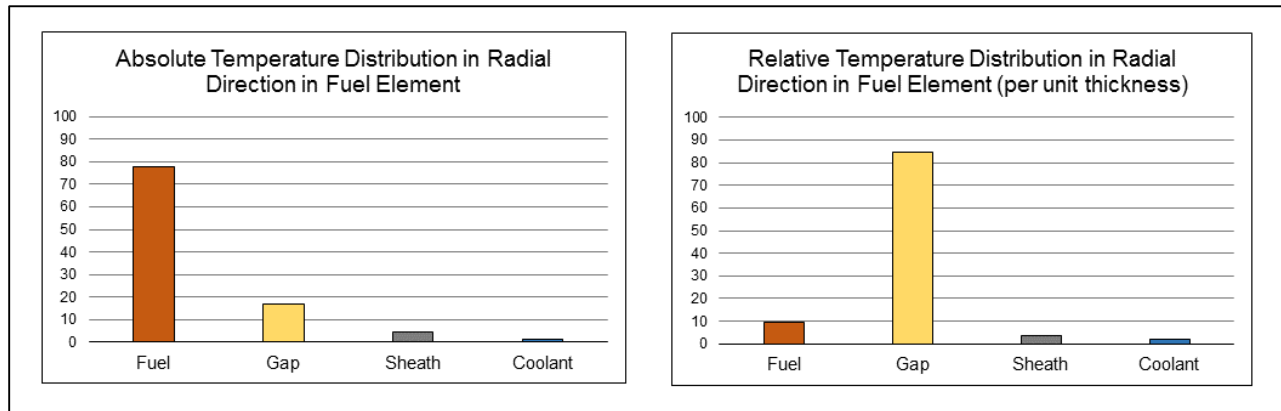


Figure 71 Radial temperature gradient per unit thickness in a fuel pin

7.4.3 Temperature distribution in the axial direction

The fuel and coolant temperature distributions depend on heat transfer in the radial direction at each position in the channel axial direction. The general heat conduction and convection equations for axial heat transfer are covered in Chapter 7.

The amount of heat generated along the fuel channel follows the neutron flux and fission reaction distribution along the fuel channel. Assuming that the reactor core does not use any techniques for balancing (i.e., flattening) the neutron flux and power generation in the axial direction, the natural axial variation of the neutron flux is given by the following relation [POP2014]:

$$\Phi(z) = \Phi_{\max} \cos\left(\frac{\pi z}{L_e}\right), \quad (186)$$

where L_e is the effective core length and Φ_{\max} is the maximum neutron flux in the middle of the core.

Axial heat generation follows the neutron flux variation and is given by the following equation:

$$q'''(z) = (q''')_{\max} \cos\left(\frac{\pi z}{L_e}\right), \quad (187)$$

where $(q''')_{\max}$ is the heat flux at the middle of the fuel element in the axial direction.

Consider a heat balance for a differential section of a fuel element of length dz , fuel cross section $A_f [m^2]$, and mass flow rate $w [kg/s]$. In a steady-state situation, the sensible heat gain by the passing coolant (assuming no phase change) is equal to the heat generated in the differential fuel element (c_p is the specific heat capacity at a given pressure $[kJ/kg \text{ } ^\circ C]$):

$$w \cdot c_p dT_c = q''' A_f dz. \quad (188)$$

The axial variation of the fluid temperature T_c can be obtained by substituting Eq. (187) into Eq. (188) and integrating [ELW1978]:

$$w c_p \int_{T_{f1}}^{T_f} dT_c = (q''')_{\max} A_f \int_{-L_e/2}^z \cos\left(\frac{\pi z}{L_e}\right) dz, \quad (189)$$

$$T_c = T_{c,in} + \frac{(q''')_{\max} A_f L_e}{\pi w c_p} \left[1 + \sin\left(\frac{\pi z}{L_e}\right) \right] = T_{c,in} + \frac{(q''')_{\max} V_f}{\pi w c_p} \left[1 + \sin\left(\frac{\pi z}{L_e}\right) \right], \quad (190)$$

where $V_f [m^3]$ is the volume of the fluid portion of the fuel element. The subscript "in" designates the entry point in the channel. In this equation, the equivalent core length is approximated by the actual core length, i.e., $L=L_e$.

The coolant temperature is measured in the middle of the fuel element for $z=0$ and has the following form:

$$T_{c,mid} = T_{c,in} + \frac{(q''')_{\max} A_f L}{\pi w c_p}. \quad (191)$$

The exit temperature of the coolant from this channel can be obtained by integrating Eq. (189) to the channel exit (labelled as 2, i.e., at $z=+L/2$):

$$T_{f,out} = T_{f,in} + \frac{2(q''')_{\max} A_f L}{\pi w c_p}. \quad (192)$$

This equation shows that the coolant temperature rise in the channel will be greater for higher heat generation rates, larger fuel elements, and longer channels and smaller for higher mass flow rates.

The heat transferred between the cladding and the coolant at any location z along the fuel channel, per unit area of cladding surface in contact with the coolant, is given by $h(T_{SH}-T_c)$, where h is the heat transfer coefficient. This coefficient can be assumed constant along the fuel channel with no boiling in the channel. Hence, the heat balance between the fuel cladding and the coolant can be expressed by the following equation:

$$h C_{SH} (T_{SH} - T_c) dz = (q''')_{\max} A_f \cos\left(\frac{\pi z}{L}\right) dz, \quad (193)$$

where $C_{SH} [m]$ is the fuel cladding circumference, $T_{SH} [^{\circ}C]$ is the cladding temperature, and $h [kJ/m^2 \text{ } ^{\circ}C]$ is the heat transfer coefficient. Substituting Eq. (190) into Eq. (193) yields the cladding temperature variation along the fuel channel:

$$T_{SH} = T_{c,in} + \frac{(q''')_{\max} A_f L}{\pi w c_p} \left[1 + \sin\left(\frac{\pi z}{L}\right) \right] + \frac{(q''')_{\max} A_f}{h C_{SH}} \cos\left(\frac{\pi z}{L}\right). \quad (194)$$

The temperature variation at the fuel pellet surface along the fuel channel and the temperature of the fuel pellet centreline along the fuel channel can be obtained by means of the following relation:

$$\frac{T_{SH} - T_c}{R_x L} = (q''')_{\max} A_f \cos\left(\frac{\pi z}{L}\right). \quad (195)$$

Hence, for fuel pellet surface temperature, the following equations can be developed:

$$\frac{T_{f,S} - T_c}{R_{f,S}L} = (q''')_{\max} A_f \cos\left(\frac{\pi z}{L}\right), \quad (196)$$

$$T_{f,S} = T_c + R_{f,S}L \left[(q''')_{\max} A_f \cos\left(\frac{\pi z}{L}\right) \right], \quad (197)$$

$$R_{f,S} = \left(\frac{1}{h_G r_F} + \frac{t_G + t_C}{k_C (r_F + t_G)} + \frac{1}{h_S (r_F + t_G + t_{SH})} \right). \quad (198)$$

The fuel pellet centreline temperature variation can be described by the following equations:

$$\frac{T_{f,CL} - T_c}{R_{f,CL}L} = (q''')_{\max} A_f \cos\left(\frac{\pi z}{L}\right), \quad (199)$$

$$T_{f,CL} = T_c + R_{f,CL}L \left[(q''')_{\max} A_f \cos\left(\frac{\pi z}{L}\right) \right], \quad (200)$$

$$R_{f,CL} = \left(\frac{1}{2k_f} + \frac{1}{h_G r_F} + \frac{t_G + t_C}{k_C (r_F + t_G)} + \frac{1}{h_S (r_F + t_G + t_{SH})} \right). \quad (201)$$

Substituting Eq. (190) into Eq. (200) yields the fuel centreline temperature:

$$T_{f,CL} = T_{c,in} + \frac{(q''')_{\max} A_f L}{\pi w C_p} \left[1 + \sin\left(\frac{\pi z}{L}\right) \right] + (q''')_{\max} A_f L R_{f,CL} \cos\left(\frac{\pi z}{L}\right). \quad (202)$$

The location of the maximum cladding temperature can be obtained by differentiating Eq. (194) and equating it to zero, i.e., $dT_{SH}/dz=0$. Hence:

$$z_{SH,m} = \frac{L}{\pi} \tan^{-1} \left(\frac{h C_{SH} L}{\pi w C_p} \right) = \frac{H}{\pi} \cot^{-1} (\pi w C_p R_{SH}), \quad (203)$$

$$R_{SH} = \frac{1}{h A_f} = \frac{1}{h C_{SH} L}. \quad (204)$$

The location of the maximum fuel pellet centreline temperature can be obtained by differentiating Eq. (202) and equating it to zero, i.e., $dT_{f,CL}/dz=0$. Hence:

$$z_{f,CL,m} = \frac{L}{\pi} \cdot \cot^{-1} (\pi w C_p R_{f,CL}). \quad (205)$$

The maximum cladding temperature can be found by substituting Eq. (203) into Eq. (194):

$$T_{SH,m} = T_{c,in} + (q''')_{\max} A_f L R_{SH} \left[\frac{1 + \sqrt{1 + \alpha^2}}{\alpha} \right], \text{ where } \alpha = \pi w C_p R_{SH}. \quad (206)$$

The maximum cladding temperature can be found by substituting Eq. (205) into Eq. (202):

$$T_{f,CL,m} = T_{c,in} + (q''')_{\max} A_f LR \left[\frac{1 + \sqrt{1 + \beta^2}}{\beta} \right], \text{ where } \beta = \pi w c_p R_{f,CL}. \quad (207)$$

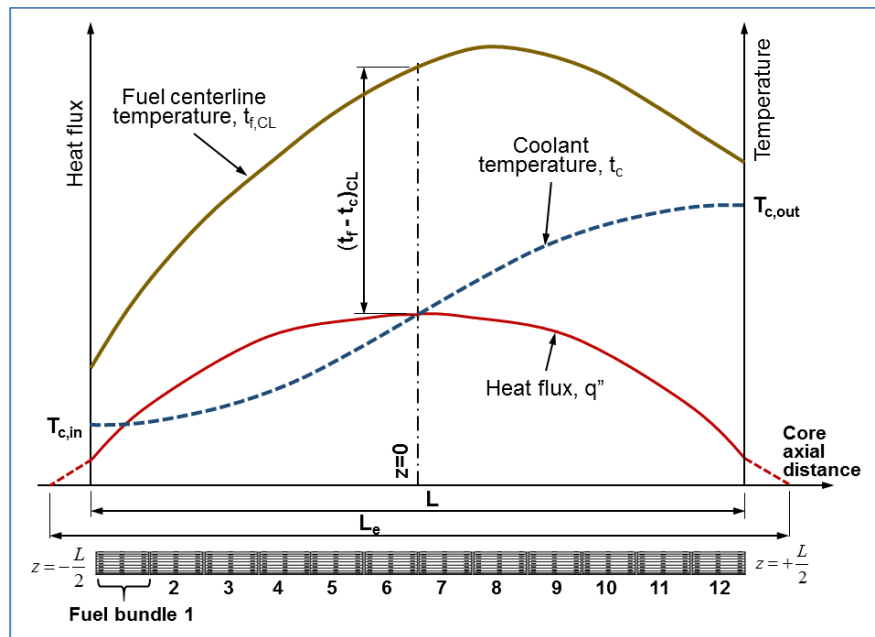


Figure 72 Temperature distribution in the axial direction in a fuel element

Figure 72 shows the temperature distribution in the coolant and the cladding plotted on the same graph with the heat flux distribution along the core [ELW1978]. The heat flux distribution is assumed to have a cosine distribution, which is more pronounced in a core in which no measures have been taken to flatten the neutron flux. In this case, the variations in the coolant and cladding temperatures are more pronounced. Note that the coolant temperature curve is symmetrical. It has a small gradient at the entry and exit parts of the core, where the heat flux is lower. The highest coolant temperature gradient is in the middle part of the core, where the heat flux is substantial. Of course, different core heat flux distributions can have a significant impact on the temperature profile. Moreover, reactivity devices and fuel channel orificing (i.e., channel-to-channel variation of flow rates) can also have significant local effects on the temperature profile.

Figure 73 shows a temperature distribution that includes the coolant (T_c), fuel sheath (T_{SH}), fuel pellet surface ($T_{f,S}$), and fuel pellet centreline ($T_{f,CL}$) temperature profiles. The positions of the maximum values of T_{SH} , $T_{f,S}$, and $T_{f,CL}$ occur at $Z_{SH,m}$, $Z_{f,S,m}$, and $Z_{f,CL,m}$, closer to the fuel element mid-plane [ELW1978].

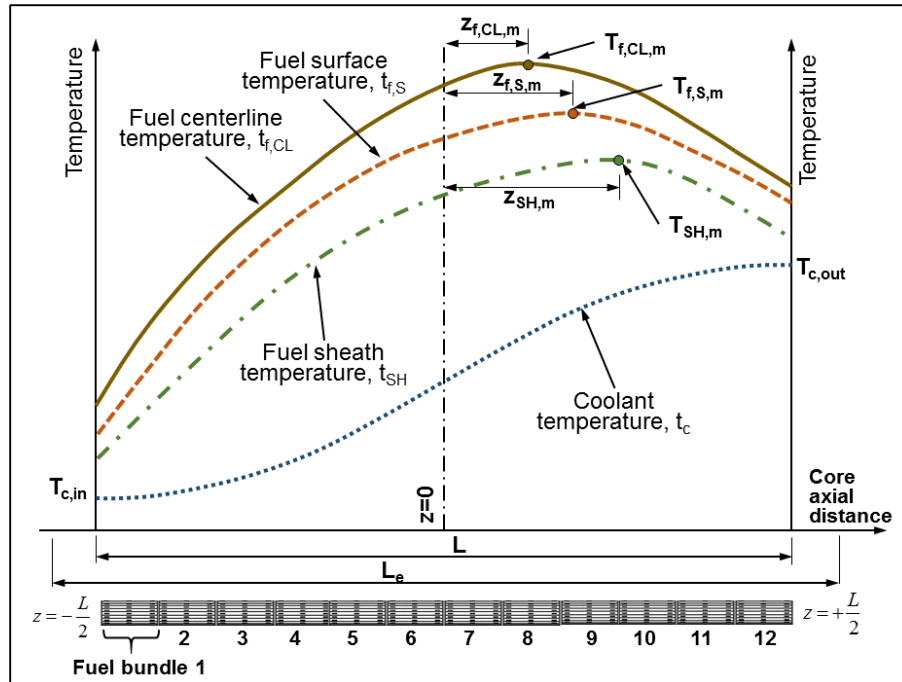


Figure 73 Temperature distribution in the fuel cladding and the fuel element

The reason that the maximum fuel centreline temperature is closer to the fuel mid-plane is that the radial heat flow through the fuel and cladding at any section along the fuel channel is proportional to the heat flux at that location. The temperature differences $(T_{SH}-T_c)$, $(T_{f,S}-T_{SH})$, and $(T_{f,CL}-T_{f,S})$ generally follow cosine-shaped functions according to the heat flux cosine profile. The maxima of the cladding and fuel temperatures are affected by the heat flux maximum (at the fuel mid-plane) and the fluid maximum (at the fuel channel exit). Because the cladding is close to the fluid, the impact of coolant temperature is strong, and hence its maximum is pulled away from the mid-plane. Because the fuel centreline temperature occurs inside the fuel, where the heat is generated, its maximum is pulled toward the mid-plane, where the heat flux maximum is located.

7.4.4 Axial distribution of quality

If the coolant boils in a fuel channel, flow quality changes along the channel. It is important in this situation to calculate the change in flow quality and the length of the channel where boiling occurs. The enthalpy of the two-phase coolant is defined using the following relation:

$$h = h_{c,sat} + xh_{fg}, \quad (208)$$

where x is the flow quality in the two-phase mixture, $h_{c,sat}$ is the saturated liquid enthalpy, and h_{fg} is the latent heat of vaporization. The heat balance over the differential part of the fuel channel yields the following equation:

$$w_f [h(z) - h_{cold}] = \int_{-L/2}^{+L/2} q'(z) dz. \quad (209)$$

In the above equation, h_{cold} is the inlet enthalpy in the channel. If the axial position where the coolant starts to boil (the point where $h(z)=h_{SAT}$) is defined as Z_{BB} , the heat balance equation, Eq. (209), transforms into the following equation:

$$w_f [h(z) - h_{c,sat}] = \int_{Z_{BB}}^z q'(z) dz = x(z) w_f h_{fg} \cdot \quad (210)$$

Using the above equation, the flow quality of the two-phase mixture can be expressed by the following equation:

$$x(z) = \frac{1}{w_f h_{fg}} \int_{Z_{BB}}^z q'(z) dz \cdot \quad (211)$$

7.4.5 Thermal conductivity and fuel element material properties

In developing Eq. (166), it has been assumed that the fuel thermal conductivity can be approximated by an average value that will apply in the range of parameters used in the present calculations. This section covers the effect of various factors on thermal conductivity and other thermal parameters that must be considered when developing a model to calculate fuel-element temperature profiles.

Many factors affect UO_2 fuel thermal conductivity. The major factors are temperature, porosity, oxygen-to-metal atomic ratio, PuO_2 content, pellet cracking, and fuel burn-up.

Figure 74 shows the temperature dependence of UO_2 thermal conductivity [ELW1978]. Experimental measurements have shown that thermal conductivity decreases with increasing fuel temperature (i.e., has a negative slope) until about 1750°C, after which it slowly increases. However, the slope is very steep from 0°C–500°C and very shallow thereafter. Nevertheless, the impact of temperature must be taken into account when calculating fuel temperature profiles, which is routinely done in thermal-hydraulic computer programs. Figure 74 also shows the integral of the thermal conductivity, which monotonically rises with temperature; this is the value to use in solving Eq. (170).

When using experimental values of thermal conductivity, one must be aware of the measurement uncertainties. Note that these uncertainties are significant, particularly at higher temperatures.

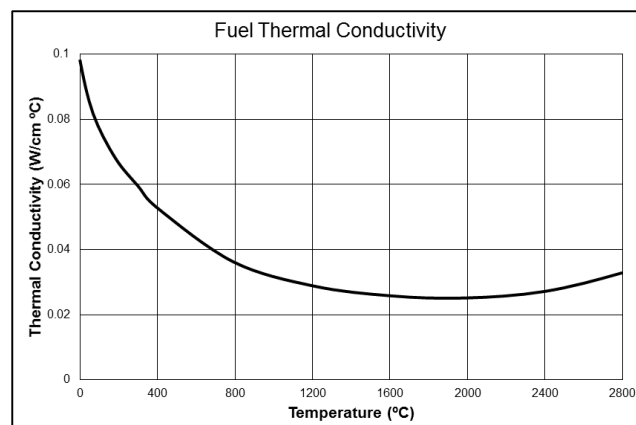


Figure 74 Thermal conductivity in a fuel pin

The oxide fuel is produced by sintering pressed powdered UO_2 or mixed oxide at high temperature. Under such conditions, for any material with a given density, usually only around 90% of the maximum possible (theoretical) density of the solid can be produced.

The thermal conductivity of a solid usually decreases with increasing presence of voids within the structure. Therefore, to maximize thermal conductivity, fuel porosity must be minimized. However, during fuel irradiation, fission gases are produced, resulting in increased internal pressures that may swell and deform the fuel. Hence, a certain degree of porosity is desirable to accommodate the fission gases and limit the possibility of swelling. This is very important for reactor cores that have high power density and therefore produce more gases per unit volume.

The oxygen-to-metal atomic ratio of UO_2 and PuO_2 can vary from the theoretical (stoichiometric) value of 2 because of fuel irradiation and burn-up. A reduction or increase in the oxygen-to-metal ratio results in a reduction of thermal conductivity, as can be clearly seen in Figure 75 for UO_2 and PuO_2 mixtures [TOD2011].

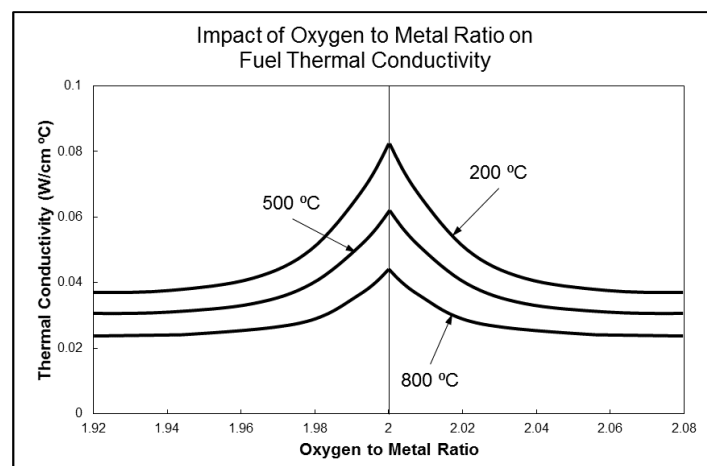


Figure 75 Impact of oxygen-to-metal ratio on the heat conduction coefficient in fuel

The thermal conductivity of mixed fuel decreases as the plutonium oxide content increases. Therefore, as fuel burns up and ages and plutonium content increases, thermal conductivity decreases.

Figure 76 shows the impact of fuel temperature on fuel heat capacity for UO_2 and PuO_2 fuels [TOF2011]. It is evident that heat capacity increases with temperature and decreases with an increase in plutonium content.

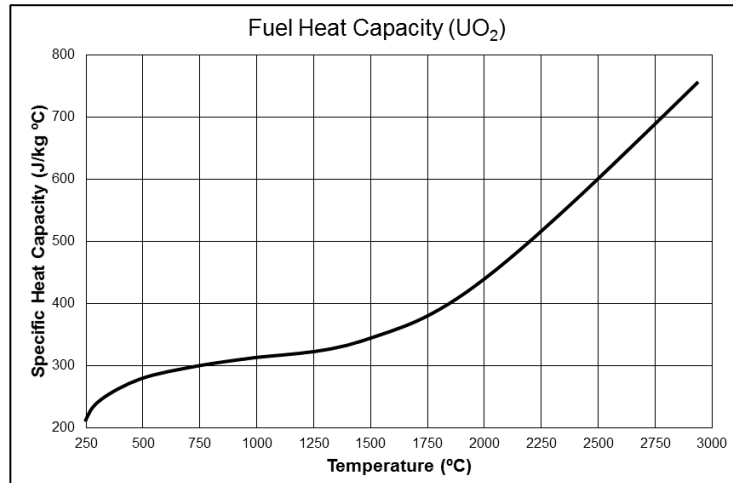


Figure 76 Heat capacity of a fuel pin

The properties of the pellet-to-cladding gap are very important. As shown in Figure 71, its contribution to thermal resistance is substantial. The gap consists of an annular space occupied by gas. Initially, its composition is fill gas, which is usually an inert gas such as helium. With burn-up, the gas composition changes as the gap is penetrated by gaseous fission products such as xenon and krypton, resulting in a gap pressure increase.

Moreover, the fuel pellet cracks with irradiation, leading to circumferential deformation of the gap and fuel pellet swelling. All this causes a reduction of thermal resistance in the gap and increases its thermal conductance with burn-up. Figure 77 shows the effect of burn-up on thermal conductance [TOD2011].

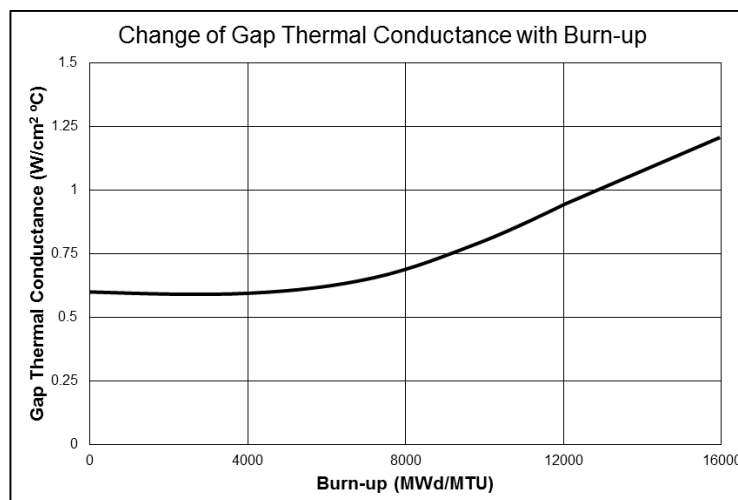


Figure 77 Gap conductance in a fuel pin

The left side of Figure 78 shows the temperature profile in the gap at nominal geometry (fresh fuel). Note that near the walls, there is a mild temperature rise towards the fuel pellet and a reduction towards the cladding because of the smaller number of molecules moving near the walls (the boundary layer effect). The right side of Figure 78 shows the effect of the deformations that occur with fuel burn-up (aging) because of swelling and cracking of the fuel

pellet and cladding. After a certain amount of irradiation, a number of peaks and valleys will develop at the pellet and cladding surfaces. These may eventually produce contact between fuel and cladding, improving thermal conductivity.

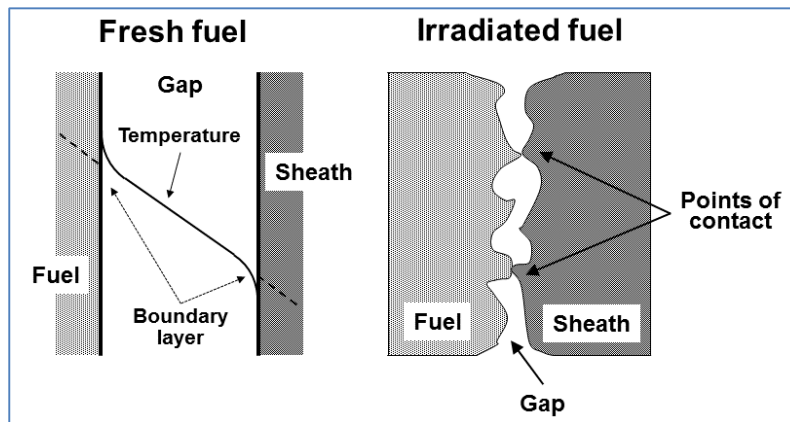


Figure 78 Fuel aging effect on temperature in a fuel pin

Figure 79 shows the typical impact of fuel aging on gap conductance for different linear heat ratings as a function of initial gap thickness [TOD2011]. Note that better thermal conductance is achieved for smaller gap thickness and for higher linear power rates, as could be expected from the above explanation. Therefore, as gap thickness becomes smaller with fuel burn-up, heat transfer is improved. In addition, this figure shows that using a smaller gap thickness for fresh fuel improves heat transfer.

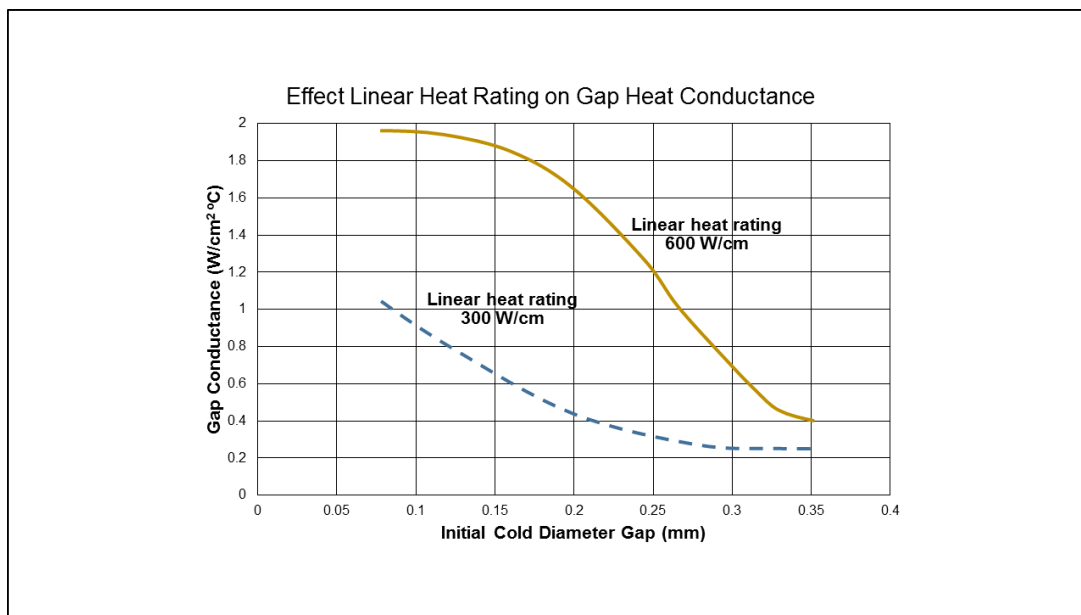


Figure 79 Impact of gap thickness and linear power on heat conductance

The temperature profiles described so far in this section were derived based on the assumption of radial symmetry across the fuel rod. This assumption was a useful way to simplify the derivation of temperature profiles across the fuel element. This assumption is acceptable for vertical reactor cores, such as in LWRs.

However, for horizontal reactor cores, such as CANDU, the assumption of radial symmetry across the fuel rod is not applicable for certain flow regimes. This is relevant for situations in which bubbly flow develops in the upper part of the fuel channel, or even more importantly, when stratification develops (e.g., under accident conditions) in the fuel channel.

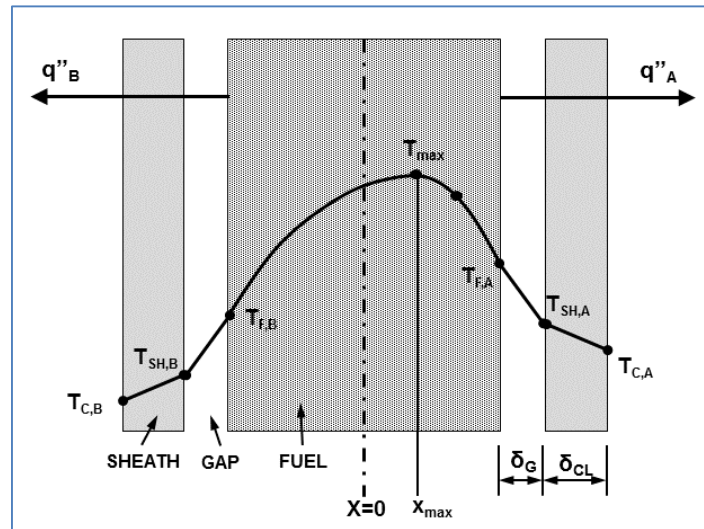


Figure 80 Asymmetric temperature profiles in a fuel pin

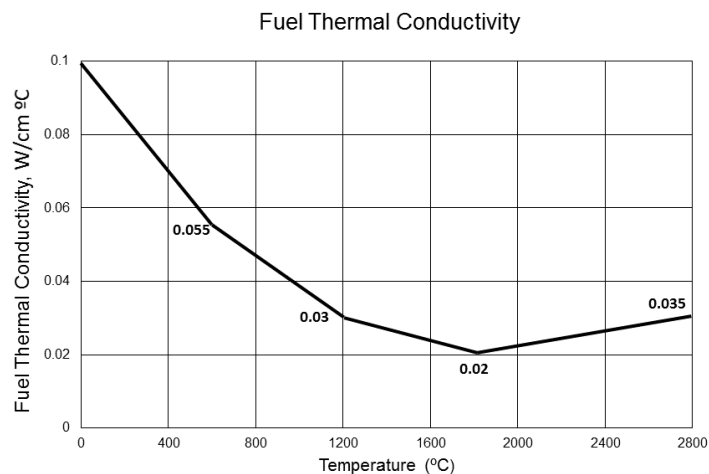
In these situations, the heat flux to the upper part of the fuel element could be smaller than to the lower part. This results in a skewed (asymmetric) temperature profile, as shown in Figure 80. In such a case, the maximum fuel pellet centreline temperature will be skewed towards the side with the smaller heat flux. This could also have an important impact on the cladding temperature, and it is particularly relevant to some postulated accidents in which channel stratification occurs.

7.4.6 Problems

1. A PWR reactor produces 2440 MWt with the following core information: UO_2 pellet diameter 0.96 cm; Zr clad inside diameter 0.98 cm; Zr clad outside diameter 1.12 cm; active fuel length 3.7 m. The core contains 220 fuel bundles each with 14 x 14 fuel pins (but 20 positions are used for control elements). The fission energy is distributed uniformly across the fuel pin. and $T_B=300^\circ\text{C}$, $k_{\text{UO}_2}=0.050 \text{ W/cm}^\circ\text{C}$, $h_{\text{cool}}=1.8 \text{ W/cm}^2 \text{ }^\circ\text{C}$, $h_{\text{gap}}=0.57 \text{ W/cm}^2 \text{ }^\circ\text{C}$, $k_{\text{clad}}=0.12 \text{ W/cm}^\circ\text{C}$. Calculate core averaged fuel pin temperature profile.
2. The core of a BWP reactor consists of 764 fuel assemblies, each containing a square array of 49 fuel rods on a 1.9 cm pitch. The fuel rods are 4.4 m long, but fuelled only along over 3.6 m of their length. The outside diameter of the fuel rods is 1.4 cm, the cladding thickness is 0.8 mm, and the fuel pellets are 1.2 cm, thus leaving a gap of 0.2 mm. The UO_2 has average density of 10.3 g/cm^3 . The radius of the core is 2.4 m, and the reactor is designed to produce 3300 MWt. The peak to average power density is 2.6. Calculate (a) the maximum heat flux in kW/m^2 ; (b) the temperature distribution at the location of maximum heat flux ignoring the gap between fuel pellet and cladding; and (c)

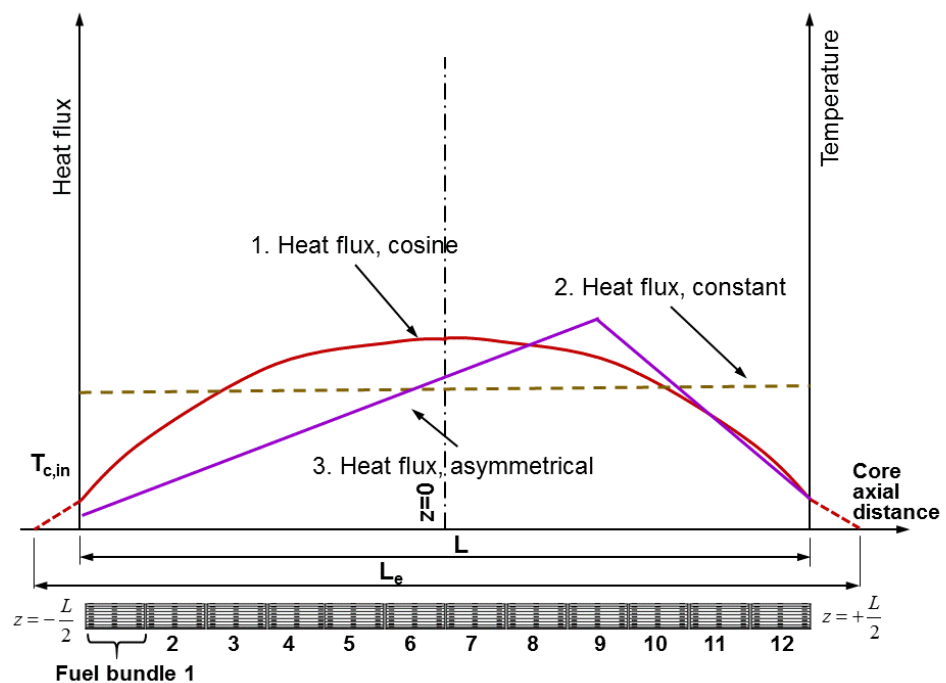
the temperature distribution at the location of maximum heat flux taking into account the gap.

3. For PWR cylindrical solid fuel pellet operating to a heat flux of 1.7 MW/m^2 and surface temperature of 400°C , calculate the maximum temperature in the pellet for two assumed values of heat conduction: $3 \text{ W/m}^\circ\text{C}$, and $k = 1 + 3e^{-0.0005T}$ where T is $^\circ\text{C}$. The UO_2 pellet diameter is 10 mm , and density is 95% of the theoretical density.
4. A CANDU channel has a typical geometry of 37 fuel elements per bundle, 12 bundles per channel, with power, pressure and inlet and outlet temperature. Assume for this channel linear power rating of 60 kW/m ; burnup at the time of peak rating of 50 MWh/kgU ; sheath-to-coolant heat transfer coefficient $40 \text{ kW/m}^2\text{K}$; pellet-to-sheath heat transfer coefficient of $60 \text{ kW/m}^2\text{K}$; and pellet density of 10.6 Mg/m^3 . Calculate coolant, cladding and fuel surface and centreline temperatures in radial direction for each bundle in axial direction assuming typical power distribution along the channel with a typical power peaking factor. Draw appropriate diagrams showing the results.
5. A fuel pin with pellet radius of 4.6 mm , clad inner radius of 4.89 mm , and outer radius of 5.46 mm , calculate the maximum liner power that can be obtained from the pellet such that the mass average temperature in the fuel does not exceed 1200°C . Take the bulk fluid temperature at 307.5°C , and the coolant heat transfer coefficient of $28.4 \text{ kW/m}^2\text{ }^\circ\text{C}$. In the gap consider only conduction heat transfer. Fuel conductivity is $3 \text{ W/m}^2\text{ }^\circ\text{C}$; clad conductivity is $18.69 \text{ W/m }^\circ\text{C}$; and helium gas conductivity is $0.277 \text{ W/m }^\circ\text{C}$.
6. Using analytical technique develop equations for calculating temperature distribution in radial direction in the fuel element (fuel pellets, gap, cladding and coolant) calculate temperature distribution in radial direction at heat loading of 40 kW/m . For the thermal conductivity in the fuel pellets assume the distribution shown in the diagram below. To solve the problem approximate the thermal conductivity by a suitably selected quadratic relationship.

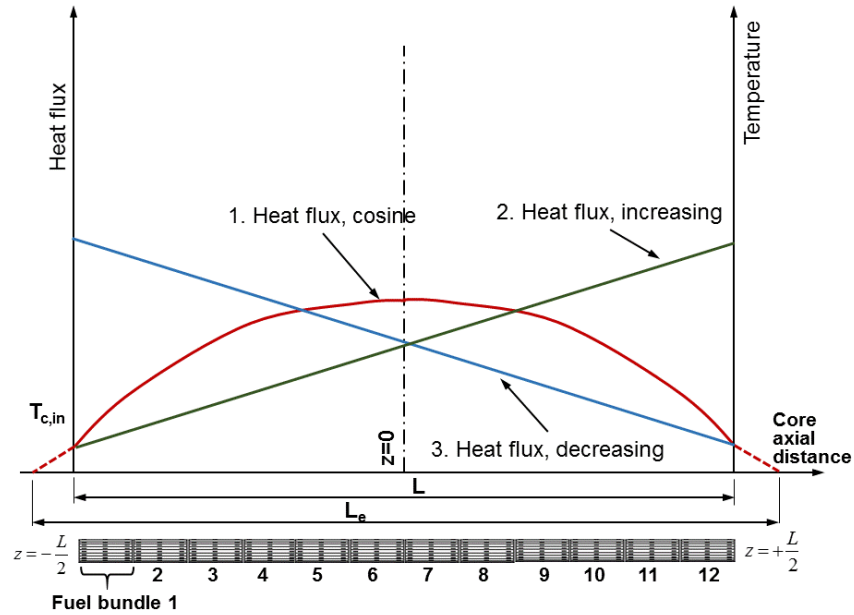


Compare the results with the case assuming constant average heat conductivity in the fuel.

7. Using a numerical technique calculate temperature distribution in radial direction in the fuel element (fuel pellets, gap, cladding and coolant) calculate temperature distribution in radial direction at heat loading of 40 kW/m. For the thermal conductivity in the fuel pellets assume the distribution shown in the diagram above. Compare the results with the case assuming constant average heat conductivity in the fuel (0.03 W/cm°C).
8. Calculate axial temperature distribution of fuel centreline, fuel surface, cladding and coolant in axial direction for a typical CANDU fuel assuming maximum fuel heat load of 50 kW/m, and average fuel load of 25 kW/m. Develop relations for and calculate the positions of maximum temperatures. As per figure below, as a base case assume (1) cosine heat flux distribution, (2) constant heat flux distribution, and (3) asymmetrical linear heat flux distribution (with maximum at bundle 9), and compare the maximum temperatures and their locations in the core.



9. Calculate axial temperature distribution of fuel centreline, fuel surface, cladding and coolant in axial direction for a typical CANDU fuel assuming maximum fuel heat load of 50 kW/m, and average fuel load of 25 kW/m. Develop relations for and calculate the positions of maximum temperatures. As per figure below, as a base case assume (1) cosine heat flux distribution, (2) linearly increasing heat flux distribution to the channel exit, and (3) linearly decreasing heat flux distribution to the channel exit, and compare the maximum temperatures and their locations in the core.



10. Using parameters of a typical CANDU channel, calculate the axial temperature distribution in a fuel channel. Identify the key parameters that affect the calculations, and investigate the sensitivity of the results to these key parameters.

7.5 Fluid flow fundamentals

The flow of coolant in the reactor primary heat transfer system is of key importance for cooling the reactor core under all operational situations, during accidents, and during reactor shutdown. This section provides information on pressure drop calculations and discusses the special topic of flow instabilities.

Design of the primary pump is of critical importance to ensure a robust reactor thermal-hydraulic design. The sources of various friction and local pressure losses around the primary heat transport system are described and compared between PWR and CANDU reactors. Calculation methods used to determine pressure losses around the loop are provided, along with an explanation of the empirical correlations used to calculate pressure losses in single- and two-phase flows in the CANDU primary heat transport system.

The reactor core has a complex geometry, particularly the CANDU fuel channels and the HTS headers and feeders. Moreover, the CANDU reactor primary heat transport system operates partially in two-phase flow. This section describes the type and nature of the experimental tests that were performed to define a number of parameters in the pressure drop calculation.

7.5.1 Introduction to pressure losses

In the nuclear industry, pressure drop calculations are important to determine the appropriate flow rate in the core and the fuel channels, thereby ensuring appropriate heat removal from the core under all possible operating modes. Because almost all reactors under some operating modes operate with two-phase flow, pressure drop calculations in this situation become complex, directly affecting power output and requiring substantial R&D support.

Two-phase pressure drop depends on many parameters, including geometric configuration, mass and volume fractions of the phases, pressure, fluid properties, mass flux, duct orientation, flow direction, and particularly flow patterns. Furthermore, two-phase flow is usually accompanied by heat transfer and changes of phase in multi-component flow. To take into account these many parameters, various empirical correlations have been developed and are used for pressure drop calculations. Mechanistic models also vary in complexity and fidelity, and often they are based on many assumptions to make them workable in a given parameter range.

It is necessary to consider the pressure loss associated with every component in the primary heat transport system. This includes distributed pressure loss due to friction; local pressure losses due to sudden variations in shape, flow area, direction, etc.; and fuel string-related losses and pressure losses due to acceleration (because of flow area variation or fluid density change) and elevation differences (gravity term).

Table 8 shows various components of pressure losses in the reactor heat transport systems in terms of geometry, fluid status, flow nature, flow pattern, flow direction, operating conditions, and driving force [IAEA2001]. Each of these situations introduces major differences in the type and complexity of pressure loss calculations.

Pressure losses must be characterized for a number of components with different geometries.

In addition to frictional pressure losses in the system, Table 9 shows the most important pressure losses in the CANDU reactor core that are specific to CANDU reactors [IAEA2001].

Table 8 Factors affecting pressure drop

Geometry	Basic shapes: Circular pipe, rectangular channel, annulus, etc.
	Other shapes: rod bundle, spacer, valve, orifice, plenum, header, pump, etc.
Fluid status	Single-phase
	Two-phase – one, two, and multiple components.
Flow nature	Laminar
	Turbulent
Flow patterns	Bubbly, slug, annular, etc.
Flow direction	Vertical up-flow
	Inclined flow
	Horizontal flow
Operating Conditions	Steady-state
	Transient
Driving force	Forced convection
	Natural convection

Table 9 CANDU distribution of pressure drop in the primary loop

Pressure Drop in Primary Loop
Entry loss from steam generator outlet pipes to header
Header to feeder entry loss
Inlet feeder bends
Inlet grayloc
Inlet grayloc to liner tube entry
Liner tube to channel entry
Fuel locator
Junction between two bundles
Channel to liner tube entry
Liner tube to outlet grayloc
Outlet grayloc
Outlet feeder bends
Feeder to header entry loss
Header to steam generator inlet pipe entry

The objective of calculating pressure losses with adequate precision is to optimize pump capacity and power requirements, as well as to determine coolant flow rate in the primary circuit, local conditions in bundles and sub-channels, and flow rates across parallel interconnected sub-channels in fuel bundles.

7.5.2 Pressure drop conservation equations

The pressure losses in the primary heat transport system are represented by direct or indirect terms in the conservation equations:

- Mass-balance (continuity) equation;
- Momentum-balance equation; and
- Energy-balance equation.

For design calculations, usually steady-state flow in a channel of uniform flow area in the axial direction is considered. Moreover, negligible variation of fluid properties over the calculation domain is assumed.

The momentum conservation equation is essential to calculate pressure losses along flow paths. The other conservation equations are covered in Chapter 7. The momentum equation can be written for homogeneous or separated flow conditions. Figure 81 shows a calculation domain (control volume) in an inclined flow situation. The forces acting on this control volume are indicated in the figure. Momentum balance over this control volume in fact means a balance of all forces acting on the control volume.

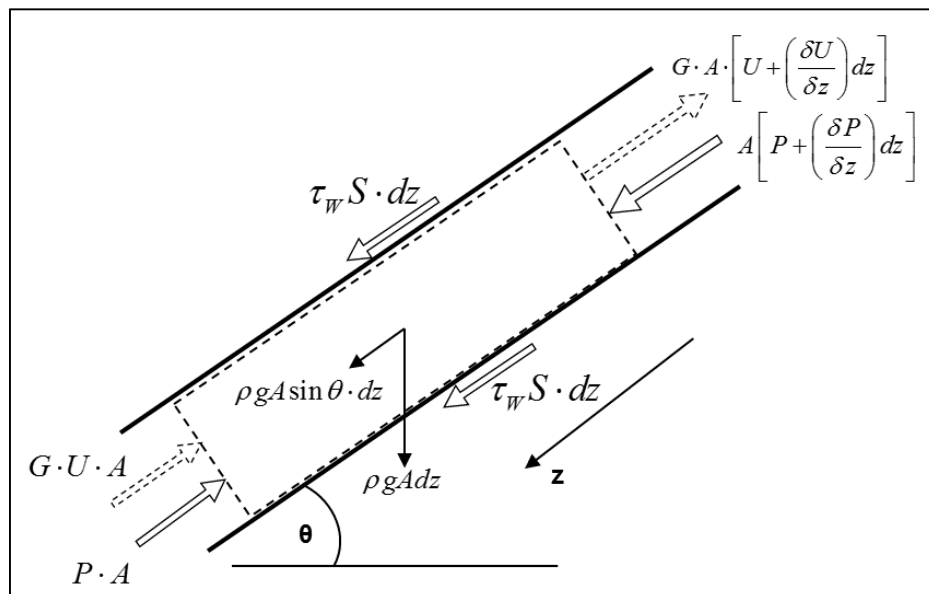


Figure 81 Force-momentum balance in a control volume

Homogeneous flow model

The momentum balance equation over the control volume using the homogeneous flow

assumption is given by Eq. (212) [BIR1960, WAL1969]:

$$\int_A \left[P - \left(P + \frac{dP}{dz} \delta z \right) \right] dA = \int_S \tau_w \delta z dS + \int_A \frac{d}{dz} (G u_m) \delta z dA + \int_A \rho_H g \cdot \sin \theta \cdot \delta z \cdot dA, \quad (212)$$

where P is the pressure, τ_w is the wall friction stress, G is the mass flux, ϑ is the inclination angle, g is the gravity acceleration, dz is the differential axial distance along the channel, δz is the infinitesimal axial distance in the channel, u_m is the mixture velocity, S is the channel circumference, A is the area of the flow channel, and ρ_H is the homogeneous mixture density as a function of flow quality, given by Eq. (213) [WAL1969]:

$$\frac{1}{\rho_H} = \frac{x_e \rho_\ell + (1-x) \rho_g}{\rho_g \cdot \rho_\ell}. \quad (213)$$

Equation (212) can be transformed into the following equation after performing some algebraic simplifications and removing the integrals:

$$-\frac{dP}{dz} = \frac{S}{A} \tau_w + \frac{d}{dz} \left(\frac{G^2}{\rho_H} \right) + \rho_H g \sin \theta. \quad (214)$$

By substituting the fluid density from Eq. (213), the pressure drop equation can be obtained in the following form:

$$-\frac{dP}{dz} = \frac{S}{A} \tau_w + G^2 \frac{d}{dz} \left(\frac{x_e}{\rho_g} + \frac{(1-x_e)}{\rho_\ell} \right) + \rho_H g \sin \theta. \quad (215)$$

Equation (215) contains three pressure drop components on the right side: friction, acceleration, and gravity:

$$-\frac{dP}{dz} = - \left[\left(\frac{dP}{dz} \right)_f + \left(\frac{dP}{dz} \right)_a + \left(\frac{dP}{dz} \right)_e \right]. \quad (216)$$

The negative sign in the above equation indicates that pressure decreases along the flow path.

Separated flow model

In a separated flow model, both flow phases are treated separately, and therefore Eq. (212) takes on the following form:

$$\int_A \left[P - \left(P + \frac{dP}{dz} \delta z \right) \right] dA = \int_S \tau_w \cdot \delta z \cdot dS + \int_A \frac{d}{dz} (G_\ell u_\ell + G_g u_g) \delta z dA + \int_A \rho_H g \cdot \sin \theta \cdot \delta z \cdot dA. \quad (217)$$

The mixture density can be assumed to be a function of the two-phase void fraction as given by the following relation:

$$\rho_{TP} = \alpha \cdot \rho_g + (1-\alpha) \cdot \rho_\ell. \quad (218)$$

By substituting Eq. (218) into Eq. (217), the pressure drop equation can be expressed as (in the same form as Eq. (215)):

$$-\frac{dP}{dz} = \frac{S}{A} \tau_w + \frac{d}{dz} \left[(1-\alpha) G_\ell u_\ell + \alpha \cdot G_g u_g \right] + \left[\alpha \cdot \rho_g + (1-\alpha) \rho_\ell \right] \cdot g \cdot \sin \theta . \quad (219)$$

Further developing the acceleration term using the relationship between the mixture and phasic mass flux leads to the following expression for the separated flow pressure drop:

$$-\frac{dP}{dz} = \frac{S}{A} \tau_w + G^2 \frac{d}{dz} \left[\frac{x_a^2}{\alpha \cdot \rho_g} + \frac{(1-x_a)^2}{(1-\alpha) \cdot \rho_\ell} \right] + \left[\alpha \cdot \rho_g + (1-\alpha) \rho_\ell \right] \cdot g \cdot \sin \theta . \quad (220)$$

The frictional pressure loss occurs between the fluid and the channel wall. It depends primarily on the fluid velocity, the tube diameter, and the fluid viscosity.

The acceleration pressure losses occur because of the change in fluid momentum between different locations in the channel. They can be significant in channels with varying flow area and fluid temperature.

The gravity-induced pressure loss in fact occurs because of a change in elevation, i.e., a change of hydrostatic head. Therefore, it is relevant in vertical channels, particularly in piston flow. In single-phase closed loops, the hydrostatic head in sections with upward flow cancels with that in sections with downward flow.

Local pressure losses can result from many different flow obstructions such as valves, orifices, bundle junctions, and appendages. In addition, changes in flow direction in elbows, T-junctions, etc., can result in pressure losses. Significant pressure losses occur with sudden changes in flow area such as sudden contractions, expansions, and orifices.

Using a term for local pressure losses as explained above, Eq. (216) can be written in the following form:

$$-\frac{dP}{dz} = - \left[\left(\frac{dP}{dz} \right)_f + \left(\frac{dP}{dz} \right)_a + \left(\frac{dP}{dz} \right)_e + \left(\frac{dP}{dz} \right)_l \right] . \quad (221)$$

7.5.3 Correlations for calculating pressure losses

Equation (221) has four terms for which correlations must be developed. Before describing these correlations, it is necessary to define them.

Frictional pressure loss

The frictional pressure loss for a single-phase liquid flow is defined by the following relation [IAEA2001]:

$$\Delta p_f = \frac{f \cdot L \cdot G^2}{2 D_{hy} \rho_\ell} = \frac{f \cdot L}{D_{hy}} \frac{W^2}{2 \rho_\ell A^2} , \quad (222)$$

where L is the pipe length, G is the mass flux, D_{hy} is the hydraulic diameter (equal to four times the flow area/the wetted perimeter), ρ_l is the liquid density, W is the mass flow rate, A is the pipe cross section, and f is the friction factor. The frictional pressure drop occurs all along the length and is hence referred to as distributed pressure drop. This equation is applicable for single-phase and homogeneous two-phase flows, although the methods of calculating the

friction factor, f , and the density, ρ , differ in the two cases. Pressure drops across tubes, rectangular channels, bare annuli, and a bare rod bundle (i.e., without spacers) are examples of this component. The challenge in the above equation is to define the appropriate friction factor f for the given flow conditions. This process is described in the following sub-sections.

Acceleration pressure loss

This reversible component of pressure loss is caused by a change in flow area or density. Expansion, contraction, and fluid flow through a heated section are examples. The acceleration pressure loss due to flow area changes can be expressed as [IAEA2001]:

$$\Delta P_a = G^2 \Delta v_l \varphi = \frac{(1 - A_r) W^2 \varphi}{2 A_0^2 \rho_l} \quad (223)$$

The term Δv_l describes the velocity difference between two points in the channel, A_r is the ratio of the smaller to the larger flow area, A_0 is the smaller flow area, and φ is equal to 1 for single-phase flow. For two-phase flow, φ is described by the following relation [IAEA2001]:

$$\phi = \left(\frac{x^3}{\rho_g^2 \alpha^2} + \frac{(1-x)^3}{\rho_l^2 (1-\alpha)^2} \right) \left(\frac{\rho_g \rho_l}{x \cdot \rho_l + (1-x) \cdot \rho_g} \right) \quad (224)$$

The acceleration pressure loss due to density change for single-phase and two-phase flows can be expressed as:

$$\Delta p_a = G^2 \left\{ \left(\frac{1}{(\rho_m)_o} \right) - \left(\frac{1}{(\rho_m)_i} \right) \right\} \quad (225)$$

For single-phase flows, this component is negligible, but it can be significant in two-phase flows. For two-phase flow, the above equation can be used with ρ_m given by [IAEA2001]:

$$\frac{1}{\rho_m} = \left(\frac{x^2}{\rho_g \cdot \alpha} + \frac{(1-x)^2}{\rho_l (1-\alpha)} \right) \quad (226)$$

To evaluate acceleration pressure loss due to density change, accurate prediction of fluid density is necessary. For single-phase flow, fluid density can be predicted reasonably well using established relationships for thermo-physical properties of fluids. For two-phase flow, it is necessary to predict the void fraction, and in turn the acceleration pressure loss, accurately to determine density. Hence, the correlation for void fraction must be chosen carefully.

Elevation pressure loss

This reversible component of pressure loss is caused by the difference in elevation and can be expressed as:

$$\Delta p_e = [\rho_g \cdot \alpha + \rho_l (1-\alpha)] \cdot g \cdot \sin \theta \cdot \Delta z \quad (227)$$

Local pressure losses

These are the localized irreversible pressure loss components caused by changes in flow

geometry and flow direction. Pressure drops across valves, elbows, tees, and spacers are examples. The local pressure loss (i.e., the form loss) is defined by the following relation [IAEA2001]:

$$\Delta p_l = K_l \frac{G^2}{2\rho_l}, \quad (228)$$

where K_l is the local form loss coefficient, which has different correlations for different geometries, single-phase flows, and two-phase flows. The challenge in the above equation is to define the local friction factor coefficient K_l properly. This topic is covered in the following subsections.

7.5.3.1 Frictional pressure drop correlations in single-phase flow

For friction pressure loss correlations, circular pipe, annuli, rectangular channels, and rod clusters are the most common applications. For local pressure loss correlations, spacers, top and bottom tie plates, and locations of flow area changes such as constrictions, expansions, bends, tees, and valves are the most common applications. For CANDU-type fuel bundles, the degree of misalignment of two adjacent fuel bundles is also important in estimating the pressure drop. In addition, in-core effects like radiation-induced creep, blister formation, swelling, and corrosion are also important factors affecting pressure drop, but are not dealt with here.

Figure 82 shows the Moody chart for friction factor as a function of Reynolds number and pipe roughness [MOO1944, IDE1996]. This logarithmic diagram is the basis for calculating friction factors in single-phase flow in pipes. On the left side is the area of laminar flow, represented by a single straight line. Towards the right side, a group of lines is shown that indicate higher friction factors for higher values of pipe roughness and slowly declining friction factors for higher Reynolds numbers.

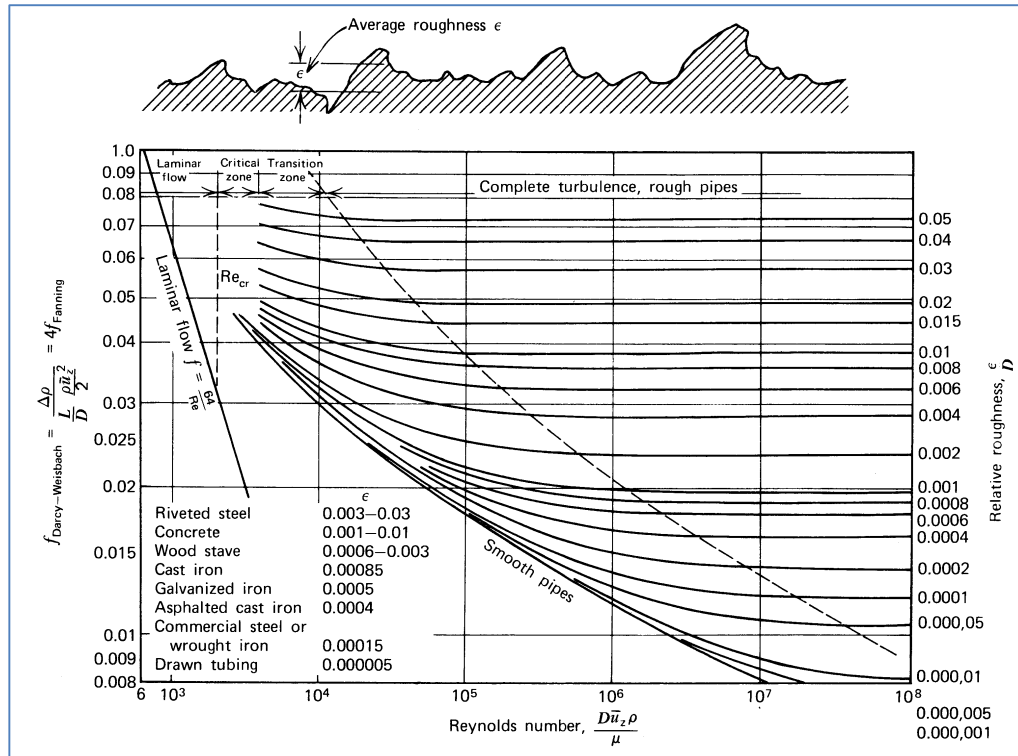


Figure 82 Moody chart for friction factors

For fully developed laminar flow, the friction factor is given by [IAEA2001]:

$$f = \frac{64}{Re}, \quad (229)$$

which is valid for Reynolds numbers less than 2000, as given by Eq. (12). This correlation is shown by a straight line on the left side of Figure 82.

For turbulent flow in smooth pipes, several friction factor correlations have been proposed and are used. A few commonly used correlations for smooth pipe are given below.

The Blasius equation [AECL2001] has the following form:

$$f = 0.316 \cdot Re^{-0.25}, \quad (230)$$

which is valid in the range of $3000 \leq Re \leq 10^5$.

The following equation, which is valid in the range of $3000 \leq Re \leq 10^5$, is also often used for design [IAEA2001]:

$$f = 0.184 \cdot Re^{-0.2}. \quad (231)$$

Colebrook-White (1938) proposed the following equation, which is valid for both smooth and rough pipes over the whole range of Reynolds numbers above 3000 [IAEA2001]:

$$\frac{1}{\sqrt{f_{tube}}} = -2 \cdot \log \left(\frac{\epsilon / D_{tube}}{3.7} + \frac{2.51}{Re \cdot \sqrt{f_{tube}}} \right). \quad (232)$$

This correlation is often used in computer codes, but it requires several iterations because it is not explicit in terms of the friction factor f . Many other correlations attempt to capture different effects such as different parameter ranges or heat transfer effects. These include changes in near-wall velocity gradient due to fluid density changes, bubble formation, sharp variations due to liquid-film thinning, and liquid-surface or vapour-surface contact. These all create different wall heating effects that have a significant impact on the friction factor, even before two-phase flow occurs.

7.5.3.2 Frictional pressure drop correlations in two-phase flow

Many two-phase flow pressure drop correlations can be found in the literature. These correlations can be classified into the following four general categories: (1) empirical correlations based on the homogeneous model; (2) empirical correlations based on the two-phase friction multiplier concept; (3) direct empirical models; and (4) flow pattern-specific models.

In addition, computer codes based on two-fluid or three-fluid models require correlations to partition wall friction among the fluids and to determine interfacial friction correlations.

The most commonly used approach is the two-phase multiplier approach, which is described in this section. In this case, the two-phase pressure drop is calculated by multiplying the single-phase pressure drop by a two-phase frictional multiplier. Equation (233) exemplifies this approach:

$$\Delta p_{f,TP} = \phi_{L0}^2 \Delta p_{f,L0} \quad \text{or} \quad \Delta p_{f,TP} = \phi_L^2 \Delta p_{f,L}, \quad \phi_{L0}^2 = \phi_L^2 (1-x)^{2-b}, \quad (233)$$

where $\Delta p_{f,L}$ is the single-phase pressure drop based on only single-phase liquid in the channel and $\Delta p_{f,L0}$ is the single-phase pressure drop based on total flow as single-phase liquid in the channel. Assuming $f = a \cdot \text{Re}^{-b}$, the relationship between ϕ_{L0}^2 and ϕ_L^2 can be expressed as $\phi_{L0}^2 = \phi_L^2 (1-x)^{2-b}$.

The two-phase frictional multipliers ϕ_L^2 or ϕ_{L0}^2 are empirical factors based on experimental data and are expressed in the form of graphs or correlations that typically depend on quality and pressure. A mass-flux effect is observed primarily at low flows (and hence is flow-regime-dependent). Surface heating has a strong impact (a near-wall effect) on two-phase multipliers in tubes and annuli, but not in bundles (due to compensating effects).

The correlation for a homogeneous two-phase frictional multiplier in its simplest form can be expressed as:

$$\phi_{L0}^2 = \frac{f_{TP}}{f_L} \frac{\rho_\ell}{\rho_{TP}} = \left[1 + x_e \left(\frac{\rho_\ell - \rho_g}{\rho_g} \right) \right] \left(\frac{\mu_\ell}{\mu_{TP}} \right)^{-b}. \quad (234)$$

The two-phase viscosity correlation can have various forms with different degrees of complexity. The simplest correlation was introduced by Cicchitti *et al.* [IAEA2001]:

$$\mu_{TP} = x_a \cdot \mu_g + (1 - x_a) \mu_l. \quad (235)$$

In general, the following definitions of two-phase frictional multipliers are often used in non-homogeneous two-phase flow:

$$\phi_{LO}^2 = \frac{(dp/dz)_{TPF}}{(dp/dz)_{LO}}, \quad \phi_{GO}^2 = \frac{(dp/dz)_{TPF}}{(dp/dz)_{GO}}, \quad (236)$$

$$\phi_L^2 = \frac{(dp/dz)_{TPF}}{(dp/dz)_L}, \quad \phi_G^2 = \frac{(dp/dz)_{TPF}}{(dp/dz)_G}, \quad (237)$$

where the denominators refer to the single-phase pressure gradient for flow in the same duct, with mass flow rates corresponding to the mixture flow rate in the case of ϕ_{LO}^2 and ϕ_{GO}^2 , and individual phases in the case of ϕ_L^2 and ϕ_G^2 . Among these, ϕ_{LO}^2 is the most popular frictional multiplier for steam-water flow. Figure 83 shows a popular form of this two-phase friction multiplier suggested by Nelson-Martinelli [COL1972]. The frictional multiplier is shown as a function of mass quality and pressure. It rises sharply when two-phase flow is initiated (even for very small mass qualities), and its value reaches 10 times the single-phase value even at low quality. Moreover, the friction multipliers are higher at low pressure than at high pressure due to the difference in volumetric and mass flow rates (as shown in Figure 22).

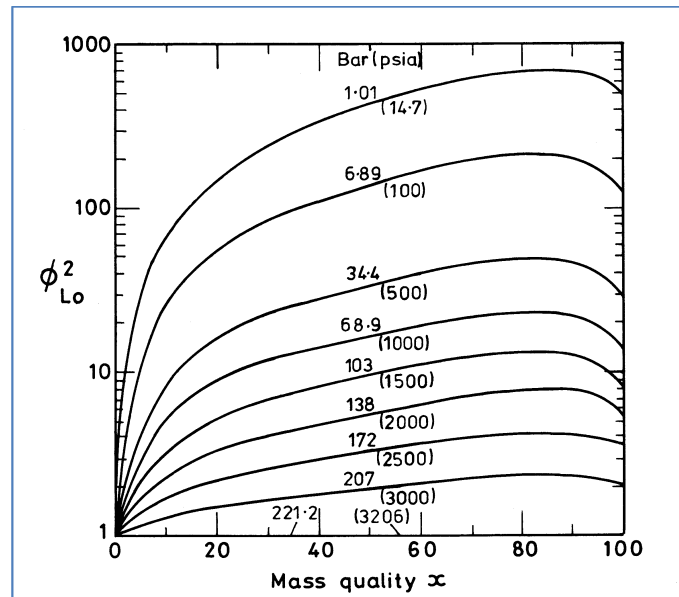


Figure 83 Martinelli-Nelson two-phase multiplier in separated flow

For diabatic two-phase flow (i.e., flow with heat transfer), the quality, void fraction, flow pattern, and other properties change along the heated section. To calculate the pressure drop in such cases, two approaches are usually followed. In the first approach, which is most commonly used, the average ϕ_{LO}^2 is calculated as:

$$\phi_{LO}^2 = \frac{1}{L} \int_0^L [\phi_{LO}^2(z)] dz. \quad (238)$$

The approach can be used in cases where $\phi_{LO}^2(z)$ is a function that can be integrated. Numerical integration is used in other cases.

In the second approach, the heated section is subdivided into a number of small segments. Based on average conditions (i.e., x_i , α_i and flow pattern) in that segment, the pressure drop is calculated as in adiabatic two-phase flow using one of the models described previously.

7.5.3.3 Local pressure drop correlations

The single-phase local pressure losses are given in Eq. (228). The two-phase local pressure losses are normally obtained using the two-phase multiplier approach. In this case, the two-phase local pressure loss is given by the following relation [IAEA2001]:

$$\Delta P_{l,TP} = \phi_{l,LO}^2 \cdot \Delta P_{l,SP}. \quad (239)$$

A simple form of the two-phase local loss multiplier can be obtained by the following relation:

$$\phi_{l,LO}^2 = 1 + x_d \left(\frac{\rho_l - \rho_g}{\rho_g} \right). \quad (240)$$

Sudden contraction

Single-phase loss coefficients for sudden contraction can be calculated based on flow-area ratio, according to the following equation [IDE1996]:

$$K_{contr} = 0.5 \left(1 - \frac{A_f}{A_o} \right)^{3/4}, \quad (241)$$

where A_f and A_o are smaller and larger pipe cross-sectional areas respectively.

In general, the irreversible pressure two-phase pressure drop due to a flow-area change is estimated from the knowledge of single-phase loss coefficient using an appropriate model.

Sudden expansion

In the case of sudden expansion, the following correlation is used, which is based on the ratio of area changes [IDE1996]:

$$K_{exp} = \left(1 - \frac{A_f}{A_o} \right)^2. \quad (242)$$

Fitzsimmons (1964) provides the following equation to calculate the pressure change across an abrupt expansion:

$$\Delta p = \frac{G^2 A_r^2}{\rho_L} \left\{ \frac{\rho_l}{\rho_g} x^2 \left(\frac{1}{\alpha_1 A_r} - \frac{1}{\alpha_2} \right) \right\} \left\{ (1-x)^2 \left(\frac{1}{(1-\alpha_1) A_r} - \frac{1}{(1-\alpha_2)} \right) \right\}, \quad (243)$$

where subscripts 1 and 2 refer respectively to the upstream and downstream locations of the abrupt expansion and $A_r = A_f / A_0$.

Fittings and bends

The single-phase pressure drop due to bends and fittings can be calculated using the appropriate loss coefficients from Idelchik [IDE1996]. For bends, the loss coefficient depends on the bend angle, i.e., on the ratio of pipe diameter to bend radius. Because pressure drop is dependent on piping component geometry, other specific configurations (i.e., end-fitting flow characterization) must be experimentally tested to determine the specific pressure drop correlations.

Orifices

The pressure loss through an orifice can be calculated using the following equation [IDE1996]:

$$\Delta p_{orf} = f_{orf} \frac{\rho W_0^2}{2} \phi_{LO}^2. \quad (244)$$

The loss coefficient in an orifice depends on the orifice geometry, particularly at the orifice entry. An extensive description of loss coefficients with different orifices in single-phase flow is provided by Idelchik [IDE1996]. For separated two-phase flow (stratified) at an orifice, Beattie [IAEA2001] obtained the following expression for ϕ_{LO}^2 :

$$\phi_{LO}^2 = \left\{ 1 + x \left(\frac{\rho_L}{\rho_G} - 1 \right) \right\}^{0.8} \left\{ 1 + x \left(\frac{\rho_L \mu_G}{\rho_L \mu_L} - 1 \right) \right\}^{0.2}. \quad (245)$$

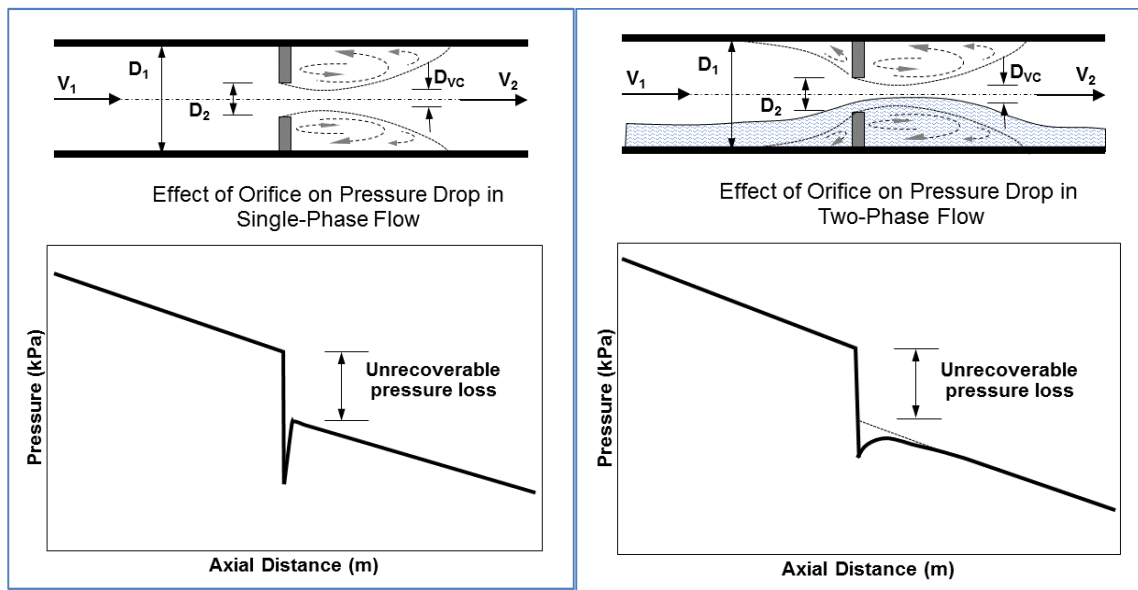


Figure 84 Single-phase pressure distribution over a square-edged orifice

Figure 85 Two-phase pressure distribution over a square-edged orifice

Figure 84 shows a diagram of a pressure loss in a square-edged orifice in a single-phase liquid

flow with 40% blocked area (a blunt-edged orifice). The pressure falls sharply over the orifice because of the sudden increase in velocity (according to the Bernoulli equation, Eq. (43)). Due to turbulence downstream of the orifice, unrecoverable losses occur because mechanical energy is dissipated into thermal energy. Therefore, downstream of the orifice, where the pipe diameter is the same as that upstream of the orifice, the pressure is lower than it would have been without the orifice.

Figure 85 shows the two-phase pressure distribution over the same orifice as in Figure 84. The pressure drop slope is much higher in two-phase flow than in single-phase flow, which signifies an increase in frictional pressure drop. In addition, the unrecoverable losses are much higher, and the pressure recovery occurs over a longer pipe section (pressure recovery is “smoother”).

Grid spacers and tie plates

Because of the variation and complexity of their geometry, it is extremely difficult to establish a pressure loss coefficient correlation of general validity for grid spacers. However, calculation methods that are reasonably accurate for design purposes can be achieved. To determine pressure drop across spacers more precisely, experimental studies are required.

Generally, tie plates are used at the ends of rod cluster fuel elements and structurally join all the fuel pins. Unlike spacers, the flow areas on the downstream and upstream sides of tie plates are different. Moreover, they are generally located in the unheated portion of the bundle. An approximate calculation for design purposes can be made using the contraction and expansion model for local pressure losses. In addition, the friction losses over the thickness of the tie plates can be calculated using the hydraulic diameter concept. For two-phase pressure losses, the homogeneous or slip model described above can be used.

7.5.3.4 Pressure losses in CANDU fuel bundles

Several short bundles are stacked end-to-end in CANDU-type PHWRs instead of the long single fuel bundle used in PWRs and BWRs. Due to this basic difference in design concept, some of the issues and geometries are unique to the CANDU design.

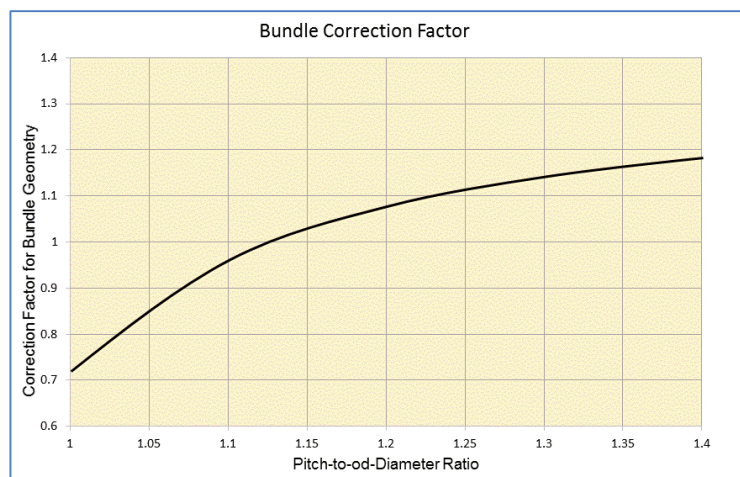


Figure 86 Bundle correction factor (37-element hexagonal bundle)

The pressure losses in CANDU bundles are calculated based on the hydraulic-equivalent

diameter approach using a tube-based equation. Several correction factors are used, including a correction for geometric effects (the differences between tubes and bundles); a correction for eccentricity effects (differences between concentric and eccentric bundles) in crept channels; a correction for channel shape effect (converging and diverging channels) in crept channels; and a correction for surface heating effect.

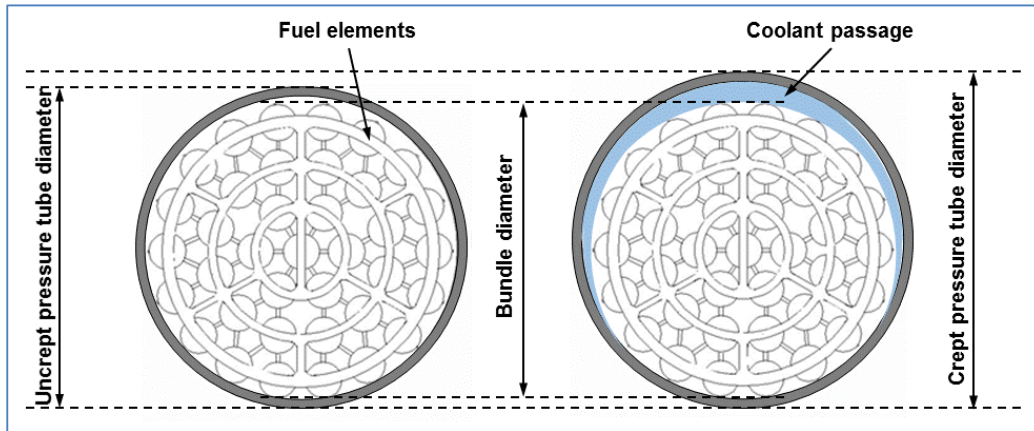


Figure 87 Eccentricity effect

Figure 86 shows a sample of the fuel bundle effect in a hexagonal fuel bundle [LEU2004]. The correction factor is given as a function of the pitch-to-rod-diameter ratio. It is evident from this figure that the correction factor can be greater than or less than one.

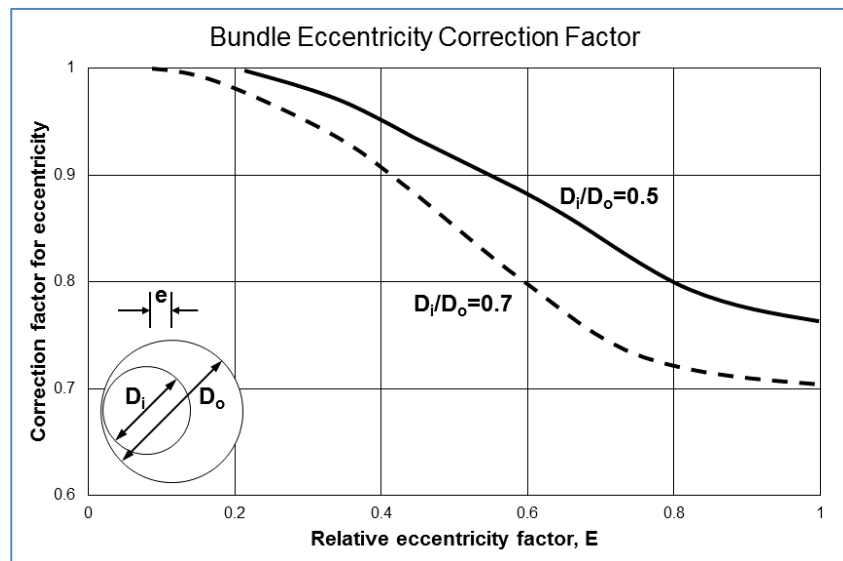


Figure 88 Eccentricity correction factor

Figure 87 shows [LEU2004] on the left side a cross section of the fresh CANDU fuel bundle in an uncrept channel, and on the right side the same bundle in a crept channel, in which the pressure tube diameter has increased after a number of years of irradiation. It is evident that the eccentricity of the irradiated fuel bundle has significantly increased. The effect of eccentricity increase in an annular channel on the friction correction factor is shown in Figure 88. This figure shows that the correction factor for eccentricity decreases from one to a certain

value that depends on the degree of eccentricity and on the ratio of the inner and outer rod diameters. Pressure tube creep and development of significant bundle eccentricity lead more fluid to flow at the top of the bundle where the resistance to flow is lower, thus leaving the bundle with reduced fluid flow. This phenomenon also results in development of a non-uniform velocity distribution in the fuel channel.

The following empirical correlation was proposed by Snoek and Ahmad [IAEA2001] for a friction factor based on experiments on a six-metre long electrically heated horizontal 37-rod cluster (this correlation has not been validated or accepted for a CANDU fuel bundle):

$$f = 0.05052 \cdot Re^{-0.05719} \quad \text{for } 108,000 \leq Re \leq 418,000. \quad (246)$$

The following empirical correlations were proposed by Venkat Raj [IAEA2001] based on a set of experiments with prototype horizontal 37-rod clusters for PHWRs with a CANDU-type spacer. They include the junction pressure drop (these correlations have not been validated or accepted for a CANDU fuel bundle):

$$f = 0.22 \cdot Re^{-0.163} \quad \text{for } 10,000 \leq Re \leq 140,000, \quad (247)$$

$$f = 0.108 \cdot Re^{-0.108} \quad \text{for } 140,000 \leq Re \leq 500,000.$$

However, in addition to the above friction factor, in a CANDU fuel bundle, a number of local pressure losses must be taken into account. The total CANDU bundle pressure losses must include: (1) friction; (2) local resistances from bundle junctions, spacers, buttons (43-element bundle), and bearing pad planes; (3) acceleration; and (4) end fittings.

Various authors have attempted to combine the above effects into a single pressure loss correlation. The friction and form losses have been combined into a bundle loss coefficient given by the following relation [LEU2004, IAEA2001]:

$$\Delta P_{sp,bundle} = K_{sp,bundle} \frac{G^2}{2\rho_\ell} = \left(\frac{f_{bundle} L_{bundle}}{D_{hy}} + K_{junction} + K_{appendage} \right) \frac{G^2}{2\rho_\ell}. \quad (248)$$

The best approach for CANDU fuel bundles is to perform experimental measurements of the pressure losses in a CANDU fuel channel experimental apparatus, i.e., in a so-called fuel bundle or fuel channel flow characterization test. Once pressure losses have been precisely measured for a fuel channel design, they can be tabulated or correlated in a convenient way for use by designers and analysts.

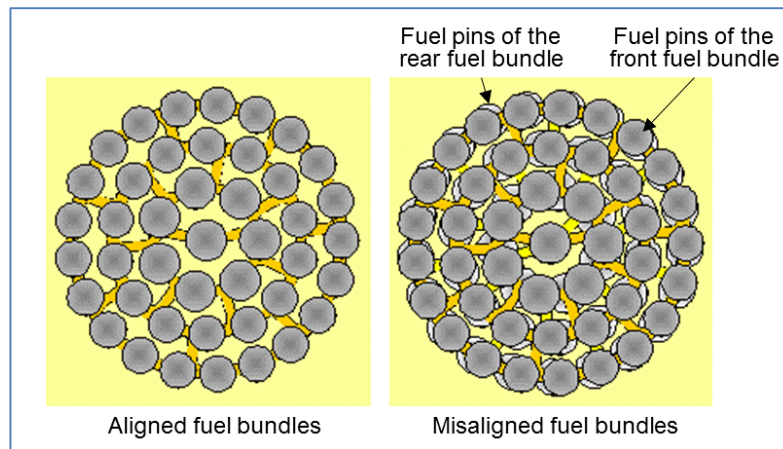


Figure 89 Bundle junction misalignment effect

One of the important contributors to pressure losses in CANDU fuel bundles is fuel bundle misalignment. Figure 89 shows two CANDU fuel channels that visually illustrate this phenomenon [LEU2004]. The channel on the left has all fuel bundles aligned, so that each fuel element is behind the previous fuel element upstream. This perfect alignment achieves the lowest possible pressure loss from local resistance at the bundle end plates. However, in practice, this perfect alignment is not possible because fuelling machines cannot ensure that bundles are always inserted in a channel in the same position. In practice, as fuel bundles are repeatedly inserted into the fuel channel, this misalignment develops a random distribution, as shown on the right side of Figure 89. Pressure loss measurements are therefore performed with various degrees of misalignment to cover all possible situations that can arise in practice.

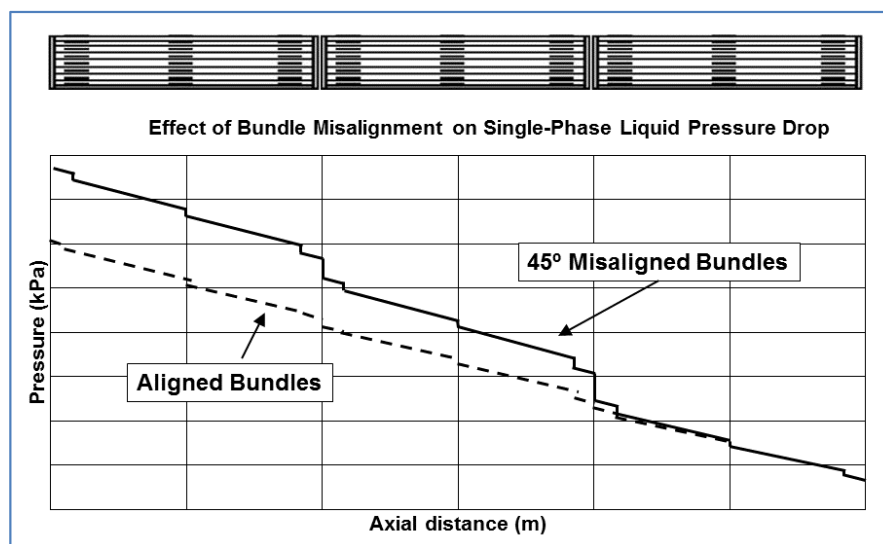


Figure 90 Typical single-phase pressure distribution over misaligned bundles

Figure 90 shows a comparison of typical pressure drops in single-phase flow with three bundles with a misalignment of 45° compared to fully aligned bundles. This figure clearly shows that at each bundle junction, an abrupt local pressure loss can be measured. If the bundles are

misaligned to a greater extent, the abrupt pressure drop at the junction will be larger.

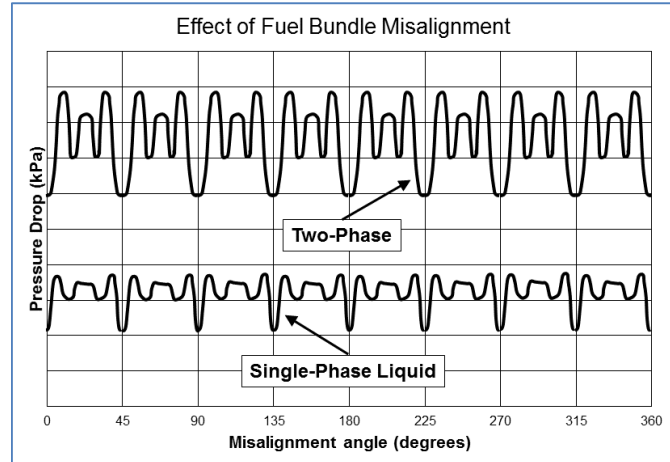


Figure 91 Typical pressure drop in misaligned fuel bundles

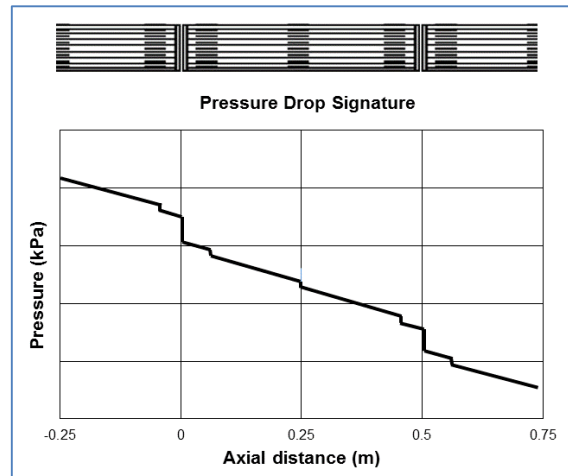


Figure 92 Typical misaligned junction pressure drop signatures

Figure 91 shows a CANDU fuel bundle flow characterization test in which actual pressure measurements were collected along the fuel bundle [LEU2004]. It is evident that each change of flow area along the fuel bundle, such as bundle end plates, spacers, buttons, and bearing pads, creates a clear pressure loss of magnitude proportional to the change in flow area. It is obvious from this figure that the pressure drop variation is symmetrical within a 45 degree cycle.

Figure 92 shows a pressure drop signature from misaligned fuel bundles [LEU2004]. It is clear that the degree of misalignment has a direct impact on the pressure drop measurements. The effect is more pronounced in the case of two-phase flow, in which case the difference in the measured pressure drops is much higher, both in absolute value and in variability with the level of misalignment.

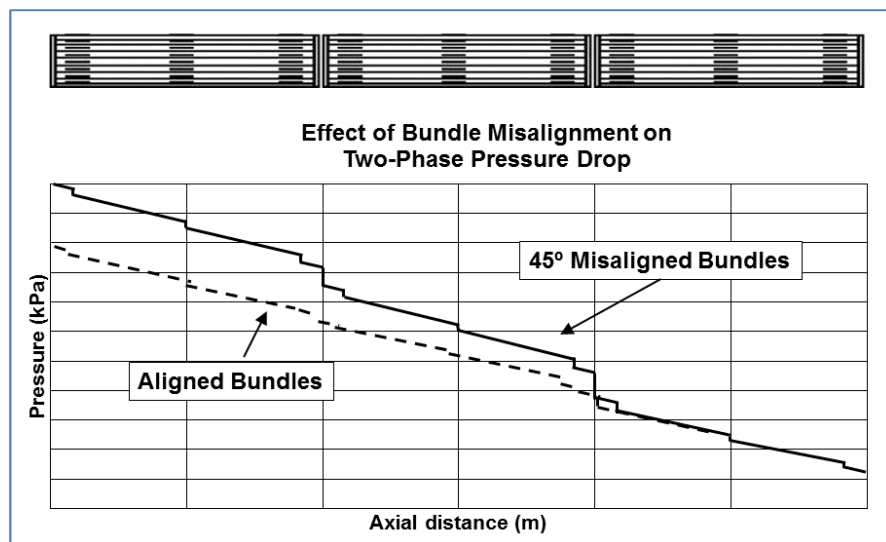


Figure 93 Typical two-phase pressure distribution over misaligned bundles

Figure 93 shows a typical pressure drop effect for misaligned fuel bundles in two-phase flow. This figure should be compared to Figure 90, which shows the same test in single-phase flow. Again, the absolute value of the pressure drop is higher in the case of two-phase flow, and the pressure losses at the bundle end plates are also higher.

7.5.3.5 Use of pressure drop measurements to define the onset of significant void (OSV)

Because pressure drop measurements show such distinctive differences in pressure drop between single-phase and two-phase cases, it has been noted that a sudden increase in pressure drop at a certain location in a thermal-hydraulic network can be used as an indication of the initiation of bulk boiling (i.e., the onset of significant void (OSV)).

Figure 94 shows pressure drop measurements for a crept fuel channel in which three different power rates were applied, resulting in different channel boiling outcomes [LEU2004, POP2014]. The coolant inlet was on the left side and the outlet on the right side. The reference case (dark blue line) is the case of sub-cooled conditions, with outlet thermodynamic quality negative and nominal channel power. When channel power was increased to greater than 200%, the pressure drop increased significantly downstream of the ninth fuel bundle because in this area boiling was initiated, resulting in slightly positive channel outlet thermodynamic quality. When the channel power was increased to three times nominal power, the outlet thermodynamic quality further increased, and the pressure drop as well. Note that when boiling starts at a certain location downstream (in this case, around the eighth fuel bundle), the pressure drop starts to increase, which indirectly indicates the point where OSV occurs in this channel. Hence, pressure drop measurements can reveal where boiling occurs in a fuel channel.

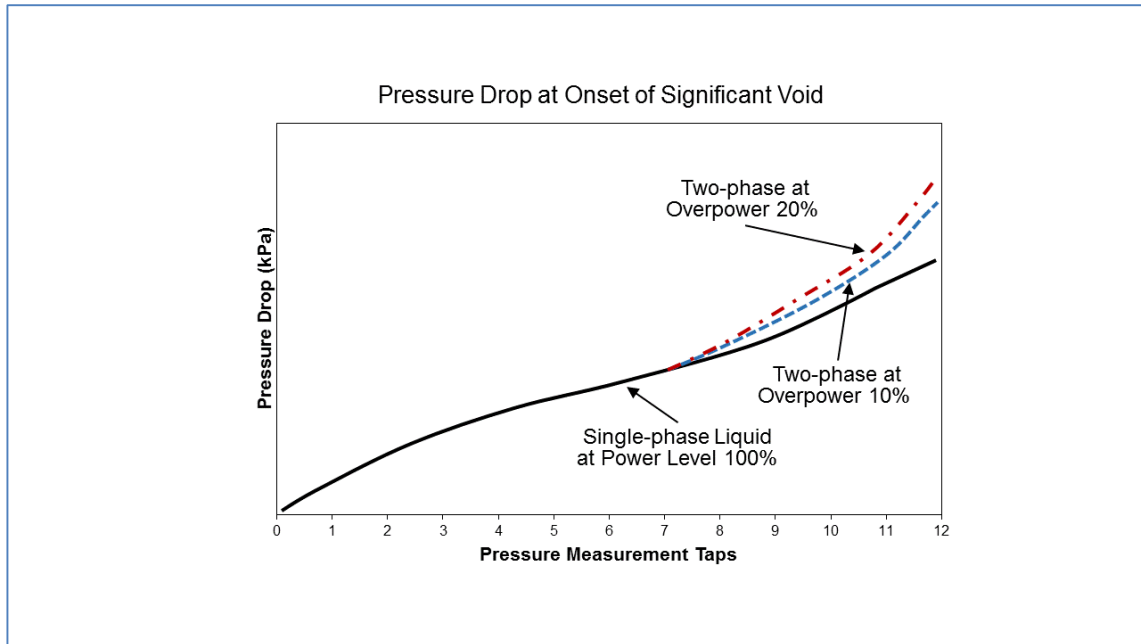


Figure 94 Pressure gradient along a flow channel in boiling

The Saha-Zuber correlation [REL2010, CAT1998, CAT2000, CAT2005] is used to calculate the OSV point in tubes and has the following form:

$$x_{OSV} = -0.0022 \frac{q \cdot D \cdot C_{pf}}{k_f \cdot H_{fg}} \quad \text{for Peclet number } (GDCp/k) < 70,000, \quad (249)$$

$$x_{OSV} = -154 \frac{q}{k_f \cdot H_{fg}} \quad \text{for Peclet number } \geq 70,000. \quad (250)$$

A modified Saha-Zuber correlation for fuel bundles is based on empirical coefficients using full-scale bundle data.

7.5.3.6 Pressure drop in pipes and orifices

The information covered in the previous sections can now be used to describe pressure drop behaviour in a channel with various changes in geometry. Figure 95 shows such an example, in which fluid comes from a pipe on the left side, flows through a pipe with a different diameter and an orifice, and then into a much larger pipe on the right side. Hence, in this example, major abrupt changes in flow cross-sectional area can be observed.

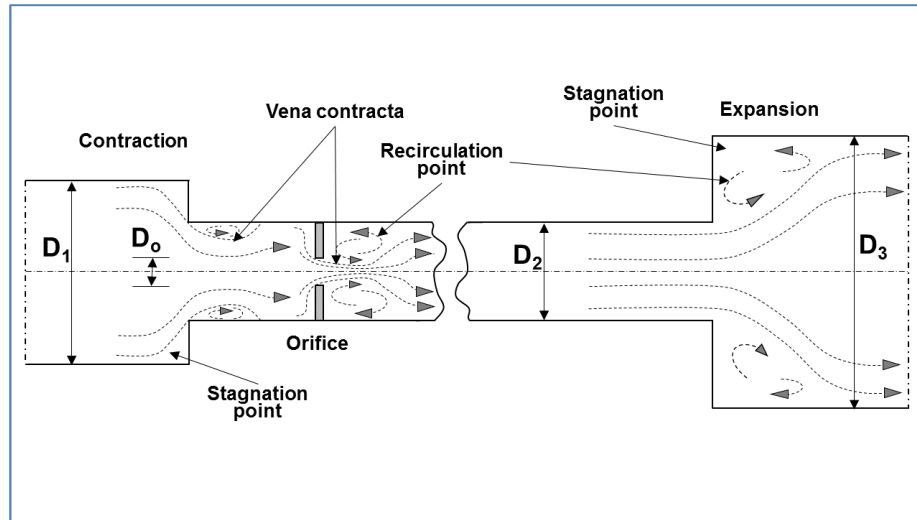


Figure 95 Example of abrupt area changes and orifice

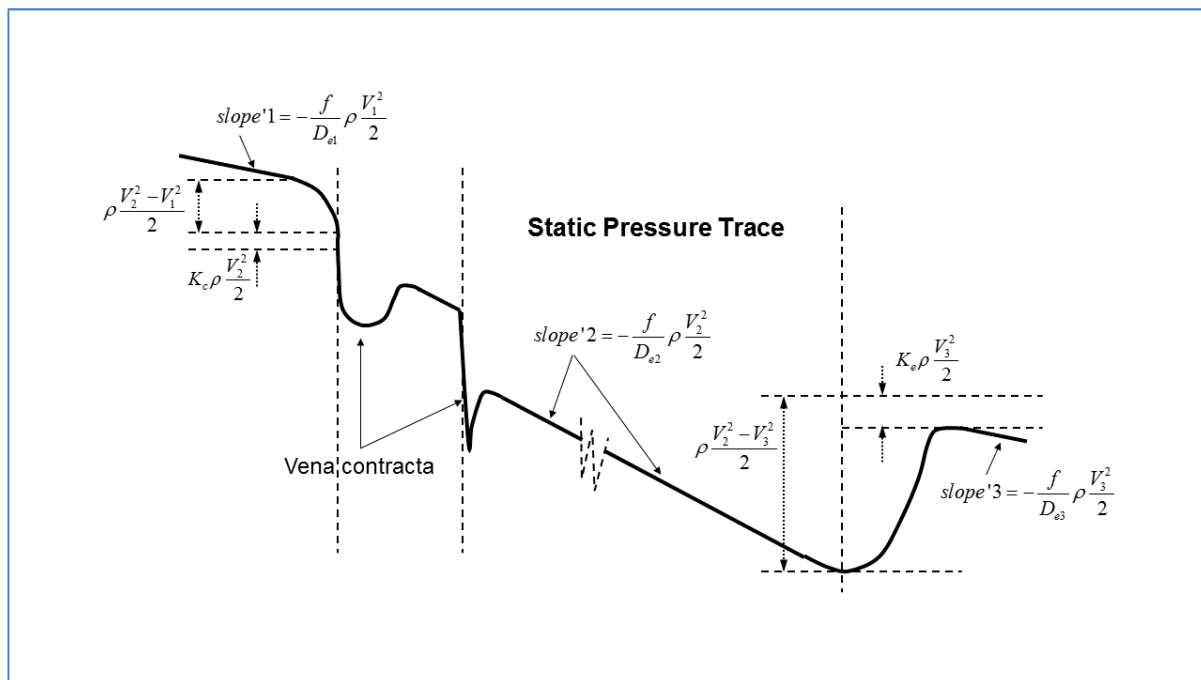


Figure 96 Pressure drop behaviour with abrupt area changes and orifice

The pressure drop diagram for this case is shown in Figure 96. At the transition point between the pipe on the left side (diameter D_1) and the middle pipe (diameter D_2), i.e., at the sudden contraction point, the velocity increases to V_2 . As it accelerates, the fluid goes through a vena contracta with eddy flow around the pipe corners. The recoverable pressure loss resulting from the fluid acceleration is equal to $\rho(V_2^2 - V_1^2)/2$, and the unrecoverable local loss (sudden

contraction) resulting from the turbulence around the vena contracta is $K_e \rho V_2^2 / 2$. The velocity in the vena contracta is higher than the velocity appropriate for the pipe with equivalent diameter D_2 . Therefore, the pressure in the vena contracta decreases further around the area occupied by the vena contracta. Downstream of the vena contracta, the pressure recovers where the influence of the vena contracta terminates, and the fluid velocity assumes the value appropriate for a pipe with diameter D_2 .

Following the sudden contraction, the flow goes through an orifice with diameter D_o , through another vena contracta, and experiences further unrecoverable pressure loss.

On the other side, where the sudden expansion from the pipe into the larger pipe (diameter D_3) occurs, the reverse happens. The velocity slows down in the larger right-hand pipe from V_2 to V_3 . Note that velocity V_3 is different from V_1 because of the different pipe size. At the sudden expansion, the unrecoverable local loss resulting from the turbulence around the vena contracta is $K_e \rho V_3^2 / 2$, and the recoverable deceleration pressure gain is $\rho (V_3^2 - V_2^2) / 2$.

Note that the slope of the pressure drop curve in the three pipes is different because of the different hydraulic diameters of the three pipes.

Having defined all the pressure loss terms in a piping configuration, it is interesting to compare their absolute values and to obtain an impression of their relative contribution to the overall pressure drop. This is done in Figure 97, in which typical pressure drop components are shown for a fuel channel in a typical BWR reactor [TOD2011].

Figure 97 shows that for low mass fluxes, the relative contributions of the friction, acceleration, and gravity terms are similar. However, with increased mass flux, the relative contribution of the friction component significantly outweighs the other components. Note that the friction component in the above figure includes both distributed and local losses.

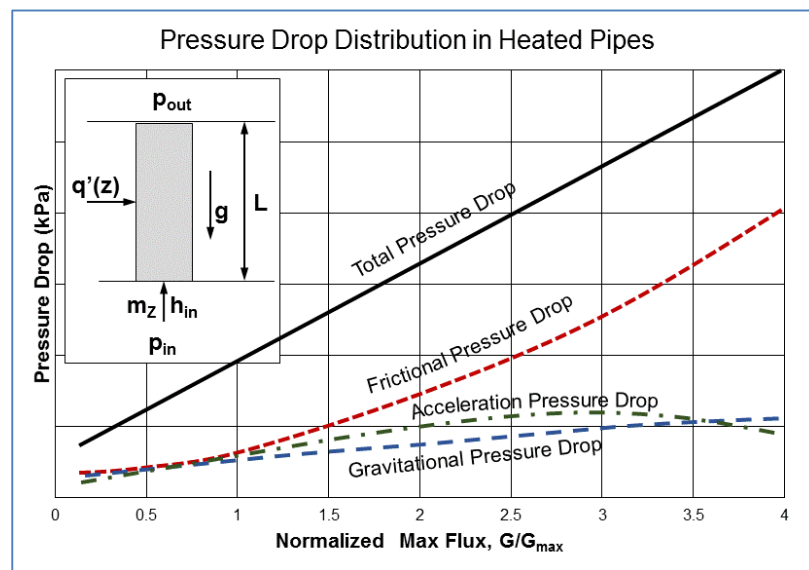


Figure 97 Pressure drop components

7.5.4 Flow Instability

7.5.4.1 Fundamentals of flow instability

Flow instabilities are of particular importance for the reactor core. Under certain flow and heat generation conditions, flow instabilities can cause significant changes in the fluid flow distribution among certain channel groups in the core, thus exposing parts of the core to insufficient cooling and consequent overheating, which can cause fuel damage. Moreover, certain types of flow instabilities can cause pump malfunctions if the pump is not properly selected. This section explains the nature of flow instabilities in the reactor core, provides information on various types of instabilities, and focusses particularly on the Ledinegg instability [TOD2011].

Understanding flow instabilities is instrumental to obtaining a good understanding of the thermal-hydraulic system behaviour of nuclear reactor heat transport systems. A fluid flow in a heated channel with a sub-cooled inlet condition undergoes large volume changes in a non-uniform manner. Because the thermal and hydraulic properties of the flow change continuously along the channel, the flow at any axial point in the channel can never become fully developed thermally or hydrodynamically. Because the flow is not in equilibrium, the flow properties fluctuate upstream and downstream of the point considered, often leading to instability. Flow instabilities are of different types depending on the system configuration and operating conditions. Flow oscillations can dramatically reduce the ability of the coolant to remove heat from the reactor core. On the basis of primary features such as oscillation periods, amplitudes, and relationships between pressure drop and flow rate, flow instabilities have been classified into several types. Flow instabilities in a heated channel are usually caused by two-phase flow and density wave effects. These instabilities are primarily classified as static or dynamic. Some static and dynamic instabilities occur particularly during start-up conditions.

The scale of instability can vary from macroscopic, involving the whole heat transport system, to microscopic, occurring locally in some component or part of the thermal-hydraulic network. In terms of the driving process, instabilities can be grouped into static or dynamic.

A “static instability” occurs when a small perturbation from the original steady-state flow leads to a new stable operating condition that is not close to the original state. The mechanism and the threshold conditions can be predicted using steady-state system characteristics. The pressure drop characteristics, nucleation properties, and flow regime transitions of a flow channel play an important part in characterizing static instabilities. Critical heat flux (CHF), which limits the heat transfer capability of boiling systems, is influenced by static instabilities. Ledinegg instability, flow pattern transition instability, geysering, chugging, and vapour burst are also categorized as static instabilities.

Dynamic instability is caused by dynamic interaction among flow rate, pressure drop, and void fraction. The mechanism involves the propagation of disturbances by pressure and void or density waves. Density wave oscillations (DWOs), parallel channel instability, and pressure drop oscillations (PDOs) are in this group.

Ledinegg instability or flow-excursive instability is characterized by a sudden change in the flow

rate to a lower value or a flow reversal. This instability will be further explained in this section.

Flow pattern transition instability is caused mainly by the different pressure drop characteristics of various flow patterns. For example, if bubbly flow changes to annular flow due to large void generation, the channel pressure drop decreases. For constant pressure drop in a heated channel, when a bubbly flow changes to an annular flow pattern, the flow rate increases, leading to decreased vapour generation. This makes the flow pattern revert to a bubbly or slug flow pattern, and the cycle is repeated.

Geysering occurs at low power and low circulation flow rates. It occurs due to bubble formation, growth, and subsequent collapse during start-up. In vertical channels during start-up, with high inlet sub-cooling, voids are generated, and a large slug of bubbles is formed, which grows due to the decrease in hydrostatic pressure head as it moves toward the exit. The vapour then mixes with the liquid in the sub-cooled riser and becomes condensed there. The condensed liquid re-enters the channel and restores non-boiling conditions. This process repeats periodically and causes flow oscillations.

Vapour burst instability occurs due to sudden vaporization of the liquid phase with a rapid decrease in mixture density. For example, a very clean and smooth heated surface may require high wall superheat for nucleation. The fluid adjacent to the surface is highly superheated, and vapour generation is rapid when nucleation starts. This in turn ejects liquid from the heated channel. Rapid vaporization cools the surface, and the cooler liquid keeps vaporization suppressed until the wall temperature reaches the required nucleation superheat, and the process repeats. Vapour burst instabilities are observed during the reflood phase during re-emergence core cooling of a reactor. Other CHF-related local instabilities are discussed in Section 7.6.

7.5.4.2 Ledinegg flow instability

Ledinegg instability or flow-excursive instability is characterized by a sudden change in the flow rate to a lower value or a flow reversal. This happens when the slope of the channel demand pressure drop vs. flow rate curve (the internal characteristics of the channel) becomes algebraically smaller than that of the loop supply pressure drop vs. flow rate curve (the external characteristics of the channel, or the pump head curve). Physically, this behaviour exists when the pressure drop decreases with increasing flow.

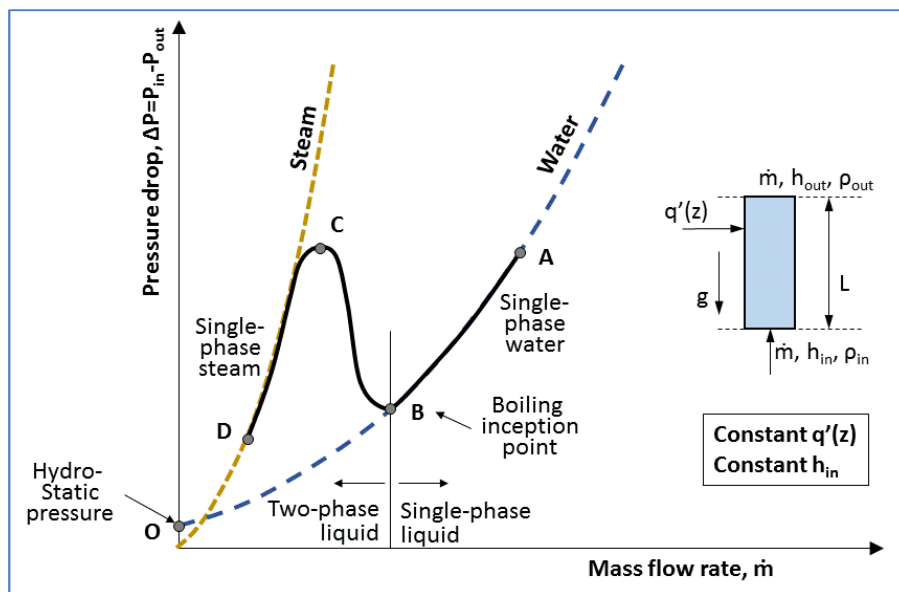


Figure 98 Concept of channel flow instability

Figure 98 shows conceptually the phenomenon of Ledinegg instability [TOD2011]. In this figure, the y-axis represents the pressure drop and the x-axis the mass flow rate. The figure represents a fuel channel in which the fluid mass flow rate and the heating from the walls are selected so that part of the channel is in sub-cooled flow and part of the channel is boiling. The right curve with a shallower slope represents the channel pressure losses for liquid flow. This curve shows the pressure loss as the square of the mass flow rate (i.e., of the fluid velocity). If the channel did not have heating, this curve would have ended at point O' on the y-axis, representing the hydrostatic head of the stagnant water in the channel.

The left curve shows the pressure drop in the channel when the flow is only gas. This curve is steeper for a given mass flow rate because the difference between the densities of water and gas is almost three orders of magnitude. Therefore, a given mass flow rate of gas results in a much higher volumetric flow of gas compared to liquid, and therefore the velocity of the gas and its associated pressure drop for a given volumetric flow are much greater than those of liquid. The gas pressure drop curve ends almost at the zero point of the y-axis because the hydrostatic pressure of gas is negligible compared to that of liquid.

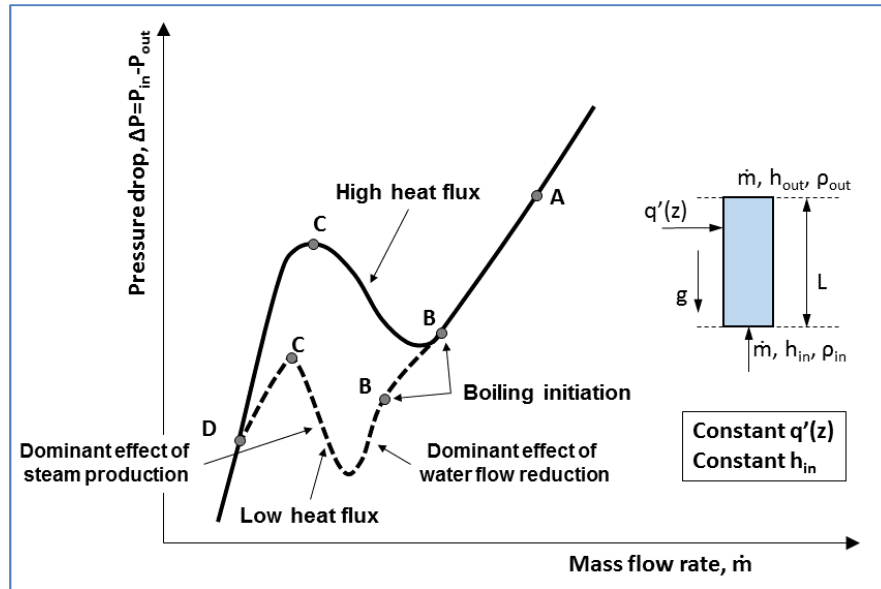


Figure 99 Channel flow instability under low heat flux

With the above explanation, it is possible to analyze the case with heating in the channel and the occurrence of two-phase flow, shown by the thicker solid line in Figure 98. When the mass flow rate is reduced to a point when two-phase flow occurs (consistent with the OSV explanation in Section 7.5.3.5), two phenomena occur:

- the volumetric flow starts to increase for the same mass flow, and therefore fluid velocity is higher for the same mass flow rate; and
- the friction factor becomes higher in two-phase flow (see Section 7.5.3.2).

The net result is that as the mass flow rate decreases, more of the liquid is converted to steam, resulting in higher volumetric flow and higher velocity, and hence the pressure drop increases. This process continues until all liquid is converted to steam, at which point the solid line joins the dashed line representing gas flow. With further reduction of flow rate beyond this point, the pressure drop simply follows the quadratic law of pressure drop vs. velocity, and no more boiling occurs.

Figure 99 shows a comparison of the system pressure drop curve with heat flux as shown in Figure 98, but with a lower heat flux (the lower curve in Figure 99) [TOD2011]. When the heat flux is lower, boiling starts at the lower mass flow rate rather than the higher, except that in this figure, the flow rate is much smaller. This is shown in Figure 99 by having point B occur at much lower mass flow rate. If the heat flux and hence the mass flow rate at boiling inception is very low, then a couple of competing phenomena can create the situation shown by the bottom curve in Figure 99. In this case, because boiling starts at a very low mass flow rate, conversion of liquid into steam results in two phenomena: (1) increase of volumetric flow and hence of liquid velocity, and (2) reduction of hydrostatic head.

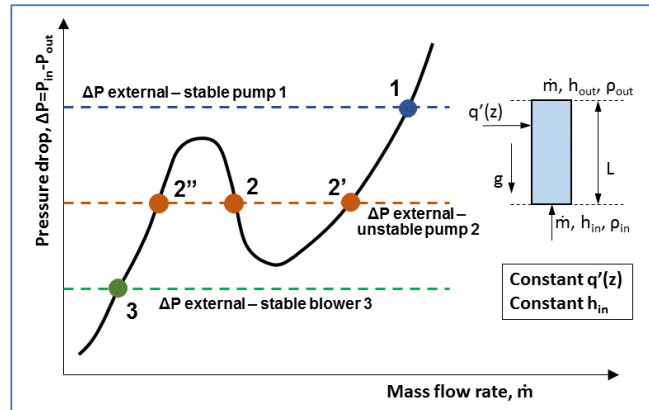


Figure 100 Impact of different pump curves on channel flow instability

After boiling inception at point B at the lower curve, reduction of the hydrostatic head temporarily dominates and creates a reduction in pressure drop. With further decrease in mass flow rate, a large increase in velocity occurs as more of the liquid is transformed into steam, resulting in a pressure drop increase.

Figure 100 shows the external pressure head generated by a pump (dashed lines) superimposed on the system pressure drop curve (solid line) [TOD2011]. It is important to observe in this figure that there are three cases of external pump head. The one on the top has one intersection point 1, at which the pump can sustain a stable operating point with liquid water. In addition, the curve at the bottom has one intersection point 3, at which a blower can have a stable operating point with gas (or steam). The curve in the middle intersects the system pressure drop curve at three points (2, 2', and 2''), and all three are possible operating points for this pump (or blower). At point 2', the pressure head device must be a pump, and at point 2'', it must be a blower. At operating point 2, neither a pump nor a blower can operate well because the fluid is in two-phase flow, in which case conventional turbo machinery cannot operate efficiently. Nevertheless, although this operation cannot be achieved by the same device, it is assumed for the moment that it works, and this case and the consequences of this “pump” operation will be further examined.

Figure 101 presents a view of flow excursion instability, continuing the explanation started in Figure 100 [TOD2011]. As explained previously, the unstable operating point is point 1. In this figure, various external pump head curves are plotted through point 1.

Case 1 (positive displacement pump with vertical pump head) represents a pump with a delivery flow that does not change with pump head. This pump is inherently stable, and although it rests on the part of the system curve with negative slope, it intersects the system loss curve at only one point (point 1).

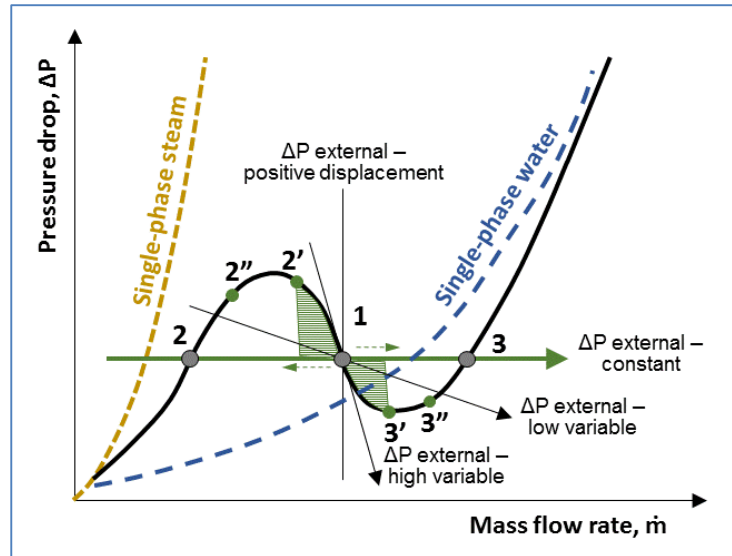


Figure 101 Definition of channel flow excursion instability in a single channel

Case 2 (constant head) represents a situation in which the head from an external pump is delivered to a channel, and hence its curve intersects the system curve at three locations. However, in this case, the pump head is constant irrespective of the flow rate in the channel. This situation can lead to excursion instability because the curve intersects the system loss curve at three points (1, 2, and 3); this will be explained further.

Case 3 (low variable head) represents a centrifugal pump for which the head and flow are related through a polynomial function. This pump head curve also intersects the system loss curve at three points and also leads to Ledinegg instability.

Case 4 (high variable head) represents a pump that is well throttled, so that a small flow change results in a large pump head change. This is a typical situation in operating BWRs, which have well-throttled external circuit pumps. Because the slope of the curve is very steep, the pump head curve intersects the system loss curve at only one point (point 1), and therefore this pump operates in an inherently stable manner regardless of where it intersects the system curve.

From the above examples, a criterion for entering Ledinegg instability can be defined by the following inequality:

$$\frac{\partial(\Delta P_{system})}{\partial w} > \frac{\partial(\Delta P_{ext})}{\partial w}. \quad (251)$$

This inequality shows that if the pump head curve is $\Delta p_{ext} > \Delta p_{system}$, the pump operation is inherently stable in such a system.

By examining Figure 101 carefully, it is clear that the source of this instability is the negative slope of the system loss curve. This means that if the pump operates at point 1, any small disturbance of the pump flow or head will lead to instability.

For example, at point 1, if pump flow decreases by an infinitesimal amount δW , the pressure

drop in the system will increase by $\delta(\Delta p)$ (the left upper green triangle). This will make the pump further reduce its flow delivery, which in turn will make the pressure drop further increase. Therefore, step by step, the pump operating point will move through points 2' and 2'' to point 2.

Inversely, if at point 1, the pump flow increases by an infinitesimal amount δW , the pressure drop in the system will decrease by $\delta(\Delta p)$ (the right lower green triangle). This will make the pump further increase its flow delivery, which in turn will make the system pressure drop further decrease. Therefore, step by step, the pump operating point will move through points 3' and 3'' to point 3.

Figure 101 clearly shows that while the pump operating point moves from one point to another, the pump head and the system losses will be in equilibrium for a period of time that depends on the system and the pump hydraulic inertia. However, given enough time, the possible operating points must be at the intersection of the two curves. However, the only sustainable stable operating point must be the intersection point of the two curves that satisfies Eq. (251).

Thermal-hydraulic designers need to examine pump curves and system loss curves carefully to ensure that pump head shape and slope satisfy Eq. (251), thereby ensuring that this type of instability will not occur.

7.5.4.3 Parallel channel flow instability

One aspect of Ledinegg instability (i.e., excursive instability) is the situation that can arise with parallel channels operating under a common pressure drop [POP2014]. This situation can occur in many thermal-hydraulic networks or components. For example, this may occur in a reactor core with two types of channels under the same pressure drop, or in a CANDU fuel channel with crept pressure tubes, in which the flow is split into two flow paths, one in the eccentricity above the fuel bundle, and one through the fuel bundle (see Section 7.5.3.4)

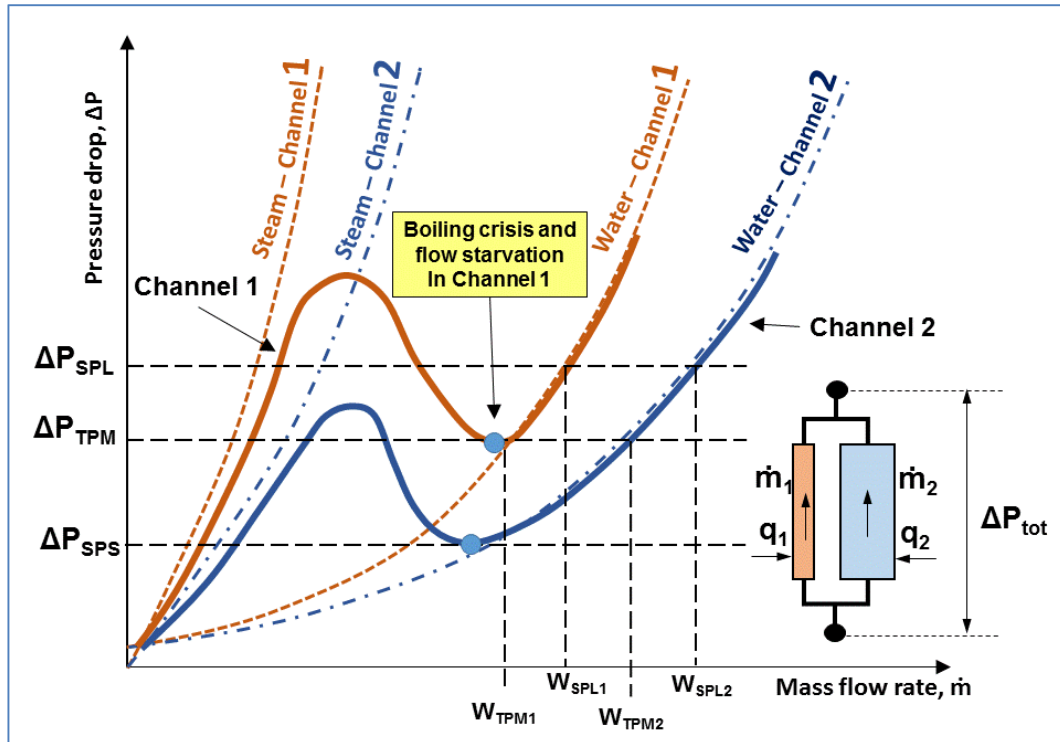


Figure 102 Principles of flow excursion instability in two parallel channels

Figure 102 shows the principles of a two-parallel-channel configuration under the same pressure drop, which is vulnerable to excursive instability. In this configuration, each channel has its own pressure loss curve, but different heat flux, total power, and flow rate. Therefore, each channel will enter the two-phase flow boiling condition at a different flow rate. The first channel that enters two-phase flow will experience an increase in channel pressure drop, which will help divert a portion of its flow to the other channel that remains in single-phase liquid flow. In other words, the channel that first enters two-phase flow will experience successive flow reductions and will eventually overheat as it loses its cooling.

Figure 103 shows an actual calculation of flow instability in a parallel channel configuration in a core with two types of fuel channels using a computer code (a similar geometry to that in Figure 102) [POP2000]. In Figure 103, the mass flow rate is on the x-axis and the pressure drop on the y-axis. Line 1 represents the total pressure drop across both channels; Lines 2 and 3 represent the pressure drop in each channel, and Line 4 provides the percentage of flow split. It is apparent in this figure that the flow split between the channels changes as the total flow to the two-channel loop decreases. Clearly, the two channels behave differently below a total flow of 0.2 kg/s. At a pressure drop of about 12 kPa, the flow starts to divert from one channel (Line 3) to the other channel (Line 2). Line 3 indicates an increase in pressure drop due to boiling, whereas Line 2 indicates an increase in pressure drop due to higher liquid flow.

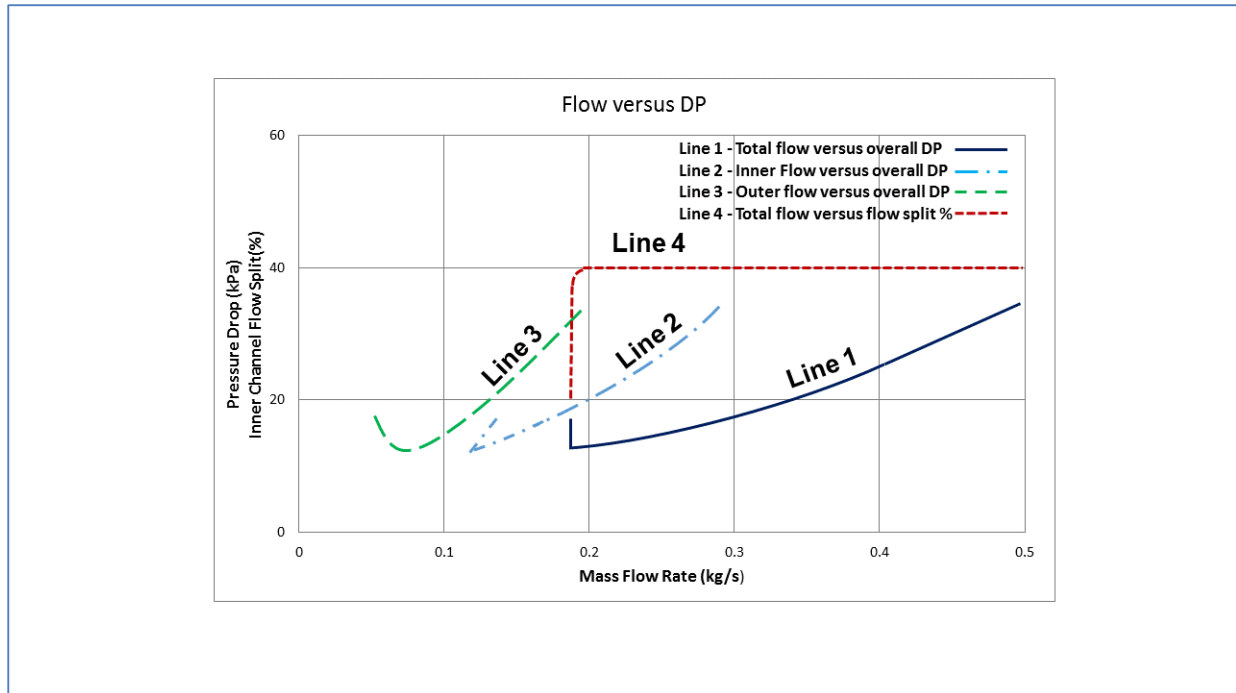


Figure 103 Results of flow excursion instability in two parallel channels

7.5.5 Problems

1. List and explain the most important factors that have significant impact on the pressure drop in the CANDU primary heat transport system. Rank the components in the CANDU primary heat transport system that contribute to the pressure losses in the system. Explain how reactor aging affects pressure drop in the main heat transport system.
2. Explain the components of pressure drop in horizontal channels, and provide information on the parameters that influence their value. Explain the approach used to calculate the pressure drop components in two-phase flow.
3. A mixture of water and steam at mass quality of 30% and temperature of 400°C flows through a 10 m long pipe with diameter of 4 inches. The mass flux in the pipe is 2000 kg/m² s. Calculate the pressure drop along this pipe using the most appropriate two-phase flow multiplier.
4. Water flows through an insulated horizontal pipeline 100 m long (no heat losses). Water enters the pipe at temperature of 250°C, and velocity of 3 m/s. Assuming that the pipe is made of carbon steel of commercial quality, calculate the pump power that is required to maintain this flow.
5. Two-phase water-steam mixture at 10% quality flows in thermal equilibrium through a horizontal pipe 6 m long with diameter of 18 mm. The water pressure is 8 MPa. Calculate the two-phase pressure gradient in this pipe, and the total pressure difference between the inlet and the outlet using the Friedel correlation provided below. The total mass flux is 2000 kg/m² s.

$$\phi_{lo}^2 = E + \frac{3.24FH}{Fr^{0.0454}} We^{0.035} \quad E = (1-x)^2 + x^2 \frac{\rho_l f_{go}}{\rho_g f_{lo}} \quad F = x^{0.78} (1-x)^{0.224}$$

$$H = \left(\frac{\rho_l}{\rho_g} \right)^{0.91} \left(\frac{\mu_g}{\mu_l} \right)^{0.19} \left(1 - \frac{\mu_g}{\mu_l} \right)^{0.7} \quad Fr = \frac{G_m^2}{g D_e \rho_m^2} \quad We = \frac{G_m^2}{\sigma \rho_m}$$

$$\rho_m = \left(\frac{x}{\rho_g} + \frac{1-x}{\rho_l} \right) \text{ for homogeneous model}$$

$$f_{jo} = \frac{64}{Re_j} \text{ if } Re_j \leq 1055$$

$$f_{jo} = \left[0.86859 \cdot \ln \left(\frac{Re_j}{1.964 \cdot \ln Re_j - 3.8215} \right) \right] \text{ for } Re_j > 1055$$

Where: x is quality, ρ is density in (kg/m^3) (g – gas, and l – liquid), f_{go} and f_{lo} are Darcy friction factors, μ is dynamic viscosity in (Pa s), (g – gas, and l – liquid), σ is surface tension in (N/m), and g is acceleration due to gravity ($=9.81 \text{ m/s}^2$).

6. Explain the cause and the impact of the Ledinegg flow instability in vertical channels. Explain the importance of this type instability for the process of pump selection.
7. Explain the cause and the impact of flow excursion instability in parallel heated channels, including the applicability and methods for avoiding or mitigating this type of instability.

7.6 Heat transfer between the fuel elements and the coolant

Section 6.1 provides the fundamentals of two-phase flow, which are needed to understand the heat transfer regimes in the reactor core. Section 7 provides the basis for heat transfer in the reactor primary heat transport system. Section 7.4 provides details on heat conduction in the fuel elements. This section now focuses on heat transfer from the fuel to the coolant.

Heat removal from the reactor core is an important issue in reactor design and operation. The main objective of heat transfer analysis for single-phase flow in the reactor is to determine the temperature field in a coolant channel such that the reactor operating temperatures are within the specified limits, including the rate of heat transfer to and from a surface or object. Because reactor power densities are typically much higher than for other conventional heat sources, the heat removal rate from any given reactor core coolant channel is quite large. Heat transfer to the coolant in single phase therefore requires a coolant with a large heat capacity.

The boiling curve shown in Figure 29 provides a good illustration of the boiling phenomenon and the boiling crisis in the fuel channel, which have an important impact on reactor thermal margins. This section discusses the wall heat flux in various heat transfer regimes and the critical heat flux (CHF) in the channel and discusses their importance and the differences between PWR and CANDU reactors. Appropriate diagrams explaining the variation of the critical heat flux with key parameters are shown and discussed. In addition, CHF correlations and calculation methods are described. The CHF is a critical parameter in reactor core thermal-hydraulic design because it sets the primary limitations on reactor thermal margins.

7.6.1 Heat transfer regimes

Various flow and heat transfer regimes that are relevant to heat transfer in the reactor core under various operating modes are illustrated in Figure 32. The heat transfer correlations are important in reactor thermal-hydraulic design because they provide the tools for a designer to calculate various parameters of interest in the design process and to verify that the design can meet the proposed objectives and requirements, primarily the capability to remove generated heat from the core during all possible operating modes.

The heat transfer from any solid surface to a coolant is given by Newton's Law in terms of heat flux:

$$q'' = h \cdot (T_s - T_b), \quad (252)$$

where T_s is the surface temperature, T_b is the bulk temperature of the coolant, and h ($W/m^2 K$) is the heat transfer coefficient. The heat transfer coefficient is dependent on coolant properties, flow parameters such as the velocity field, the temperature fields in the solid surface and the coolant, and solid surface condition and geometry.

A considerable amount of experimental and theoretical research has been published on the heat transfer coefficient for turbulent flow in channels. Although most correlations have been developed based on circular pipes, with appropriate corrective factors, they can be applied to various geometries.

For fully developed turbulent flow of non-metallic fluid, the general heat transfer correlation can be expressed as [ELW1978]:

$$Nu = C \cdot Re^a Pr^b \left(\frac{\mu_w}{\mu} \right)^d, \quad (253)$$

where μ_w is the fluid viscosity at the wall temperature and a, b, c, d are constants that depend on fluid and channel geometry.

Heat transport with phase change such as in boiling or condensation is an efficient method to transfer heat because latent heat per unit mass is very large compared with sensible heat. For single-component fluids, the interface temperature difference involved for heat transfer in evaporation and condensation is relatively small. However, when more than one component is present in a system, the temperature difference can be higher. An example is condensation of vapours in the presence of non-condensable gases. The two-phase heat transfer phenomena relevant to reactors include pool boiling, evaporation in vertical or horizontal fuel channels, and condensation inside or outside tubes.

As indicated in Figure 32, many flow and heat transfer regimes are possible in reactor channels in two-phase flow, depending on many parameters. In addition, fuel and channel geometry, heat transport conditions, characteristics, and materials have a significant influence on the type and magnitude of heat transfer from fuel to coolant. As a result, in the literature, many heat transfer correlations have been proposed, adopted, and used by various designers and analysts. This section provides a brief overview of the most important correlations, focussing on the critical heat flux correlations because of their significance for reactor thermal margins.

7.6.2 Convective heat transfer in turbulent forced flow

The convective heat transfer coefficient in turbulent forced flow of non-metallic fluids follows the form given by Eq. (253). The Prandtl number, given by Eq. (16), for non-metallic fluids such as light and heavy water is close to unity. For non-metallic fluids, the Nusselt number given by Eq. (15) is insensitive to wall surface conditions. Moreover, the Nusselt number varies little in the case of constant heat flux and constant mass flux.

Even for this relatively well-known situation, many heat transfer correlation variations have been proposed by different authors. The best-known is the Dittus-Boelter correlation, which is given by the following relation [ELW1978]:

$$Nu = 0.023 \cdot Re^{0.8} Pr^{0.4}. \quad (254)$$

Hence, using the Nusselt number, the heat transfer correlation can be obtained as follows (using a simplified version for plate geometry):

$$h_c = 0.023 \cdot k_f L \cdot Re^{0.8} Pr^{0.4}. \quad (255)$$

This is the best-known correlation used for single-phase convective heat transfer, as shown in the first part of the left side of Figure 29. In this correlation, the physical properties in dimensionless numbers are evaluated at the bulk temperature of the fluid. The correlation does not take into account the effect of temperature variation from the tube wall to the bulk fluid. Clearly, for laminar flow, this correlation does not apply, and other correlations are used.

For forced convection in fuel bundles, the following correlation was proposed by Weisman [ELW1978]:

$$Nu = C \cdot Re^{0.8} Pr^{1/3}, \quad (256)$$

where the constant C has the following form for square and triangular lattices respectively (S is the fuel rod pitch, and D is the fuel rod diameter):

$$\begin{aligned} C &= 0.042 \frac{S}{D} - 0.024, \quad 1.1 \leq \frac{S}{D} \leq 1.3 \\ C &= 0.026 \frac{S}{D} - 0.006, \quad 1.1 \leq \frac{S}{D} \leq 1.5, \end{aligned} \quad (257)$$

7.6.3 Sub-cooled boiling heat transfer in forced flow

Heat transfer from the walls to the liquid at relatively high heat flux, starting from the sub-cooled condition at the entrance of a channel, brings CANDU fuel cladding walls to and beyond saturation somewhere downstream in the reactor fuel channel. When the liquid layer next to the wall and adjacent to the wall becomes superheated, bubble nucleation sites are activated. This point is denoted in Figure 29 as the onset of sub-cooled boiling. Bubbles are generated at the wall cavities by the heat transferred from the wall as latent heat of evaporation. As soon as they depart from the wall, they encounter sub-cooled bulk liquid and condense, releasing the latent heat of vaporization to the bulk liquid. This process helps enhance heat transfer from the wall, partly by evaporation of the liquid and partly by enhancing turbulence near the wall. Note that heat transfer by latent heat of evaporation is much more effective than heat transfer by convective heating of liquid.

The point at which sub-cooled nucleate boiling starts is defined by the following criterion proposed by Bergles and Rohsenow [AHM2009]:

$$q_{w,SB}^* = 1082 p^{1.156} \left[1.799 (T_w - T_{sat})_{SB} \right]^{2.3/p^{0.0234}}. \quad (258)$$

Equation (258) is valid for pressures between 0.1 and 13.6 MPa, and p is in bar, temperatures in °C, and $q_{w,SB}$ in W/m².

For the nucleate boiling heat transfer regime, the best-known and most widely used correlation is the Chen correlation [CAT2005, ELW1978, TOD2011]. This correlation calculates the heat transfer coefficient as a sum of the convective and nucleate boiling parts as follows:

$$h_{SB} = h_C + h_{NB}. \quad (259)$$

The convective heat transfer is calculated using a variation of the Dittus-Boelter correlation given by Eq. (255):

$$h_C = 0.023 \left(\frac{G(1-x)D_e}{\mu_f} \right)^{0.8} Pr^{0.4} \frac{k_f}{D_e} F, \quad (260)$$

$$F = 1.0 \text{ for } \frac{1}{X_{tt}} < 0.1$$

$$F = 2.35 \left(0.213 + \frac{1}{X_{tt}} \right)^{0.736} \text{ for } \frac{1}{X_{tt}} \geq 0.1 \quad (261)$$

The Lockhart-Martinelli parameter X_{tt} is defined as:

$$\frac{1}{X_{tt}} = \left(\frac{x}{(1-x)} \right)^{0.9} \left(\frac{\rho_l}{\rho_g} \right)^{0.5} \left(\frac{\mu_g}{\mu_l} \right)^{0.1} \quad (262)$$

The nucleate boiling part of the sub-cooled boiling correlation is defined as:

$$h_{NB} = \frac{S (0.00122) \cdot \Delta T^{0.24} \Delta p^{0.75} c_p^{0.45} \rho_l^{0.49} k_l^{0.79}}{\sigma^{0.5} h_{lg}^{0.24} \mu_l^{0.29} \rho_g^{0.24}} \quad (263)$$

The parameter S is defined as follows:

$$S = \frac{1}{1 + 2.53 \cdot 10^{-6} Re^{1.17}} \text{ where } Re = Re_l F^{1.25} \quad (264)$$

The Chen correlation is valid for pressures of 0.17–3.5 MPa, liquid inlet velocities of 0.06–4.5 m/s, and heat fluxes up to 2.4 MW/m².

When the bulk liquid temperature increases to a certain point, as shown in Figure 29, conditions for onset of significant void, i.e., bulk boiling, are established. The criteria that determine the onset of bulk boiling are defined by various correlations, of which the best-known is the Saha-Zuber correlation provided in Eqs. (249) and (250), which is expressed in terms of quality at the OSV point. However, it is useful to express Eqs. (249) and (250) in terms of bulk fluid temperature to estimate the level of coolant sub-cooling at the point of OSV. Figure 32 shows the sub-cooled boiling phases, with OSV labelled as the onset of net vapour generation, which is upstream of the point at which bulk saturation is reached.

Equations (249) and (250) can be transformed into a relation that defines the wall temperature at the onset of bulk boiling:

$$T_{bulk,OSV} = T_{sat} - 0.0022 \frac{q'' D_e}{k_l} \text{ for } Pe < 7 \cdot 10^4$$

$$T_{bulk,OSV} = T_{sat} - 154 \frac{q''}{G \cdot c_p} \text{ for } Pe > 7 \cdot 10^4 \quad (265)$$

where the Peclet number is defined according to the following relation:

$$Pe = \frac{G \cdot D_e \cdot c_p}{k_l} \quad (266)$$

The Saha-Zuber correlation is valid for pressures of 0.1–13.8 MPa, mass fluxes of 95–2760 kg/m²s, and heat fluxes of 0.28–1.89 MW/m².

7.6.4 Critical heat flux (CHF)

When the wall surface temperature is further increased beyond the point that results in sub-cooled boiling, as shown in Figure 29, it may reach a value that results in a heat flux referred to as *critical heat flux* (CHF). This is the maximum heat flux at which continuous liquid contact in a tube or fuel channel is maintained. Further increase in the wall heat flux will result in an increase in wall temperature to values that result in a sustained vapour film on the wall surface (along the horizontal dashed line in Figure 29). Usually, for reactors designed to operate with liquid water in contact with the fuel cladding, this large increase in cladding temperature could result in melting and destruction of the cladding. The primary objective of thermal-hydraulic design is to ensure that this does not happen.

7.6.4.1 Outline of CHF phenomena

The CHF is a complex thermal-hydraulic phenomenon that varies with a large number of parameters. This section explains the CHF phenomenon for various combinations of key parameters and provides a discussion of CHF parametric trends. In addition, heat transfer correlations for pre-CHF heat transfer regimes are provided and discussed [IAEA2001, TOD2011, BER1981, DEL1981, COL1972, LWU2004].

Development of the CHF correlation requires a significant amount of experimental testing because of the complex reactor core fuel geometry in PWRs as well as in CANDUs. This section also provides a brief explanation of the experimental tests and their use to develop CHF correlations.

In forced convective boiling, the boiling crisis occurs when the heat flux is raised to such a high level that the heated surface can no longer support continuous liquid contact. This heat flux is referred to as the critical heat flux (CHF). It is characterized either by a sudden rise in surface temperature caused by blanketing of the heated surface by a stable vapour layer, or by small surface temperature spikes corresponding to the appearance and disappearance of dry patches. The CHF normally limits the amount of power transferred, both in nuclear fuel bundles and in conventional boilers. Failure of the heated surface may occur once the CHF is exceeded. This is especially true for highly sub-cooled CHF conditions. At high flows and positive dryout qualities, the post-dryout heat transfer is reasonably effective in keeping the heated surface temperatures at moderate levels, and operation under dryout conditions may be sustained safely for some time, particularly in BWRs or CANDUs.

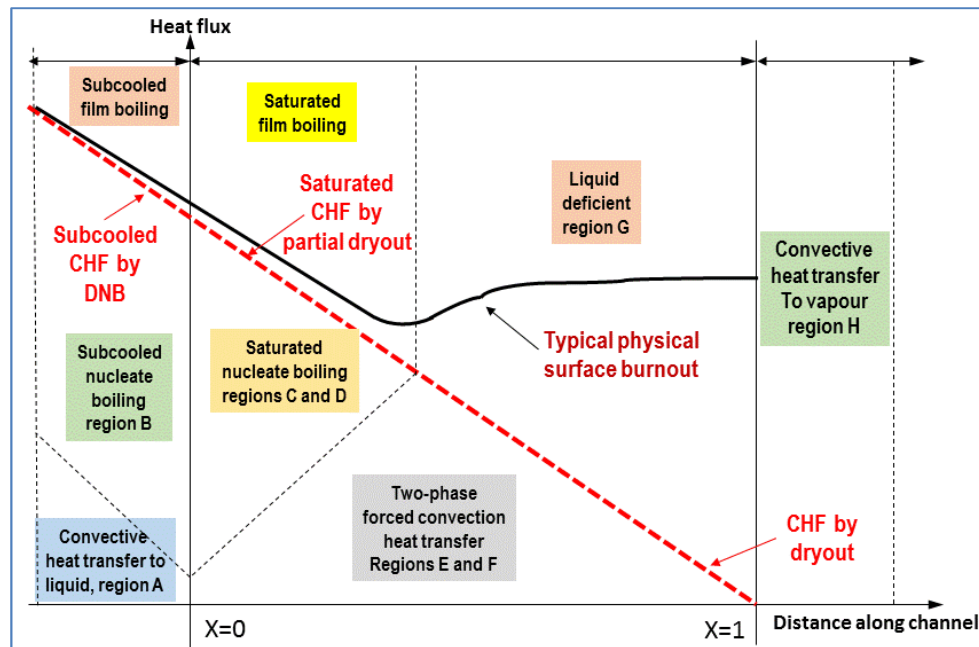


Figure 104 Concepts of CHF, dryout, and burnout

Figure 104 [COL1972] is of key importance in understanding the various mechanisms and the definition of the CHF phenomenon, as well as the consequences of CHF occurrence in a reactor fuel channel (note that this figure is not to scale, values are not shown, and the intent is to illustrate CHF conceptually for various coolant qualities).

Figure 104 shows the basic concept of CHF occurrence and the terms used to describe the various stages and types of the CHF phenomenon. On the y-axis, this figure shows the relative value of the heat flux as given, whereas on the x-axis, the thermodynamic quality is provided, starting from sub-cooled conditions (negative values), moving to values between 0 and 1 (two-phase flow), and then to values beyond 1 (superheated steam). The straight solid line with a negative slope intersecting the x-axis at $x_e=1$ is the locus of CHF. Above this straight line, a line is shown which is labelled as the *burnout locus*—this is the wall heat flux that can destroy the cladding surface under various conditions. On the left side, under sub-cooled conditions, various heat transfer regimes are illustrated moving from bottom to top in the figure: convective heat transfer at the bottom (no boiling), sub-cooled nucleate boiling, and sub-cooled film boiling. In the two-phase region in the middle of the diagram, various heat transfer regimes are shown: two-phase forced convection, saturated bulk boiling, saturated film boiling, and liquid-deficient saturated boiling. On the right side of the diagram, convective heat transfer to steam is shown. These regimes are also illustrated in Figure 26 and Figure 33.

With respect to the diagram in Figure 104, the following terms can be defined. They are related to the CHF, but have a slightly different meaning:

- **Boiling crisis**. Refers to sub-cooled or saturated boiling when the amount of steam produced by boiling surpasses the amount of steam that can be removed from the wall, thus creating a situation in which heat removal from the wall is limited.
- **CHF**. Refers to the general condition of limited heat flux in sub-cooled or saturated

boiling; it can include all terms shown on this list.

- **Dryout**. Refers to conditions at the fuel cladding surface when continuing contact with liquid water can no longer be maintained. Note that under dryout conditions, there may still be abundant liquid water in the pipe or fuel channel (so that the void fraction may be very low), but the cladding surface may still be insulated from the water by a stable steam film.
- **Departure from nucleate boiling (DNB)**. This term refers to the CHF that occurs under significantly sub-cooled conditions (as in PWRs). In this case, CHF happens when the fuel cladding surface can no longer support sub-cooled boiling.
- **Burnout**. This term refers to the destruction of the cladding surface as it begins to melt. This can happen very quickly under sub-cooled conditions after CHF is reached. At saturated conditions (for higher equilibrium quality or void fraction), as shown in Figure 104, burnout can occur only when the heat flux is greater than the CHF (note that the burnout curve moves further away from the CHF curve in Figure 104 as quality rises, particularly for qualities $x > 0$).

Figure 105 [POP2014] shows a different CHF mechanism in a reactor fuel channel superimposed on the CHF diagram from Figure 104. In this figure, heat flux is indicated on the y-axis and thermo-dynamic quality on the x-axis. There are four distinctive CHF mechanism types: nucleation induced under highly sub-cooled conditions, a bubbly layer induced under sub-cooled conditions, entrainment-induced film depletion at low quality, and deposition-controlled film depletion at very high quality.

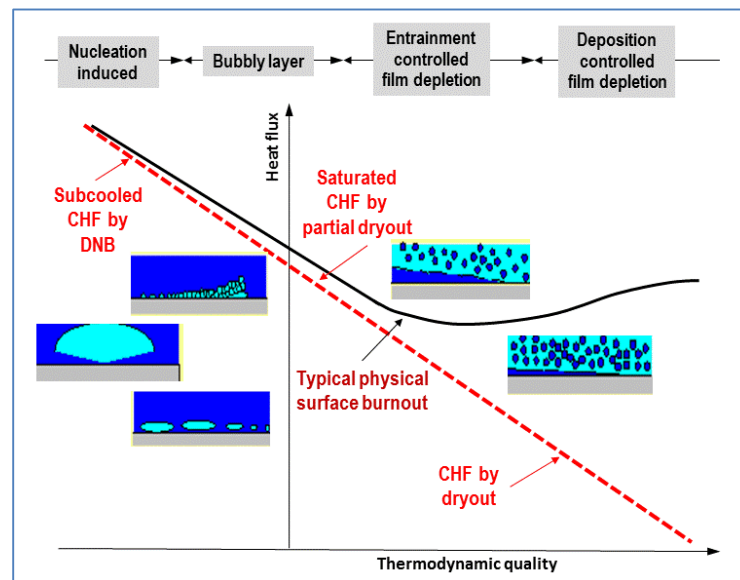


Figure 105 Transitions among CHF mechanisms

Like other thermal-hydraulic phenomena, CHF occurs differently in pool boiling than in forced-flow boiling. In pool boiling, no forced flow is provided to the liquid container. In this situation, CHF usually occurs because of either counter-current flow (Helmholtz) instability or micro-layer evaporation (for highly sub-cooled conditions only).

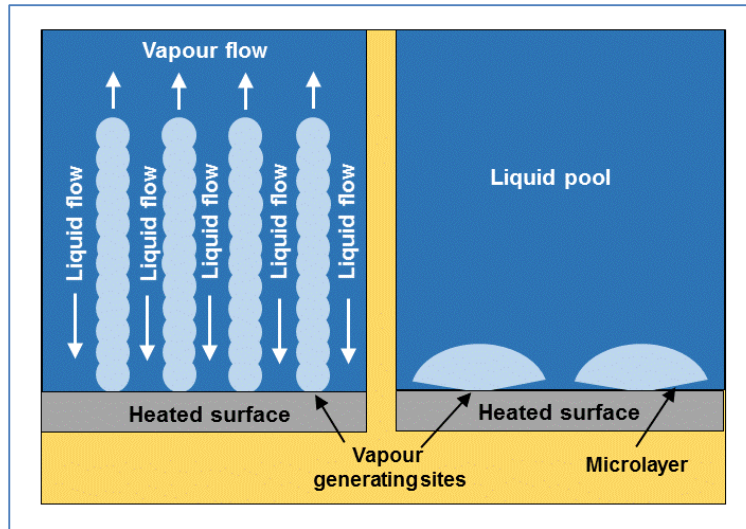


Figure 106 Pool boiling CHF mechanisms

The left side of Figure 106 shows the counter-current flow instability (i.e., the Helmholtz instability) [LEU2004]. In this case, the heated surface is covered by a rising vapour column with counter-current liquid jets flowing downwards due to gravity to compensate for liquid removal by evaporation. Ultimately, at very high heat flux levels (vapour removal rates), the relative velocity between liquid and vapour can be so high that an unstable flow situation is created in which due to interfacial friction, liquid jets cannot penetrate downwards because of the high flow rate of rising bubbles, resulting in a CHF condition. The right side of Figure 106 shows a micro-bubble developed in a cavity on the heated surface. As the bubble grows, a microlayer of thin liquid film develops below the bubble. This microlayer is unstable because of the large heat flux and can break and leave the surface uncovered, i.e., can form a dry patch, leading to CHF.

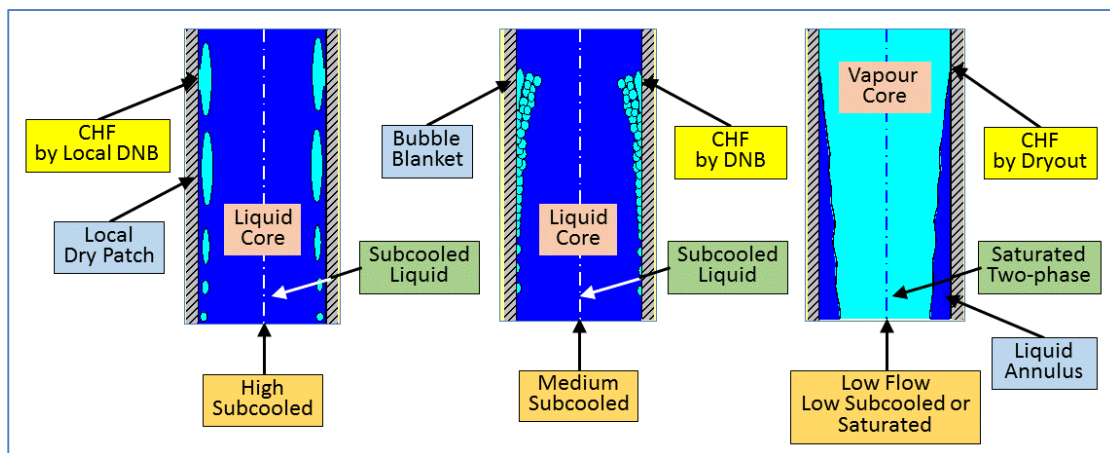


Figure 107 Flow boiling CHF mechanisms

In forced-flow boiling, CHF usually occurs because of one of the following three phenomena: collapse of the liquid sub-layer, bubble crowding, or film depletion. Figure 107 shows these three phenomena [LEU2004]. On the left side of this figure, the collapse of the liquid sub-layer

occurs with highly sub-cooled liquid. CHF occurrence is due to the spreading of a dry patch following microlayer evaporation under a bubble and coalescence of adjacent bubbles. The occurrence of CHF in this case depends on local surface heat flux and flow conditions; it is not affected by upstream heat flux distribution.

Bubble crowding is shown in the middle of Figure 107 for moderate sub-cooling or saturated conditions and high flow rate. The bubble population density near the heated surface increases with increasing heat flux, and a so-called bubble boundary layer often forms a short distance away from the surface. If this layer is sufficiently thick, it can impede the flow of coolant to the heated surface. This in turn leads to a further increase in the bubble population until the wall becomes so hot that a vapour patch forms over the heated surface. This type of boiling crisis is also characterized by a fast rise in heated surface temperature (fast dryout).

At the right side of Figure 107, the film depletion type of CHF is illustrated, which is possible with a relatively low mass flux of saturated liquid in high void fraction flow. In the annular dispersed flow regime (high void fraction and high volumetric flow), the liquid will be in the form of a liquid film covering the walls and entrained droplets moving at a higher velocity in the pipe core. Continuous thinning of the liquid film will take place due to the combined effect of entrainment and evaporation. Near the dryout location, the liquid film becomes very thin, and due to the absence of roll waves (which normally occur at higher liquid film flow rates), entrainment is suppressed. If the net droplet deposition rate does not balance the evaporation rate, the liquid film must break down. The temperature rise accompanying this film breakdown is usually moderate (stable dryout).

Related to the above explanation of dryout resulting from a high void fraction, high flow rate situation in a tube is CHF dryout in a fuel channel. This situation is typical of CANDU reactors in which towards the end of the fuel channels, saturated liquid with significant void fraction and mass flux flows through a densely packed fuel channel. Because the two-phase flow is very well mixed, dryout occurs gradually, and fuel is not exposed to sustained loss of contact with liquid, i.e., slow dryout occurs. During a slow dryout, the heated surface does not experience the usual dryout temperature excursions; instead, a gradual increase in surface temperature with power is observed. A slow dryout is usually encountered in flow regimes where the phases are distributed homogeneously, such as froth flow or highly dispersed annular flow at high mass velocities and void fractions. Under these conditions, liquid-wall interaction is significant, limiting the temperature rise with dryout.

Calculations based on cooling by vapour flow indicate only that post-CHF temperatures are below the minimum film boiling (Leidenfrost) temperature; hence, depositing droplets may wet the surface, increasing the heat transfer coefficient. In a CANDU reactor, because the coolant is close to saturation over most of the channel and at relatively high mass flux and void fraction downstream of the reactor mid-plane, the most probable CHF mechanism is slow dryout. Therefore, in a CANDU reactor, the consequences of reaching CHF are not as serious as in a highly sub-cooled PWR because the fuel surface can still be well cooled by passing steam and droplets.

7.6.4.2 CHF parametric trends

As explained above, CHF is a complex phenomenon that depends on many parameters and can be caused by different phenomena. Table 10 shows various parameters that affect the type and intensity of CHF in fuel bundles. Discussion of all these effects is beyond the scope of this textbook; details can be found in the literature [IAEA2001].

Table 10 Separate CHF effects in fuel bundles

GENERAL	DETAILS OF SEPARATE EFFECTS
Global Flow Area Effects	<ul style="list-style-type: none"> ▪ n-rod bundle where $n \gg 3$ and all sub-channels are identical except for corners or cold-wall-adjacent sub-channels (e.g., square or triangular arrays of sub-channels) ▪ n-rods where $n \gg 3$ and adjacent sub-channels are generally not equal (e.g., 37-rod bundle geometries inside round tubes)
	<ul style="list-style-type: none"> ▪ Sub-channel size/shape (similarity to tube) ▪ Cold wall effect ▪ Distorted sub-channels (due to bowing, cladding stain, PT creep) ▪ Misaligned bundles (CANDU case)
Length Effects	<ul style="list-style-type: none"> ▪ Similar to appendage effects
	<ul style="list-style-type: none"> ▪ Mixing grids ▪ Attached spacers/ bearing pads/ endplates (CANDU)
Flow Orientation Effects	<ul style="list-style-type: none"> ▪ Vertically upward ▪ Vertically downward ▪ Horizontal
	<ul style="list-style-type: none"> ▪ Axial flux distribution (flux peaking/global flux distribution) ▪ Radial flux distribution (global RFD effect, cold wall effect, flux tilt across an element)
Flow Parameter Effects	<ul style="list-style-type: none"> ▪ Mass flow (including zero flow or boiling/flow stagnation case)
	<ul style="list-style-type: none"> ▪ Power/flow/pressure transients ▪ Combined transients
Effect of Fluid Type	<ul style="list-style-type: none"> ▪ Light water ▪ Heavy water ▪ Modelling fluids (Freon) in conjunction with a CHF fluid-to-fluid modelling technique

A number of studies have been conducted by various researchers to investigate the effects of various parameters on CHF. An overview of the parametric trends is provided in this section. These parametric trends are provided for two different CHF approaches.

The approach based on fuel channel inlet conditions is very often used in CHF R&D because of the convenience of using inlet conditions because these are easily measured and maintained in CHF experiments. The other method is based on local conditions, i.e., the conditions locally where CHF occurs. This approach is used in computer-based algorithms because a computer program can easily calculate local conditions at the CHF location.

The discussion of parametric trends provided here must be related to the general trends described in Section 6.1, particularly those illustrated in Figure 30 and Figure 31.

The most influential parameters affecting CHF are the fluid pressure, mass flux, level of sub-cooling, and hydraulic diameter [IAEA2001]:

$$CHF = f(P, G, X_{DO}, D_{hy}). \quad (267)$$

The general parametric trends on CHF based on inlet conditions are as follows:

1. Heated length has a very high impact on CHF because it affects the amount of heat transferred to the fluid; hence, CHF strongly decreases with increase of heated length and quality.
2. CHF increases with an increase in inlet sub-cooling (a decrease in inlet fluid temperatures).
3. CHF decreases with a decrease in outlet pressure (decrease of channel pressure).
4. For sub-cooled conditions, CHF increases with an increase in mass flow.
5. For saturated conditions, CHF increases with a decrease in mass flow.
6. CHF decreases with a decrease in tube diameter (which decreases the level of mixing and turbulence).

The general parametric trends related to CHF and based on local conditions are as follows:

1. The effect of heated length on local CHF is negligible.
2. Local CHF decreases with an increase in thermodynamic quality.
3. For sub-cooled conditions, local CHF increases with an increase in mass flow.
4. For saturated conditions, local CHF increases with a decrease in mass flow.
5. Local CHF increases with an increase in outlet pressure.
6. Local CHF decreases with an increase in channel diameter.

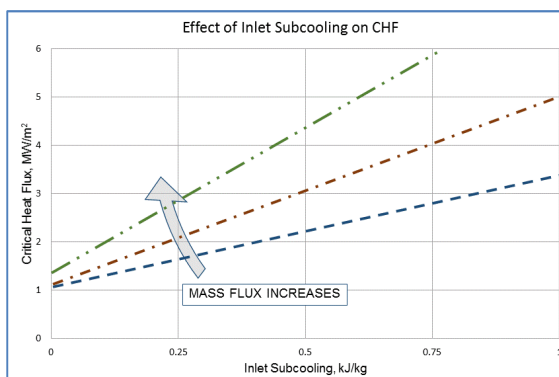


Figure 108 Effect of inlet temperature and mass flux

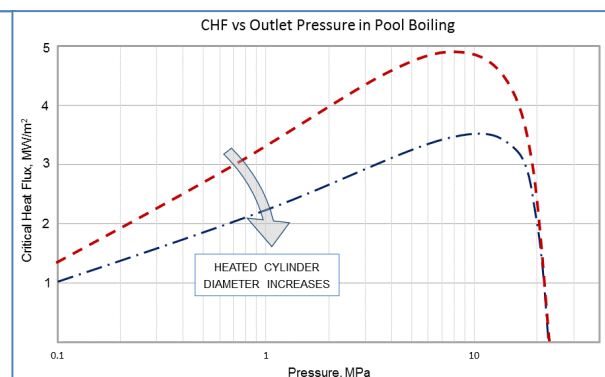


Figure 109 Effect of outlet pressure in pool boiling

Figure 108 shows the relationship between CHF (y-axis) and inlet sub-cooling (x-axis in enthalpy difference below saturation) for several mass flux values in a straight heated tube [LEU2004]. This figure is drawn in terms of channel inlet conditions. Note that CHF increases with mass flux and with the degree of sub-cooling. In other words, reactors that have more highly sub-cooled coolant and higher mass flux can use higher heat flux before reaching CHF. This is an important fact that demonstrates the strategy of operating PWRs.

In general, pressure has two key effects on heat transfer and CHF, one resulting from a change in the saturation temperature, and the other from a change in the latent heat of vaporization. As pressure increases, the saturation temperature increases, but the latent heat of vaporization

decreases. As a result, CHF increases with pressure, as indicated in Figure 109 [TOD2011]. However, as the pressure approaches the critical pressure, the latent heat of vaporization decreases to zero, reducing the CHF.

Figure 110 shows the effect of coolant outlet pressure (x-axis) for several sub-cooling levels for forced flow in a heated tube [LEU2004]. This figure is also drawn for a given level of channel inlet sub-cooling. Again, this figure confirms that higher inlet sub-cooling results in higher CHF. The impact of outlet pressure must be analyzed in combination with the channel inlet pressure, quality, and volumetric flux distribution along the channel (the channel length is 3.658 m).

Figure 111, Figure 112, and Figure 113 show CHF parametric trends for local conditions in heated pipes [LEU2004].

The effect of heated length is shown in Figure 111. It is evident that CHF decreases with increasing outlet quality in the channel. Moreover, as the heated length of the channel increases, the CHF value decreases significantly. Hence, for a very short heated length, CHF can be five times larger than for long heated lengths. This is another important observation in terms of CANDU reactor design. Because in CANDU the fuel bundles are relatively short, the bundle endplates and other bundle appendages can significantly improve the CHF value (further explanations in other sections below).

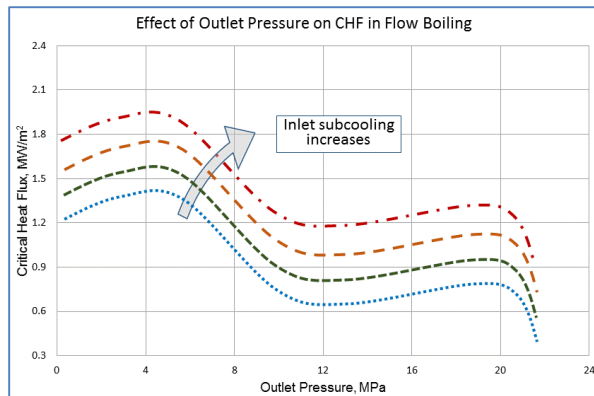


Figure 110 Effect of outlet pressure on flow boiling

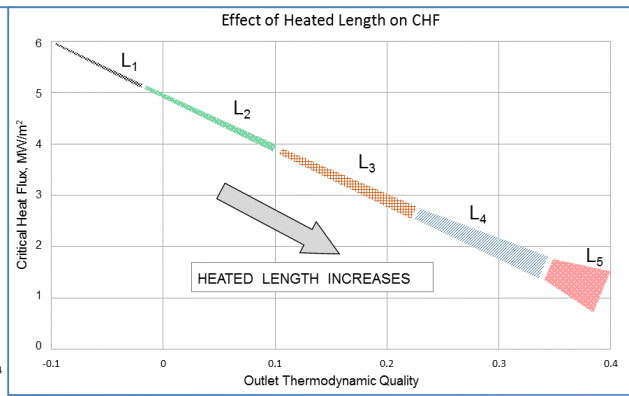


Figure 111 Effect of heated length on local CHF

Figure 112 shows the effect of mass flux under local conditions [LEU2004]. Similar behaviour can be observed with regard to the impact of sub-cooling on heat flux (for negative thermodynamic qualities). For saturated conditions, the effect of mass flux is not as important and should be analyzed in combination with volumetric flux.

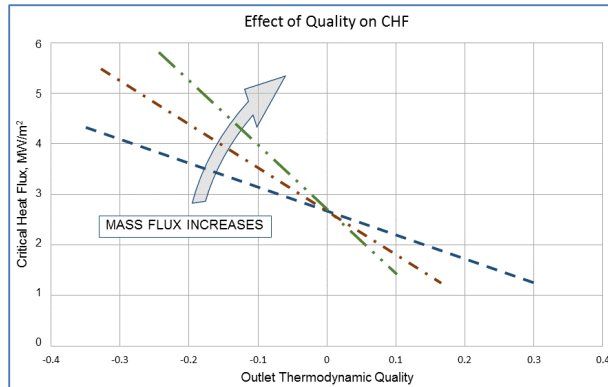


Figure 112 Effect of quality on local CHF

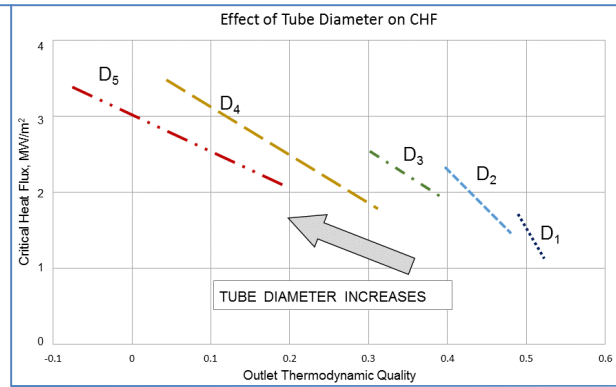


Figure 113 Effect of tube diameter on local CHF

Figure **113** shows, for local conditions, the impact of pipe diameter on CHF for various outlet thermodynamic qualities [LEU2004]. It is evident that larger hydraulic diameters provide a higher value of CHF for a given quality. Moreover, this figure confirms that for a given pipe diameter, CHF decreases with increasing thermodynamic quality.

7.6.4.3 CHF prediction methods

Because of the many possible fuel bundle geometries, the wide range of possible flow conditions, and the various flux distributions for advanced water-cooled reactors, it is impossible to predict the CHF for all cases using a single CHF prediction method and achieve a reasonable degree of accuracy. Over 400 correlations for CHF in tubes are currently in existence [IAEA2001]. The present proliferation of correlations illustrates the complex state of the art in predicting the CHF phenomenon, even for a simple geometry at steady-state flow conditions. The complexity of predicting the CHF increases significantly for fuel bundle geometries during severe transients, when additional parameters characterizing the transient are required. This demonstrates the need to categorize the important CHF-controlling parameters and their ranges of interest.

CHF prediction methods can be conveniently grouped into the following categories:

- Analytical models,
- Empirical correlations, and
- Look-up table methods.

Analytical CHF models

Analytical CHF models are based on physical mechanisms and satisfy the conservation equations [IAEA2001]. They generally require a two-fluid model approach, but occasionally must use a three-field approach (e.g., dispersed annular flow). Although these models have been improved significantly and usually predict the correct asymptotic trends, the evaluation process is complex and time-consuming. Furthermore, because of our limited understanding of the mechanisms involved and the lack of measurements of interfacial parameters, the models are still less accurate than empirical correlations over the range of their database. In addition, the analytical models have limited application because they can be used only in situations that

resemble the conditions upon which the model assumptions are based.

The annular film dryout model is based on a mass balance on the liquid film in annular flow and postulates that CHF corresponds to depletion of this liquid film. Equations for droplet entrainment and deposition have been proposed. The model provides reasonable predictions of CHF for annular flow at medium to high pressures and flows and void fractions exceeding 50%.

The bubbly layer model postulates that CHF first occurs in the lower quality regime when the bubble layer covering the heated surface becomes so thick and saturated with bubbles that liquid mixing between the heated surface and the cooler core liquid becomes insufficient.

The Helmholtz instability model is applicable to pool boiling, where the boiling crisis is reached when the flow of vapour leaving the heated surface is so large that it prevents a sufficient amount of liquid from reaching the surface to maintain the heated surface in the wet condition. The phenomenon that limits the inflow of liquid is the Helmholtz instability, which occurs when a counter-current flow of vapour and liquid becomes unstable.

Empirical CHF prediction methods

Empirical CHF prediction methods can be subdivided into those based on inlet conditions and those based on local cross-sectional average (CSA) conditions [IAEA2001].

The empirical correlations based on inlet conditions (*overall power correlations*) are all in the form of empirical correlations based on CSA inlet conditions (P , G , T_{in} , or ΔH_{in}) and usually assume the “overall power” hypothesis. This hypothesis states that, for a given geometry and set of inlet conditions, the critical power (the power corresponding to the first occurrence of CHF for that geometry) is independent of axial or radial heat flux distribution. This assumption permits the use of CHF correlations derived from uniformly heated bundle data to predict dryout power in non-uniformly heated bundles of identical geometry (i.e., identical cross section and heated length). This technique is a reasonable one for obtaining a first estimate of dryout power; it gives reasonable estimates of dryout power in the annular flow regime for symmetric flux profiles and form factors close to unity. However, it is not recommended for form factors significantly different from unity. This approach can also be used to predict the critical power of fuel channels with a fixed cross section, heated length, axial flux distribution (AFD), and radial flux distribution (RFD), irrespective of the form factor. If the experimental AFD and RFD represent the worst flux shapes from a CHF point of view, then the empirical correlations can be used for lower-bound predictions. The overall power correlations have generally good prediction accuracy. The best examples of this group are the Bowring correlation for tubes and the EPRI-2 correlation for fuel bundles [IAEA2001, TON1996, DEL1981, BER1981, CAT2005].

The overall power correlations have limitations, including applicability only to specific geometries, heated lengths, heat-flux profiles, and the range of conditions in the database. Hence, any variation of these parameters (i.e., extrapolation outside the database) may affect CHF prediction and hence predicted reactor, channel, and bundle power. Moreover, these correlations do not exhibit the correct asymptotic and parametric trends, and the axial and radial CHF locations cannot be predicted.

The local CHF correlations satisfy the local-conditions hypothesis, which states that the local CHF is dependent only on local conditions and not on upstream history. In principle, the local-conditions hypothesis is sound if it is based on true local cross-sectional average conditions. The reference formulation of local correlations is based on the linear trend of CHF with critical quality (transformed from the linear trend of critical power with inlet sub-cooling). Additional terms are included for separate effects (such as axial and radial heat-flux distributions). The local correlations must be used together with the heat-balance equation to determine critical power and CHF location (which requires iteration). The best examples of these correlations are the Biasi correlation for tubes and the Becker correlation for fuel bundles [IAEA2001, TON1996, DEL1981, BER1981, CAT2005].

An important disadvantage of local correlations is a larger prediction scatter than with overall power correlations. They are valid only for specific geometries, heat-flux profiles, and the range of conditions in the database; any variation of these parameters may affect local flow and enthalpy distributions and hence CHF. As with any correlations of this type, extrapolation of the applicability range may result in incorrect predictions. Moreover, these correlations have incorrect asymptotic and parametric trends, and radial CHF location cannot be predicted.

CHF table look-up method

Because most empirical correlations and analytical models have a limited range of application, a more general technique is needed. This approach is based on developing a table of measured values for different geometries and flow conditions and supplementing them in terms of key parameters that affect CHF. This approach has become known as a *look-up table method*. The look-up table includes normalized CHF data banks for reference tubes, triangular-array fuel bundles, and CANDU fuel bundles of natural-uranium fuel in a nominal channel. The look-up table is developed using generalized correlations and trends, and then experimental data are superimposed to improve accuracy and ensure that parametric trends are captured. The look-up table can be statistically extended to table matrix conditions.

The empirical bundle CHF prediction method requires an extensive database with an adequate range of the parameters of interest. It is suitable for design calculations and for reactor power evaluations.

The sub-channel codes predict enthalpy and flow in each fuel sub-channel. They require a sub-channel CHF prediction method (tube-based) and a spacer mixing/enhancement model.

The enthalpy imbalance approach uses enthalpy imbalance (in terms of thermodynamic quality) between the critical sub-channel and the bundle cross-sectional average values. It is used in the tube-data-based CHF prediction method with a modified thermodynamic quality to account for the enthalpy imbalance.

Currently, CANDU 6 design and safety analysis are based on the look-up table prediction method. This method is applicable to other geometries or flow conditions through modification factors embedded in the table. The present CHF values used in design analysis are included in the look-up table for uniformly heated, vertical tubes of 8 mm inside diameter, cooled with an upward flow of water. They cover the widest range of flow conditions (all possible CHF regimes) and exhibit correct asymptotic and parametric trends (smooth transition

between various CHF regimes). In addition, detailed prediction uncertainty is available at sub-region levels. To this point November 13 early afternoon

A sample of the CANDU look-up table is shown in Table 11 [LEU2004, IAEA2001], where CHF values are provided in a table format as a function of pressure, mass flux, and quality. For values of these parameters that fall between the values given in the table, an interpolation is made to calculate the appropriate CHF value.

Table 11 Sample of CHF look-up table

PRESSURE (kPa)	MASS FLUX ($\text{kg m}^{-2} \text{s}^{-1}$)	QUALITY									
		-0.5	-0.4	-0.3	-0.2	0.6	0.7	0.8	0.9
...
...
7000	2500	10882	9986	8709	7496	261	204	99	51
7000	3000	11730	10850	9620	8170	346	263	112	52
7000	3500	12535	11558	10344	8740	409	317	135	57
7000	4000	13317	12216	10929	9320	470	317	136	58
7000	4500	14070	12839	11469	9769	492	317	137	59
7000	5000	14792	13465	11954	10124	521	326	138	63
7000	5500	15509	14000	12474	10713	582	348	153	70
7000	6000	16208	14521	12931	11464	655	379	179	84
7000	6500	16875	15091	13336	12214	725	422	210	99
7000	7000	17529	15640	13763	12432	795	476	243	116
7000	7500	18170	16174	14182	12682	866	530	277	132
7000	8000	18806	16673	14610	12995	936	581	312	149
8000	0	5101	4795	4484	4175	542	456	423	364
8000	50	5714	5359	5025	4744	1183	980	938	720
8000	100	6229	5834	5487	5235	1678	1457	1449	1050
8000	300	6685	6179	5792	5654	2144	1877	1538	1083
8000	500	6958	6354	5920	5763	2068	1858	1427	917
...
...

Compared to other available prediction methods, the look-up table approach has the following advantages: (i) greater accuracy; (ii) wider range of application; (iii) correct asymptotic trend; (iv) requires less computing time; and (v) can be easily updated if additional data become available. Applying the tables to transient heat transfer in bundles requires adjustment factors to correct for geometry, flux shape, and possibly transient effects. Here the advantages of the tabular technique (wide range of application, greater accuracy, and greater computing efficiency) are particularly important to the user.

The look-up table approach has some disadvantages: (i) it is a purely empirical prediction method, and hence it does not properly reflect the physics, and (ii) it could introduce erroneous trends if the underlying database were subject to experimental errors.

7.6.4.3.1 CHF correlations in CANDU bundles

Several CHF correlations have been developed for CANDU bundle geometry. These are mainly based on full-scale bundle data and are used for critical channel power calculations.

An example of a general form of a flux-corrected local CHF correlation for uncrept channels is given by [LEU2004, IAEA2001]:

$$CHF_{local} = \left(a_1 P^{a_2} G^{a_3} + a_4 P^{a_5} G^{a_6} x_{cr} \right) \left(\frac{q_{local}}{q_{average}} \right)^{a_7}. \quad (268)$$

An example of a general form of boiling-length-average CHF correlation for uncrept and crept channels is given by [LEU2004, IAEA2001]:

$$CHF_{BLA} = \left(b_1 P^{b_2} G^{b_3} + b_4 P^{b_5} G^{b_6} x_{cr} \right) \left[1 - b_7 \left(\frac{q_{local}}{q_{average}} \right)^{b_8} \right]. \quad (269)$$

The values of the parameters in the above equations are of a proprietary nature.

7.6.4.3.2 CHF correlations in fuel assemblies

Providing precise CHF predictions for the fuel bundles of advanced water-cooled reactors is a very difficult task. Advanced water-cooled reactors designs includes a variety of bundle geometries, as well as a variety of element spacer designs.

The basis of almost any generic bundle prediction method is a tube CHF prediction method because (i) parametric trends with pressure, mass flux, and quality are similar in tubes and in bundles, and (ii) tube CHF prediction methods are generally used in sub-channel codes to predict CHF in bundles.

One of the well-known correlations for PWR fuel bundles is the Westinghouse and Tong [IAEA2001, TON1996] correlation, which can be given by the following expression:

$$q_{cr,DNB}'' = \frac{q_{cr}''}{F}, \quad F = \frac{C \int_0^l q''(z') \cdot e^{-C(l-z')} dz'}{q''(l) [1 - e^{-Cl}]}, \quad C = \frac{4.23 \cdot 10^6 [1 - x_e(l)]^{7.9}}{G^{1.72}} \quad [m^{-1}], \quad (270)$$

$$q_{cr}'' = \left[(2.022 - 0.06238 \cdot p) + (0.1722 - 0.001427 \cdot p) \cdot e^{18.177 - 0.5987 \cdot p} x_e \right] \\ \left[(0.1484 - 1.596 \cdot x_e + 0.1729 \cdot x_e |x_e|) \cdot 2.32 \cdot G + 3271 \right] [1.157 - 0.869 \cdot x_e]. \quad (271) \\ \left[0.2664 + 0.837 \cdot e^{-124 \cdot D_h} \right] \left[0.8258 + 0.0003413 (h_l - h_{in}) \right]$$

The critical heat flux at the DNB, $q_{cr,DNB}''$ (kW/m^2), is at the local heat flux (for non-uniform heat flux), l (m) is the distance to the DNB, and x_e is the local steam thermodynamic quality. The above correlation is valid for the following parameter ranges: pressures of 5.5–13.8 (MPa), mass fluxes of 1350–6789 (kg/m^2s), hydraulic diameters of 0.005–0.0178 (m), thermodynamic qualities of -0.15–0.15, and channel lengths of 0.254–3.658 (m).

Another useful correlation for PWR fuel bundles is given by Bowring [IAEA2001, TON1996]:

$$q_{cr}'' = \frac{A - B \cdot h_{fg} x}{C}, \quad A = \frac{2.317 \cdot (h_{fg} D \cdot G / 4) \cdot F_1}{1 + 0.0143 \cdot F_2 \cdot D^{1/2} G}, \quad B = \frac{D \cdot G}{4},$$

$$C = \frac{0.077 \cdot F_3 D \cdot G}{1 + 0.347 \cdot F_4 (G / 1356)^n}, \quad p_R = 0.145 \cdot p \quad (272)$$

$$F_1 = \{p_R^{18.942} \exp[20.89(1 - p_R)] + 0.197\} / 1.917$$

$$F_2 = F_1 / \left\{ p_R^{1.316} \exp[2.444(1 - p_R)] + 0.309 \right\} / 1.309 \quad \text{For } p_R < 1 \text{ MPa}, \quad (273)$$

$$F_3 = \{p_R^{17.023} \exp[16.658(1 - p_R)] + 0.667\} / 1.667$$

$$F_4 = F_3 p_R^{1.649}$$

$$F_1 = p_R^{-0.368} \exp[0.648(1 - p_R)]$$

$$F_2 = F_1 / \left\{ p_R^{-0.448} \exp[0.245(1 - p_R)] \right\} \quad \text{For } p_R \geq 1 \text{ MPa}. \quad (274)$$

$$F_3 = p_R^{0.219}$$

$$F_4 = F_3 p_R^{1.649}$$

The above correlation is valid for channel lengths of 0.15–3.7 (m), pressures of 0.2–19 (MPa), and mass fluxes of 136–18,600 (kg/m²s).

The CANDU fuel CHF correlation is based on the CHF look-up table and is given by the following expression (note that CANDU 6 uses the look-up table method, whereas the Bruce and Darlington designs use correlations [IAEA2001]):

$$CHF = CHF_{TABLE} K_1 K_2 K_3 K_4 K_5 K_6 K_7 K_8 K_9, \quad (275)$$

where K_1 to K_9 are modification factors to account for sub-channel specific effects (e.g., element gap size, sub-channel equivalent diameter, adjacent heated/unheated surfaces, upstream spacers, etc.) and are defined as: K_1 – tube diameter factor; K_2 – bundle geometry factor; K_3 – spacer-effect factor; K_4 – heated-length factor; K_5 – axial-flux-shape factor; K_6 – circumferential-flux factor; K_7 – horizontal flow factor; K_8 – low-flow factor; K_9 – transient-effect factor.

7.6.4.4 CHF margin evaluation

CHF evaluation in the reactor core is of primary importance for estimating the reactor operating margins with adequate precision and a good understanding of uncertainties. Figure 114 shows the concept of reactor operating margin evaluation as a function of reactor operation (aging) [LEU2004, POP2014].

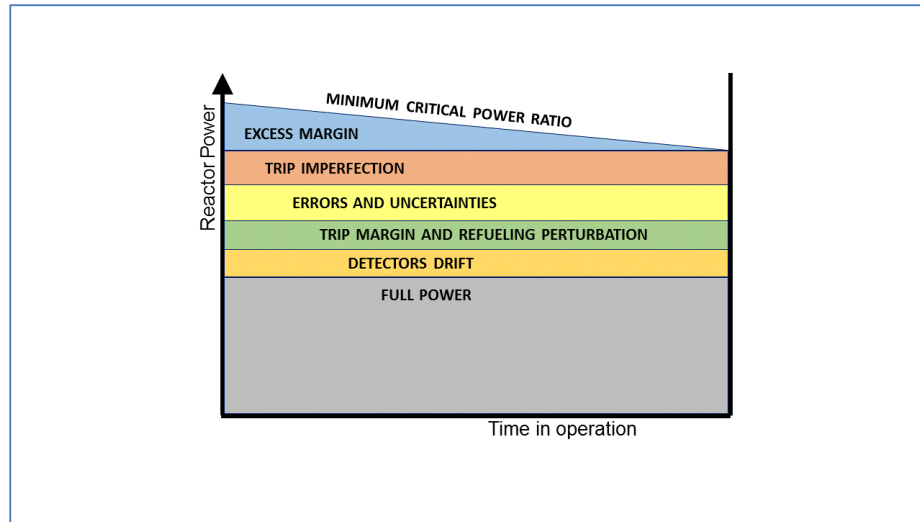


Figure 114 Concept of operating margins

This diagram assumes that the nominal power will remain unchanged during the reactor's life. Above the full nominal power are the detector drift margin and the operator's trip margin/fuelling/operating perturbation margin, which are also assumed to remain unchanged during the reactor life. On top of these are the error and uncertainties margin and the trip imperfection margin, which are also assumed to remain unchanged during the reactor life. However, the excess margin that is embedded in the reactor core design, and which represents all aging mechanisms having an impact on the reactor power margin, such as pressure-tube creep, continually decreases during the reactor life (i.e., the pressure-tube life). When all these margins are evaluated and added on top of the full nominal power, the resulting maximum power should still be less than the reactor critical power at which CHF occurs in some fuel channels.

From the above discussion, it is clear that CHF prediction is an important part of reactor thermal power margin evaluation. Hence, CHF evaluation and application focusses on the following concerns:

- i. To set the operating power with a comfortable margin to avoid CHF occurrence, in terms of the following parameters: (a) minimum CHF ratio (MCHFR) at constant pressure, mass flux, and critical quality; (b) minimum CHF power ratio (MCHFPR) at constant pressure, mass flux, and inlet fluid temperature; or (c) minimum power ratio (MCPR) at constant pressure, pump characteristic, and inlet fluid temperature
- ii. To evaluate the maximum sheath temperature during LOCA, LOFA, or LORA, which is usually concerned with the first (initial) CHF location;
- iii. To evaluate the thermal-hydraulic and neutronic responses to CHF occurrence in a reactor core (trip set points), based on knowledge of how CHF spreads in the reactor core; best-estimate predictions of average CHF and/or area in dryout as a function of power.

For reactor transient (accident) analyzes, it is important to determine sheath and fuel

temperatures. In this case, CHF is considered as the reference point for post-dryout analyzes. The set of transient analyzes includes the following scenarios: loss of regulation, loss of flow, loss of Class IV power, loss of coolant (small and large breaks), etc. More details are provided in Chapter 16.

The following terminology is used when evaluating CHF margins:

- 1) Dryout (or critical heat flux, CHF) occurs when the fuel sheath can no longer maintain continuous liquid contact. Current licensing criteria are no burnout or dryout at any location in the fuel channel (details depend on whether the first or second trip is considered in the analysis).
- 2) Critical power (CP) (also known as critical channel power, CCP) is the power corresponding to the first CHF occurrence (at constant pump head). Determining this requires knowledge of various disciplines (physics, fuel, fuel channel, thermal-hydraulics, etc.).
- 3) Critical power ratio (CPR) is the ratio of critical power to operating power.
- 4) Regional overpower protection (ROP) or neutron overpower protection (NOP) is aimed at preventing burnout in any fuel assembly during a slow LOR event. It includes full-core analysis of all possible scenarios and establishment of trip set points for various detectors.

Figure 115 shows the concept of critical channel power (CPR) used in the CANDU CHF margin methodology, with channel flow shown on the y-axis and channel power on the x-axis [IAEA2001, LEU2004, POP2014]. In this diagram, a critical parameter is any parameter associated with the critical heat flux (CHF). Below the diagram, a CANDU fuel channel is shown, with 12 fuel bundles and associated feeders connecting the channel to the reactor inlet and outlet header.

The channel hydraulic curve (blue line) determines the level of channel power that can be removed by a certain flow rate. Therefore, as power rises, the mass quality will also rise (two-phase flow behaviour), which would result in a reduction in the mass flow rate that can be pushed through the channel. To this point November 14 afternoon

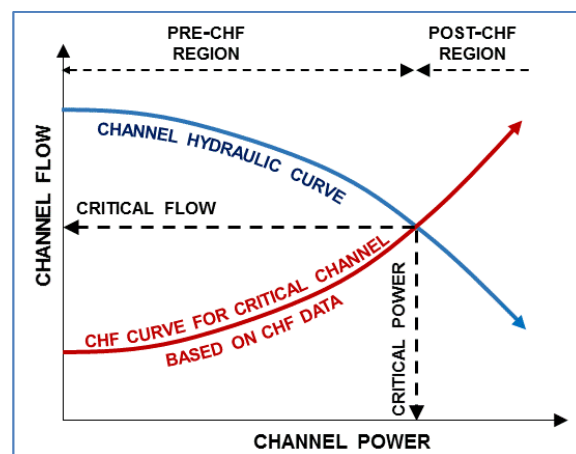


Figure 115 Critical channel power

The CHF curve (red line) shows the CHF values for certain combinations of channel power and flow rate. As explained in previous sections, at higher flow rates, the channel power at CHF will also rise (with the square of the flow rate). The intersection of these two curves shows the actual point at which CHF will be reached in the channel for a given flow rate and power. Hence, the intersection point defines the critical flow and the critical power at CHF. The left part of the diagram for which power is less than the critical power is defined as the pre-CHF region, and the right side of the diagram is the post-CHF region.

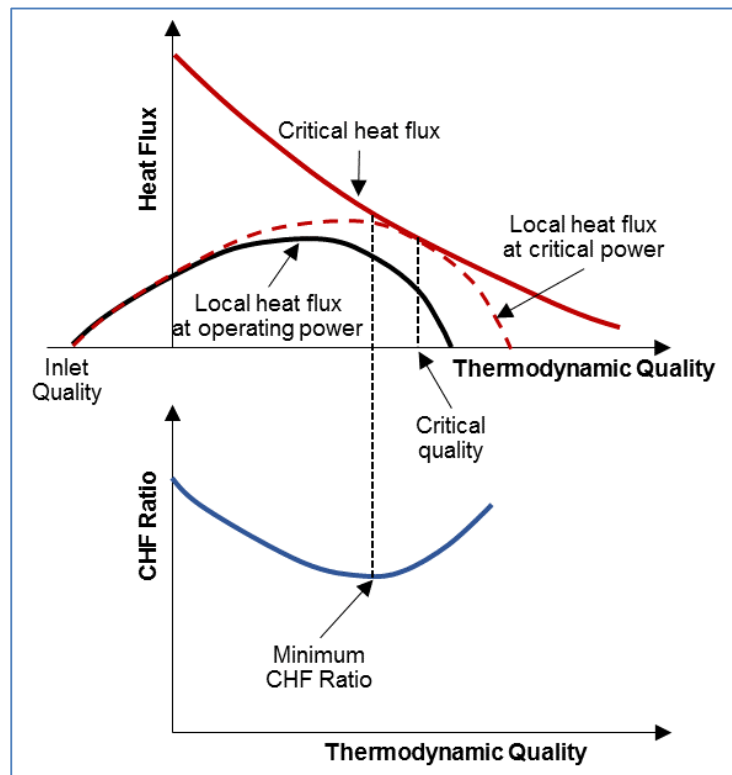


Figure 116 CHF margin definitions

The concept of CHF margin is explained in Figure 116 [IAEA2001, POP2014]. The top diagram on this figure shows heat flux on the y-axis and thermodynamic quality on the x-axis. The red solid curve shows a prediction of CHF as a function of thermodynamic quality. Of course, thermodynamic quality depends on channel power among other parameters, and therefore in turn, the shape and value of the CHF curve depend on channel power.

The solid black curve shows local heat flux as a function of quality, i.e., axial position in the channel as quality changes along the channel. Normally, under nominal conditions, the heat flux is less than the CHF, and therefore the black curve does not touch the red curve for any quality value. However, if the channel power is increased, the local heat flux along the channel also increases. At a certain value of the channel power, the local heat flux will touch the CHF at a certain position, and this position represents the power value that causes CHF (red dashed line). On the bottom diagram, the CHF ratio is shown, defined by the ratio of the critical heat flux (CHF) to the flux corresponding to the nominal operating power (NOP):

$$CHF_{RATIO} = \frac{CHF}{q_{local}}. \quad (276)$$

The above relation assumes constant inlet thermodynamic quality, constant outlet pressure, and mass flux.

Figure 117 shows a comparison of CHF margin evaluation methods: the CHF ratio, the CHF power ratio, and the critical power ratio [IAEA2001, POP2014]. The above explanation along with Eq. (276) is illustrated on the left side of Figure 117. The MCHFR method is easy to understand and implement. However, it does not provide a clear account of reactor power margins because it uses heat flux instead of channel power, which makes it cumbersome to use for power reactor applications (however, it is often used for research reactor applications).

The CHFPR method is shown on the right side of Figure 117 [IAEA2001, POP2014]. In this method, rather than a ratio of channel heat fluxes, a ratio of channel powers is used that represent a certain value of operating heat flux and CHF. This method provides a better understanding of channel and reactor power margins with respect to CHF. However, it does not provide a clear account of margins because as channel power rises to reach the CHF line, the CHF line will also change position because it indirectly depends on channel power.

The most useful method in CANDU reactor applications is the *critical power* (CPR) method. The principles of this method are explained above and illustrated in Figure 115 [IAEA2001, POP2014]. The critical power ratio is defined by the following relation:

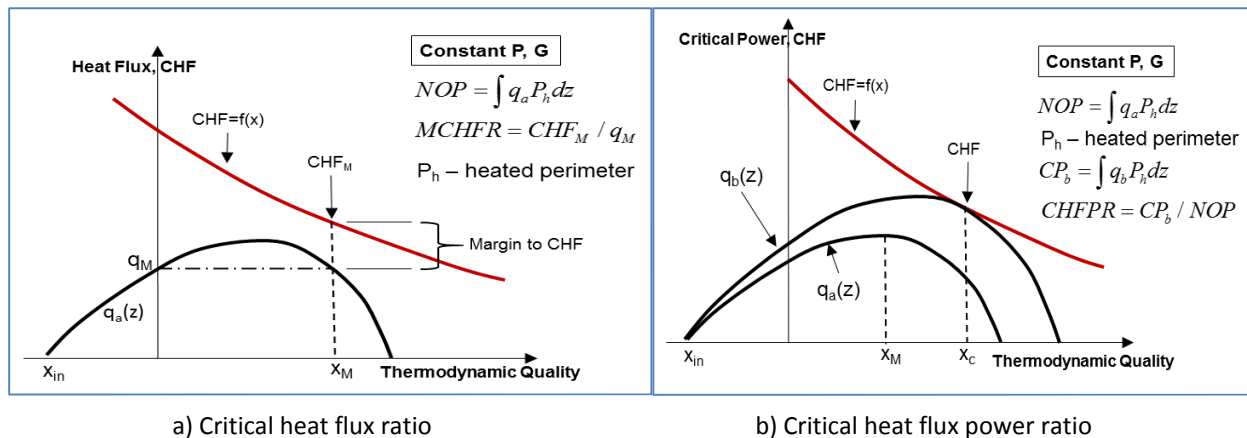
$$CP_{RATIO} = \frac{Critical\ Power}{Operating\ Power}. \quad (277)$$

This relation holds for constant inlet fluid temperature and pressure and a fixed pump curve. As is evident from this diagram, channel flow at point NOP on the hydraulic curve corresponds to NOP power. Keeping the flow at point NOP, the corresponding heat flux that would have resulted in CHF is at point CHF₁ (the top blue point on the CHF curve), corresponding to the critical power. CP₁. The flow at point CHF (lower blue point on the CHF curve) corresponds to the channel power. CP₂.

Hence, the critical power ratio is given by the relation:

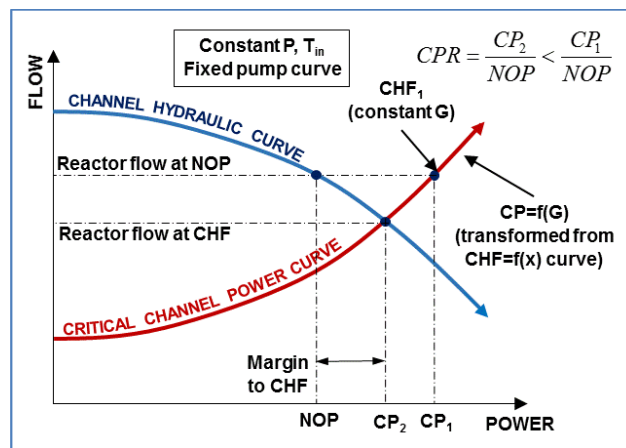
$$CPR = \frac{CP_2}{NOP}. \quad (278)$$

The margin to CHF is shown as the distance between points NOP and CP₂, as can be observed on the right side of Figure 117.



a) Critical heat flux ratio

b) Critical heat flux power ratio



c) Critical power ratio

Figure 117 CHF margin evaluation methods (a, b, c)

There are a number of uncertainties in the development and application of the CHF prediction methods and CHF margin methods covered in this section. These uncertainties need to be well understood, classified, and evaluated and then taken into account in reactor applications. The uncertainties can be broadly grouped into the following categories:

- i. Uncertainties in CHF measurements using bundle simulators. These uncertainties can result from errors in flow, power, pressure, and inlet temperature measurements that are caused by (a) inadequate CHF detection methods, (b) variations in flux distribution across/along the bundle, and (c) geometric tolerances;
- ii. Prediction uncertainties in CHF correlations or sub-channel codes;
- iii. Uncertainties in reactor conditions, including (a) reactor flow, pressure, and temperature (calculated from system safety codes) and (b) reactor power measurements (from detectors); and
- iv. Uncertainties in extrapolation to in-reactor conditions resulting from (a) electrical vs. nuclear heating; (b) flux tilts across elements, the bundle, and the core; and reactor aging effects (creep, fouling of pipes, etc.).

7.6.4.5 CHF bundle effects – R&D testing and application

Extensive R&D support is required to gain a better understanding of CHF phenomena, including support for development of CHF correlations and look-up tables and development of computer tools. Any changes in design or operating parameters trigger a need for supporting R&D to provide evidence of the applicability of the current CHF models. The general strategy in performing supporting CHF R&D is to conduct it in an incremental fashion to minimize the cost and optimize the work scope.

CHF experiments are usually based on constant flow conditions (inlet or outlet pressure, inlet mass flow rate, and inlet-fluid temperature) and constant geometric factors (hydraulic diameter and heated length) in each test series. The primary interest in these CHF experiments is measurement of fuel power at CHF. However, determining CHF locations (both axially and radially) is also an objective. The other measurements of interest are circumferential CHF location, subsequent CHF occurrences (CHF spreading, or dry patch spreading), and pressure drops along a channel experiencing CHF.

A number of CHF experiments are performed in a simple geometry consisting of one fuel element simulator. In such case, the experimental setup consists of a pipe in which heating is provided by direct electrical current flowing through the pipe wall and coolant flowing past the pipe outside surface. Another option is to use indirect heating by a coil embedded in the pipe interior, through which electrical current is supplied. In either case, the heat flux from the pipe wall to the fluid is directly proportional to the strength of the electrical current. Axial power profiles can be obtained by varying the pipe wall thickness in direct heating, or by changing the number of coils per unit length in the case of indirect heating.

The pipe is equipped with various instruments to measure important parameters. Stationary or movable thermocouples are used for wall temperature measurements. The stationary thermocouples can measure only temperatures, i.e., burnout/dryout at specific locations in the pipe. Therefore, these may not capture initial CHF value and location. Moreover, no information on subsequent CHF and dry-patch spreading can be obtained with these thermocouples. Moveable thermocouples provide coverage almost over the entire heated length because they are moved during the experiment along the internal wall of the heated pipe. They provide measurements of initial CHF, subsequent CHF occurrences, and dry-patch spreading. However, they are more conservative, expensive, and time-consuming (when scanning the entire pipe surface area).

More complex and sophisticated CHF measurements are performed in CANDU fuel bundle simulators. One such simulator is shown in Figure 118 [LEU2004]. This fuel bundle simulator consists of a 37-element full-scale bundle 6 m long. The bundle is provided with a simulator of junctions and appendages and fully resembles a CANDU fuel channel. The wall heating distribution takes into account bundle endplates and fuel distribution along the string of fuel bundles. This device can simulate non-uniform axial and radial power distribution. Sliding thermocouples are inserted into a number of fuel element simulators that are indirectly heated by coils connected to the electric current source. Figure 119 shows an axial power distribution in such a fuel bundle simulator, and as is evident in the figure, any axial variation in heat flux can easily be simulated. Figure 120 shows a close-up view of one part of a fuel bundle and a

sliding thermocouple moving inside along the fuel element, with a sample of a measured fuel sheath temperature [LEU2004].

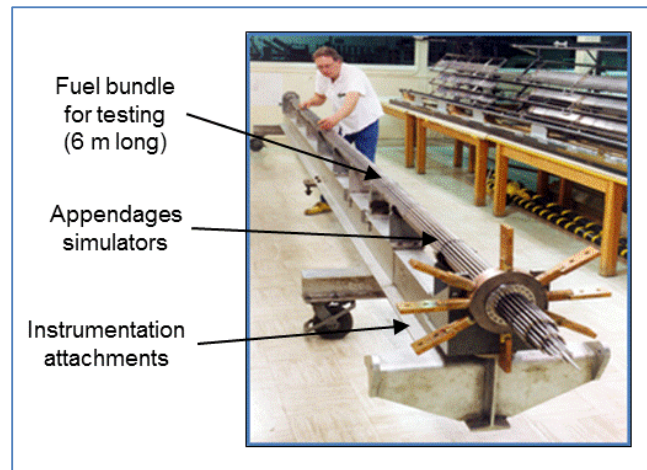


Figure 118 CANDU bundle experimental simulator

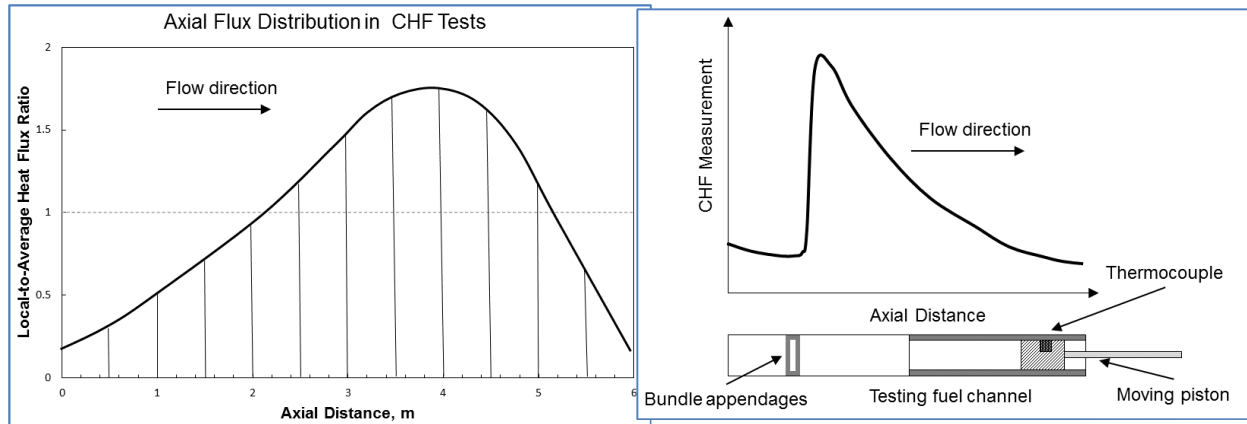


Figure 119 Axial flux distribution in full-scale bundle test

Figure 120 CHF variation along a heated surface

One of the most important aspects and of CHF in fuel bundles is the impact of spacing devices, which enhances CHF as the spacing value increases. In addition, the impact of radial power distribution is important because it can result in asymmetric CHF occurrence in the bundle. However, the 37-element and 43-element CANDU fuel bundle designs have enhanced features that improve CHF design.

Figure 121 shows various spacer devices used in fuel bundle design for various reactor types [IAEA2001]. These devices have a dual purpose: to keep the bundle tight, i.e., to minimize radial vibration, and to enhance turbulence and thus improve CHF robustness (i.e., increase the CHF value). In general, turbulence in pipes and fuel bundles creates better fluid mixing and therefore easier removal of bubbles generated in sub-cooled boiling on the walls. This in turn enables a fuel element to achieve higher heat fluxes without causing CHF by bubble crowding on the fuel sheath surface.

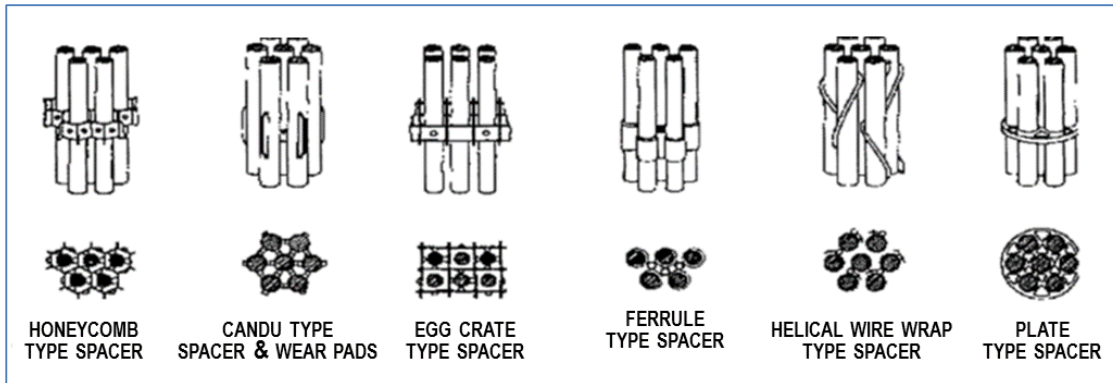


Figure 121 Different types of spacer devices for CHF robustness

Figure 122 presents an illustrative example of the impact of spacer devices on CHF [IAEA2001]. On the y-axis, local critical heat flux is shown. The flow along this CANDU channel is from left to right. Because sub-cooling is higher at the inlet, CHF is also higher. As fluid moves along the channel, the pressure decreases, quality increases, and bulk boiling starts. The net effect of these changes is a reduction in the CHF along the channel. However, as fluid approaches a bundle spacer, fluid turbulence increases, causing a sharp CHF increase. If the fuel rods were smooth along the length of the fuel channel and there were no spacers or other appendages, the CHF would have been reduced much faster.

The benefits of more turbulence as a method of enhancing CHF robustness must be weighed against the negative impact of higher turbulence and local pressure losses on the primary pump head. Therefore, having too much turbulence and local pressure loss causes the primary pump head, pump design, and particularly pump operation to become prohibitively expensive, which may outweigh the benefit with regard to CHF.

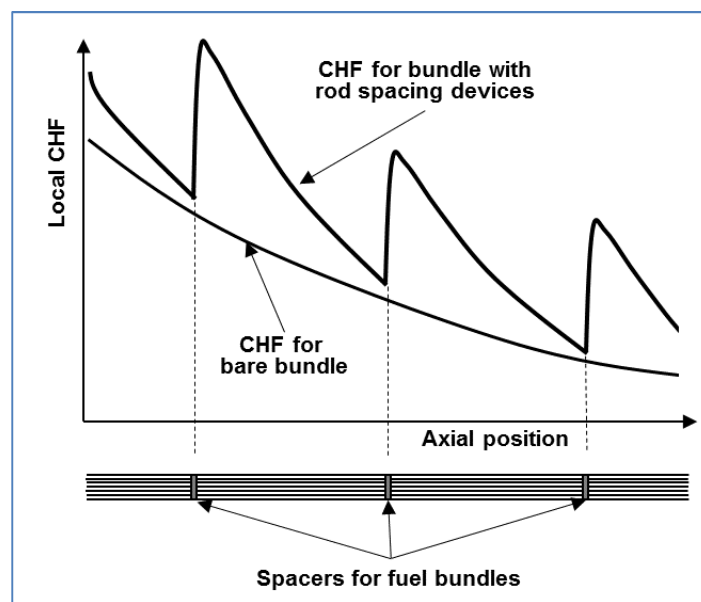


Figure 122 CHF behaviour around fuel bundle spacer devices

CHF data have a wide range of application, and this is one of the most important R&D areas for

reactor design, safety analysis, and licensing. CHF margins are the central issue in the licensing submissions for nuclear reactors, and this application is a strong driver for full-scale fuel bundle data, for quantification of the impact of separate effects, and for assessment of CHF uncertainties.

CHF R&D work is important to reach an adequate understanding of the phenomena involved using fundamental and bundle-specific studies and parametric and separate-effects tests. Certainly, CHF R&D is essential to develop prediction methods, i.e., CHF correlations and models, and to validate these correlations, models, and reactor safety codes. The CHF tests used for this purpose are a combination of bundle and separate-effects tests. The key applications of CHF prediction methods are in ROP (or NOP) and reactor safety codes, fuel channel behaviour codes, and fuel behaviour codes.

Experimentally measured CHF values are based on tests with defined inlet conditions. CHF values based on inlet-flow conditions are limited to a specific channel geometry and heated length. However, reactor safety analyzes use the local-conditions approach based on local pressure, mass flux, and quality to predict local CHF. For given inlet conditions, the local CHF conditions may vary in terms of thermodynamic quality (or enthalpy). In such cases, low quality (or enthalpy) is appropriate for short heated lengths and high quality (or enthalpy) for long heated lengths. It is important to evaluate local thermodynamic quality using inlet flow conditions and power.

When using CHF data, it is important to mention that all CHF data are obtained under steady-state conditions in terms of power, mass flux, and sub-cooling. In safety analysis, CHF prediction tools developed for steady-state conditions are used to simulate reactor transients. If the transient is slow, i.e., longer than 10 s, no significant impact on the models is expected. However, for fast transients (shorter than 1 s), a significant effect on CHF is likely.

Another important CHF application is related to thermal-hydraulic and neutronic responses to CHF occurrence (partial bundle dryout). This application is strongly affected by the level of success in predicting the spread of dryout in a fuel bundle. It has been experimentally observed that the average CHF value that occurs over a large portion of the fuel sheath surface can be much higher than the initial CHF at some cross-sectional locations. To capture such important effects in dryout spreading, sub-channel codes are the most promising tool.

7.6.5 Transition and film boiling heat transfer

Reactor fuel channel operation beyond dryout (beyond CHF) is possible in certain transient and accident regimes. This section provides information on post-dryout heat transfer phenomena and on the correlations used for these heat transfer regimes.

Post-CHF (or post-dryout) heat transfer occurs when the surface temperature becomes too high to maintain continuous liquid contact and the surface becomes covered by a continuous or intermittent vapour blanket. Post-CHF heat transfer includes transition boiling, illustrated in Figure 29 and Figure 123, where intermittent wetting of the heated surface takes place, and film boiling, where the heated surface is too hot to permit liquid contact. The boundary between these post-CHF heat transfer modes is the minimum film boiling temperature, or T_{MFB} . Due to the poor heat transport properties of vapour, high heated surface temperatures are often encountered during film boiling.

7.6.5.1 Post-dryout phenomena

Several figures presented in previous sub-sections of this chapter are relevant to post-dryout heat transfer. Figure 26 shows heat transfer regimes in vertical fuel channels, with clearly shown areas of post-dryout heat transfer regimes in the upper part of the channel. Figure 28 shows a 3-D representation of the boiling surface for water, with transition and film boiling indicated. Figure 29 shows a conceptual illustration of the boiling curve, again showing post-dryout heat transfer beyond the CHF point. Figure 33 shows temperature profiles along a vertical fuel channel experiencing various flow and heat transfer regimes, including post-dryout heat transfer regimes in the upper part of the figure.

Post-CHF heat transfer is initiated as soon as the CHF condition is exceeded and continues until quenching (rewetting) of the surface is achieved. Depending on the particular scenario and flow conditions present, various heat transfer modes of the boiling curve may be distributed along a heated surface, or a series of heat transfer modes can succeed each other over time at the same location, as is the case during transients.

During sustained post-dryout heat transfer, the heated surface is cooled mainly by vapour flow. Because of the relatively low heat-transfer coefficient for this heat transfer regime, the fuel sheath is exposed to high temperature that may lead to damage. In this respect, it is important to understand and determine the surface conditions and the coolant flow parameters at the time CHF is reached, because these determine the impact of the post-dryout condition on the fuel sheath.

Figure 123 shows various post-dryout flow types and heat transfer regimes on a vertical surface [LEU2004, POP2014]. These are highly similar to those that occur in a horizontal fuel channel. Type I post-dryout identifies a situation in which the heated surface has lost contact with the liquid, but at one location, contact has been re-established, and this point acts as a heat sink. In this case, heat transfer from the internal parts of the wall and from surrounding areas occurs towards this heat sink, thus cooling the wall near the liquid-wall contact and preparing it for quenching.

Type II represents a situation in which a heated surface in post-dryout regime is flooded by

liquid water from the top. This figure clearly shows the quench front moving downward. The upper part of the surface is well cooled, and obviously heat transfer occurs from the lower, hotter portions of the wall upwards towards the cooler area, which therefore acts as a local heat sink, preparing the lower part of the surface for quenching. Type III represents a situation similar to Type II, but in this case, quenching proceeds in an upward direction by flooding from the bottom. Type II and Type III post-dryout regimes combine into one regime for a horizontal surface.

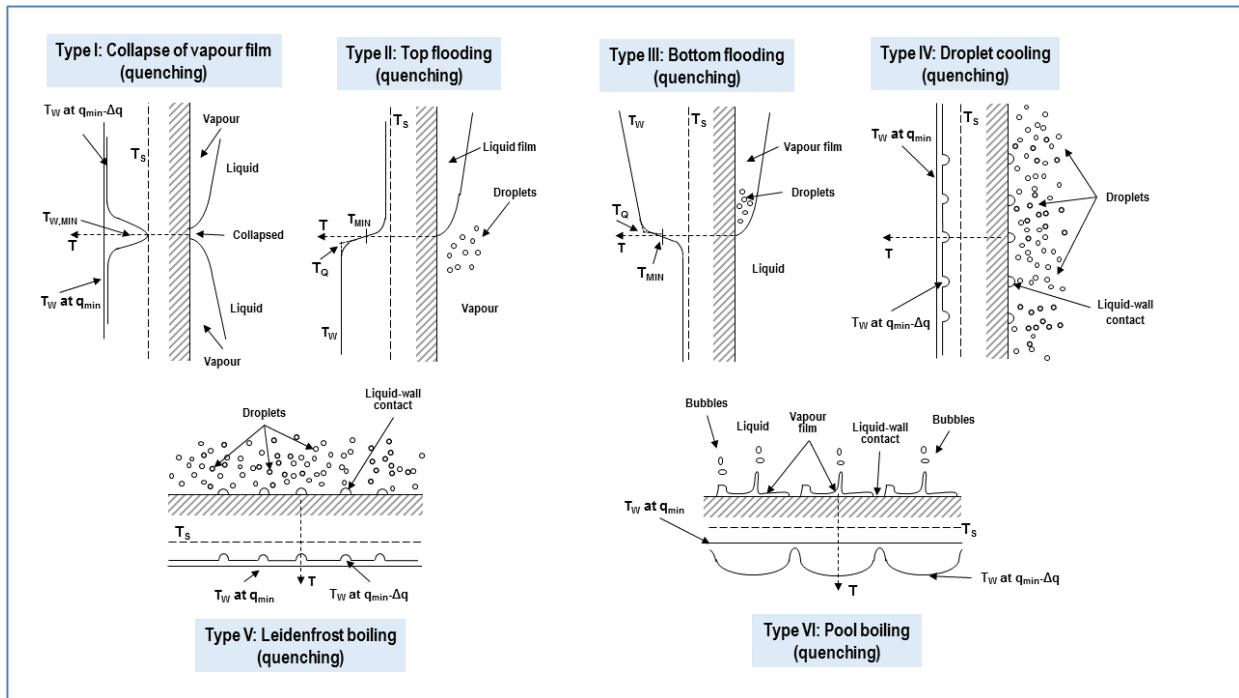


Figure 123 Types of transition boiling and film

Type IV mode occurs when the heated surface in post-dryout regime is cooled by impingement of droplets flowing past the heated wall. Each droplet impingement on the heated surface provides a quick intermittent miniature local heat sink. However, although local surface cooling by one droplet impingement is infinitesimally small, as many droplets impinge on the surface, the integral effect of heat removal is significant, thus preparing the surface for rewetting.

Types V and VI apply to horizontal surfaces in pool boiling. Type V shows droplets impinging on the surface, with an effect similar to Type IV, whereas Type VI represents a regime in which a water layer floats on top of a vapour film, a situation similar to that described for Type I.

Transition Boiling

Berenson [IAEA2001] provides one of the best definitions of transition boiling: a combination of unstable film boiling and unstable nucleate boiling alternately existing at any given location on a heating surface. The variation in heat transfer rate with temperature is primarily the result of a change in the fraction of time that each boiling regime exists at a given location.

Figure 124 conceptually shows transition boiling in a pool boiling regime. Pockets of vapour are

visible on the heated surface and may move intermittently back and forth along the surface, as is typical for this pool boiling situation. At any surface temperature in excess of the CHF temperature, the heated surface is partially covered with unstable vapour patches varying over space and time, with frequent replacement of vapour patches by fluid. Although this may seem similar to transition pool boiling as described above, the introduction of the convective component improves the film boiling component by reducing the vapour film thickness and changing the heat transfer mode, whether dry or wet, from free convection to forced convection.

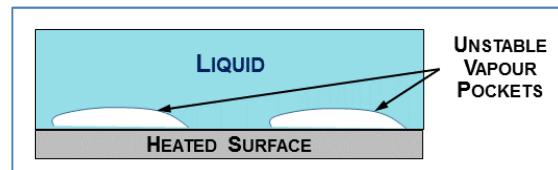


Figure 124 Concept of transition boiling in pool boiling

As shown in Figure 29, the slope of the curve for transition boiling is negative, which means that this is an unstable heat transfer regime. This heat transfer regime can occur on a temperature-controlled surface at conditions beyond CHF. Examples of temperature-controlled surfaces are surfaces with high thermal inertia, surfaces heated by condensing steam (which controls temperature at the saturation point), and fuel element surfaces during fast transients.

A heat-flux-controlled surface at conditions beyond CHF can experience transition boiling only under conditions under which the slope of the transition boiling curve is positive ($dq/dt > 0$), which is possible for mass quality above 50%, as shown in Figure 31. Note that as temperature increases gradually with increasing heat flux, transition boiling intermittently wets and dries the surface. In the case of high quality, even when the surface is continuously dry, the temperature increase is not drastic due to effective convective heat transfer. Examples of heat-flux-controlled surfaces are electric heaters and fuel elements during fast transients.

If the slope of the transition boiling curve is negative ($dq/dt < 0$), a rapid transition from nucleate boiling to film boiling usually occurs, and therefore transition boiling is not encountered (or occurs very briefly).

The periodic contacts between liquid and heated surface in the transition boiling region of the boiling curve result in formation of large amounts of vapour, which force liquid away from the surface and create an unstable vapour film or blanket. Because of this, the surface heat flux and the surface temperature can vary both with time and with position on the heater. The average heat transfer coefficient decreases as the temperature increases because the time of contact between the liquid and the heater surface is decreased.

Heat transfer in transition boiling occurs primarily by liquid-solid contact. At the critical heat flux point, the contact-area (or time) fraction is generally 100%, i.e., most of the surface is in good contact with the liquid. Post-CHF conditions result in a sudden large decrease of the contact fraction between the liquid and the heated wall surface. Thereafter, most of the heat transferred during transition boiling will be due to droplet-wall interaction. Initially, at surface

temperatures just in excess of the boiling crisis temperature, a significant fraction of the droplets deposit on the heated surface, but at higher wall superheats, vapour repulsion forces become significant in repelling most of the droplets before they can contact the heated surface. The repelled droplets contribute to heat transfer by inducing turbulence in the boundary layer to enhance convective heat transfer to the vapour.

Figure 29 shows that transition boiling ends when the heated wall surface temperature drops to a minimum value, called the minimum film boiling temperature, T_{MFB} . Several names are given to the minimum film boiling temperature. They include rewetting temperature, quench temperature, Leidenfrost temperature, film boiling collapse temperature, and others.

During dryout and wall temperature increase, the minimum film boiling temperature separates the high-temperature region, where film boiling or vapour cooling takes place, from the lower-temperature region, where much more efficient heat transfer in transition boiling occurs. Knowledge of the minimum film boiling temperature is particularly important in reactor safety assessments.

During surface quenching (such as emergency core cooling), rewetting commences at the minimum film boiling temperature and proceeds until nucleate boiling is established at a much lower wall temperature. For this reason, predicting the minimum film boiling temperature as a function of the system parameters is very important because heat transfer coefficients on either side of the minimum film boiling temperature can differ by orders of magnitude. Generally, T_{MFB} is defined as the temperature at the minimum heat flux.

In summary, no liquid/sheath contact is possible for $T_W > T_{MFB}$, but possible liquid/fuel sheath contact exists for $T_W < T_{MFB}$:

$$\Delta T_{W,MIN} = \frac{q_{MIN}}{h_{FB}}. \quad (279)$$

Film boiling

Two theories have been proposed for analytical prediction of the minimum film boiling temperature. One theory says that the minimum temperature is a thermodynamic property of the fluid (i.e., the maximum liquid temperature) and therefore is primarily a function of pressure. According to this theory, the minimum film boiling temperature is associated with the maximum liquid superheat (beyond which the nucleation rate is infinite and liquid cannot exist). This theory comes from the equation of state and from homogeneous nucleation theory.

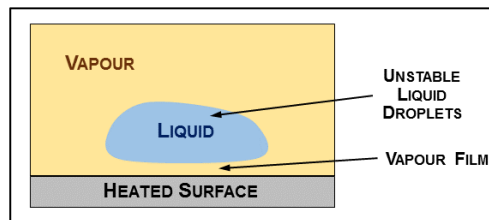


Figure 125 Minimum film pool boiling – Taylor instability

The other minimum film boiling theory suggests that rewetting commences due to hydrodynamic instabilities that depend on the velocities, densities, and viscosities of both phases as well as the surface tension at the liquid-vapour interface. By this theory, the minimum heat flux associated with the minimum film boiling temperature can be predicted from Taylor's instability criterion. Figure 125 illustrates the theory of Taylor's instability [LEU2004, POP2014, DEL1981, BER1981]. This figure shows a chunk of liquid that floats on top of a vapour film above a heated surface. The instability results from gravity acting on the liquid as a heavier phase on the top, and on the vapour as a much lighter phase at the bottom.

During fast transitions, where insufficient time is available to develop hydrodynamic forces fully, rewetting can be expected to be thermodynamically controlled, whereas for low flows and low pressures, where sufficient time is available and the volumetric expansion of the fluid near the wall is large, rewetting is more likely to be hydrodynamically controlled. Once rewetting has occurred locally, the rewetting front can then propagate at a rate controlled primarily by axial heat conduction in the heated wall.

Figure 126 [LEU2004, POP2014] shows various film boiling types in pool boiling and forced convection flow situations.

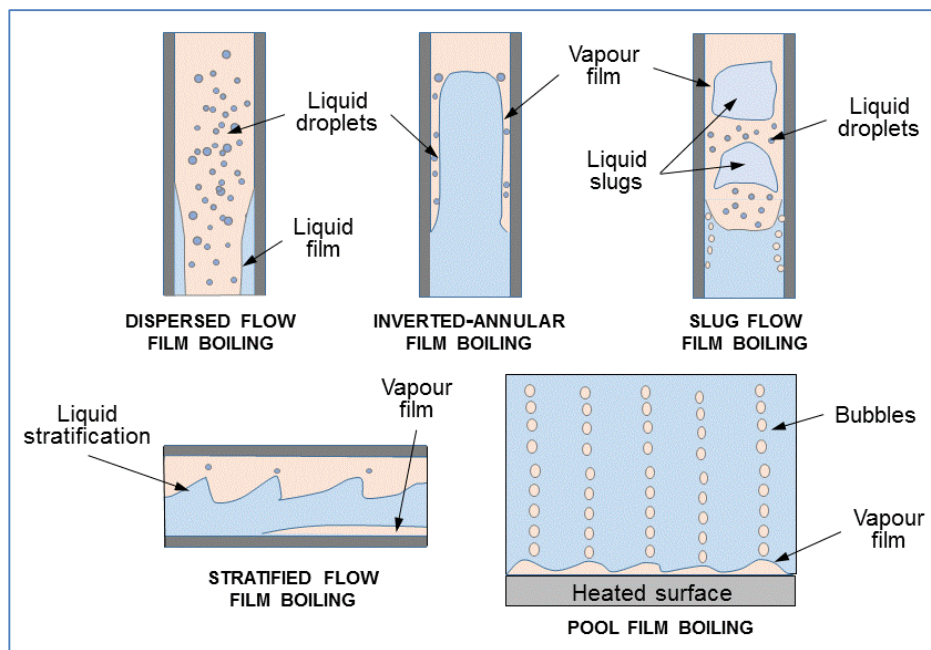


Figure 126 Film boiling types

Film boiling is generally defined as that mode of boiling heat transfer in which only the vapour phase is in contact with the heated surface (see Figure 125 and Figure 126). The term is used in forced convective boiling to refer to conditions under which the liquid does not contact the heated surface, but is usually in one of the following forms (shown on Figure 126 and Figure 32)

- a dispersed spray of droplets, normally encountered at void fractions in excess of 80% (liquid-deficient or dispersed-flow film boiling regime);

- b) a continuous liquid core (surrounded by a vapour annulus which may contain entrained droplets), usually encountered at void fractions below 40% (inverted annular film boiling or inverted annular-flow boiling regime (IAFB)); and
- c) a transition between these two cases, which can take the form of an inverted slug flow for low to medium flow.

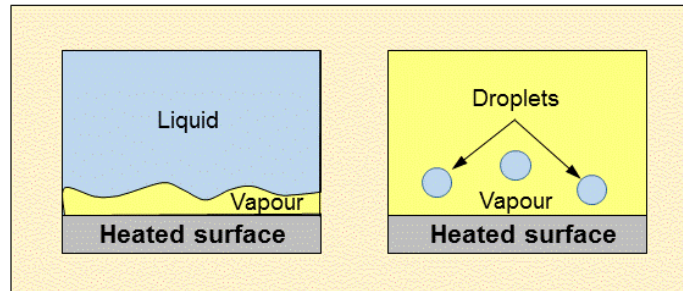


Figure 127 Pool film boiling mechanisms with horizontal heated wall

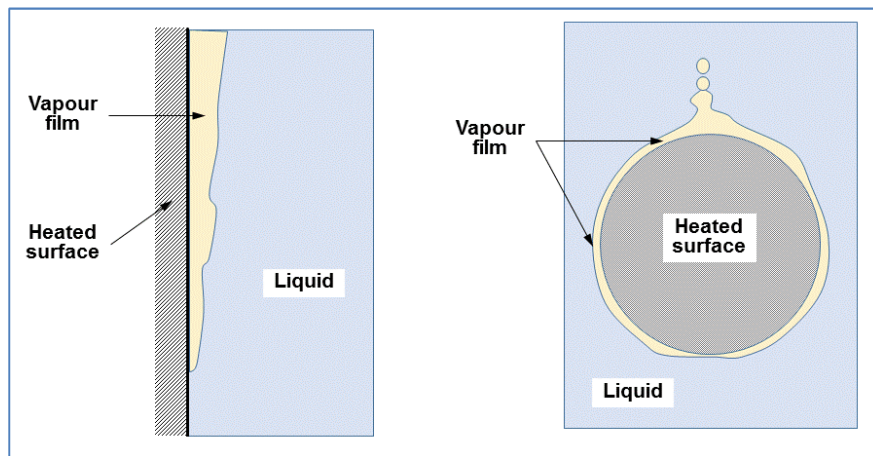


Figure 128 Pool film boiling patterns

The flow and heat transfer regimes types described above are illustrated in Figure 126. This figure also shows an example of stratified flow film boiling that is relevant to CANDU reactor channels. Figure 128 shows pool film boiling at a vertical wall and at a horizontal cylinder in stagnant water.

The dispersed flow film boiling regime, shown in Figure 129 at the bottom, is the most commonly encountered and has been well studied. Its heated surface temperature is moderate. In the inverted annular and inverted slug flow regimes, shown at the top of Figure 129, excessive surface temperatures are frequently encountered (see Figure 104 and Figure 105). Radiation heat transfer, which is unimportant in transition boiling, becomes important in film boiling, particularly at low flows, low void fractions, and surface temperatures in excess of 700°C.

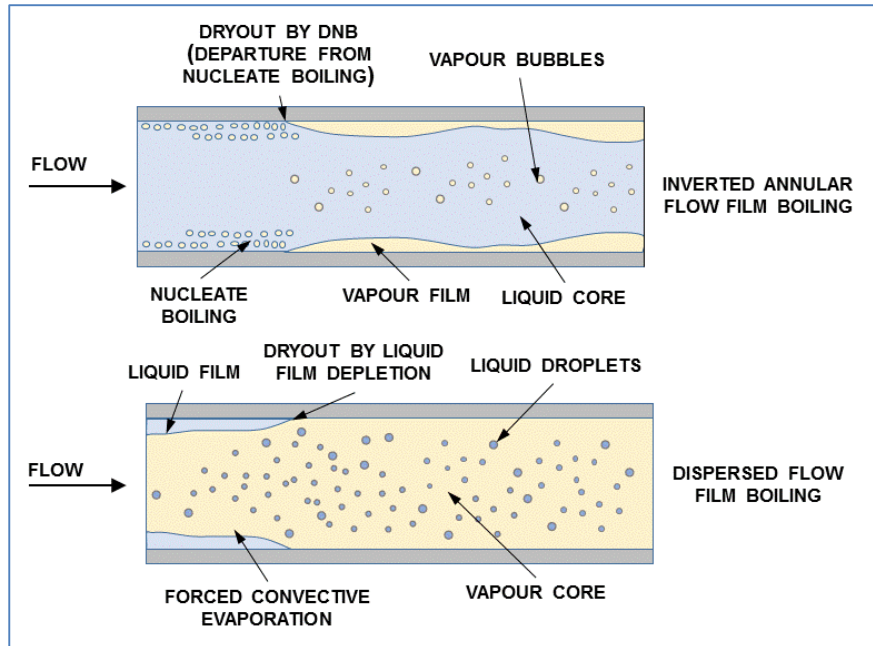


Figure 129 Forced convection film boiling patterns

When the flow and heat transfer regime is film boiling with the presence of liquid, several heat transfer regimes occur, as shown in Figure 130. On the left side of Figure 130, a film boiling regime with droplets in the middle of the pipe is illustrated. On the right side of Figure 130, a film boiling regime with a liquid core in the middle of the pipe is illustrated [POP2014, LEU2004]. These two flow regimes correspond to the regimes shown in Figure 129. The y-axis represents temperature or velocity, whereas the x-axis represents distance from the heated wall, along with heat flux direction.

In both cases, close to the wall, a gradual change of temperature or velocity is indicated, as appropriate for a boundary layer in a laminar flow regime. On the left side, the liquid droplets are assumed to be small, as is appropriate for dispersed flow. In such a case, the droplets are assumed to be at saturation. Hence, the temperature profile in the channel shows a superheated wall (temperature above the saturation temperature for a given pressure) and superheated steam in the pipe core.

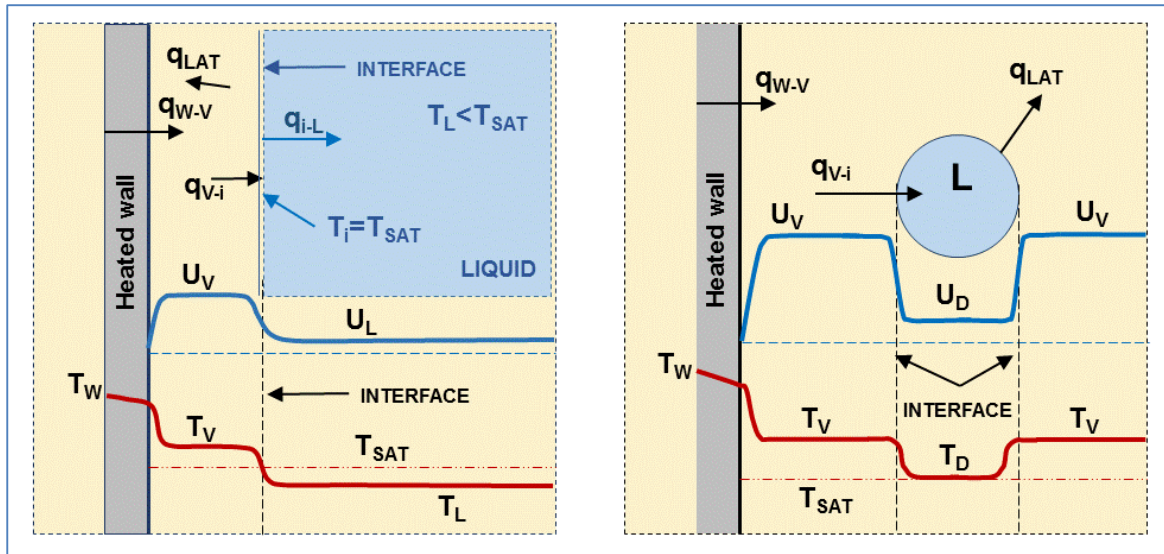


Figure 130 Film boiling heat transfer temperature and velocity profiles

Away from the wall, temperature drops quickly to a lower value in the boundary layer, but still remains above saturation. At the steam-droplet interface, temperature is close to saturation and continues to be at saturation inside the droplet. The velocity is near zero along the wall and rises in the boundary layer to a value representing steam bulk velocity. The steam velocity is higher than the liquid velocity, and this velocity difference, and the associated interfacial friction between the phases, carries the droplets upward. Because water is a much heavier fluid than steam, a large velocity difference between water and steam is needed to produce sufficient interfacial friction to carry the droplets in steam flow.

The heat flux direction on the left side of Figure 130 is from the wall to the vapour, and then from the vapour to the liquid-droplet interface. Because the liquid droplets are saturated, any heat added to the droplets results in a certain mass of liquid evaporating and joining the vapour flow, and therefore liquid droplets continue to lose mass as they flow along the superheated vapour flow. Heat radiation from the wall to the vapour and the droplets is important only if the wall temperature is substantially above the saturation and steam temperatures.

The right side of Figure 130 shows a film boiling regime with a liquid core in the pipe. In this case, the velocity profile is similar to the one on the left, with the vapour velocity being higher than the liquid velocity because the vapour is a much lighter fluid. The temperature profile from the heated wall to the vapour is also similar. However, because the liquid core contains a large volume of liquid, its internal temperature is assumed to be sub-cooled. Hence, the vapour-liquid interface must be at saturation to maintain a continuous temperature profile. A thin thermal boundary layer around the vapour-liquid interface with a steep temperature change is evident.

In the inverted annular flow regime, few entrained droplets can be present in the steam film, whereas the bulk of the liquid is in the form of a continuous liquid core that may contain entrained bubbles. In dryout, the continuous liquid core becomes separated from the wall by a

steam layer that can accommodate steep velocity gradients. As a stable steam blanket is formed, heat is transferred from the wall to the steam and subsequently from the steam to the liquid core. For very thin steam films, heat transfer from the wall to the liquid is primarily by conduction across a laminar steam film. For thicker steam films, turbulent flow occurs in the film, and the liquid-steam interface becomes agitated. Heat transfer across the wavy steam-liquid interface takes place by forced convection. This mode of heat transfer is much more efficient than single-phase convective heat transfer between the smooth wall and the steam. Hence, it is assumed that the bulk of the steam is at or close to the liquid core interface temperature (i.e., the saturation temperature).

The heat flux direction on the right side of Figure 130 is from the wall to the steam, from the steam to the liquid interface, and from the liquid interface to the liquid internal body. Note that the heat flux from the steam to the liquid interface is partitioned into a part that is used to evaporate a portion of the liquid interface and a part that is directed to the internal liquid body as convective heating of the liquid. As mentioned above, heat radiation from the wall to the steam and the liquid core is important only if the wall temperature is substantially above the saturation and steam temperatures.

Heat transfer from the wall to the vapour and from the vapour to the liquid will depend on the conditions of the surfaces, the flow patterns, and other parameters. This topic and the specific heat transfer correlations are described in the section below.

Figure 131 shows various heat transfer regimes in film boiling of a dispersed droplet regime, as described above [POP2014, LEU2004]. Solid lines in this figure indicate heat fluxes and their directions, whereas the dashed line indicates mass transfer by evaporation.

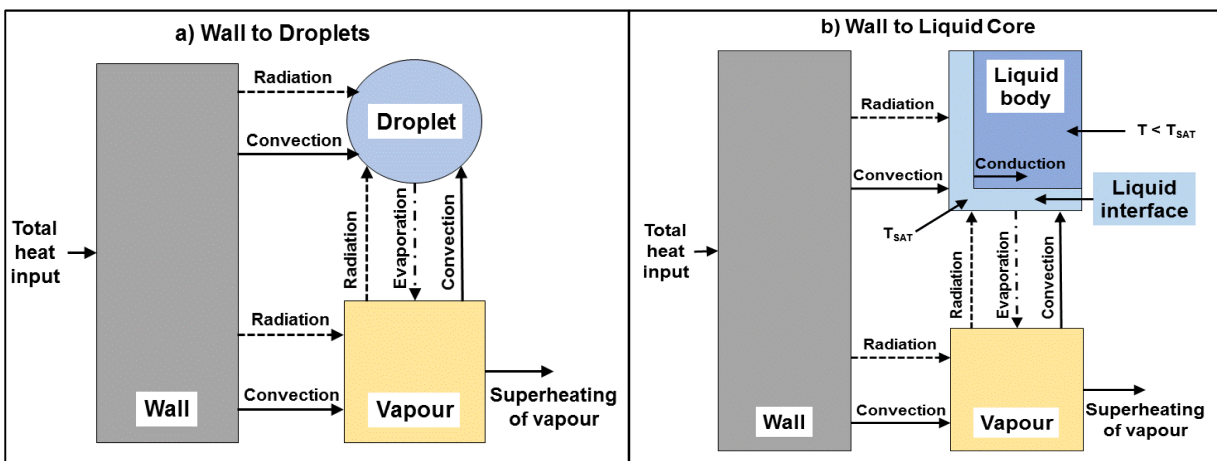


Figure 131 Film boiling heat transfer mechanisms

7.6.5.2 Post-dryout prediction methods and heat transfer correlations

As mentioned before for other heat transfer regimes, many heat transfer correlations have been developed for post-dryout heat transfer regimes. The key correlations and those that are most widely in use are covered in this section.

Accurate prediction of wall temperature in the film boiling regime is of vital importance in accident safety analysis of the core and steam generators of advanced water-cooled reactors.

The following four methods for estimating film boiling heat transfer are commonly used:

- i. Semi-theoretical equations for pool film boiling;
- ii. Semi-theoretical models to predict flow film boiling. They are based on the appropriate constitutive equations, some of which are empirical in nature;
- iii. Purely empirical correlations for flow film boiling, which do not account for any of the physics, but instead assume a forced convective-type correlation; and
- iv. Phenomenological equations for flow film boiling, which account for thermal disequilibrium and attempt to predict the “true” vapour quality and vapour temperature.

Transition boiling

The wall temperature at the initiation of transition boiling can be calculated using the CHF correlation (the lower limit temperature) [IAEA2001]:

$$T_{W,CHF} = \frac{q_{CHF}}{h_{NB}} + T_{SAT} , \quad (280)$$

where q_{CHF} is the heat flux at CHF and h_{NB} is the nucleate boiling heat transfer coefficient.

The upper wall temperature limit that occurs in transition boiling is the minimum wall film boiling temperature:

$$T_{MFB} = \frac{q_{MFB}}{h_{MFB}} + T_{SAT} , \quad (281)$$

where q_{MFB} is the minimum film-boiling heat flux and h_{FB} is the film-boiling heat transfer coefficient. Note that in general, heat transfer coefficients decrease from nucleate boiling to transition boiling and then to film boiling, i.e., $h_{NB} > h_{TB} > h_{FB}$.

Transition boiling is encountered only within a relatively narrow temperature range. For example, for water at 10 MPa, the transition boiling wall temperature range is $300^{\circ}\text{C} < T_{TB} < 373^{\circ}\text{C}$.

Tong [IAEA2001, TON1996] has developed a transition boiling correlation that is frequently used:

$$h_{TB} = 39.75 \cdot e^{-0.144\Delta T} + 2.3 \cdot 10^{-5} \frac{k_g}{D_e} e^{-105/\Delta T} Re_v^{0.8} Pr_v^{0.4} . \quad (282)$$

Very often, correlations containing boiling and convective components (valid for transition and film boiling) are used, such as [IAEA2001]:

$$h_{TB} = A \cdot e^{-B \cdot \Delta T_{SAT}} + \left(\frac{k_v}{D} \right) \cdot a \cdot Re_v^b \cdot Pr_v^c . \quad (283)$$

An example of a phenomenological correlation (valid for transition and film boiling) is the one proposed by Tong & Young and by Iloeje [IAEA2001]:

$$q = q_{dc} + q_{ndc} + q_{conv} \quad (284)$$

An example of an empirical correlation (valid for transition boiling only) independent of CHF and minimum film boiling has been proposed by Ellion [IAEA2001]:

$$q_{TB} = 4.56 \cdot 10^{11} \cdot (\Delta T_{SAT})^{-2.4} \quad (285)$$

Film boiling

In addition to the above correlations, which are applicable to both transition and film boiling, the minimum film boiling temperature can be given by the following correlation [IAEA2001, DEL1981, COL1972]:

$$T_{W,MIN} = 284.7 + 0.0441 P - 3.72 \cdot 10^{-6} P^2 + \frac{\Delta h \cdot 10^4}{(2.82 + 0.00122 P) h_{fg}}, \text{ Pressure} < 9000 \text{ kPa} \quad (286)$$

$$T_{W,MIN} = T_{SAT} + \Delta T_{W,MIN,9000kPa} \frac{P_{CRIT} - P}{P_{CRIT} - 9000}, \text{ Pressure} \geq 9000 \text{ kPa}$$

There is general agreement that the modified Bromley equation [IAEA2001] for film boiling can be used for horizontal surfaces in pool boiling:

$$h_{FB} = 0.62 \cdot \left[\frac{\lambda_v^3 \cdot \rho_v (\rho_l - \rho_v) \cdot r \cdot g}{\Delta T_s \cdot \mu_v} \cdot \frac{1}{2\pi} \sqrt{\frac{g (\rho_l - \rho_v)}{\sigma}} \right]^{1/4} \quad (287)$$

This correlation is valid for pressures of 100–9000 kPa, mass fluxes of 50–4500 kg.m⁻².s⁻¹, qualities of 0.15–0.40, sub-cooling of 0°C–50°C, and tube diameters of 9–12 mm.

A general correlation for post-CHF conditions in tubes has been proposed by Groeneveld (1973) [IAEA2001]:

$$h_{pcr,ld} = \frac{a \cdot k_g}{D_e} \left\{ Re_g \left[x + \left(\frac{\rho_g}{\rho_l} \right) (1-x) \right] \right\}^b Pr_g^c Y^d \quad (288)$$

$$Y = 1 - 0.1 \left(\frac{\rho_l}{\rho_g} - 1 \right)^{0.4} (1-x), \quad Re_g = \frac{G \cdot D_e}{\mu_g}$$

For tubes, $a=1.09 \cdot 10^{-3}$, $b=0.989$, $c=1.41$, $d=-1.15$. This correlation is valid for equivalent diameters of 2.5–25 mm, pressures of 6.8–21.5 MPa, mass fluxes of 700–5300 kg/m².s, heat fluxes of 120–2100 kW/m², and qualities of 0.1–0.9.

Post-dryout look-up table

The post-dryout bundle look-up table method appears to be a suitable approach for the following reasons:

- i. Relatively simple to use;
- ii. Provides correct asymptotic and parametric trends;

- iii. Uses the most universal method with the best overall fit to the fully developed film boiling data base; and
- iv. With embedded modifications for complex geometries, it can be used to account for CANDU fuel bundle effects such as geometry and spacer devices.

Table 12 Sample of PDO look-up table [IAEA2001]

e	$\Delta T_w = 50 \text{ K}$	$\Delta T_w = 100 \text{ K}$	$\Delta T_w = 200 \text{ K}$	$\Delta T_w = 300 \text{ K}$	$\Delta T_w = 400 \text{ K}$	$\Delta T_w = 500 \text{ K}$	$\Delta T_w = 600 \text{ K}$	$\Delta T_w = 750 \text{ K}$	$\Delta T_w = 900 \text{ K}$	$\Delta T_w = 1050 \text{ K}$	$\Delta T_w = 1200 \text{ K}$
-0.10	1.5664	1.504	1.474	1.358	1.177	1.134	1.280	1.395	1.532	1.705	1.833
-0.05	1.414	1.311	1.275	1.194	1.026	0.981	1.131	1.210	1.356	1.499	1.625
0.00	1.257	1.164	1.106	1.071	1.006	1.048	1.120	1.198	1.283	1.369	1.456
0.05	1.513	1.393	1.223	1.126	1.141	1.270	1.273	1.352	1.371	1.397	1.430
0.10	1.654	1.547	1.318	1.264	1.361	1.476	1.459	1.492	1.483	1.483	1.472
0.20	1.700	1.617	1.427	1.394	1.504	1.655	1.643	1.704	1.704	1.712	1.688
0.40	2.629	2.582	2.547	2.368	2.334	2.393	2.401	2.447	2.456	2.470	2.479
0.60	4.229	4.008	3.750	3.483	3.324	3.285	3.344	3.046	3.119	3.188	3.249
0.80	5.507	5.203	4.488	4.088	3.983	3.936	3.963	3.906	3.955	4.012	4.088
1.00	8.103	7.061	5.500	4.692	4.446	4.605	4.796	5.061	5.264	5.457	5.627
1.20	10.27	8.893	6.784	5.176	5.028	5.471	5.639	6.038	6.296	6.549	6.775
1.40	10.80	9.683	7.906	6.412	5.854	6.206	5.983	6.632	6.846	7.065	7.275
1.60	8.327	8.087	7.856	7.222	6.694	6.780	6.763	6.936	7.107	7.277	7.477

(2001 Film Boiling Table, $P=9000 \text{ kPa}$, $G=1500 \text{ kg}\cdot\text{m}^{-2}$, H in $\text{kW}\cdot\text{m}\cdot\text{K}^{-1}$)

A sample extract from a post-dryout look-up table is provided in Table 12. This table provides the heat transfer coefficient for given values of pressure, mass flux, quality, and wall superheat.

Current look-up tables do not yet properly account for developing flow effects, in particular those that usually occur during accident scenarios. This effect is accounted for using specific correction factors. The film boiling look-up table method has been used for the following applications:

- i. As a normalized database for validation of film boiling models; and
- ii. As an alternative to certain film boiling models which cover only limited ranges of flow conditions.

7.6.5.3 Post-dryout heat transfer R&D in CANDU fuel bundles

Prediction of post-dryout heat transfer in fuel bundles, particularly film boiling heat transfer, is much more complex than that of CHF. Aside from requiring a fourth parameter in the look-up table ("heat flux"), non-equilibrium effects must also be considered, especially in the region just downstream of the quench, near flow obstructions, and at low flows. Fuel bundles are equipped with bundle appendages (as in CANDUs) or grid spacers. These appendages have a CHF- and heat transfer-enhancing effect and also a de-superheating effect, thus reducing the degree of disequilibrium. They can also create multiple quench fronts.

Many experimental tests have been conducted with regard to post-dryout heat transfer to investigate phenomena, develop correlations, and test prediction methods. For such experiments, well-instrumented fuel bundles are required. Figure 132 show a cross section of a fuel bundle with 37 elements at the dryout plane and the appendages plane. A number of fuel element simulators were equipped with movable temperature thermocouples. For each of the

instrumented fuel elements, using different colour codes, dry-patch spreading is indicated by a circular line around the element for each overpower test. Different behaviour is evident for different fuel elements, depending on the flow and heat transfer regimes that occur. These experiments provide very useful information about post-dryout heat transfer in a fuel bundle.

The objective of these experiments is to measure temperature profiles in various flow regimes, such as dispersed flow film boiling, and to measure dryout or dry-patch spreading around the bundle. The sheath temperature in such a heat transfer regime rises gradually with power or decreasing flow, i.e., it is controllable with flow condition variation. Maximum sheath temperature is predictable and occurs at locations just upstream of appendage planes. Dry patches are stable and propagate gradually with flow condition variations, which makes these experiments easily controllable and measurable. In Figure 132, it can be readily seen that at different overpower levels (i.e., power above nominal power), a different extent of wall circumference was in dryout for different fuel pins [LEU2004]. On the left side, a test fuel bundle is shown, with instrumented fuel pins shaded. The right side shows, using different colours, the portions of the circumference of a fuel pin that were measured to be in dryout at different overpower levels. Generally, the higher the power above nominal power, the larger was the portion of the circumference that was in dryout.

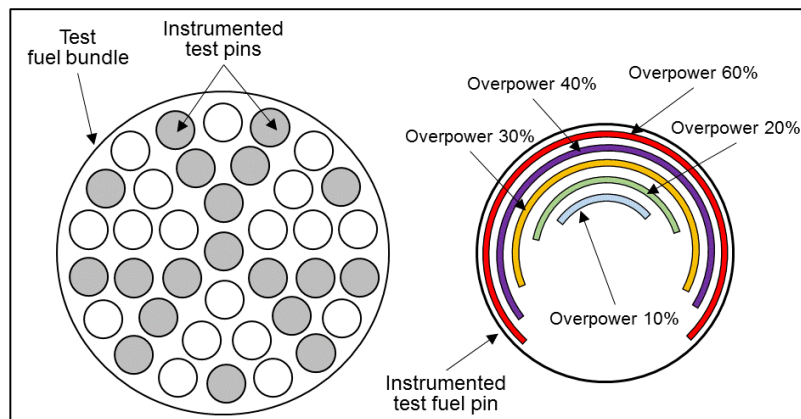


Figure 132 Bundle dry patches in the dryout plane

Two types of tests were conducted, with water and with Freon. The water experiments provided direct confirmation of post-dryout behaviour and closely resembled the phenomena that occur in a CANDU fuel channel. However, these experiments are rather expensive. Freon experiments use a lighter element, Freon R134a, which has a much lower saturation pressure, and therefore these experiments are easier to perform, induce less burden on the survivability of the materials at post-dryout conditions, and enable reuse of the experimental test equipment. However, for these experiments, scaling techniques are needed to convert the collected information to conditions applicable to CANDU.

Many post-dryout water experiments with fuel bundles have used fixed thermocouples attached to the sheath. In these experiments, surface coverage was limited; details of sheath-temperature variation downstream of appendages and spacer grids were not available; and the extent of dry patches, in both axial and circumferential directions, could not be quantified.

Experiments have also been performed with CANDU 37-element bundles in high-pressure

steam-water flow using movable thermocouples. In this case, increased surface coverage was achieved, i.e., more temperature measurements were collected at different places along the fuel element. However, a limited range of powers was applied to avoid damaging the fuel simulator.

A CANDU fuel bundle simulator for post-dryout water experiments is shown in Figure 118. It consists of a 6 m-long full-scale bundle string of fuel elements with junctions and appendages. In these experiments, a uniform axial power profile and a non-uniform radial power profile were used, simulating natural uranium fuel. Sliding thermocouples were installed inside rods at several downstream bundles in the string.

CANDU bundle post-dryout Freon experiments were also performed with movable thermocouples inside the elements of a CANDU 37-element bundle simulator. In these experiments, because of the lower power, temperature, and pressure conditions, fine axial and radial movements were achievable, providing detailed temperature profiles. Freon-134a was used as a coolant, enabling low operating power and sheath temperature and high overpower ratios (i.e., local-to-critical power ratios). With Freon, a relatively wide range of test conditions could be investigated because these experiments were not as expensive as the water experiments.

Figure 133 shows a circumferential distribution of sheath temperatures in a Freon-cooled post-dryout bundle experiment as a function of overpower percentage [LEU2004]. Nominal power means 0% overpower. This figure shows the results of tests on various overpower situations, up to 60% higher than nominal power.

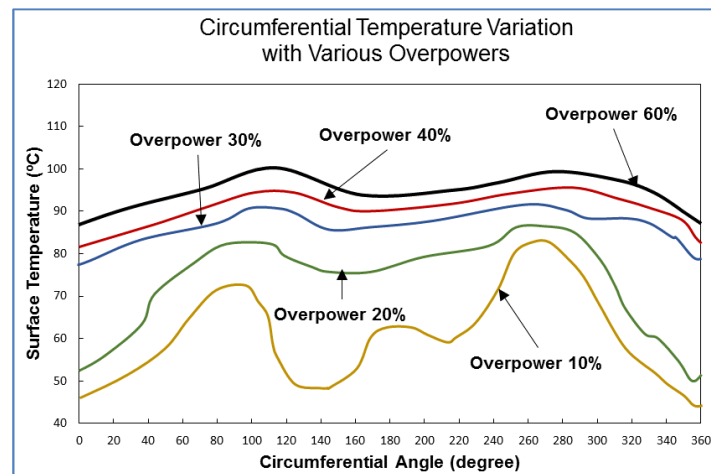


Figure 133 Bundle circumferential temperature profiles

Virtually all film boiling prediction methods are based on correlations derived for tubes. Using them to predict fuel-bundle sheath temperatures is common practice, but the following bundle-specific factors and impacts must be considered:

- i. Bundle enthalpy and flow imbalance;
- ii. Heat transfer enhancement downstream of grids or spacers;
- iii. Adjacent surface wetness or cooling near the pressure tube wall;

- iv. Narrow gaps between elements
- v. Lower wall friction in dry portions of bundles (resulting in higher flow in dry sub-channels);
- vi. Non-circular sub-channel cross-sectional shape;
- vii. Presence of axial dry streaks in partially dry fuel bundles.

Reactor safety codes, particularly sub-channel codes that can model variation of flow parameters across a fuel bundle, may account for some, but not all of these effects. When the heat flux of a rod surface facing a given sub-channel exceeds the local CHF, both the wall-fluid heat transfer coefficient and the wall friction factor are reduced drastically. By keeping track of the circumferential dry-patch fraction (CDF) and the axial dry-patch length (ADL) for each rod facing each sub-channel, the flow and enthalpy distribution as well as that of the film-boiling heat transfer coefficient can be evaluated. This enables evaluation of the fuel temperature distribution and prediction of the extent of fuel melting. This approach is now being incorporated in some sub-channel codes to enable detailed prediction of the cladding temperature distribution.

Aside from cross-sectional differences, the global and local effects of the grid or spacers on wall heat transfer, quench behaviour, and interface mass and energy transport are usually not well known, or at best are included by means of an empirical fix for each grid spacer configuration. In general, (grid) spacers can have the following effects:

- i. Promote rewetting downstream of the grid due to the higher turbulence level (i.e., can induce multiple quench fronts);
- ii. Act as cooling fins;
- iii. Cause de-superheating of vapour;
- iv. Cause an increase in the liquid-vapour interfacial area by breaking up droplets or liquid core;
- v. Homogenize flow by promoting turbulence.

7.6.5.4 Post-dryout applications and analyzes

The application of post-dryout heat transfer is focussed on the safety analysis of postulated events in power reactors, including CANDU. More details about safety analysis of power reactors are provided in Chapter 16, and in this section, these topics are considered only from the perspective of heat transfer.

7.6.6 Single-phase heat transfer to vapour

Single-phase heat transfer to superheated steam is important because it provides an asymptotic value for film boiling heat transfer for cases when the actual quality approached 100%. A number of tube-based correlations have been proposed; all are of the Dittus-Boelter type and give similar predictions. The following equation is frequently used.

Miropolskiy (1975) equation [IAEA2001, DEL1981, BER1981]:

$$Nu_g = h_g D / \lambda_g = 0.028 \cdot Re_g^{0.8} Pr_g^{0.4} (\rho_w / \rho_g)^{1.15}, \quad (289)$$

where $Re_g = G \cdot X \cdot D / \mu_g$ and ρ_w is vapour density at wall surface temperature. This correlation is valid for pressures of 4–22 MPa, mass fluxes up to 0.42 Mg·m⁻²·s⁻¹, $\rho_l/\rho_g=0.5$ –0.9, and $Re=10^5$ – 10^6 .

7.6.7 Problems

1. Explain the most important aspects of the three approaches of calculating reactor dryout margins: by CHF ratio, by critical CHF power ratio, and by critical power ratio. Provide comments on the applicability of these three approaches.
2. Describe the three main mechanisms that lead to dryout in forced flow in horizontal heated pipes. With respect to these mechanisms, provide explanation on the difference between heated tubes and fuel channels with fuel bundles.
3. Provide explanation about the difference in the following terms boiling crises CHF, dryout, burnout, departure from nucleate boiling, and post-dryout in fuel bundles. Provide examples of conditions where these terms are applicable.
4. Explain the most important parameters that affect CHF, and explain the parametric trends that are used to gain appropriate understanding of the dryout in heated pipes and fuel bundles.
5. Explain the main transition boiling and film boiling types in vertical and horizontal pipes and channels, list the heat transfer modes and provide explanation on the importance of these modes.
6. A PWR reactor uses UO₂ cylindrical fuel pellets, 12.7-mm diameter, with a helium-filled gap of 0.075 mm, and Zr cladding of 0.762 mm. The fuel rods are arranged in a square lattice, with a pitch of 1.8 cm. At a particular section, the bulk water temperature and velocity are 270°C and 4.5 m/s respectively. The volumetric heat generation at this location is 5 x 10⁴ kW/m³. Calculate (a) the convective heat transfer coefficient using the Dittus-Boelter equation, and (b) the minimum system pressure so that no boiling occurs in the film.
7. Calculate the local CHF for vertical upward flow of water inside a uniformly heated tube (0.012 m ID) at the following conditions: pressure 8200 kPa, mass flux 5000 kg·m⁻²·s⁻¹, and quality 0.175. Use the most appropriate correlation for these flow conditions.
8. Using the most appropriate correlation calculate the post-dryout wall temperature for a vertical water-cooled tube of 0.015 m inside diameter. The following parameters are given: inlet temperature 250°C, inlet pressure 9 500 kPa, mass flux 3961 kg·m⁻²·s⁻¹, local pressure 9400 kPa, local heat flux 1500 kW/m², local quality 0.225.
9. Evaluate the dryout power for a 3658-m-long tube of 0.0095 m ID, heated with a symmetric-cosine heat flux. The flux profile has been discretized as

Length (m)	0.0	0.05 1	0.20 3	0.40 6	0.60 7	0.81 3	1.01 6	1.21 9	1.42 2	1.62 6	1.82 9
q_{loc}/q_{avg}	0.3	0.37	0.45	0.66	0.86	1.03	1.17	1.27	1.33	1.38	1.35
Length (m)	2.03 2	2.23 5	2.43 8	2.64 2	2.84 5	3.04 8	3.25 1	3.45 4	3.60 7	3.65 8	
q_{loc}/q_{avg}	1.38	1.33	1.27	1.17	1.03	0.86	0.66	0.45	0.37	0.30	

More nodes can be introduced to improve the accuracy of the predictions of dryout location and power. Theoretically, an infinite number of nodes should be used for a smooth profile. For a stepped profile, the number of nodes corresponds to the number of steps since dryout generally occurs at the end of a step.

The flow conditions are: pressure 6930 kPa, mass flux 2050 $\text{kg}\cdot\text{m}^{-2}\cdot\text{s}^{-1}$, and inlet subcooling 280.75 kJ/kg.

10. A pressure tube, with inside diameter of 103.86 mm, contains twelve 37-element bundles of the following dimension: bundle length: 495.3 mm, and fuel element outer diameter 13.06 mm.

Total power generated over the bundle string is 6.3 MW, and the axial power profile is uniform. The channel is cooled with a flow of light water at the following conditions: outlet pressure 9 MPa, mass flow rate: 17 kg/s, inlet fluid temperature 265C.

Evaluate dryout power ratio for this channel, and surface temperature distribution along the bundle string at an overpower of 10% (overpower is defined as $(\text{String-Power}/\text{Dryout-Power} - 1) \cdot 100\%$).

Previous research findings appropriate to this problem:

- Heat-transfer coefficient at nucleate boiling for the 37-element bundle is 120 $\text{kW}/(\text{m}^2\text{K})$ at the pressure of 9 MPa, mass flux of 5 $\text{Mg}/(\text{m}^2 \text{ s})$ and quality of 20%.
- Heat-transfer coefficient at single-phase liquid flow is about 50% of that at nucleate boiling.
- CHF in the 37-element bundle is 20% lower than that in tubes based on cross-sectional average flow conditions.
- Heat-transfer coefficient at fully developed film boiling for the 37-element bundle is the same as that for tubes.
- Overall loss coefficient is 1.7 for a 37-element bundle inside a pressure tube of 103.86 mm.
- The homogeneous equation is the most appropriate for two-phase multiplier.

Basic assumptions:

- Nucleate boiling heat transfer coefficient does not vary with flow conditions.
 - Fully developed film-boiling heat transfer is reached once local heat flux exceeds CHF.
 - Equilibrium flow in the channel.
 - Pressure drop due to acceleration is negligible.
11. In the middle of a reactor channel of a PWR reactor the bulk coolant temperature of the turbulent coolant flow is 310°C at pressure of 14 MPa. The heat transfer coefficient in nuclear boiling is $4.44 \text{ MW/m}^2 \text{ }^{\circ}\text{K}$. Calculate the minimum heat flux at that location to initiate nucleate boiling.
 12. Water enters a heated tube of 2.5 cm diameter at 12 MPa and velocity of 2.5 m/s. The linear heat load in the tube is constant at 100 kW/m. Calculate the distance in the tube at which nucleate boiling starts, and distance at which it converts to bulk boiling. Compare the heat transfer coefficients for forced convective heat transfer with these for nucleate boiling and bulk boiling.
 13. A pipe of 15 mm diameter and 3.5 m length is heated with a constant heat flux, and total heat load of 200 kW (appropriately insulated, i.e., no heat losses). The pipe is cooled by water at 150°C and pressure of 2 MPa, which flows through the pipe with enters into the pipe with a velocity of 3 m/s. Calculate the mass flux of the water, and the minimum ratio of the heat flux in the pipe and the critical heat flux.
 14. Boiling water reactor operates at average pressure in the core of 8 MPa, and the recirculation ratio of 7:1. The average velocity of the two-phase mixture in the core is 8 m/s. Calculate the critical heat flux at the exit of the reactor core channel.
 15. List and explain the most important geometrical factors that have significant impact on CHF in horizontal fuel channels.

7.7 Critical flow

Consider a situation in which fluid discharges from a container at high pressure to a container at lower pressure, or to ambient at lower pressure (back-pressure). When the back-pressure is reduced below a constant upstream pressure in a flow system, flow begins because of the pressure gradient established in the connecting channel between the upstream container and downstream towards the channel exit. The flow increases as the back-pressure is reduced further. When the back-pressure is sufficiently reduced to cause the flow velocity at the channel exit to be equal to the speed of sound at the channel exit temperature and pressure, the mass flow at the exit attains a maximum value. Further reduction in the back-pressure results in no further increase in mass flow rate; the flow remains at the maximum value and is referred to as “critical”. The channel, and the flow, are also called “restricted” or “choked”. Because the back-pressure is less than the pressure resulting in critical flow, free fluid expansion can occur between the exit (at exit pressure) and the ambient (at back-pressure) outside the channel, and the flow takes on a paraboloid shape in this region. This situation can be observed by many flow and measurement systems.

The critical flow phenomenon occurs in both single- and two- phase flow when the velocity of the two-phase mixture is controlled by its upper limit, i.e., the sonic velocity of the mixture. That velocity is a very strong function of quality, varying from ~300 m/s for single-phase steam to ~1400 m/s for single-phase liquid water.

In nuclear reactors, this phenomenon is important for safety analysis of both boiling and pressurized systems. A break in a primary coolant pipe causes two-phase critical flow in either system because even in a pressurized reactor, the reduction in hot coolant pressure from about 10 MPa to near-atmospheric causes flashing and two-phase flow. This kind of break results in a rapid loss of coolant and is considered to be a credible design basis accident in power reactors built to date. This is further explained in Chapter 16.

An evaluation of the flow rate in critical two-phase systems is therefore important for designing emergency cooling systems and for determining the extent and causes of damage in accidents. Further details on modelling critical flow in nuclear reactor primary heat transport systems are provided in Chapter 7.

7.8 Water hammer

Water hammer is an important phenomenon that requires attention by thermal-hydraulic designers and plant operators. This phenomenon can result in equipment damage and can affect the performance or functionality of certain equipment. Therefore, it is important to have a good understanding of this phenomenon so that appropriate prevention, mitigation, and accommodation measures can be undertaken to reduce the risk of its occurrence in nuclear power plant cooling systems.

Detailed coverage of the water hammer phenomenon and its prevention, mitigation, and accommodation are beyond the scope of this textbook, but appropriate information can be found in the literature [EPRI1996] and in the suggestions for further reading at the end of this textbook. This section reviews basic information about water hammer and provides

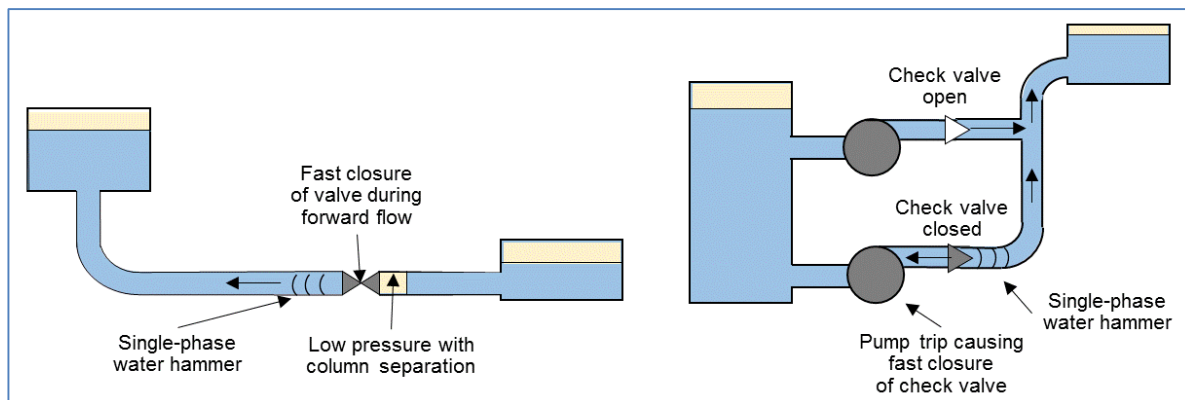
elementary guidance to thermal-hydraulic engineers and designers.

7.8.1 Types of water hammer

Water hammer events have been observed and reported widely in PWR, BWR, CANDU, and other nuclear power plants in various coolant or support systems. These events have provided valuable information on the types and strength of the water hammer effect, which has been used to develop defensive strategies.

Water hammer events can be classified into two broad groups: water hammer events in single-phase liquid or gas, and two-phase water hammer events.

Most water hammer events in nuclear power plants fall into the first group and are caused by rapid acceleration or deceleration of single-phase liquid flowing in a piping system. Rapid acceleration can be created by rapid valve closure, which results in pressure waves that propagate in the piping system at sonic velocity. Figure 134 shows two examples of single-phase water hammer; Case A shows rapid valve closure causing water hammer. Case B shows check-valve action downstream of a pump triggering water hammer [EPRI1996].



a) Fast valve closure

b) Pump check valve closure

Figure 134 Rapid valve operation

The necessary physical and mechanical conditions required for water hammer to occur exist all the time in nuclear power plants. Most nuclear power plants have design and operational provisions to prevent severe water hammer from occurring, but nevertheless, in unanticipated situations, water hammer events do occur. Usually water hammer transients are typically caused by pump start, pump trip, control or isolation valve operation, check valve closure, safety or relief valve operation, main steam turbine trip, and filling of empty systems. All these normally occur in single-phase flow conditions and can be easily predicted by conventional water hammer analysis techniques.

Two-phase water hammer events can be of several types. These events are more complex to analyze, have a strong impact on pump operation, and can cause significant damage to pipe components and pipe supports. Six transient scenarios lead to water hammer events with various probabilities and strengths, with most of them related to steam condensation-induced water hammer.

1. Flow of sub-cooled water with condensing steam in a vertical pipe (Figure 135)

This type of water hammer is a typical BWR case in which, during a large LOCA event, steam lines discharge water into the suppression pool. If the valve is quickly closed or reduced significantly, a steam pocket remaining in the steam line can condense rapidly, which pulls water from the suppression pool towards the valve, thus creating water hammer [EPRI1996, POP2014].

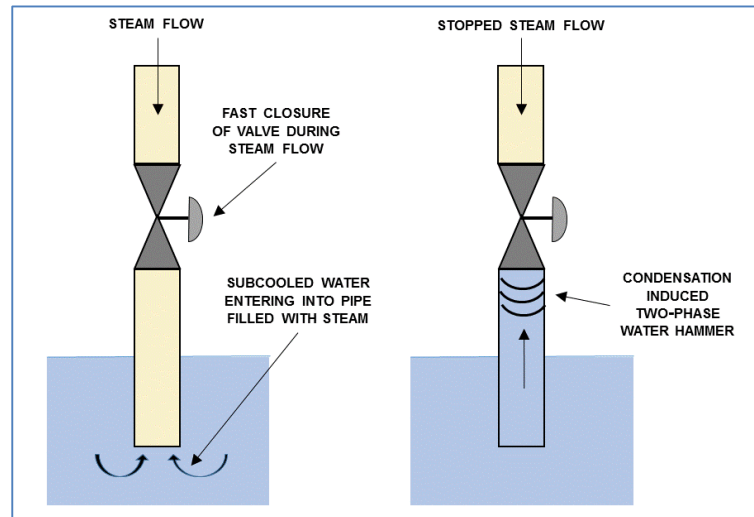


Figure 135 Flow of sub-cooled water with steam condensing in vertical pipe (water cannon)

2. Counter-current flow of steam and water in a horizontal pipe (Figure 136)

This situation occurs in PWR feedwater lines and in CANDU feeders [POP2014]. In horizontal stratified flow, a large interface area exists between sub-cooled water and steam. Therefore, the steam flow is subjected to fast condensation, which induces an increase in steam flow from the upper pipe. Under certain conditions, the counter-current flow can transition to slug flow and create a steam pocket. When the steam pocket collapses as a result of condensation, severe water hammer can occur. Long feeder sections are particularly vulnerable to steam trapping and this type of water hammer. The advanced CANDU design addresses this problem by having feeders slightly tilted, so that an escape route for steam is provided.

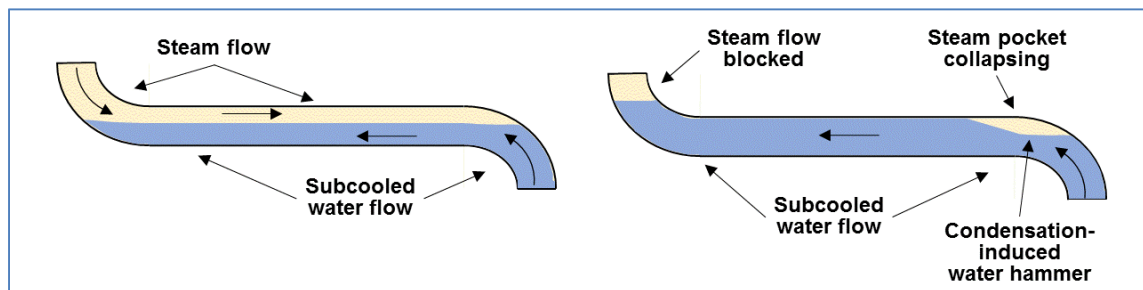


Figure 136 Counter-current flow of steam and water in a horizontal pipe

3. Pressurized water entering a vertical pipe filled with steam (Figure 137)

This type of water hammer can occur in any of the PWR and BWR reactors with refilling of a steam-filled pipe either from the bottom or from the top [EPRI1996]. If pressurized sub-cooled water enters a pipe filled with steam in a piston flow regime, it can create steam trapping. The filling rate for this situation is determined by the inertia of the liquid and the pressure induced by the pump or other refilling device. Water hammer occurs in this situation if the refilling rate is higher than the bubble rise velocity for the top refilling case. This type of water hammer can also occur in CANDU reactors.

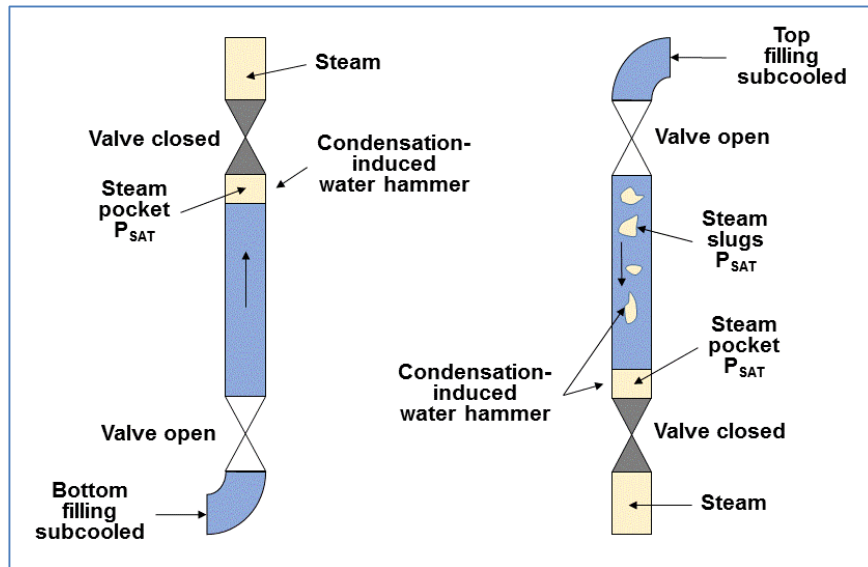


Figure 137 Pressurized water flowing in a vertical pipe filled with steam

4. Hot water entering a low-pressure line (Figure 138)

This type of water hammer can occur in PWRs, BWRs, and CANDUs. In this case, hot water flowing down the pipe will flash and create a pressure wave flowing upstream, thus creating water hammer on the upstream valve. The cold part of the sub-cooled water that was initially outside and below the pressure vessel can create water hammer on the downstream valve as it enters the steam-filled part of the pipe [EPRI1996].

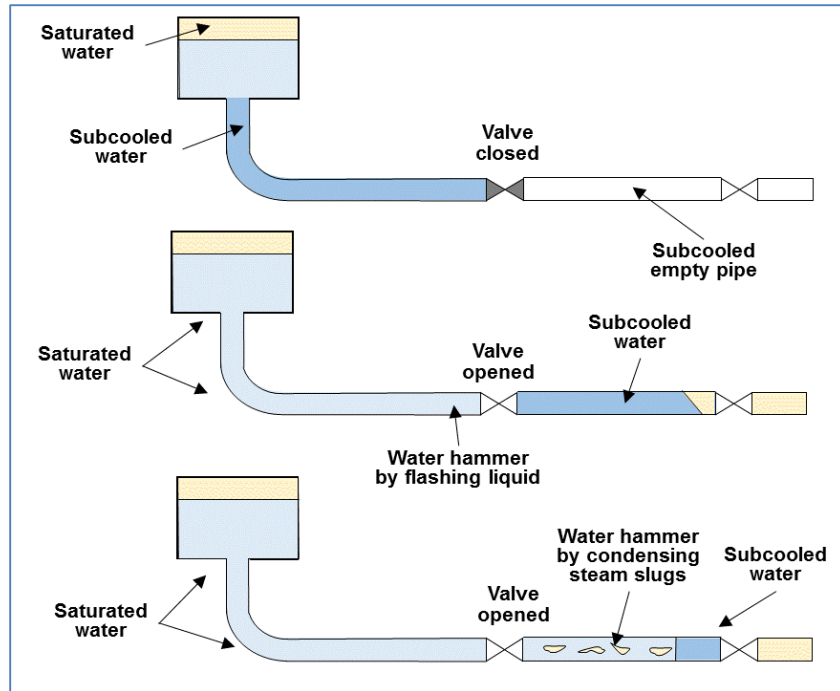


Figure 138 Hot water entering a lower-pressure line

5. Water slug driven by steam (Figure 139)

This type of water hammer can occur in a piping system that collects condensate upstream of a closed valve or can collect condensate in certain portions of the piping systems that are normally filled with steam. Water hammer can occur when the valve opens and this steam drives the water slug at high speed. The slug can be accelerated significantly and can create a water hammer effect in a restricted part or at the closed end of the pipe [EPRI1996].

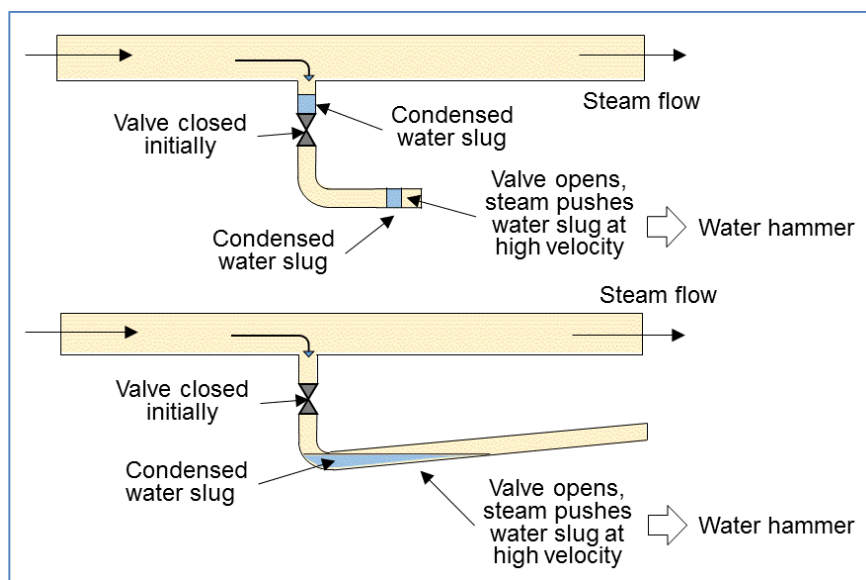


Figure 139 Steam-driven water slug in piping system

6. Water filling a voided pipe line (Figure 140)

In this situation, as a pump trips, water from the vertical section recedes downwards and creates an empty vacuum-filled space above. When the pump restarts, it will push water to refill the pipe (and perhaps condense some residual steam), thus creating a significant water hammer [EPRI1996].

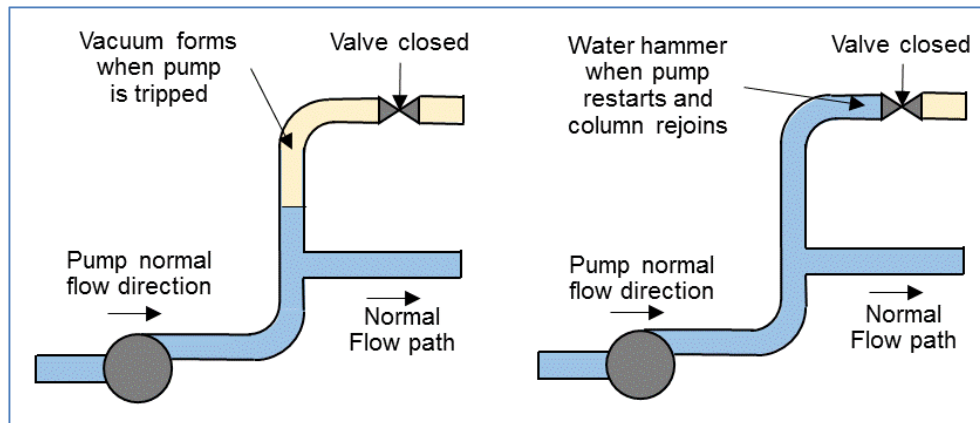


Figure 140 Filling of voided piping system

7.8.2 Analytical models and computer codes for water hammer analysis

Water hammer assessment is performed using analytical models and computer programs designed for this purpose. A detailed discussion of this topic is beyond the scope of this textbook, and hence this chapter provides only a brief summary.

The analytical models consist of governing differential equations for transient single-phase or two-phase flow. Usually, the flow is assumed to be one-dimensional because it describes flow in piping systems. The governing differential equations are solved by appropriate numerical techniques. Then a network model is created in which physical representations of various system components are introduced as boundary conditions. Usually, a number of constitutive correlations are used to cover system-specific phenomena.

Usually, analytical models for liquid, gas, or two-phase mixtures are based on rigid and elastic column theories of the piping system. It is important to recognize that the severity of water hammer is proportional to the level of rigidity of the piping system. Therefore, an increased level of piping elasticity reduces the consequences of water hammer because elastic pipe systems can absorb the energy of the pressure waves traveling through the system.

Software packages vary in complexity depending on the processes modelled. The more sophisticated packages may have one or more of the following features:

- Multiphase flow capabilities;
- An algorithm for cavitation growth and collapse;
- Unsteady-state friction: the pressure waves dampen as turbulence is generated and due to variations in the flow velocity distribution;
- Varying bulk modulus for higher pressures (water becomes less compressible);

- Fluid-structure interaction: the pipeline reacts on the varying pressures and causes pressure waves itself.

Most computer programs that can model water hammer are the same as those used to model general piping networks. However, computer codes may not be completely successful in modelling all types of water hammer, particularly condensation-induced water hammer, which is quite challenging. The RELAP5 code [REL2010] is an example of such a network code that can model certain types of water hammer for PWRs and BWRs. For CANDU reactors, the CATHENA computer code [CAT1998, CAT2000, CAT2005] has been validated for use in analysis of certain types of water hammer.

7.8.3 Diagnostics and assessment of water hammer

Diagnostic and assessment techniques for water hammer consist of systematic review of a thermal-hydraulic network in terms of vulnerabilities to and consequences of water hammer. The assessment principles are based mainly on lessons learned and root cause analysis. Nuclear power plant design features and operating characteristics require specific water hammer inspection processes.

The general diagnostic analysis consists of three major steps: study of deformation evidence, determination of water hammer source, and determination of root causes. Each of these steps consists of several sub-steps as follows:

- a) Collect evidence of water hammer impact by field inspections, interviews, and review of operating conditions;
- b) Identify pipe network characteristics that may lead to water hammer;
- c) Determine water hammer consequences by identifying pipe movement, pipe deformations, and pipe support deformations;
- d) Determine the piping or other thermal-hydraulic equipment initial conditions (for example, water-filled or steam-filled piping);
- e) Determine the source of water hammer by identifying the origin point of the pressure wave or water slug;
- f) Compare the operating conditions and consequences of the various possible water hammer mechanisms;
- g) Determine the root causes; and
- h) Define possible corrective action in design space and/or procedural space.

The review of systems and equipment susceptibility to water hammer usually consists of the following activities:

- i. Collection of plant data to establish plant-specific thermal-hydraulic network configurations and identify component features and functions;
- ii. Determine industry practices with respect to thermal-hydraulic network testing, maintenance, and operating procedures that result in water hammer vulnerabilities;
- iii. Perform plant assessment with respect to prevention, diagnosis, and assessment of water hammer;

- iv. Review plant-specific thermal-hydraulic system operating procedures and designs with respect to water hammer occurrence;
- v. Document the findings of the above assessment; and
- vi. Develop recommendations for improving plant-specific design features or operating procedures to reduce the probability of water hammer.

7.8.4 Prevention, mitigation, and accommodation of water hammer

This section provides general high-level information on measures taken to prevent, mitigate, and/or accommodate certain types of water hammer events in nuclear power plants. The measures that can be taken can be broadly grouped into design measures and operational (procedural) measures.

Prevention of water hammer is the best option when and where possible. It includes design and operational measures aimed at preventing or significantly reducing the water hammer hazard. However, this option may not be available in many situations, especially in thermal-hydraulic equipment operating in a transient following an accident.

Mitigation of water hammer includes design and operational measures to reduce the impact of water hammer in cases where it cannot be prevented. This technique is mostly used in situations in which prevention is not possible.

If a water hammer hazard cannot be eliminated by design or operational procedure, the next step is to accommodate the residual impact that cannot be mitigated. A number of techniques can be used to achieve this, such as strengthening and reinforcement of pipe support systems, or designing piping systems that take water hammer loads into account.

General recommendations for reducing water hammer hazard are the following:

- Avoid direct contact of steam with sub-cooled water in a horizontal pipe (this is particularly important for CANDU feeder horizontal runs);
- Avoid opening a valve adjacent to a steam pocket (identified or suspected), or ensure that the valve opens slowly to provide an escape path for the steam pocket;
- Open isolation valves slowly where stagnant hot water coexists with hot water in the same line upstream and downstream of the valve;
- Inspect condensate removal systems to avoid accumulation of a water slug in the steam line;
- Inspect check valves routinely, especially those located on a pump discharge line, to ensure that the valve is not stuck open;
- Avoid starting a pump to fill a long line at significantly higher elevation, which could be voided for various reasons (such as leaking valves).

Specific recommendations for reducing each type of water hammer are provided in the following points [EPRI1996].

1. Rapid valve operation

Rapid valve actuation is defined as rapid closure of a stuck-open check valve or

malfunctioning of a valve actuator. Hence, any system with this type of valve is at risk of experiencing this type of water hammer.

Prevention or mitigation by design involves valve modifications to prevent this type of valve operation. Mitigation or prevention by procedure aims to avoid valve cycling in systems with significant flow, or perhaps uses a special monitoring capability to sense a pressure difference across a valve and to use it as a signal for actuating the valve.

2. Flow of sub-cooled water with condensing steam in a vertical pipe

This water hammer phenomenon is unique to steam turbine exhaust piping that discharges into a body of water. This happens when reduced steam supply to the turbine traps steam in the exhaust piping.

The only way to prevent or mitigate this type of water hammer is to install a vacuum breaker with sufficient capacity to replace the condensing steam in the exhaust piping from a tripped turbine.

3. Counter-current flow of steam and water in a horizontal pipe

This type of water hammer happens in steam generators when a horizontal feedwater pipe is slowly filled in counter-current flow. It can also happen in horizontal sections of CANDU feeders when injecting cold ECC water.

One design option for mitigation is to shorten the horizontal portions of piping systems, or to have the horizontal piping slightly inclined. A procedural modification may involve better control of the water flow to affected areas.

4. Pressurized water entering a vertical pipe filled with steam

This type of water hammer can happen unexpectedly due to valve leakage, which can lead to accumulating hot water pockets (which could quickly flash or condense) in the closed parts of piping systems. This kind of water hammer can also occur if high-pressure water is pumped into a system filled with steam (such as injection of ECC into steam-filled CANDU headers or feeders).

One mitigation design change involves keeping the system full of water and preventing valve leakage. In addition, installation of void detection devices at places where valve back-leakage may occur can be a solution. A procedural modification may involve venting steam pockets before injecting water or starting pumps.

5. Hot water entering a low-pressure line

This type of water hammer is typical of heater drain systems in cases where a reservoir of hot water is being discharged into low-pressure piping.

A possible preventative design change is to modify the control system to avoid cyclic dumping of hot water. Installing a flow control valve with slowly increasing flow can also address this problem. A procedural change may involve placing a high-pressure feedwater heater back in operation without inadvertently actuating the emergency dump system.

6. Water slug driven by steam

This type of water hammer can happen in pipes in which condensate accumulation occurs upstream or downstream of a closed valve.

A design fix for this water hammer is to ensure proper inclination and condensate drainage from piping systems. Pipes subject to sagging could also be better supported to avoid sags that can collect condensate. A procedural change could involve slowly initiating steam flow after opening a closed valve to ensure gradual acceleration of the condensate pocket.

7. Water filling a voided pipe line

This type of water hammer happens typically in long piping systems with an elevation change of 10 m or more. In this situation, stopping the water flow can result in formation of a vacuum in the upper parts of the pipe. Restarting the flow leads to refilling the pipe and to interaction of water and steam surfaces.

A design fix for this kind of water hammer is to keep the system filled with water. Installing a vacuum breaker can also help. A procedural improvement could involve keeping the pump discharge valve closed and then opening it slowly as the pump is restarted.

7.8.5 Problems

1. Explain the reasons and consequences of water hammer in thermal-hydraulic equipment. Provide examples of possible water hammer situations in the CANDU heat transport systems, and indicate the strategies for mitigating the effects.
2. List the types of water hammer in CANDU heat transport system, and for each type list and explain the strategy for avoiding or mitigating it.

7.9 Natural circulation

New generations of nuclear reactor designs under development rely on passive systems, including use of natural circulation. All Generation IV reactors are required to make use of natural circulation as a heat transfer mechanism for removing heat from the reactor core, for some designs even under normal operating conditions. However, currently operating reactors are also required to use natural circulation to remove decay heat in accident situations when forced circulation in the core is lost.

Natural circulation occurs in many different situations, such as a heater immersed into a fluid; an open flame in air; a chimney-driven fire; a surge of hot water into a pool of cold water; a heat source and heat sink connected by piping and located at different elevations; hot steam and cold air mixing in a containment building. In all these situations, natural circulation plays an essential role in transferring heat from one part of a system to another, or between systems.

7.9.1 Natural circulation phenomenon

Natural circulation will occur in a reactor primary loop in the absence of pumped flow whenever buoyant forces caused by differences in loop fluid densities are sufficient to overcome the flow resistance of loop components (steam generators, primary coolant pumps, etc.). Fluid density differences occur as a result of fluid heating in the core region (causing the liquid to become less dense) and fluid cooling in the steam generators (causing the fluid to become denser). Figure 141 shows the principles of natural circulation in a closed loop with a heat source located at a low elevation and a heat sink at a high elevation connected by piping. On the right side of this figure, a similar loop is shown in two-phase operation with a steam drum extracting steam and adding feedwater to the loop. This figure is similar to the situation in a nuclear power plant. Note that in this figure, two-phase flow is indicated out of the reactor, which is typical of BWR and CANDU reactors.

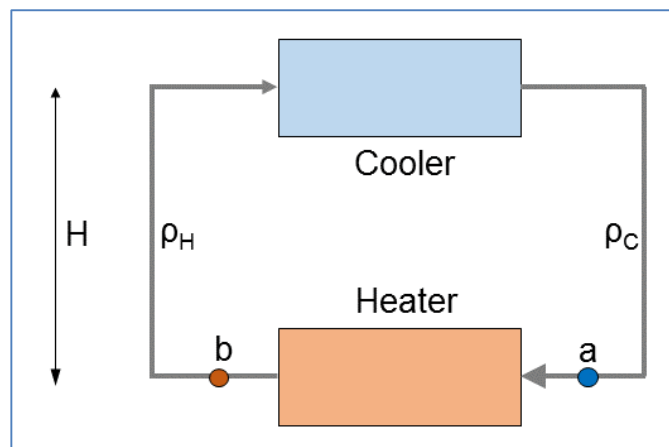


Figure 141 Principles of natural circulation

The buoyancy forces resulting from these density differences cause fluid to circulate through the primary loops, providing a means of removing core decay heat. Depending on the primary loop fluid inventory, natural circulation consists of three distinct cooling modes: single-phase,

two-phase (liquid continuous), and reflux condensation (or boiler-condenser mode for once-through steam generators). Progression from the single-phase mode through the two-phase and reflux condensation modes occurs as primary system liquid inventory decreases, as shown in Figure 142 [IAEA2005, IAEA2012, POP2012a]. Natural circulation flow in a sub-cooled primary heat transport loop (such as in PWRs) is driven by temperature-induced density gradients, enhanced by a thermal centre elevation difference between the hot (core) and cold (steam generator) regions in the primary loop. This density gradient produces a buoyancy force that drives the natural circulation flow. Hence, single-phase natural circulation is the flow of an essentially sub-cooled primary liquid driven by liquid density differences within the primary loop.

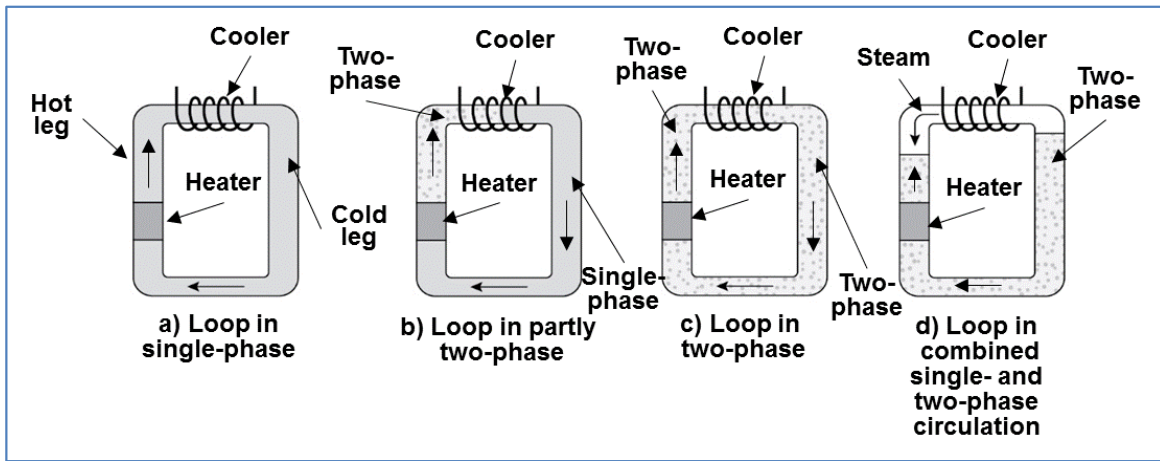


Figure 142 Various types of natural circulation

In a reactor where boiling occurs in the primary heat transport system, vapour generated in the core enters the hot leg and flows along with the saturated liquid to the steam generator, where at least some of the vapour is condensed. Hence, density gradients are affected in two-phase mode, not only by temperature differences, but also by voids in the primary loop. In both single-phase and two-phase natural circulation, the mass flow rate is the most important heat removal parameter.

In reflux condensation, the vapour generated in the core flows through the hot leg, is condensed in the steam generator, and flows back to the core as a liquid. In this mode, the loop mass flow rate has a negligible effect because the primary heat removal mechanism is vapour condensation.

The three modes of natural circulation are distinguishable based upon characteristic mass flow rates, loop temperature differences, and basic phenomenological differences. The dominant heat transfer mechanism in single-phase natural circulation cooling is convection, making the loop flow rate the most important parameter governing heat removal. Heat generated by the core is transported away from the reactor vessel through the hot leg to steam generators (heat sink) by means of the sub-cooled primary liquid.

Advantages of natural circulation

- a) Elimination of pumps. Elimination of the primary circulating pumps in some Generation 4 designs not only reduces capital, operating, and maintenance costs, but also eliminates all safety issues associated with circulating pump failure.
- b) Better flow distribution. Use of pumps can cause misdistributions of pressure in the headers, leading to misdistribution of flow in the parallel channels. Moreover, using pumps requires orificing to provide flow in the fuel channels corresponding to each channel's power. Natural circulation provides a natural channel flow distribution.
- c) Flow characteristics. In a natural circulation system, flow increases with power, whereas in a forced-circulation two-phase system, flow decreases with increasing power. This has specific advantages in steam generating power plants.
- d) Safety aspects. Because natural circulation is based on a natural physical law, it is not expected to fail, unlike fluid-moving machines such as pumps. This aspect of natural circulation has enabled its application in many safety systems. In all current designs of nuclear power reactors, natural circulation is a backup for decay heat removal in the event of a pumping power failure.
- e) Simplicity. Because of the need to minimize pressure losses to enhance flow rates, designers of natural circulation systems tend to eliminate all unnecessary pipe bends, elbows, etc. The result is a system with a simple piping layout that can be fabricated in the factory.

Challenges of natural circulation

- a) Low driving force. One of the drawbacks of natural circulation systems is that their driving force is low. The most straightforward way to increase the driving force is to increase the loop height, which may not be economical. In addition, use of tall risers can make natural circulation systems slender in structure and may raise seismic concerns. Due to these reasons, the incremental height of natural circulation systems compared to the corresponding forced circulation systems is often limited to less than 10 m.

This challenge has a specific impact on channel-type reactors such as CANDU. As explained in this section, at low driving force in a CANDU, certain channels in the core may not sustain forward flow, i.e., channel flow direction cannot be accurately estimated.

- b) Low system pressure losses. With low driving force, the only way to obtain reasonably large flow rates is to design for low pressure losses. There are several measures to achieve low system pressure losses:
 - i. Use of large-diameter components and pipes. The most straightforward way to reduce pressure losses is to use large-diameter components. However, this also results in increased cost and enhanced system volume, both of which have economic and safety implications.

- ii. Simplified system. Generally refers to the simplified piping and equipment layout of the system, such as minimization of U-bends, elbows, loop seals, etc. This not only results in a simplified system, but also results in low pressure losses and prevents phase separation from promoting natural circulation flow.
 - iii. Elimination of components. An example in this case is the possible elimination of mechanical separators.
- c) Low mass flux. Low driving force and the consequent use of large-diameter components result in low mass flux in natural circulation systems compared to forced circulation systems. With low mass flux, the allowable maximum channel power is lower, leading to larger core volume than in a forced circulation system of the same rating.
- d) Instability effects. Although instability is common to both forced and natural circulation systems, the latter are inherently less stable than forced circulation systems. This is attributable to the nonlinear nature of the natural circulation phenomenon, where any change in the driving force affects the flow, which in turn affects the driving force, possibly leading to oscillatory behaviour.
- e) Low pressure and low flow regime. In natural circulation systems, the flow rate is a strong function of power and system pressure. Moreover, the flow is stagnant when the reactor power is zero during initial start-up. The operating conditions of natural circulation systems can fall into the low-power, low-flow regime, where validated thermal-hydraulic relationships are not readily available.
- f) Specification of a start-up and operating procedure. It is well known that most boiling systems exhibit instabilities at low pressures and low qualities. Therefore, natural circulation reactors must be started up from a stagnant low-pressure, low-temperature condition. During the pressure and power raising process, passing through an unstable zone shall be avoided because instability can cause premature CHF occurrence.
- g) Low CHF. The basis for thermal margin is the CHF, which depends on geometric and operating parameters. Because flow in natural circulation reactors is less, designers of these reactors tend to use the maximum allowable exit quality to minimize their size. This means that the CHF value of the reactor tends to be significantly lower than in the forced circulation case. This calls for several measures to increase CHF.

As shown on the left side of Figure 141, due to the difference in densities between the vertical legs, a pressure difference is created between stations 'a' and 'b', which is the cause of the flow. At steady state, the driving buoyancy force is balanced by the retarding frictional force, thus providing a basis for flow rate estimation using the following equation [IAEA2005, IAEA2012]:

$$gH(\rho_c - \rho_h) = \frac{R \cdot W^2}{2\bar{\rho}}, \quad (290)$$

where g (m/s^2) is acceleration due to gravity, R (m^{-4}) is hydraulic resistance, and W (kg/s) is mass flow rate. Hence, the mass flow rate induced by natural circulation is given by:

$$W = \left[\frac{2\bar{\rho}A^2(\rho_c - \rho_h)gH}{R} \right]^{\frac{1}{2}}. \quad (291)$$

Natural circulation flow is enhanced by increasing the loop height H and the density difference $(\rho_c - \rho_h)$, as well as by decreasing the hydraulic resistance R .

By introducing loop resistance models, the above equation can be further expanded into the following form:

$$W = \left[\frac{2\bar{\rho}A^2(\rho_c - \rho_h)gH}{\sum_{i=1}^{N_i} \left(\frac{f_i L_i}{D_i} + K_i \right)} \right]^{\frac{1}{2}}. \quad (292)$$

The natural circulation phenomenon can be classified in terms of the state of the working fluid, the interactions with the surroundings, loop geometry, body force field, system inventory, and number of heated channels. Figure 142 shows certain types of natural circulation in a rectangular geometry.

The state of the working fluid can be single-phase, two-phase, or supercritical. The single-phase natural circulation is important as a decay power removal mechanism in many operating and new designs of nuclear power reactors. Two-phase natural circulation normally occurs in BWRs and CANDUs under certain operating regimes.

In terms of interactions with the surroundings, closed-loop and open-loop natural circulation can be distinguished. The closed loop involves only energy exchange with the surroundings, whereas the open loop involves both energy and mass exchange.

In terms of loop geometry, natural circulation can occur in rectangular, U-tube, toroidal, and figure-of-eight forms (the last being specific to the CANDU design). The body force field has an important impact and can be gravitation (in most cases), centrifugal force, or both for certain specific applications.

In terms of system inventory, natural circulation can occur in full systems (in single-phase mode), in partially filled systems (in two-phase mode), or with boiling in reflux condensation mode. In any of these types, natural circulation can occur in single-channel or parallel-channel loops, as with the CANDU design.

Natural circulation in a containment building is a specific form of single-phase multi-component natural circulation.

7.9.2 CANDU natural circulation

CANDU reactors have a very different design than LWR reactors, and therefore the effectiveness of natural circulation must be carefully assessed. The performance of natural circulation in a CANDU reactor is an important part of reactor safety under certain operating or accident conditions. Therefore, a natural circulation test is performed in each CANDU plant during commissioning to demonstrate that natural circulation works adequately and that the

computer codes predict the observed behaviour sufficiently well.

Figure 143 shows a CANDU primary heat transport system on the left side and a view of the CANDU header on the right side [POP2012a, POP2014]. The CANDU header plays an important role in natural circulation, particularly the outlet header because it contains flows of about 2%–4% quality.

A CANDU reactor cooling system is arranged in a figure-of-eight loop configuration, typically with two loops (i.e., two figure-of-eight loops). Figure 143 shows on the left side an elevation indication for various components. The height difference between the bottom channel and the top of the steam generators is about 22 metres. The height difference between the reactor top channels and the bottom of the steam generators is about 3 metres. Due to the difference in densities between the vertical branches, a pressure difference is created, which creates the potential for natural circulation flow around the loop.

From Figure 143, it is clear that the height difference in CANDU is greater than in PWRs, and according to Eq. (291), this enhances natural circulation. However, flow resistance in the CANDU primary loop is greater than in LWRs because of the relatively small-diameter feeders, channel end-fittings, and shorter fuel bundles, which according to Eq. (291), reduces the natural circulation driving force. In addition, the CANDU core consists of many fuel channels in parallel that have similar geometry, but are at different elevations. This will create differences in the natural circulation driving force.

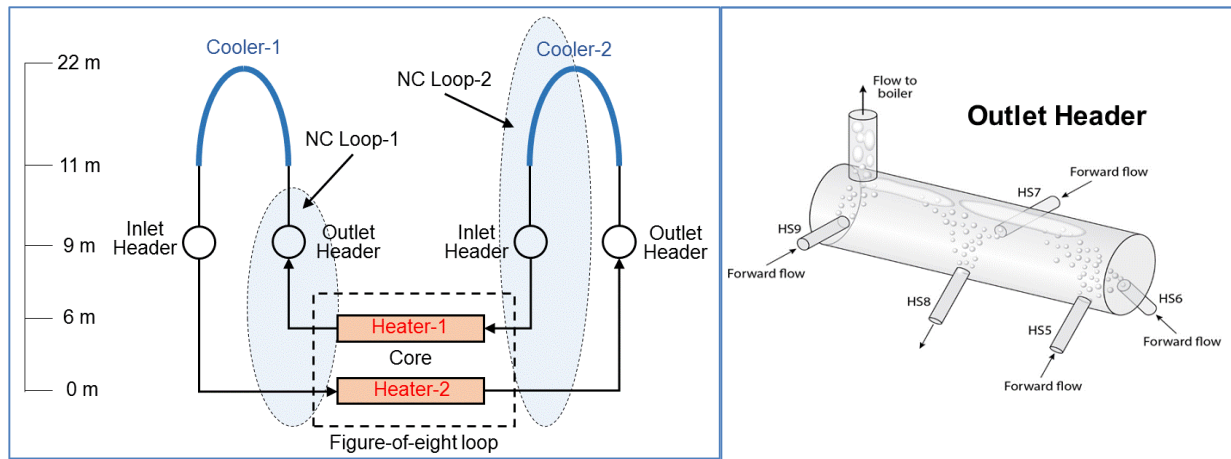


Figure 143 Natural circulation in CANDU

A CANDU header, shown on the right side of Figure 143, has multiple feeder connections at different elevations and angles. When the header is partly voided, this geometry can result in interesting phenomena. One of these is vapour pool-through, in which steam is sucked into the feeder even if the feeder connection to the header is below the collapsed liquid level in the header. Because the scope of this textbook is limited, details of this phenomenon cannot be covered in this section.

At very low pressure drop between inlet and outlet headers, the feeder flow is low and could possibly reverse direction in some feeders and channels. However, flow direction in the channel is not as important as the mass flow rate. Hence, as long as there is sufficient flow in

the feeders and the fuel channel, decay heat generated in the core can be removed effectively, regardless of the flow direction. Experiments have provided information on flow direction in CANDU feeders and core channels under natural circulation and have demonstrated that decay heat removal can be adequate during natural circulation for certain combinations of decay power levels and loop inventory.

The key parameters for CANDU natural circulation are the primary coolant inventory in the core, the secondary pressure, and the primary power. At very low powers in CANDU, two natural circulation loops are created: one between channels and headers, and the other one from headers to steam generators (see Figure 143). This is important because it demonstrates that channel flow direction is not an essential parameter in determining the effectiveness of natural circulation for decay heat removal.

Figure 144 [ING1992, POP2012b]] shows the experimentally observed onset of bi-directional flow in a CANDU core under natural circulation. It is evident that the heat transport system inventory plays an important role, along with channel power and pressure. Figure 145 [POP2012a, POP2012b] shows the criteria for flow reversal in a CANDU core. The upper and lower boundaries are shown in terms of secondary-side pressure and loop-integrated void. It is evident that at higher loop void and lower pressure, the flow reversal band is significantly expanded.

One very specific application of natural circulation in CANDU is heat rejection by the feeders to the containment environment. At very low powers, decay heat can be passively rejected by the feeder pipes directly to the containment atmosphere.

The Canadian Nuclear Safety Commission issued Generic Action Item GAI 90G02 in 1990, requesting utilities to demonstrate reactor cooling adequacy in natural circulation and address uncertainty in the RD-14M experiments with respect to core cooling with reduced loop water inventory in a CANDU loop (LOCA combined with loss of forced circulation). This GAI was closed for all CANDU stations in Canada, thus demonstrating the cooling adequacy of natural circulation in CANDU.

CANDU core cooling in the absence of forced flow (CCAFF), i.e., natural circulation, has been extensively studied over the past 50 years. The CANDU CCAFF terminology defines the following natural circulation modes: a) single-phase thermo-siphoning; b) two-phase thermo-siphoning, c) intermittent buoyancy-induced flow (IBIF), and continuous steam venting.

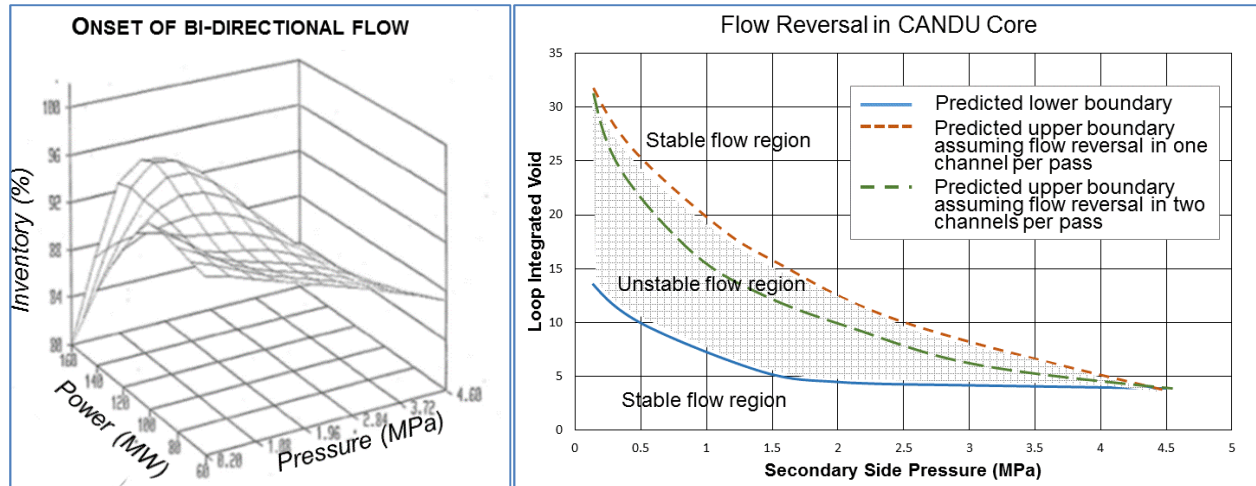


Figure 144 Onset of bi-directional flow in CANDU

Figure 145 Criteria for flow reversal in a CANDU core

Single-phase thermo-siphoning

In this CCAFF mode, continuous heat input to the coolant raises the temperature in the fuel channel (as shown in Figure 143). This induces a buoyancy force whereby the hot liquid rises to the steam generator and deposits its heat. From the steam generator, a lower-temperature (denser) liquid continues to flow down back to the core. In this case, the buoyancy forces are sufficient to overcome the static pressure caused by the elevation of the boilers with respect to the fuel channels. This is a continuous process and is capable of removing a substantial amount of decay heat indefinitely as long as the loop does not drain beyond about 70%, and as long as the heat is removed from the steam generators.

Two-phase thermo-siphoning

This is a similar phenomenon to liquid thermo-siphoning, but with continuous boiling of the liquid, and thus steam content in the flow provides an additional buoyancy force for heat transfer to the steam generators (resulting from the liquid-vapour density difference). It has been experimentally demonstrated that flow is still continuous in a given direction, with a large quantity of vapour at the channel outlet. For this thermo-siphoning mode, it is important to maintain a certain flow rate rather than a certain flow direction. The flow rate in this type of natural circulation depends on the amount of void in the system and the channel power.

Intermittent buoyancy-induced flow (IBIF)

If the flow rate is reduced to a very small value, or if the fluid stagnates in the channel, the IBIF phenomenon occurs. Numerous analytical and experimental studies of IBIF have been conducted in recent decades to address the Canadian Nuclear Safety Commission-issued Generic Action Item GAI 90G02 on CCAFF. The closure of this GAI provided answers to many issues related to fuel and fuel channel behaviour in a CANDU channel when the flow stops, such as:

- First channel in which boiling occurs;

- Role of static pressure (i.e., channel elevation);
- Location in the channel where boiling occurs;
- Vapour accumulation and outflow from the channel;
- Heat transfer from uncovered fuel elements;
- Impact of void rate generation;
- Fuel sheath temperature for uncovered fuel elements.

Figure 146 shows the four steps in the IBIF cycle, which are explained below [POP2012a, POP2014]. The IBIF cycle repeats itself, providing channel cooling when the flow is stopped. Figure 146a shows a CANDU fuel channel in which flow has stopped and the power profile has a certain cosine shape. As forced circulation is lost, flow almost stagnates in the channel, and therefore heat transfer and removal from the fuel are lost. As a result, because of decay power generation, fuel temperature rises, along with fluid temperature. After some time, the coolant in the channel reaches saturation and thermal stratification. Steam starts to develop at the top of the channel.

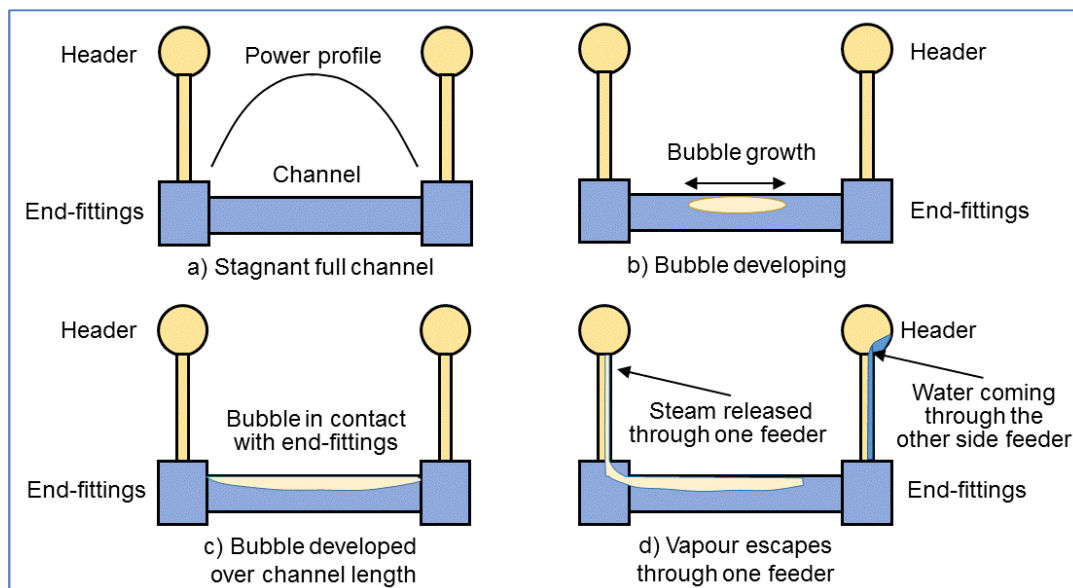


Figure 146 Intermittent buoyancy-induced flow in CANDU

Figure 146b shows a large bubble being generated because of liquid evaporation. The uncovered fuel elements begin to heat up faster (and local heating of the pressure tube occurs). The large vapour bubble grows outward from the centre of the channel towards the end-fittings, and uncovered fuel-element sections stop producing vapour.

Figure 146c shows further progression of an IBIF cycle, as steam reaches and heats up the end-fittings. Because the end-fittings have a very large mass of relatively cold material (during a reactor shutdown, everything approaches 60°C), and it takes a while to heat it up before the bubble can “push” itself by. This delays venting because the longer the fuel is uncovered, the hotter it gets. Before steam can push through, several sub-cycles may occur, with steam condensation at the end-fitting edge. The process continues until the steam creates a flow path to the feeders.

Figure 146d shows the last part of an IBIF cycle, when the steam pushes through to the feeder and the header. Usually steam push-through happens on one side or the other first. It does not necessarily follow the usual flow direction. Once one side starts to “vent” (vapour rushes out of that side of the channel), this creates a pressure force, which sucks in cold liquid from the opposite header.

After venting is completed, the fuel channel refills with sub-cooled or saturated water from the other header. At this point, the previous IBIF cycle is completed, and a new cycle begins.

Figure 147 shows an envelope of CANDU fuel sheath temperature histories during an IBIF cycle [POP2012a, POP2014]. While the channel is full and sub-cooled, the sheath temperatures are below saturation (left part of the diagram). As the channel saturates and remains saturated for a certain time, sheath temperatures remain near saturation. Then, as bubbles are generated in the upper part of the channel and fuel elements are exposed, the fuel sheath temperatures of these fuel elements rise to above 400°C (during the heating period, and depending on fuel element power). When steam venting occurs at the end of an IBIF cycle and the channel is refilled with water from the other header, sheath temperatures fall to and below saturation (the last part of the diagram).

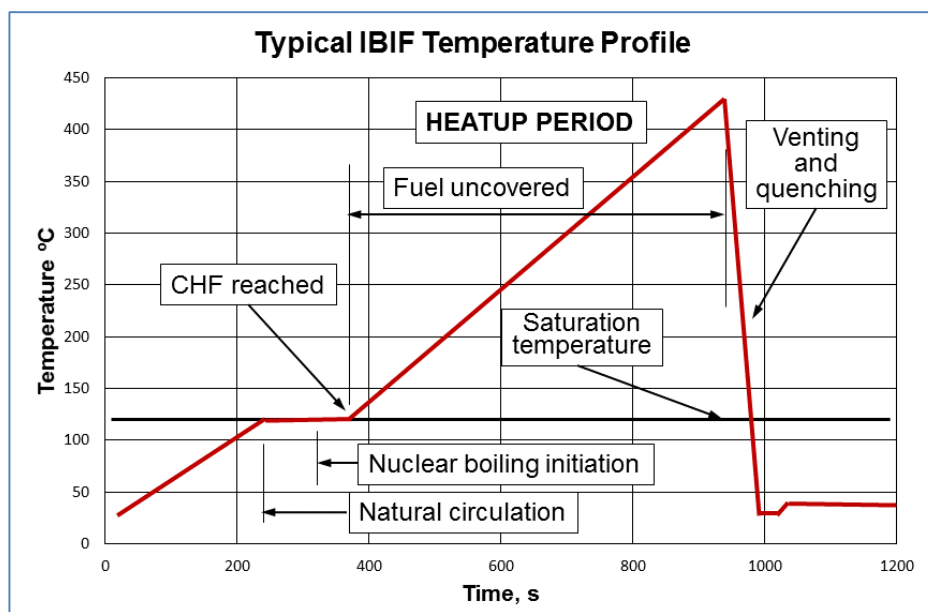


Figure 147 Typical temperature histories in a CANDU channel in natural circulation

7.9.3 CANDU natural circulation experimental studies

In support of natural circulation knowledge base development, numerous experimental tests and assessments have been conducted in Canada on CANDU-typical experimental facilities. The most important experimental facilities in this area are:

- RD-14 natural circulation experiments. RD-14 is a full-scale, full-elevation CANDU-typical experimental facility at AECL with two figure-of-eight passes containing one fuel channel in each loop.
- RD-14M natural circulation experiments. RD-14M is a full-scale, full-elevation CANDU-

typical experimental facility at AECL with two figure-of-eight passes containing five fuel channels in each loop.

- CWIT standing-start experiments. CWIT is a full-scale experimental facility containing two full-scale fuel channels connected to inlet and outlet header at the Stern Laboratories.

More details of these experimental facilities, experimental results, and conclusions are provided in [IAEA2005, IAEA2012]. The experimental work in this area was performed to improve the knowledge base and to provide data for development and validation of computer programs and models.

7.9.4 Natural circulation calculations and predictions

Mathematical modelling of natural circulation is based on several approaches, including empirical models based on experimental data; analytical mechanistic models based on fundamental principles approaches that use conveniently established simplifying assumptions; and general-purpose computer programs based on detailed application of field conservation equations.

CATHENA [CAT2005], TUF [TUF2001], and RELAP [2010] are examples of large one-dimensional two-fluid thermal-hydraulic computer codes used to simulate natural circulation. Recently, more attention has been devoted to use of CFD computer models [HAS2012] for natural circulation analysis in cases where more detailed information is needed. More details about the use of thermal-hydraulic computer programs are provided in Chapter 7.

Various mechanistic models have been proposed in the literature to analyze natural circulation in the CANDU reactor core and feeder system. These models use mass, momentum, and energy conservation accompanied by drift-flux momentum equations. Often, a macroscopic mass, momentum, and energy balance in a six-equation configuration is also used. Details of this topic are beyond the scope of this textbook, but information can be found in the section for suggested further reading. One example of one mechanistic model is provided below.

Algebraic equations or field equations properly solved by simplified numerical models or by complex computer codes can be used to predict natural circulation performance under a wide variety of geometrical conditions and technological systems. The fundamental principles approach is based on the following assumptions: constant core inlet enthalpy; cross-section averaged fluid properties; homogeneous two-phase flow; thermal equilibrium; form losses dominating loop resistance. These assumptions are applied to the mass, momentum, and energy equations for each loop component to obtain the conservation equations. The equations are then integrated over their respective single-phase and two-phase regions to obtain the loop balance equations.

Assuming the natural circulation loop shown in Figure 141, the transient momentum equation can be written as:

$$\sum_{i=1}^N \left(\frac{L_i}{A_i} \right) \cdot \frac{dW}{dt} = g(\rho_l - \rho_{TP}) H_{nc} - \frac{W^2}{\rho_l A_c^2} \left\{ \sum_{SP} \left[\frac{1}{2} \left(\frac{fL}{D_h} + K \right) \left(\frac{A_c}{A_i} \right)^2 \right] + \frac{\rho_l}{\rho_{TP}} \sum_{TP} \left[\frac{1}{2} \left(\frac{fL}{D_h} + K \right) \left(\frac{A_c}{A_i} \right)^2 \right] \right\}. \quad (293)$$

The energy balance equation for transient natural circulation can be written as:

$$M_{loop} \frac{d(e_M - e_l)}{dt} = W(h_{TP} - h_l) - \dot{q}_{SG} - \dot{q}_{loss}. \quad (294)$$

The equilibrium two-phase quality in the core exit can be defined as:

$$x_e = \frac{h_{TP} - h_l}{h_{lg}}. \quad (295)$$

The homogeneous mixture density is defined using the following relation:

$$\rho_{TP} = \frac{\rho_l}{1 + x_e \left(\frac{\rho_l - \rho_g}{\rho_g} \right)}, \quad (296)$$

where:

L_i	is the length of a loop component;	K	is the coefficient of local resistance;
A_i	is the area of a loop component;	e_M	is the mixture internal energy;
A_c	is the area of a loop restriction;	e_l	is the liquid internal energy;
H_{nc}	is the elevation difference driving the natural circulation	\dot{q}_{SG}	is the steam generator heat sink [kJ/s];
D_i	is the loop element diameter;	\dot{q}_{loss}	is the loop heat losses;
f	is the friction factor;	h_{TP}	is two-phase enthalpy;
		h_l	is liquid enthalpy,

These equations can be manipulated to yield the following equations for steady-state mass flow rate in a two-phase natural circulation loop with uniform diameter:

$$W_{ss} = \left[\frac{2}{P} \frac{g \cdot \rho_r \beta_{TP} H_{nc} Q_h D_r^b A_r^{2-b} \rho_l}{\mu_r^b N_G} \right]. \quad (297)$$

The geometric contribution to the friction factor is defined as:

$$N_G = \frac{L_t}{D_r} \left[\sum_{i=1}^{N_{SP}} \left(\frac{l_{eff}}{D_i^{1+b} A_i^{2-b}} \right) + \bar{\phi}_{LO}^2 \sum_{i=N_{SP}+1}^{N_B} \left(\frac{l_{eff}}{D_i^{1+b} A_i^{2-b}} \right)_i + \bar{\phi}_{LO}^2 \sum_{i=N_B+1}^{N_{TP}} \left(\frac{l_{eff}}{D_i^{1+b} A_i^{2-b}} \right)_i \right]. \quad (298)$$

The Reynolds and Grashoff mixture numbers are defined as:

$$Re_m = \frac{D_r W_{ss}}{A_r \mu_l} \quad Gr_m = \frac{D_r^3 \rho_l^3 \bar{\beta}_h g Q_h \Delta z}{A_r \mu_l^3}. \quad (299)$$

In these equations:

β_h is the thermal expansion coefficient

Q_h ($^{\circ}\text{C}$)

Δz is the total heat input rate (W);

is the centreline elevation difference in the loop between cooler and heater

l_{eff} is the effective length of a component;

A is the flow area (m^2);

μ is the dynamic viscosity (Ns/m^2);

r is a subscript indicating a reference value.

7.9.5 Problems

1. Explain the importance of natural circulation in the CANDU primary heat transport system, and the design decisions that help to enhance it.
2. Explain the key aspects of the Intermittent Buoyancy Induced Flow (IBIF) in CANDU channels, list and explain the key IBIF parameters.
3. Calculate natural circulation flow in a PWR reactor primary cooling loop assuming typical geometrical and thermal-hydraulic parameters for a PWR reactor (primary loop is in subcooled boiling flow in normal operation, i.e., single phase liquid flow).

8 References

- [AECL1978] G.A. Pon, "Evolution of CANDU Reactor Design", AECL-6351, August 1978.
- [AECL1981] "CANDU Nuclear Power System", AECL-TDSI-105, January 1981.
- [AECL1997] "Canada Enters the Nuclear Age – A Technical History of Atomic Energy of Canada Limited", AECL, McGill-Queen's University Press, Toronto, 1997.
- [AECL2005] "CANDU 6 Technical Outline", AECL, September 2005.
- [AECL2009a] "Enhanced CANDU 6 Technical Summary", AECL, 2009.
- [AECL2009b] "ACR-1000 Technical Description", AECL 10820-01371-TED-001, 2009.
- [AECL2010] "*Enhanced CANDU 6 (EC6) Design Description*", IAEA Advanced Water-Cooled Reactors Web-Based Report, 2010.
- [AHM2009] R. Ahmadi, A. Nouri-Borujardi, J. Jafari, I. Tabatabari, "Experimental Study of Onset of Subcooled Annular Flow Boiling", *Progress in Nuclear Energy Journal*, Vol 51, pp.361-365, 2009.
- [APR2011] "Advanced Pressurized Reactor (AP1000)", Design Control Document, Rev. 19, Westinghouse, USNRC Website, 2011.
- [BER1981] A.E. Bergles, *et al.*, *Two-Phase Flow and Heat Transfer in the Power and Process Industries*, Hemisphere Publishing, 1981.
- [BIR1960] R.B. Bird, W.E. Stewart, and E.N. Lightfoot, *Transport Phenomena*, Wiley, New York, 1960.
- [BPR2000] "Bruce: A Safety Report", Brice Power, 2000.
- [CAR2015] "Carnot Principle", Wikipedia, Internet, 2015.
- [CAT1998] B.N. Hanna, *et al.*, "CATHENA: A Thermal-Hydraulic Code for CANDU Analysis", *Nuclear Engineering and Design* 180 (1998) 113-131, and AECL-1194.
- [CAT2000] "CATHENA Mod 3.5c/Mod o Theory Manual", COG-00-008, Nov. 2000.
- [CAT2005] "CATHENA Mod 3.5d Theory Manual", AECL, 153-112020-STM-001, Dec. 2005.
- [CLA2015] "Clausius Statement", Wikipedia, Internet, 2015.
- [COL1972] J.C. Collier, *Convective Boiling and Condensation*, McGraw-Hill, 1972.
- [CRA1957] *Flow of Fluids Through Valves, Fittings, and Pipes*, Crane, 1957.
- [DEL1981] J.M. Delhay, *et al.*, *Thermo-Hydraulics of Two-Phase Systems for Industrial Design and Nuclear Engineering*, Hemisphere Publishing, 1981.
- [ELW1978] M.M. El-Wakil, *Nuclear Heat Transport*, American Nuclear Society, 1978.
- [ELW1990] M.M. El-Wakil, *Nuclear Energy Conversion*, American Nuclear Society, 1990.
- [EPRI1999] *Nuclear Reactor Generations*, EPRI document EPRI NP-6780-L, Volume 1, 1999.
- [EPRI1996] *Water Hammer Handbook for Nuclear Plant Engineers and Operators*, EPRI Technical Report, Palo Alto, California, 1996.

- [GAR1999] B. Garland, “Reactor Thermal-Hydraulic Design”, Graduate course EP716 lectures, Engineering Physics, McMaster University, 1999.
- [GLA1967] S. Glasstone, A. Sesonske, Nuclear Reactor Engineering, Van Nostrand Reinhold, 1967.
- [HAS2012] Y.A. Hassan, Computational Fluid Dynamics for Natural Circulation, Texas A&M University, Texas, USA, for the N.I.N.E Nuclear and Industrial Engineering Natural Circulation Course, Beijing, China, 27 July–31 Aug. 2012.
- [HET1982] G. Hetsroni, Handbook of Multiphase Systems, Hemisphere and McGraw-Hill, Washington, 1992.
- [IAEA2001] Thermal-Hydraulic Relationships for Advanced Water-Cooled Reactors, IAEA TECDOC-1203, Vienna, 2001.
- [IAEA2005] Natural Circulation in Water-Cooled Nuclear Power Plants, IAEA TECDOC-1474, Vienna, 2005.
- [IAEA2012] Natural Circulation Phenomena and Modelling for Advanced Water-Cooled Reactors, IAEA TECDOC-1677, Vienna, 2012.
- [IDE1996] I.E. Idelchik, Handbook of Hydraulic Resistance, 3rd Edition, Begell House, New York, 1996.
- [ING1992] P.J. Ingham, Natural Circulation Experiments in the RD_14M Multiple Channel Thermal-Hydraulic Loop, AERCL, Pinawa, Manitoba, Canada, 1992.
- [KEV2015] “Kelvin Statement”, Wikipedia, Internet, 2015.
- [KNI2002] R.A. Knief, Nuclear Engineering—Theory and Technology of Commercial Power, American Nuclear Society, 2008.
- [KRI1987] V.S. Krishnan, P. Gulshani, “Stability of Natural-Circulation Flow in a CANDU-Type Fuel Channel”, AECL, Pinawa, Manitoba, Canada, in Journal of Nuclear Engineering and Design, Vol. 99, pp. 403–412, 1987.
- [KPL2015] Kelvin-Planck Statement, Wikipedia, Internet, 2015.
- [KOK2009] K.D. Kok (Ed.), Nuclear Engineering Textbook, CRC Press, 2009.
- [LAH1977] R.T. Lahey, Jr., and F.J. Moody, The Thermal Hydraulics of a Boiling Water Nuclear Reactor, ANS&AEC Monograph Series on Nuclear Science and Technology, ANS, 1977.
- [LEU2004] L. Leung, Reactor Thermal-Hydraulic Design: CHF, Post-Dryout, and Pressure Drop Lectures, Graduate course UN804 lectures, UNENE graduate courses, Chalk River Laboratories, AECL, 2004.
- [MOO1944] L.F. Moody, “Friction in Pipes”, Transactions of the ASME, pp. 666-671, 1944.
- [OPG2002] Darlington Safety Report, Ontario Power Generation, 2002.
- [OPG2000] Pickering: A Safety Report, Ontario Power Generation, 2000.
- [PLA2015] Planck Principle, Wikipedia, Internet, 2015.
- [POP2000] N.K. Popov, U.S. Rohatgi, H.E.C. Rummens, R.B. Duffy, “Two-Phase Flow Stability in Low-Pressure Parallel Vertical Heated Annuli”, ICONE8, Baltimore, MD, USA, April 2–6, 2000.

- [POP2012a] N.K. Popov, Natural Circulation Behaviour in PHWRs, Engineering Physics, McMaster University, Hamilton, Canada, for the N.I.N.E Nuclear and Industrial Engineering, Natural Circulation Course, Beijing, China, 27 July–31 August 2012.
- [POP2012b] N.K. Popov, PHWR Natural Circulation Experimental Program in Canada, Engineering Physics, McMaster University, Hamilton, Canada, for the N.I.N.E Nuclear and Industrial Engineering, Natural Circulation Course, Beijing, China, 27 July–31 August 2012.
- [POP2013] N. Popov, Reactor Thermal-Hydraulic Design, Graduate course UN804 lectures, UNENE Graduate Courses, 2013.
- [POP2014] N. Popov, Reactor Thermal-Hydraulic Design, Graduate course EP716 lectures, Engineering Physics, McMaster University, 2014.
- [REL2005] “RELAP5 - A Computer Program for Transient Thermal-Hydraulic Analysis of Nuclear Reactors and Related Systems”, INEEL-EXT-98-00834, September 1996.
- [REL2010] “RELAP5/MOD 3.3 Code Manual”, USNRC, NUREG/CR-5535/Rev P4, October 2010.
- [ROH1983] W.M. Rohsenov, J.P. Hartnett, E.N. Ganic, Handbook of Heat Transfer Fundamentals, McGraw-Hill, New York, 1985.
- [SOP1975] Y.F. Chang, “The SOPHT Program and its Applications”, Proceedings, Simulation Symposium on Reactor Dynamics and Plant Control, May 26–27, CRNL, published as CRNL 1369, 1975.
- [SAA1966] M.A. Saad, Thermodynamics for Engineers, Prentice-Hall, 1996.
- [SOP1977] Y.F. Chang, A Thermal-Hydraulic System Simulation Model of the Reactor, Boiler, and Heat Transport System (SOPHT), CNS-37-2, Ontario Hydro, September 1977.
- [TOD1990a] N.E. Todreas, M.S. Kazimi, Nuclear Systems I—Thermal Hydraulic Fundamentals, MIT, CRC Press, Taylor & Francis, 2011.
- [TOD1990b] N.E. Todreas, M.S. Kazimi, Nuclear Systems II—Elements of Thermal Hydraulic Design, MIT, CRC Press, Taylor & Francis, 1990.
- [TON1965] L.S. Tong, Boiling Heat Transfer and Two-Phase Flow, Wiley, 1965.
- [TON1975] L.S. Tong, Boiling Heat Transfer and Two-Phase Flow, Krieger, 1975.
- [TON1996] L.S. Tong, J. Weisman, Thermal Analysis of Pressurized Water Reactors, American Nuclear Society, 1996.
- [TUF2010] TUF Thermal-Hydraulics Computer Program, N-REP-06631.02-10010 R00, Ontario Power Generation, October 2001.
- [WAL1969] G.B. Wallis, One-Dimensional Two-Phase Flow, McGraw-Hill, 1969.
- [WEI1977] J. Weisman, Elements of Nuclear Reactor Design, Elsevier, 1983.
- [WIK2015] “Steam-Water Diagrams”, Internet, Wikipedia, 2015.

[WNA2009] “Nuclear Reactor Generations”, WNA Web site, 2009.

9 Further Reading

- [DUD1976] J.J. Duderstadt, L.J. Hamilton, Nuclear Reactor Analysis, Wiley, New York, ISBN 0-471-22363-8, 1976.
- [GIN1981] J.J. Ginoux ,Two-Phase Flows and Heat Transfer with Application to Nuclear Reactor Design Problems, Hemisphere, 1981.
- [GOV1972] G.W. Govier, K. Aziz, The Flow of Complex Mixtures in Pipes, Van Nostrand Reinhold, 1972.
- [HSU1976] Y. Hsu, R. Graham, Transport Processes in Boiling and Two-Phase Systems, Hemisphere, 1976.
- [ISH1975] M. Ishii, T. Hibiki, Thermo-Fluid Dynamic Theory of Two-Phase Flow, Springer, 2010.
- [LAM1977] J.R. Lamarsh, Introduction to Nuclear Engineering, Addison-Wesley, 2001.
- [LEW1977] E.E. Lewis, Nuclear Reactor Safety, Wiley, 1977.
- [ROA1976] P.J. Roache, Computational Fluid Dynamics, Hermosa, 1976.

10 Glossary

ACR	Advanced CANDU Reactor	MCHFR	Minimum CHF Ratio
ADL	Axial Dry-Patch Fraction	MCHFPR	Minimum CHF Power Ratio
AECL	Atomic Energy of Canada Limited	MCPR	Minimum Power Ratio
AFD	Axial Flux Distribution	NPSH	Net Positive Suction Head
AGR	Advanced Gas-Cooled Reactor	NPSHA	Net Positive Suction Head Available
BP	Bruce Power	NPSHR	Net Positive Suction Head Required
BWR	Boiling Water Reactor	NOP	Nominal Operating Power
CANDU	CANada Deuterium Uranium	NOP	Neutron Overpower Protection
CANFLEX	CANDU Flexible Fuelling	NPD	Nuclear Demonstration Plant
CCAFF	Core Cooling in Absence of Forced Flow	NPP	Nuclear Power Plant
CDF	Circumferential Drypatch Fraction	OCR	Organic Coolant Reactor
CHF	Critical Heat Flux	OH	Ontario Hydro
CHFR	CHF Ratio	OPG	Ontario Power generation
CHFPR	CHF Power	OSV	Onset of Significant Void
CP	Critical Power	PHTS	Primary Heat Transport System
CPR	Critical Power Ratio	PHWR	Pressurized Heavy Water Reactor
DNB	Departure from Nucleate Boiling	PWR	Pressurized Water Reactor
ECC	Emergency Core Cooling	RBMK	High Power Channel Type Reactor
ECI	Emergency Coolant Injection	RCS	Reactor Cooling System
EPRI	Electric Power Research Institute	RFD	Radial Flux Distribution
GAI	Generic Action Item	RIH	Reactor Inlet Header
HTGCR	High Temperature Gas Cooled Reactor	ROH	Reactor Outlet Header
HTS	Heat Transport System	ROP	Reactor Overpower Protection
IAEA	International Atomic Energy Agency	R&D	Research & Development
IBIF	Intermittent Buoyancy-Induced Flow	R&M	Reliability and Maintainability
LMFBR	Liquid Metal Breeder Reactor	SGHWR	Steam Generating Heavy Water Reactor
LOCA	Loss of Coolant Accident	QA	Quality Assurance
LOFA	Loss of Flow Accident	WNA	World Nuclear Association
LORA	Loss of Reactivity Accident	WWER	Water Cooled and Moderated Power Reactor (from Russian VVER)
LWR	Light Water Reactors		

11 Nomenclature

A	cross section area, [m ²]	v	fluid velocity, [m/s]
CHF	critical heat flux, [kW/m ²]	W	mass flow rate, [kg/s], work, [kJ]
c _p	specific heat at constant pressure, [J/(kg K)]	w	specific work, [kJ/kg]
c _v	specific heat at constant volume, [J/(kg K)]	We	Weber number
D _H	hydraulic diameter, [m]	x	mass quality
d	diameter, [m]	x _{th}	thermodynamic quality
d _h	hydraulic diameter, [m]	Z	height, [m]
dx	axial derivative		
E _K	kinetic energy, [kJ]	<u>Greek Symbols</u>	
E _P	potential energy, [kJ]	α	void fraction, thermal diffusivity, [m ² /s]
E _U	internal energy, [kJ]	γ	adiabatic exponent, SG pinch fraction
e	specific energy, [kJ/kg]	ΔP	pressure drop, [kPa/m ²]
f	friction factor	σ	surface tension, [N/m]
G	mass flux, [kg/s-m ²]	η _t	thermodynamic efficiency
g	gravitational constant, [m/s ²]	μ	dynamic viscosity of the fluid [Pa·s], [N·s/m ²], [kg/(m·s)]
H	total enthalpy, [kJ]	ρ	density [kg/m ³]
H	pump head, [m]	σ	surface tension, [N/m]
h	specific enthalpy [kJ/kg]	τ	pump torque, [Nm], friction stress, [N/m ²]
h	convective heat transfer coefficient, [kW/m ² °K]	ν	specific volume, [m ³ /kg], kinematic viscosity, [m ² /s]
h _{fg}	latent heat of vapourization, [kJ/(kg °K)]	Φ	neutron flux, [neutron/(m ² -s)]
j	volumetric flux (superficial velocity) [m/s]	φ	two-phase friction multiplier
K	concentrated friction factor	ω	pump rotational speed
k	thermal conductivity, [kW/m °K]		
L	length, characteristic linear dimension, [m]	<u>Subscripts</u>	
l	characteristic length, typically the droplet diameter, [m]	a	acceleration
M, m	mass, [kg]	C	cold, cladding, fuel sheath
ṁ	mass flow, [kg/s]	CL	centreline
NOP	neutron over power	cold	cold side
Nu	Nusselt number	CRIT	critical
P	perimeter, [m]	DNB	departure of nuclear boiling
p	fluid pressure, [kPa]	e	equivalent
Pr	Prandtl number	G	gap
Q	Core power, [kW], volumetric flow, [m ³ /s]	g	gas, gap
Q'''	Core power density, [kW/m ³]	F	fuel
q'''	volumetric heat generation rate, [kW/m ³]	f	fuel, liquid
q''	surface heat flux, [kW/m ²]	fg	latent heat of vapourization
q'	linear power, [kW/m]	FL	fluid
q	energy generation per fuel element, [kW]	FW	feed water
R	gas constant, [N·m/(kg °K)], [J/(kg °K)]	H	hot, homogenous
r	radius, [m]	Hot	hot side
Re	Reynolds number	h	hydraulic
ROP	reactor over power	MFB	minimum film boiling
S	slip ratio, S total entropy, [kJ]	m	mixture
s	specific entropy, [kJ/kg]	n	vector perpendicular to surface
T	temperature, [°K]	P, p	primary
t	time, [s]	S	steam, saturation
t	thickness, [m]	SG	steam generator
U	steam generator heat transfer coefficient, [kJ/(m ² -s)]	SH	sheath
U	internal energy, [kJ]	TB	transition boiling
u	specific internal energy, [kJ/kg]	w	wall
V	volume, [m ³]		

12 Acknowledgements

I gratefully thank the following reviewers for their hard work and excellent comments during the development of this Chapter. Their feedback has much improved it. Of course, the responsibility for any errors or omissions is entirely the author's.

Bill Garland

Lawrence Leung

Dave Novog

Terry Rogers

Victor Snell

Dave Wright

I also thank Diana Bouchard for expertly editing and assembling the final copy.

13 APPENDIX A – Reactor Types

13.1 General evolution of reactor designs

The categorization of reactor designs into generations was originally suggested by the U.S. DOE and only reflected the technology evolution timeline. The attributes were assigned later, based on observed characteristics.

The nuclear industry typically categorizes nuclear reactors as follows (see Figure 148):

- Generation I – early prototype reactor designs
- Generation II – commercial power reactor designs
- Generation III/III+ – designs with significant improvements in safety and economics
- Generation IV – future designs.

Note that most currently operating reactors are of Gen II design, and reactors currently under construction are of Gen III/III+ design.

As reactor safety and economics became an important benchmark, the Gen III/III+ reactors were given certain attributes to characterize them more fully. Two separate sets of attributes (requirements or guidelines) were developed by EPRI in 1999 and by WNA in 2009.

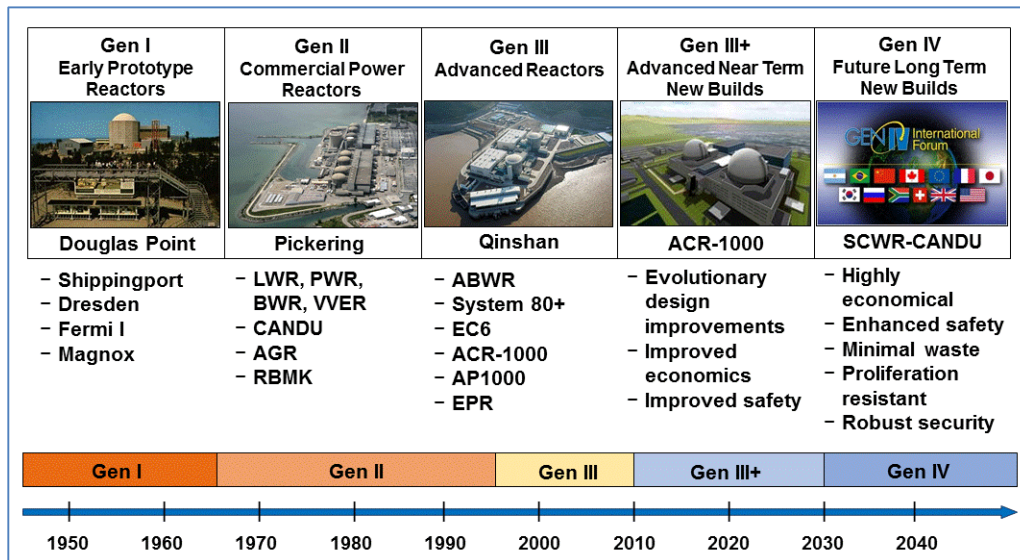


Figure 148 Reactor generations

In the EPRI documentation [EPRI1999], the following attributes are shown to be typically possessed by a Gen III/III+ design:

- | | | |
|------------------------------------|--------------------------------|-----------------------------------|
| 1. design simplification; | 6. regulatory stabilization; | 12. adequate quality |
| 2. design margins; | 7. technology standardization; | assurance; |
| 3. human factors; | 8. proven nature of design; | 13. improved security and |
| 4. reactor safety; | 9. enhanced maintainability; | sabotage protection; and |
| 5. design basis and safety margin; | 10. enhanced constructability; | 14. reduced environmental impact. |
| | 11. improved economics; | |

The WNA definition of the third generation [WNA2009] suggested the following attributes for Gen III/III+ designs:

- | | | |
|---|---|--------------------------------|
| 1. standard design to expedite licensing; | 4. higher availability and longer operating life; | 9. less waste; |
| 2. reduced cost and construction time; | 5. reduced possibility of core meltdown; | 10. use of burnable absorbers; |
| 3. simpler and more rugged design for easier operation and maintenance; | 6. resistance to damage; | 11. more passive systems; |
| | 7. reduced radiation release; | 12. load following. |
| | 8. higher burn-up; | |

Because the above two sets of guidelines overlap somewhat and expectations are not quantified, it is difficult to compare designs in quantifiable terms. More importantly, there are conflicting expectations, such as expecting changes to improve safety and at the same time expecting the design to be well proven. A detailed discussion of implementation and compliance with these objectives of current advanced design is beyond the objectives of this section, but note that none of the modern advanced designs claims to achieve all the expectations described above.

13.2 Pressurized water reactors

13.2.1 General information

Pressurized water reactors (PWRs) are currently one of the most commercially successful reactor types in operation; they originate from the U.S. nuclear industry. PWRs have been built in large numbers around the world, with many different versions and design variations. However, they all share the common characteristics of a light water coolant and moderator and enriched uranium fuel. This section provides an overview of the PWR reactor type, particularly from the perspective of thermal-hydraulic design of the reactor cooling system (RCS).

The PWR has, to date, been the world's most widely accepted power reactor type [KNI2002, KOK2009, WEI1997, TON1996, APR2011, LAH1977]. It got its start in the development of PWR propulsion reactors for United States (U.S.) nuclear submarines. The first PWR power reactor was designed and built by Westinghouse Electric Company at Shippingport in the United States, followed by a number of designs and units built in the United States by a number of vendors.

In France, during the early stage of development, Framatome designed and built a number of units as a licensee to Westinghouse until 1984. Later, Framatome, presently renamed Areva,

continued the development of PWRs in France. In this way, France became a world leader in PWR development and implementation.

In Japan, Mitsubishi continued development of PWR reactors. In Russia, following submarine and icebreaker design and technology, a similar PWR design, the water-cooled, water-moderated power reactor (WWER), was developed.

Typical PWR reactor thermal-hydraulic parameters are provided in Table 13 [APR2011, POP2014]. To ensure efficient energy conversion from the reactor core to the steam turbine, the primary coolant pressure is typically 10–15 MPa and the primary coolant temperature 290°C–330°C, whereas the secondary loop pressure is typically 5–7 MPa.

In the PWR reactor design, ordinary light water is used both as coolant and moderator. A simplified reactor flow diagram is shown in Figure 149. The reactor coolant loops include primary, secondary, and tertiary loops. In the primary coolant loop, the coolant picks up the heat produced in the core and leaves the reactor at a temperature that is sufficient to generate steam in the steam generator. Then the coolant is returned to the reactor core by means of pumps. In the secondary loop, the steam generated in the steam generator expands in the steam turbine, where its energy is transferred into mechanical energy. In the tertiary loop, the exhaust steam from the turbine is condensed in the condenser, thus transferring heat to the outside heat sink.

Table 13 Typical PWR reactor parameters

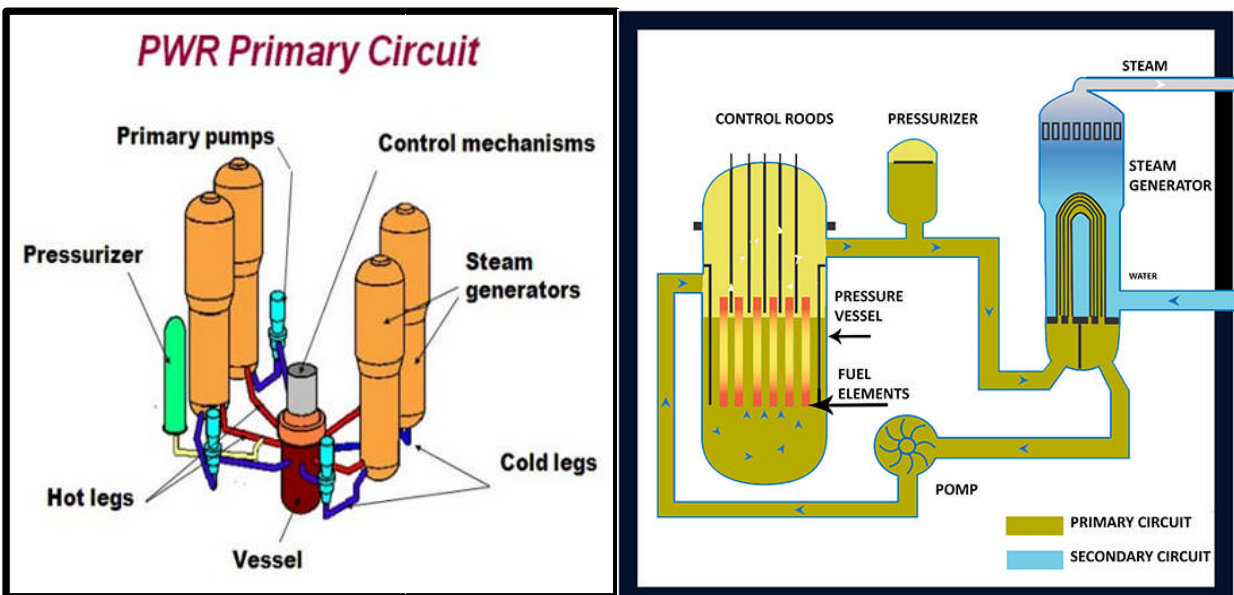
Reactor		Fuel	
Thermal output, MW _{th}	3800	Fuel pellet material	UO ₂
Electrical output, MW _e	1300	Pellet outer diameter, mm	8.19
Thermal efficiency, %	34	Rod outer diameter, mm	9.5
Specific power, kW/kg(U)	33	Zircaloy cladding thickness, mm	0.57
Power density, kW/L	102	Rods per bundle (17 x 17)	264
Ave. linear heat flux, kW/m	17.5	Bundles in core	193
Rod heat flux ave./max, MW/m ²	0.584/1.46		
Vessel		Core	
Outer diameter, m	4.4	Length, m	4.17
Height, m	13.6	Outer diameter, m	3.37
Wall thickness, m	0.22	Pressure, MPa	15.5
Steam generator		Inlet temperature, °C	292
No.	4	Outlet temperature, °C	329
Outlet pressure, MPa	6.9	Mass flow rate, kg/s	531
Outlet temperature, °C	284		
Mass flow rate, kg/s	528		

A typical PWR plant and a typical single primary coolant system loop are shown schematically in Figure 149a, and an isometric view with four primary coolant loops is shown in Figure 149b. The number of loops, usually two to four, is determined by the reactor power so that the size of the primary pumps and steam generators is reasonable and obtainable from a commercial vendor. Each primary coolant loop has one primary pump and one steam generator. All loops are

connected through the reactor vessel; one of the loops has a pressurizer connected.

13.2.2 Reactor vessel

Several typical PWR reactor vessel designs are illustrated in Figure 150 [KNI2002, KOK2009, WEI1997, TON1996, APR2011]. Figure 150a shows a quarter section view of the vessel internal structures, in which the reactor core and the fuel elements are also shown. Figure 150b shows a cross section of the reactor vessel body with the internal structures of the core and the control guide tubes above the core. Figure 150c shows an external view of the reactor vessel with a number of inlet and outlet openings for connection to the inlet and outlet piping. The reactor pressure vessel height and diameter depend on the design and the thermal power produced, with a typical height of about 12–14 m and a diameter of 5–7 m. The vessel is constructed of forged low-alloy carbon steel with a wall thickness of 20–25 cm (depending on coolant conditions) and an approximately 3-mm stainless-steel cladding on the inner surface to increase robustness to water corrosion and erosion.



a) PWR four-loop primary system

b) PWR primary coolant loop cross section

Figure 149 PWR primary reactor cooling system

As shown in Figure 149a, the nuclear reactor core and fuel assemblies are located in the reactor pressure vessel. The water coolant at high pressure (~ 14 MPa) is circulated by external pumps into the reactor vessel, flows upwards through the fuel assemblies, out of the vessel to heat exchangers, and from the heat exchangers back to the pumps. The water temperature at the exit of the reactor core is lower than the saturation temperature, i.e., the water is sub-cooled, which has an important impact on reactor thermal-hydraulic margins, as will be explained in later sections of this chapter.

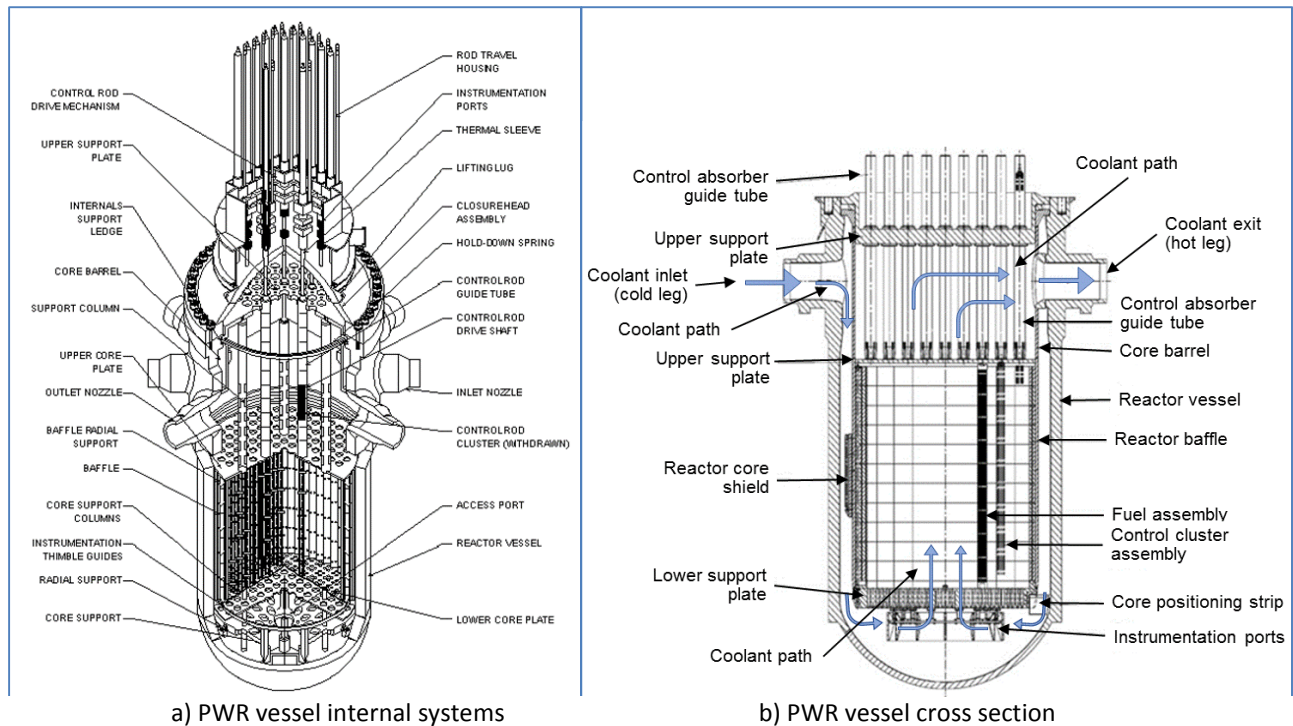


Figure 150 Typical PWR reactor vessel

Figure 150a and Figure 150b show the internal structures of a typical PWR vessel. The reactor core is located in the lower part of the reactor vessel and is surrounded by a cylindrical inner vessel called the core barrel. On the inner side of the core barrel, the fuel bundles are surrounded by a multi-faced shroud that constrains flow in the radial direction. The bottom of the core barrel has radial sliding pins that give the barrel freedom to accommodate thermal expansion, but do not allow barrel rotation. Around the outside of the core barrel is a metal jacket called the thermal shield (approximately one-third of the core length, situated around the core centre). The role of these thermal shrouds is to absorb core neutron radiation in the radial direction, preventing excessive radiation impact on the reactor vessel and thus reducing radiation aging effects on the vessel.

The top and bottom of the reactor core are supported by the upper core plate and the lower support plate. Both plates support the fuel assemblies in appropriate positions in the core. The reactor control elements and safety shutdown rods pass through the guide tubes that penetrate the upper core plate. The reactor instrumentation typically (in older designs) passes through the lower part of the reactor vessel and penetrates the core through the lower support plate.

The reactor coolant enters the vessel through the inlet pipes (the so-called “cold legs” shown in Figure 149a), then turn downwards in the so-called reactor downcomer and along the outside of the reactor barrel and inside the reactor vessel, thus coming down to the reactor lower plenum. There, the coolant turns upwards, flows through the lower support plate, and enters the core from the bottom. The coolant flows through the core upward and exits in the reactor upper plenum. From there, the coolant flow exits the vessel through the exit pipes (the “hot legs”). The upward flow in the core provides good conditions for thermo-siphoning should primary

pump flow be lost in certain design basis accidents.

13.2.3 Steam generators

Steam generators transfer the heat generated by the reactor in the primary loop to the secondary loop, where the steam turbine transfers the thermal energy into mechanical energy, which in the electric generator is further transferred into electrical energy. Therefore, steam generators are an important part of the heat transfer path connecting the two loops.

Figure 7 shows a typical vertical U-tube steam generator (some PWRs use once-through vertical steam generators, and the Russian WWER design uses horizontal double U-tube steam generators). A typical vertical steam generator is typically 21 m high and 4.5 m wide in the upper portion. Primary coolant enters the steam generator at the bottom inlet chamber and flows upward through the support plate into a U-shaped bundle of small-diameter tubes. Then it flows back down to the outlet chamber at the bottom of the steam generator. Thus, the outside surface of the U-tubes in the steam generators transfers heat from the primary to the secondary side.

On the secondary side of the steam generators, water boils, producing saturated steam that drives the turbine. This steam is generated in the steam generator at ~5–7 MPa depending on the station design. The feedwater coming into the steam generator secondary loop enters at the side, at the bottom above the support plate. It passes through the pre-heater region, where it is heated to saturation temperature and then boils, passes through two sets of steam dryers, and exits the upper plenum, which is located at the top of the steam generator.

The design of the steam generators is similar between the CANDU and the PWR designs. However, some PWR steam generator designs do not have a pre-heater designed at the feedwater entrance to the steam generator secondary side.

13.2.4 Primary pumps

Figure 9 presents a view of a typical PWR primary pump [KNI2002, KOK2009, WEI1997, TON1996, APR2011]. It contains a single-stage impeller and an impeller casing. This is the most important part of the pump because it provides the driving force for the primary flow. Above the impeller casing, the rest of the pump consists of a number of pump seals to insulate the primary flow, a flywheel set to provide inertia for the pump to continue operating for some time after power is lost, and an electric pump motor.

The primary pumps are a vital component in the reactor heat transport system because they drive the coolant flow by forced circulation through the primary heat transport system. Hence, they are essential to fulfill the primary function of the reactor cooling system, to provide continuous cooling of the reactor core in normal operation, during transients, and during reactor shutdown. The pump start-up and shut-down sequences are routine operations of the reactor heat transport system.

Pump failures, whether due to loss of power or inadvertent operator action, are events that must be considered explicitly in the reactor design. The reactor primary cooling system is designed to allow and enhance natural circulation in the absence of pump flow. This is achieved

by placing the reactor core (heat source) at the lowest point in the primary loop and the pumps and steam generators (heat sinks) at the highest point in the primary loop.

The design of the primary pump is similar between CANDU and PWR reactors.

13.2.5 Pressurizer

The pressure in the reactor primary coolant system is maintained at a certain level by a pressurizer. Figure 8 shows a view of a typical pressurizer.

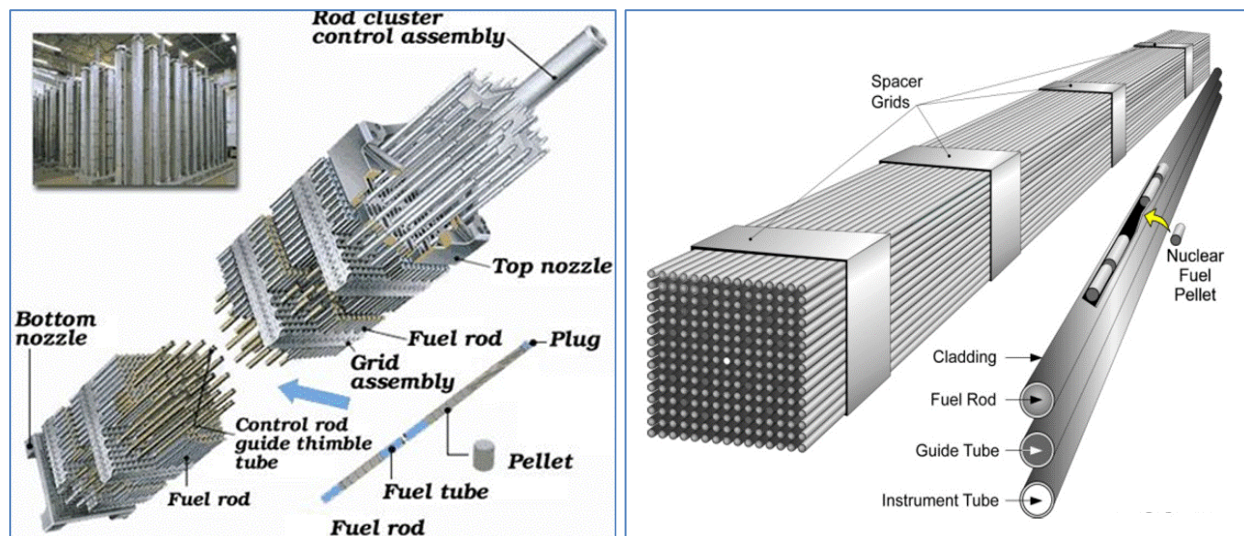
13.2.6 Reactor refuelling and reactivity control

The fuel is in the form of assemblies (or bundles) of enriched UO_2 rods, clad in zirconium alloy (or in some earlier designs, in austenitic stainless steel). As shown in Figure 151, these fuel assemblies are square or hexagonal in shape (depending on the reactor type) and contain an array of fuel rods within each assembly. The fuel assemblies are arranged in a tightly packed lattice configuration, with either square or triangular pitch (depending on the reactor type). Typically, reactors designed by GE-Westinghouse use a square fuel assembly and square lattice pitch, whereas the Russian-designed WWERs use a hexagonal fuel assembly arranged in a triangular pitch.

The fuel assemblies have an open lattice, which enables radial cross flow of the cooling water, i.e., mixing of coolant between adjacent fuel assemblies. The coolant does not boil in the core because its temperature at the core exit is still below saturation.

To refuel a PWR reactor, it must be shut down and the primary loop cooled and depressurized. Several days after reactor shutdown, the decay heat load of the primary loop decreases sufficiently to enable reactor depressurization and the start of refuelling operations. Following cooling and depressurization, the reactor pit (or reactor bunker) is filled with water to at least a 10-m height above the reactor head to provide adequate radiation shielding for the refuelling personnel working at the top of the reactor pit. Then the reactor head is opened and removed, enabling access to the reactor core. The fuel assemblies are individually manipulated underwater, repositioned in the core, fresh fuel assemblies brought into the core, and some irradiated assemblies removed from the core. Typically, the fresh fuel assemblies and irradiated fuel assemblies are positioned and reshuffled in the core in a predetermined sequence. The refuelling crew typically uses computer programs to ensure optimal fuel bundle distribution and to monitor fuel bundle histories in the core.

The irradiated fuel bundles that are removed from the core are transported underwater to the irradiated fuel bay for storage and cooling for a number of years. Removing the fuel from the irradiated fuel bays depends on the national policies of specific jurisdictions for handling highly radioactive irradiated fuel or subjecting it to reprocessing.



a) Typical fuel assembly structure

b) Typical fuel assembly view

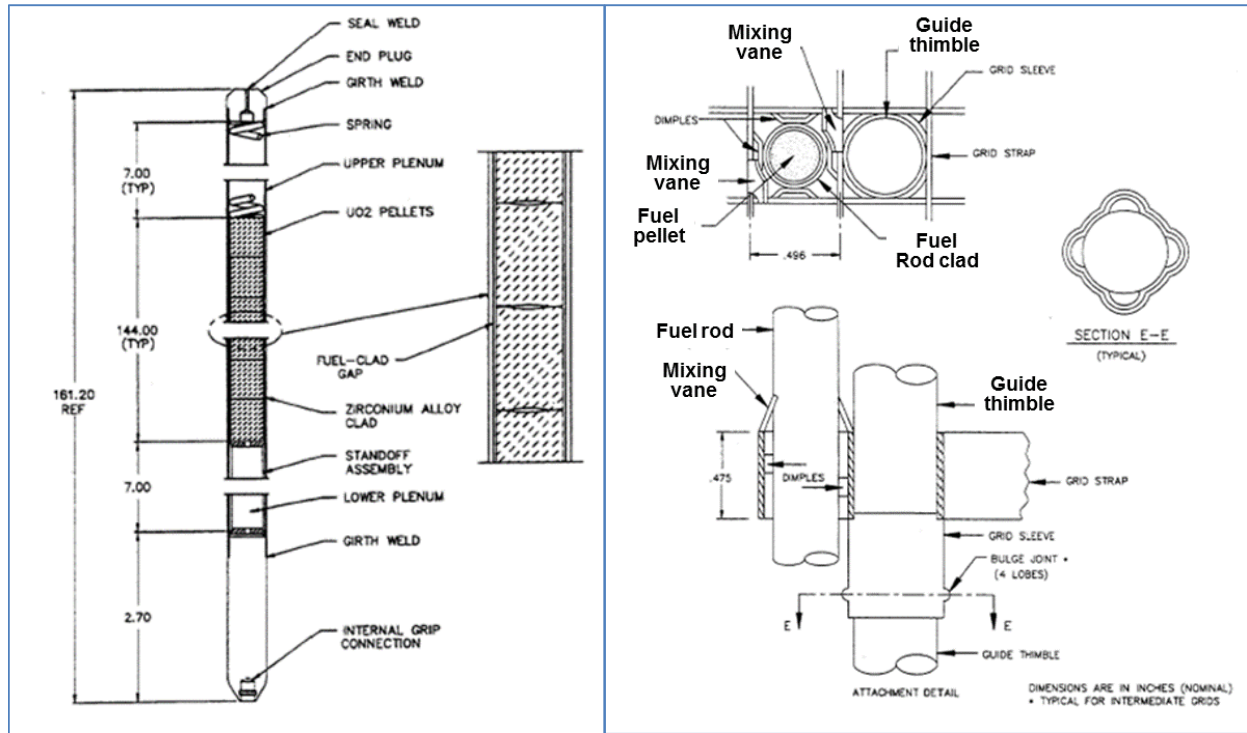
Figure 151 Typical PWR square fuel assembly design

Refuelling is normally done on an 18–24 month basis and typically takes 4–5 days. However, refuelling outages in PWRs can last up to one month or sometimes longer when the preparations, cooldown, maintenance activities, and return to full power are taken into account. To operate for long periods without refuelling, the new fuel is enriched in ^{235}U (up to a maximum of 5%). When the fuel is fresh, the excess reactivity in the reactor core is compensated for by a neutron poison dissolved in the coolant/moderator water and by other devices. As the fuel burns up, the dissolved poison in the coolant/moderator is gradually removed by ion-exchange columns.

Reactivity control in a PWR reactor is performed by full-length control rods. Levelling neutron flux and heat generation in the core is performed by various control rod banks of full or partial length, and by other means in newer PWR designs (i.e., burnable absorber material in fuel and in “grey” control rods). Intermediate- and long-term reactivity control in the core is achieved by soluble poison (called “chemical shim”); typically, boric acid is used for this purpose. The critical soluble boron concentration is reduced in the core with core burn-up, i.e., with buildup of ^{135}Xe and ^{149}Sm . Therefore, during the initial burn-up of a few hundred MWd/t, the boron concentration is reduced sharply by up to 40%, followed later by a more gradual reduction to compensate for fuel burn-up and generation of fission products in the fuel.

13.2.7 Fuel assembly and fuel pin design

Figure 151 shows a typical PWR fuel assembly design [KNI2002, KOK2009, WEI1997, TON1996, APR2011]. As shown in Figure 151a, the fuel assembly typically consists of fuel pins (also called fuel rods or fuel elements) arranged in a square pitch with a certain number of grid plates (spacers) that hold the fuel pins in position and constrain them in the radial direction. Other than by the support plates, the PWR fuel bundle does not restrict the coolant flow in the radial direction because there is no flow tube around the bundle. Therefore, all fuel pins in the core create a continuous matrix of fuel pins throughout the core.



a) Typical fuel rod design

b) Typical fuel rod grid design

Figure 152 Typical PWR fuel design

The guide tubes shown in Figure 151a are provided for each fuel assembly. They are intended to receive the control rods (shown in Figure 151a) from the top as a cluster control assembly with a certain number of control rods. Fuel assemblies that do not have control assemblies are plugged from the top by a special plugging device to prevent coolant bypass through them (they have a larger hydraulic diameter than the rest of the fuel matrix).

The top and bottom nozzles are welded with the guide tubes and create a rigid fuel assembly structure. The fuel pins pass through the grid plates, but are not welded to the grid plates to allow for unrestricted thermal expansion. The bottom nozzle contains four openings at the four support legs, which fit into the reactor core bottom plate, and which deliver coolant to the fuel assembly.

Figure 152 shows the fuel pin design [POP2014]. The fuel pin design is similar for the LWR and CANDU designs. In fact, all LWRs and CANDUs, regardless of the manufacturer and country of origin, have a similar fuel pin design.

The fuel pin consists of a Zircaloy tube into which fuel pellets are inserted. The tube is then filled with gas and sealed. The fuel pellets have a height-to-diameter ratio of about 1.5 and have dished surfaces on both ends, which help to align them properly in the vertical direction, accommodate fuel swelling, and collect gases generated during fission. Numerous fuel pellets are located in each fuel pin and form a vertical fuel pellet stack within the pin. At the top end of the fuel pin, the fuel pellets are held tightly in a vertical direction by a spring that is installed and sealed in the tube.

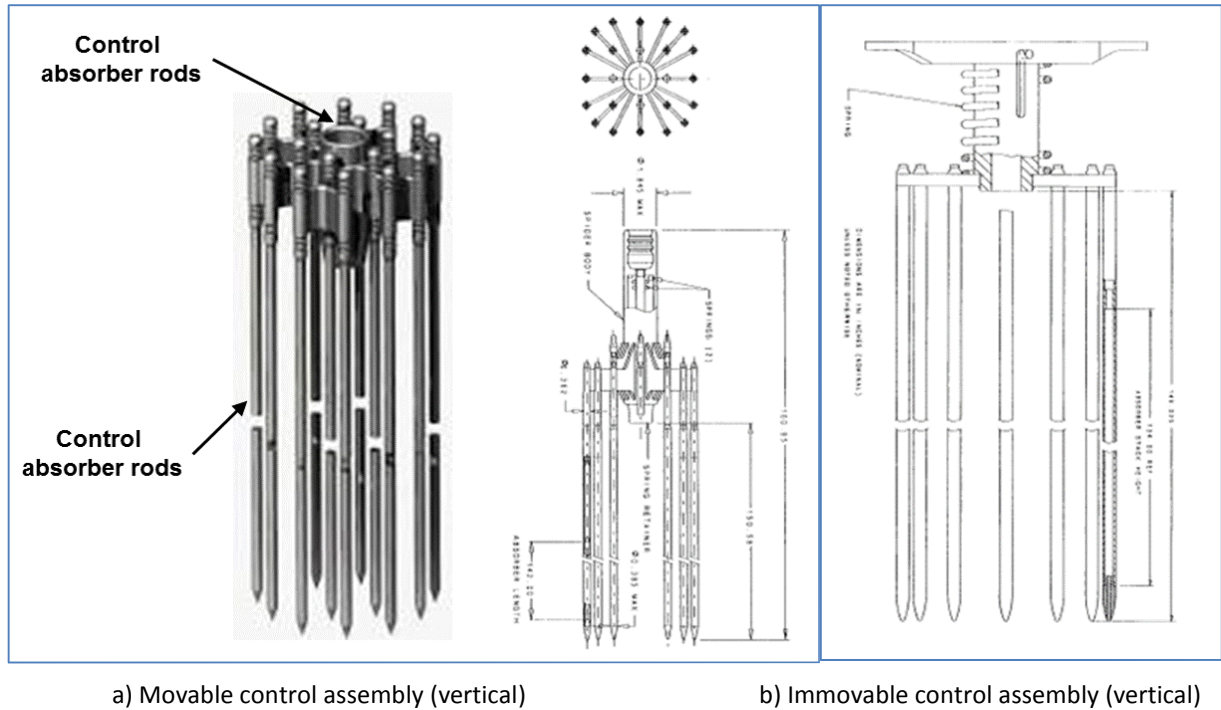


Figure 155 Typical PWR control assembly (cluster) design

Figure 156 shows a typical PWR control rod design [POP2014]. The control rods are of various design and material composition depending on their role in the reactor core. The control rods that are part of the reactor control system are filled with neutron-absorbing material along their full length in the core (usually a mix of 80% silver, 15% indium, and 5% cadmium, which is the material with the largest neutron-absorption capability used in modern reactors). The immovable control rods (Figure 156a) can be filled over their full length or partially filled at the top, bottom, or middle. They can also be filled with neutron-absorbing material of various thicknesses in the annulus (Figure 156a). The immovable control rods are filled with a mix of neutron-absorbing material that reduces absorption capability by neutron capture (diminishing absorption potential per unit volume with radiation exposure), or by materials that retain absorption capability over several control isotope generations.

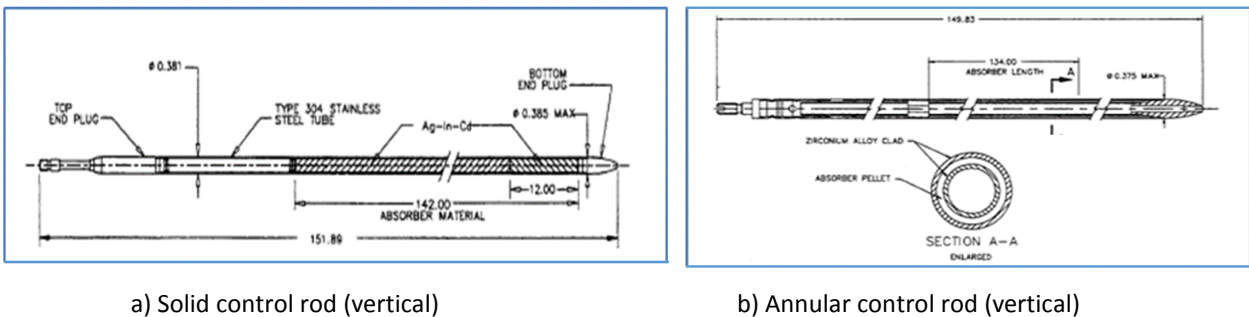


Figure 156 Typical PWR control-rod design

PWR control-rod guide tubes penetrate through the reactor pressure vessel head and hold each

control assembly cluster in place. The control assemblies are driven in and out of the core by control-rod drive devices that are located outside the reactor vessel. The control-rod shaft is located in the guide tubes that extend through the reactor cap, in the space above the core, and holds the control-rod top. Special attention is devoted to the seals of the control-rod guide tubes and assemblies because they are located in the vessel at a pressure of 15 MPa, whereas their shafts and guide tubes are at atmospheric pressure. Because of the large pressure difference between the inside of the vessel and the atmosphere outside of the reactor vessel, special attention is devoted to preventing control-rod ejection from the vessel, which can create a severe large positive reactivity insertion.

13.2.8 Reactor core design

The fuel assemblies in the reactor core are typically 3.6–4.2 m long and have from 14 x 14 to 19 x 19 fuel rod positions. There are typically 120–170 fuel assemblies in the core, depending on the reactor thermal power and reactor type, arranged in a square or hexagonal lattice in the core. The fuel assemblies are enveloped by a metal shroud which follows the core shape at the sides of the peripheral assemblies (see Figure 150a). The metal shroud does not permit fluid movement in the radial direction, but fluid movement in the radial direction is not restricted by the fuel assemblies themselves.

The core flow is in the upward direction, which in the absence of forced circulation (when the primary pumps are off) enhances the potential for natural circulation, thus removing core decay heat.

13.2.9 WWER reactor design

The WWER reactors are of Russian design, and their design follows in principle the original U.S. PWR design [KNI2002, KOK2009,. Figure 157a shows an isometric view of the primary cooling loop and the reactor vessel. The primary cooling system is similar to the PWR primary cooling system, with three or four primary loops depending on reactor power. There are some differences in the fuel assembly design, the most significant being that it is not open in the radial direction because it is surrounded by guide tubes. Figure 157b shows a reactor vessel similar to the American PWR vessel design. Figure 157c shows a WWER steam generator of horizontal design and containing double horizontal U-tube assemblies on the primary side connected at the middle of the steam generator. In addition, steam is collected at the top of the steam generator in a separate steam collector tube.

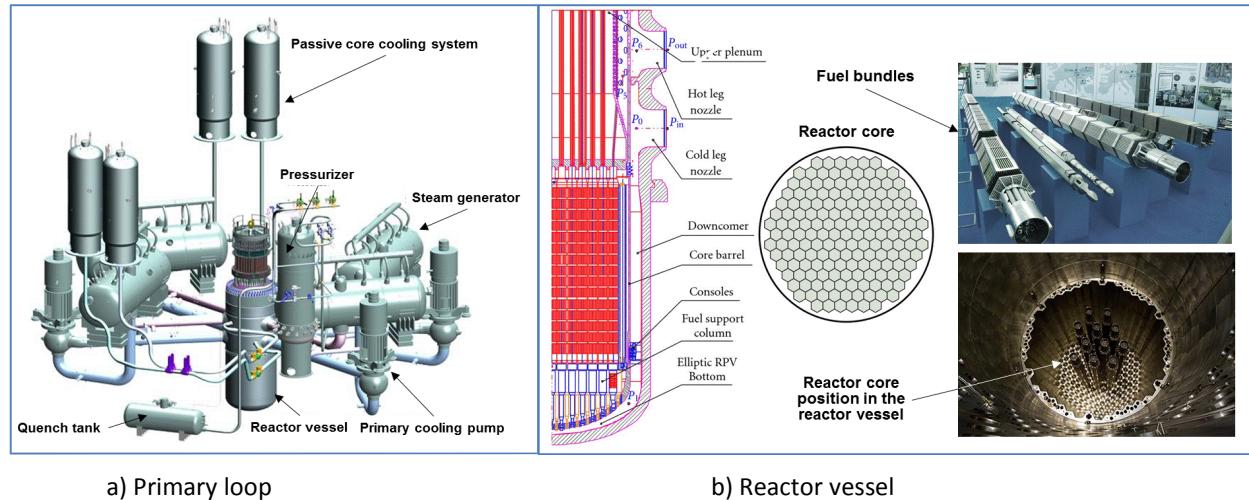


Figure 157 Russian WWWR reactor design

13.3 Boiling water reactors

Boiling water reactors (BWRs) also originate from the U.S. nuclear industry, but unlike PWRs, they are designed to allow coolant boiling in the reactor vessel, and hence they do not have a separate heat exchanger (steam generator) for steam production. There are numerous BWRs in operation around the world, although fewer than the PWR designs. BWRs feature a lower primary heat transport system pressure than PWRs for the same power output, which results in decreased thickness of the reactor pressure vessel (which amounts to an economic benefit). Figure 158 shows two BWR reactor versions, BWR/4 and BWR/6 [KNI2002, KOK2009, LAH1977, POP2014].

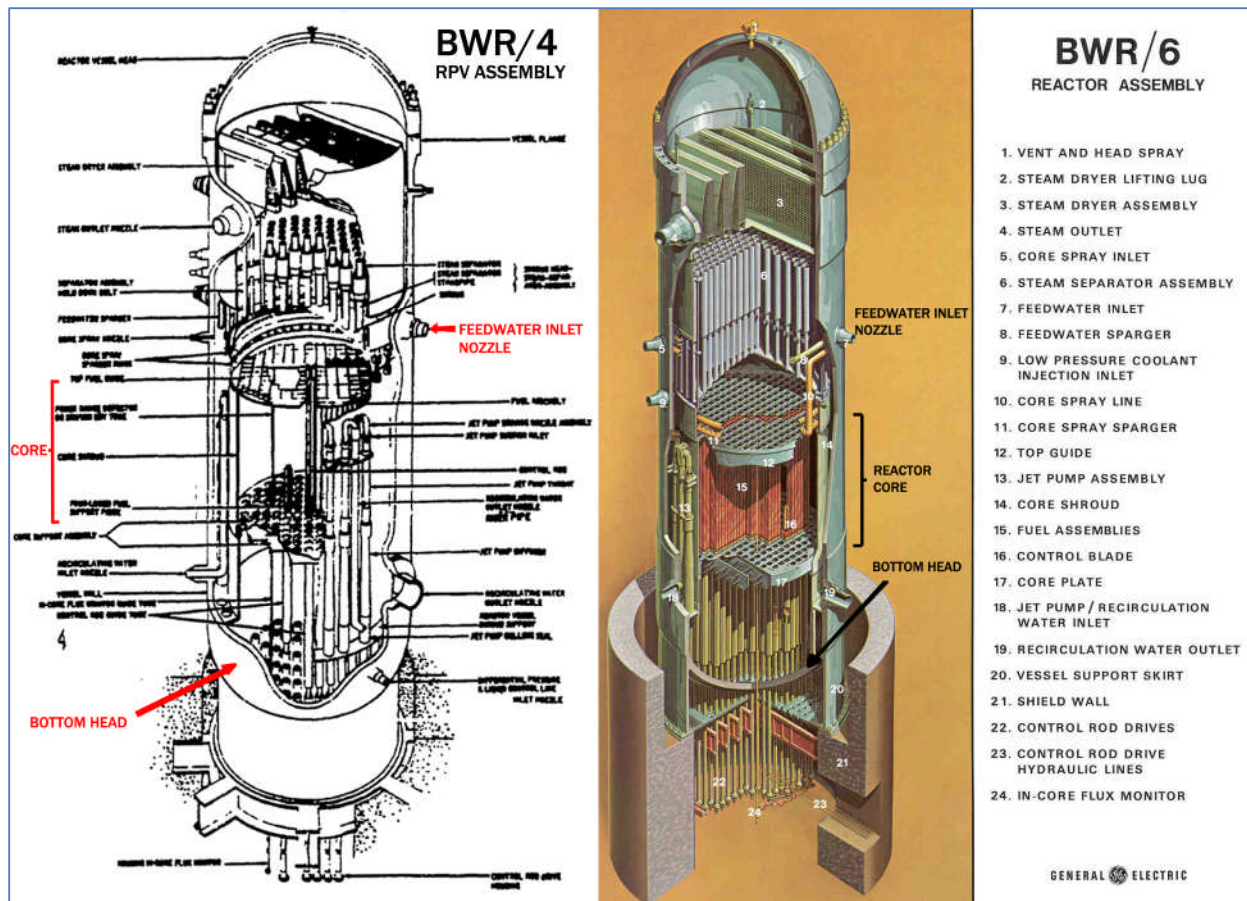


Figure 158 BWR reactor design

BWR plants have been designed in two main design streams: direct-cycle and dual-cycle. In a direct-cycle plant, which is the most common in operation, steam is produced in the steam generator and is moved to the turbine generator as dry steam. In a dual-cycle plant, in addition to steam production in the reactor, steam is also produced in a secondary steam generator fed by saturated water from the moisture separator.

Figure 159 shows a simplified flow diagram of a direct-cycle BWR system [LAH1977]. The direct cycle has the advantages of lower capital cost and simplicity, which increases system reliability. There is no separate steam generator in the cooling system because the reactor generates steam. Older BWR designs could not follow the load, but are to a certain extent self-controlling due to the negative void reactivity. Modern BWR designs are capable of load following by coolant recirculation control.

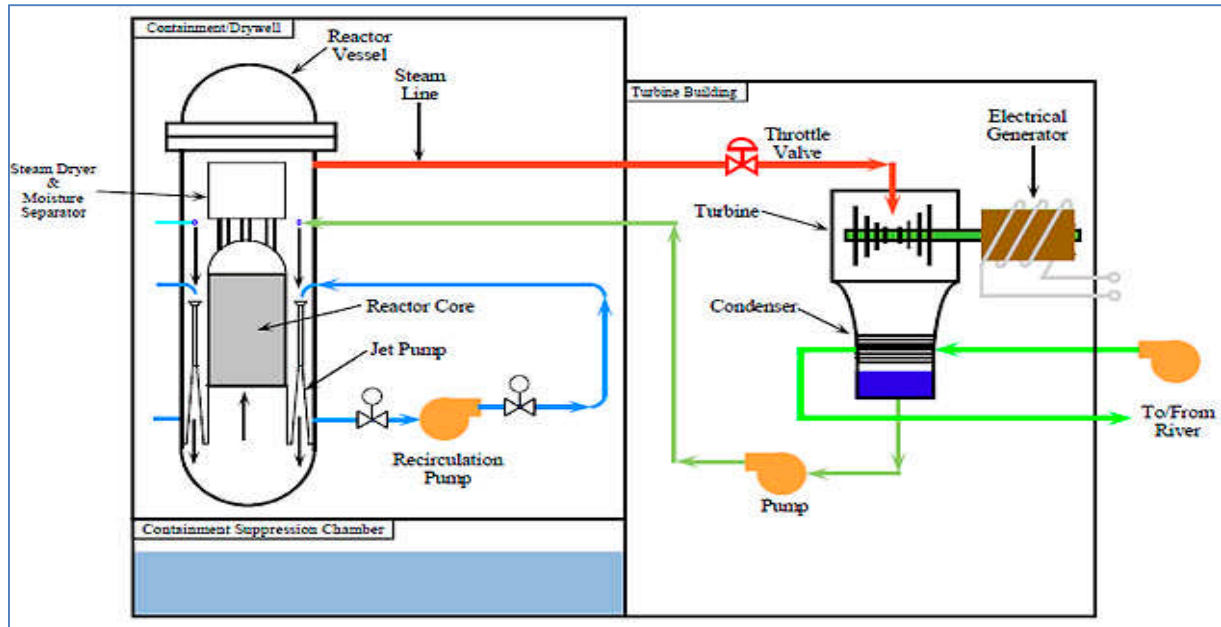


Figure 159 Typical BWR reactor vessel coolant circulation

With this arrangement, the turbine plant is “active” due to activity induced in the reactor coolant (primarily N-16). As a result, the turbine generator plant is less accessible during operation; fortunately, however, this activity decays quickly following shutdown, permitting normal direct access for maintenance.

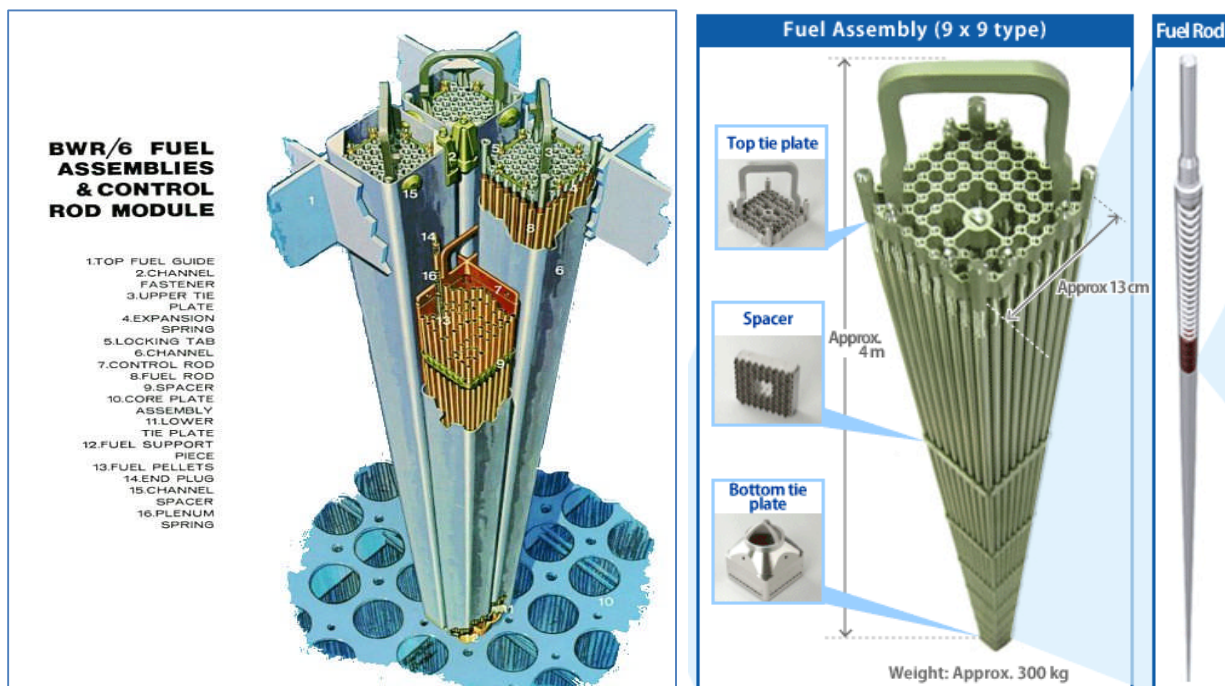


Figure 160 BWR reactor fuel assemblies in the core

The typical BWR reactor vessel, shown in Figure 158, has the steam production and collection part in the upper part of the vessel, the reactor core in the middle of the vessel, and the control

assembly and instrumentation access through the reactor bottom and the lower plenum. The reactor core has an active length of typically 3.5–4 m, similar to PWRs. The core contains between 500 and 800 fuel assemblies, each containing arrays of fuel rods with a similar design to those in PWRs.

Figure 159 shows the coolant circulation in the BWR core. The recirculation system consists of recirculation pump loops located on the sides of the reactor vessel. In the BWR design illustrated, the reactor vessel downcomer jet internal pumps are located on the outer core periphery, arranged in pairs, with each having a common inlet riser. The driving flow from the external pumps passes through the jet pump nozzles and acquires high velocity and momentum. The momentum exchange entrains the recirculation flow, usually called suction flow. The combination of the external pump-driven flow and the suction flow enters the throat of the jet pump, thus ensuring adequate flow through the core. The jet pump design has the advantages of fewer moving parts, higher reliability, and robustness in accident situations. The feedwater inlet is in the upper part of the core, and the coolant falls down by gravity towards the inlet of the jet pumps.

BWR fuel assemblies are typically of square design (see the left part of Figure 160), but the fuel rods are situated in a square flow tube which does not allow flow mixing in the radial direction (see the right part of Figure 160) [KNI2002, KOK2009]. Because the BWR reactor is designed to operate with saturated water that boils in the core, a good level of turbulence is already achieved, and therefore there is no need to promote radial mixing to enhance turbulence, as in the PWR design. The left side of Figure 160 shows a BWR fuel assembly with a square tube and the spacer grids inside holding the fuel pins.

Figure 161 shows a cross section of four fuel assemblies, on the left 10 x 10, and on the right 7 x 7 fuel rod arrays [KNI2002, KOK2009, LAH1977, POP2014]. The cruciform control assembly is located between the fuel bundles. Clearly, between the fuel assemblies, a gap is maintained for the control assembly to move in a vertical direction through the core.

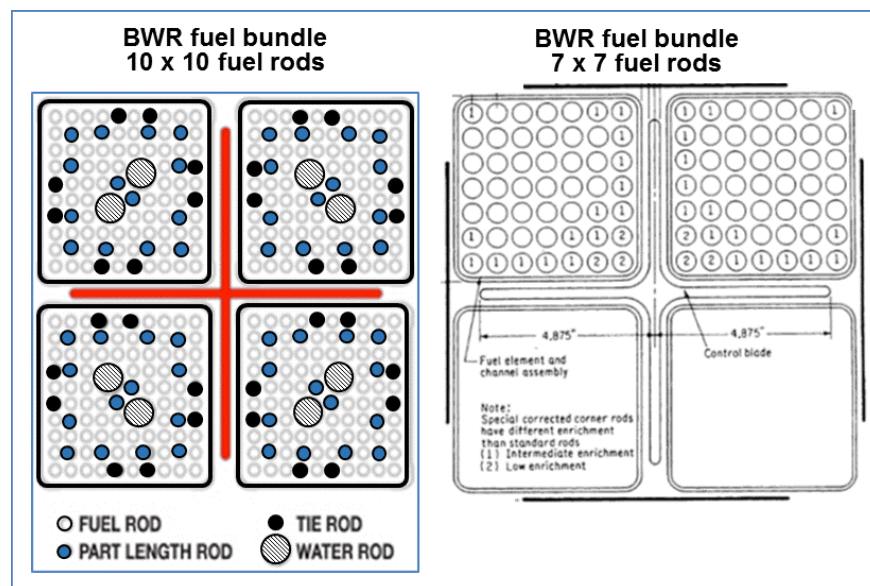


Figure 161 BWR fuel and control assemblies

The control assembly is moved through the core from the bottom of the reactor. Therefore, the control assembly holding the plate and drive mechanisms is at the bottom of the core and needs to work against gravity.

13.4 Gas-cooled reactors

Gas-cooled reactors (AGRs) have been in operation for many years and were promoted by the U.K. nuclear industry due to their potential for higher thermal efficiency and relatively low stored energy in the primary coolant, which reduced containment requirements. AGRs were primarily designed and built in the United Kingdom. They use gas as the reactor coolant and natural or enriched uranium as fuel. In recent years, some of these reactors have been shut down, and others are planned for shutdown soon. The U.K. nuclear industry has abandoned this design and does not plan to use it for future reactors. This section provides a brief overview of the AGR reactor type and a brief history of its development in recent decades.

13.4.1 Magnox reactors

Magnox reactors are graphite-moderated, CO₂ gas-cooled reactors fuelled with natural uranium metal clad with a magnesium alloy called Magnox. They derived their generic name from this last feature. Figure 162 shows a schematic arrangement of one version of this reactor type [POP2014].

This type of reactor was pioneered by the British and French and was a natural outgrowth of earlier air-cooled, graphite-moderated research and plutonium production reactors. A significant number were built in Britain and France, with a few exported to other countries. Early versions used steel reactor pressure vessels with external heat exchangers (boilers) and gas circulating blowers. Later versions, as shown in Figure 163, used pre-stressed concrete pressure vessels incorporating the reactor core, heat exchangers, and coolant circulation blowers. This was primarily a cost reduction measure, although safety advantages in terms of low risk of coolant system rupture were also claimed.

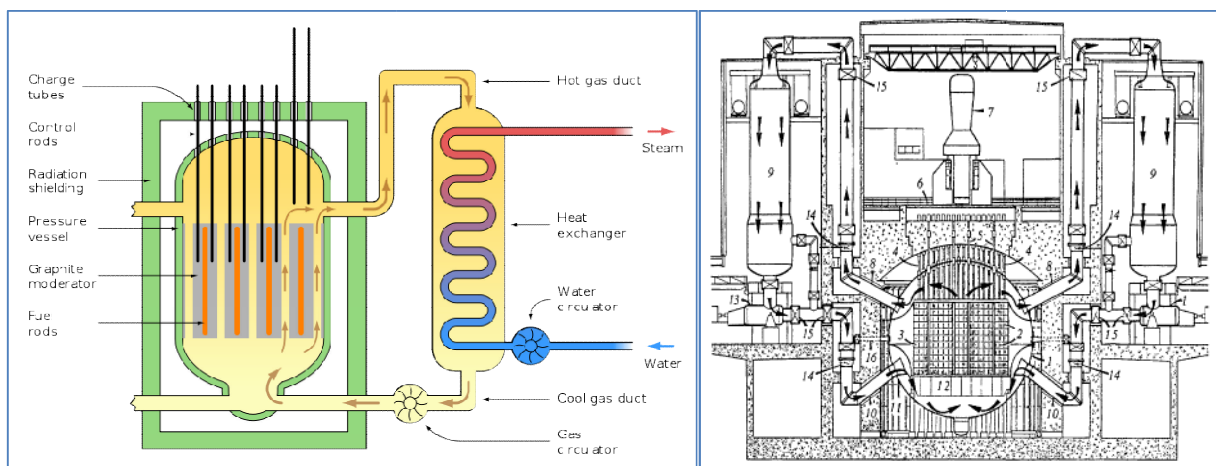


Figure 162 Typical Magnox reactor design

Primarily because of coolant temperature limitations imposed by the uranium metal fuel and the

Magnox cladding, only relatively modest turbine steam conditions are achievable, limiting the station overall efficiency to ~30%.

As is typical of all natural uranium power reactors, the Magnox reactors are fuelled on-load. This is necessary because large quantities of excess reactivity, in the form of additional U-235, are not “built into” the new fuel.

The in-service availability of the Magnox reactors has proven to be relatively good. On-load refuelling helps in this regard. Nevertheless, their relatively high capital cost and relatively modest achievable fuel utilization has led to the abandonment of plans for constructing further reactors of this type. Presently, in the United Kingdom, all Magnox reactors are shut down and undergoing decommissioning.

13.4.2 AGR reactors

The AGR (advanced gas-cooled reactor) was developed in the United Kingdom as a successor to the Magnox line of reactors [POP2014]. A number of these reactors were successfully operating in the United Kingdom, but presently they are aging and require replacement. They differ from the latest Magnox reactors primarily in the fuel used. The fuel is UO_2 clad in stainless steel. This design permits higher fuel temperatures and coolant temperatures to be achieved, leading to conditions similar to those in conventional fossil-fuel steam plants (16.5 MPa, 550°C).

The fuel is designed as a cluster of small-diameter rods, which permits relatively high power levels. This reduces the size of the reactor core relative to the Magnox reactors, where the fuel is in the form of large single elements. However, because of these fuel changes, the AGR requires some fuel enrichment. Figure 163 shows a view of an AGR reactor type diagram.

The British have decided that the AGR is not fully competitive with other types of power reactors. Hence, this design, like the Magnox type, appears to be “dead-ended” and is being replaced by other reactor types, such as advanced PWRs and advanced BWRs.

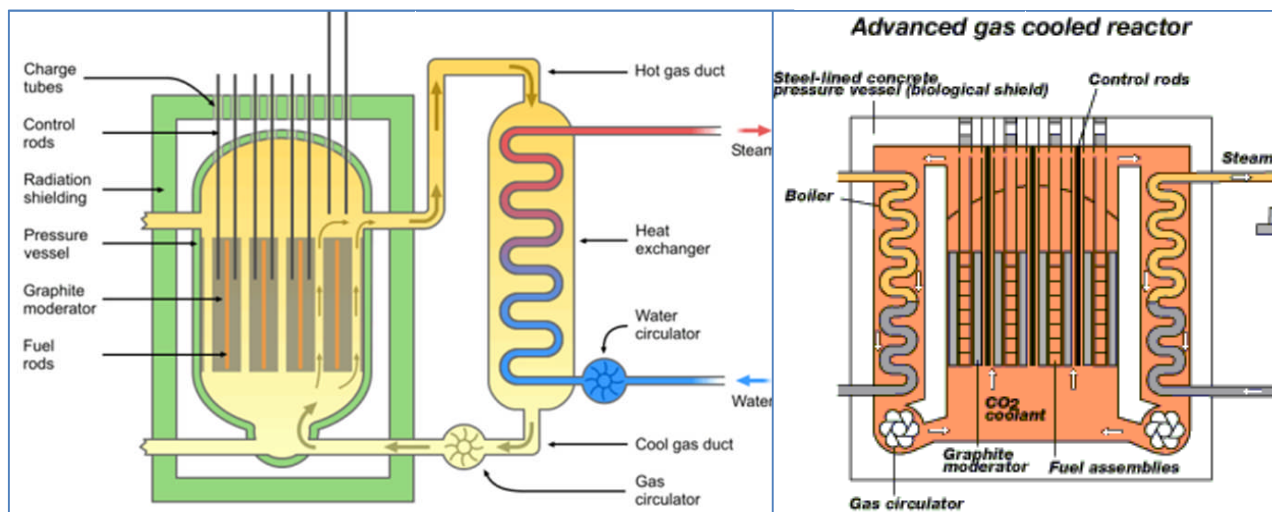


Figure 163 Typical AGR reactor design

13.4.3 HTGCR Reactors

The high temperature gas cooled reactor (HTGCR) differs from the AGR in two major respects [POP2014]. The first is the use of helium as the coolant in place of CO_2 . This permits even higher coolant temperatures without inducing a chemical reaction with the graphite moderator. The second relates to the fuel. In very early designs, the fuel was supposed to be fully enriched (93%) U-235 mixed with thorium. Thorium absorbs neutrons and is converted, after a radioactive decay chain, to U-233, which is fissile. As a result, the reactivity of the fuel remains high even after very long irradiation, the U-233 replacing the U-235 as the latter is burned up. The fuel is in the form of mixed carbides. It is manufactured in very small spheres which are coated with pyrolytic graphite, the latter providing the cladding. These spheres are compacted into holes in large graphite assemblies, forming an integral fuel and moderator assembly.

Figure 164 shows an advanced version of the HTGCR reactor design currently being developed as part of the Generation IV development efforts. The very high coolant temperatures achievable lead to high steam cycle efficiencies, or alternatively make possible the ultimate use of gas turbines directly driven by the coolant. The development of the direct-cycle gas turbine version would be particularly attractive in this regard.

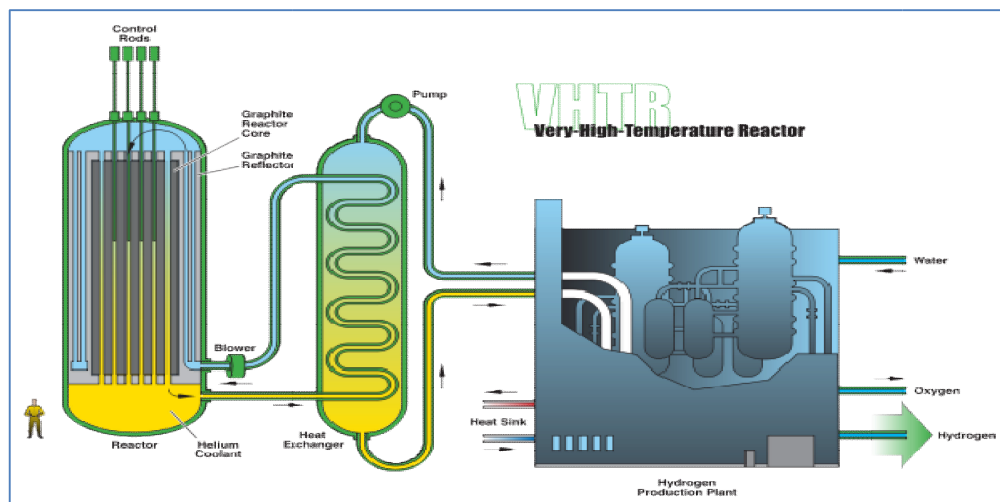


Figure 164 Typical HTGCR reactor design

13.5 Channel-type reactors

13.5.1 SGHWR reactor

The steam generating heavy water reactor (SGHWR) has been developed and operated in the United Kingdom, Japan, and Italy for a number of years. The best example of this reactor type that operated successfully in Japan for more than 20 years is the Fugen reactor (currently decommissioned) [POP2014].

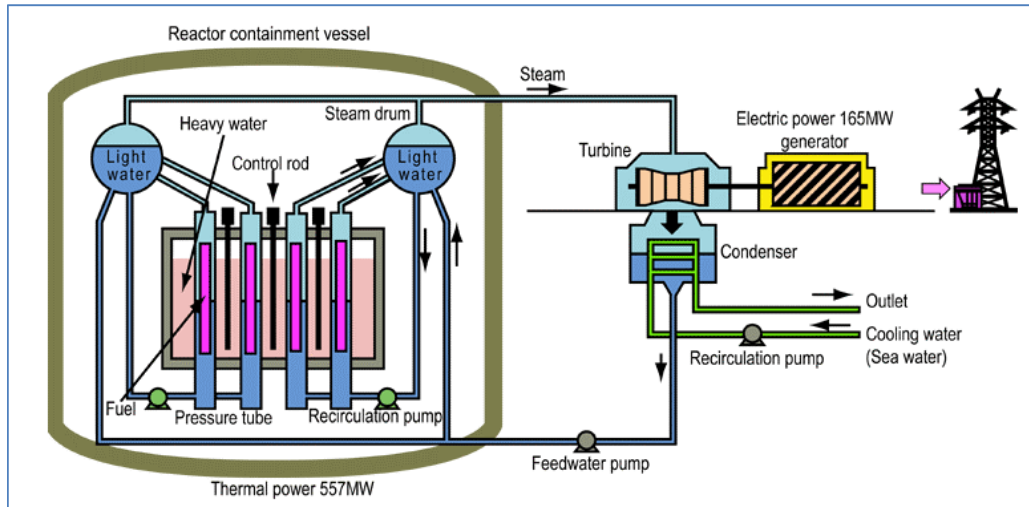


Figure 165 SGHWR reactor

Figure 165 shows a schematic of this reactor type. The heat transport system contains vertical pressure tubes, light water coolant, heavy water moderator in a calandria vessel, and recirculating pumps used to return water from steam drums to the lower end of pressure tubes. The fuel was low-enriched uranium with on-power refuelling. The reactor heat transport system was located in a containment building, thus providing protection during accidents.

Another type of SGHWR design was the CANDU Gentilly-1 reactor, which was shut down and is now decommissioned. It also used vertical pressure tubes with natural uranium, heavy water moderator, and light water coolant.

13.5.2 CANDU reactor

The CANDU fuel channel type reactors have been developed in Canada, have achieved great commercial success around the world, and are being still developed and prepared for new builds in Canada and internationally. Figure 2 shows the CANDU reactor cooling systems and Figure 3 the reactor heat transport system and moderator cooling system.

13.5.3 RBMK reactor

The Russian version of the channel reactor is the RBMK reactor (an acronym for High Power Channel Type Reactor in Russian) [POP2014]. This reactor design was built in Russia and in neighbouring states in the 1980s and 1990s. The RBMK reactors had two basic power levels, one around 1000 MWe, the other around 1400 MWe.

Following the Chernobyl accident, many of these reactors were shut down, and they continue to be shut down, with the exception of a few, such as the Kursk and Leningrad reactors that will continue to operate until the early 2020s. The RBMK design was abandoned by the Russian nuclear industry after the Chernobyl accident. However, many design changes have been implemented in the operating units to improve their safety during their remaining operational life.

Figure 166 shows the reactor cooling systems (primary, secondary, and tertiary), a view of the

reactor core, and a cross section of a RBMK plant. The reactor core is very large (21.6 x 21.6 x 25.5 m). The vessel contains the graphite stack filled with a helium-nitrogen mixture to ensure an inert atmosphere. The reactor fuel is UO_2 with a fuel rod design similar to the LWR design, with 2%–4% enrichment in U-235. Refuelling is performed on-power to achieve a better balance of neutron flux and core utilization and to optimize production of Pu-239.

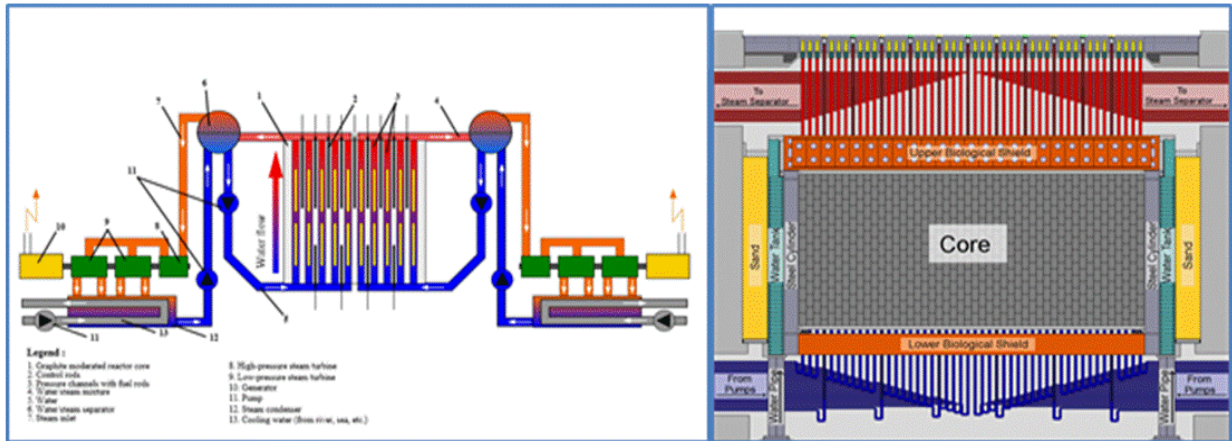


Figure 166 RBMK reactor design

The reactor has two independent cooling circuits, each with four primary circulation pumps (including one stand-by). The cooling water is fed to the reactor through lower water lines to a common header, which is split into 22 distribution headers, each feeding 38–41 fuel channels, in which water boils. The mixture of water and steam is conveyed by the upper steam lines, one for each fuel channel, from the reactor top to the steam separators. Steam with 15% quality is taken from the separators by two steam collectors per separator, combined, and then conveyed to the turbine hall. The nominal total flow through the core is $\sim 46,000\text{--}48,000\text{ m}^3/\text{h}$. The nominal temperature of the water at the inlet of the reactor is about 270°C and the outlet temperature 284°C , at a pressure of 6.9 MPa.

The fuel channels consist of Zircaloy pressure tubes that pass through the channels in the centre of the graphite blocks. There are 1661 fuel channels in the core and 211 control channels. There is only a small clearance between each pressure channel and a graphite block, which makes the design vulnerable to damage. If a pressure tube channel deforms due to high internal pressure in an accident situation, the deformation can cause significant pressure straining of the graphite blocks and lead to damage, which can then possibly propagate to neighbouring channels.

Light water was used as coolant and graphite as moderator. This combination of core materials leads to a highly positive void coefficient, which results in high power excursions in the case of a loss of coolant accident.

Because of certain similarities to the CANDU design, and because of the unpopular experience with the RBMK reactors, CANDU has often been criticized as potentially vulnerable in the same way as the RBMK reactors. As described in Chapter 16, many studies have been performed since the Chernobyl accident and have demonstrated that CANDU has different physical

characteristics that make the CANDU design behave quite differently from the RBMK reactors, and that therefore CANDU reactors are not as vulnerable in accidents as RBMK reactors.

13.6 Fast breeder reactors

Liquid metal fast breeder reactors (LMFBRs) were designed many years ago, and some were built as prototype versions in the United States, France, and Russia, and later by other countries as part of pilot programs. These pilot-prototype versions had varying degrees of operational success, and therefore many were shut down or restarted over the past several decades. These reactors use a fast neutron spectrum to maintain the fission chain reaction and are cooled by molten metal coolants. Figure 167 shows the design sketch of a typical pool-type (left) and a loop-type fast breeder reactor [POP2014].

Whereas all the reactors previously described are of the thermal type, i.e., the fissions in the fuel are primarily induced by thermal neutrons, it is also possible to sustain a chain reaction with high-energy neutrons, i.e., fission neutrons, provided that the fuel is highly enriched with fissile material such as U-235 or Pu-239. Furthermore, on average, more than two neutrons are born per fission. One of these neutrons is required to induce the next fission, leaving a surplus of somewhat more than one neutron which can be absorbed by a “fertile” material such as U-238, producing fissile Pu-239. It is therefore possible to produce fissile material as rapidly as it is used up; this is called “breeding”. In fact, it is possible to produce more fissile material than is used because the average number of neutrons produced per fission is greater than 2. The excess is referred to as the “breeding gain”. This can be achieved only if the neutron economy is high, i.e., if relatively few neutrons are wasted.

This possibility of breeding is a very attractive means of extending the power available from uranium because less than 1% of natural uranium is fissile. If a substantial part of the other ~99% could be converted to fissile Pu-239 as a by-product of reactor operation, then the world’s uranium reserves could be stretched enormously. The fast breeder reactor is one way of doing this, which explains the widespread interest in this concept.

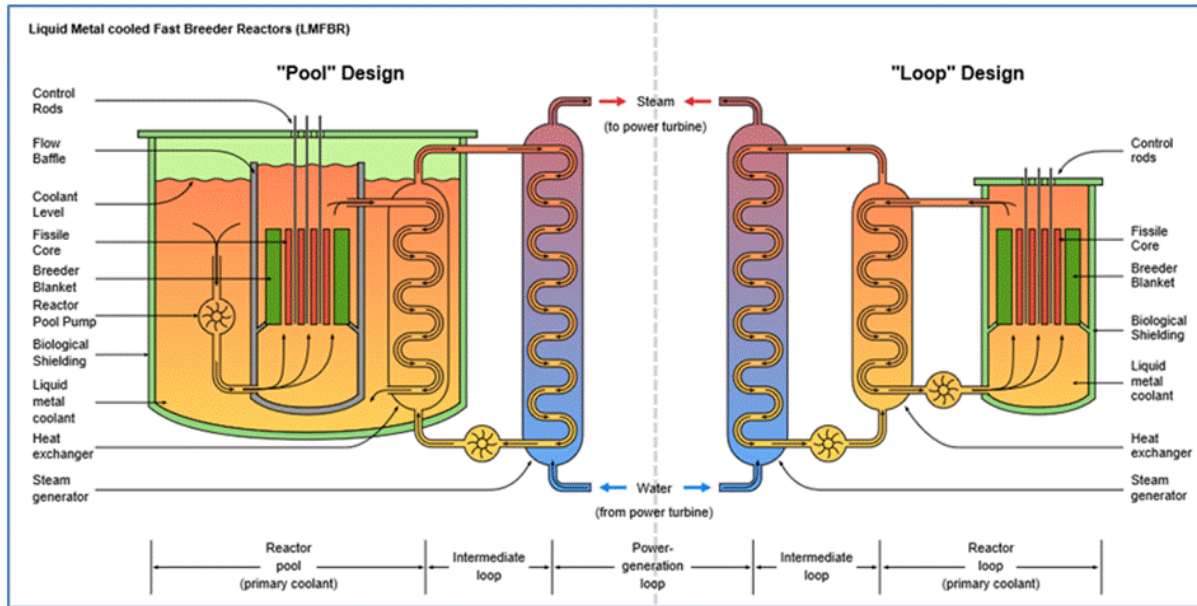


Figure 167 Fast reactor design

The basic arrangement of a liquid metal-cooled fast breeder reactor is shown in Figure 167. The reactor core consists of a closely packed array of highly enriched (U-235 or Pu-239) oxide rods clad in a high temperature-resistant metal. This core is surrounded on all sides by a "breeder blanket" of fertile U-238 rods (also in clad oxide form). The excess fission neutrons produced in the core "leak" out of the core and are absorbed in the blanket rods. Both the core and blanket are cooled by a flow of liquid sodium. This sodium is in turn cooled in heat exchangers and returned to the reactor by more or less conventional centrifugal pumps. The heat exchangers are cooled by a second flow of sodium, which in turn is cooled in a second set of heat exchangers, which produce steam for the turbine. The purpose of this intermediate sodium loop is to provide isolation between the sodium cooling the reactor and the steam and water in the turbine cycle, thereby practically eliminating the in-leakage of water and preventing it from contaminating the reactor coolant.

Despite this intermediate loop, the reactor operating temperature is sufficiently high to permit steam to be produced under modern fossil-fuelled plant conditions (~ 16.5 MPa with a single reheat to 540°C). There are a number of new Generation IV designs for fast breeder reactors, but none of them has been built yet, even as a prototype.

